Institut national de la recherche scientifique
Centre Énergie, Matériaux et Télécommunications

Ambient-Processed Halide Perovskites for Photovoltaic and Optoelectronic Devices

by

Ivy Mawusi ASUO

Thesis presented for the degree of
Doctor of Philosophy (Ph.D.) in Energy and Materials Science

Evaluation Committee

President of jury and internal examiner	Prof. Fiorenzo VETRONE INRS-EMT
External examiner	Dr. Joseph BERRY National Renewable Energy Laboratory (NREL), Golden Co. USA
External examiner	Prof. Jean-Michel NUNZI Department of Chemistry, Queen's University, Canada
Research director	Prof. Alain PIGNOLET INRS-EMT
Research Co-director	Prof. Sylvain G. CLOUTIER École de technologie supérieure (ETS), Montréal
Research Co-director	Dr. Riad NECHACHE INRS-EMT

Ambient-Processed Halide Perovskites for Photovoltaic and Optoelectronic Devices

Dedicated to my daughter Elorm Karyss and husband Nutifafa Y. Doumon

ACKNOWLEDGEMENTS

The completion of this piece of work has been an accumulation of hard work, passion, and guidance. As the Ghanaian proverb states: "*When one wants to climb a tree, one begins from the bottom*," this journey began years ago, and through perseverance and determination, it is now accomplished. Again, in Ghana, we say: "*A child who is to be successful is not to be reared exclusively in one home*." Thus, many individuals have partaken in this achievement. To this end, I would like to appreciate them. First, to the almighty God. Great is thy faithfulness. You are at the center of it all. I am thankful for your protection, provision, and strength.

Next, I wish to express my deepest gratitude to my supervisors Prof. Pignolet, Prof. Cloutier, and Dr. Nechache, for making this journey purposeful. As "*A good child takes advice from the wise and elderly*", I am privileged to have you all as my advisors to the successful completion of this thesis. Thank you for your guidance, training, knowledge transfer, and professional support. Your encouragements and persistent assistance enabled me to go through tough times. You have sharpened my skills to become a scientific researcher, for which I am sincerely grateful.

Special thanks go to my evaluation committee, Prof. Vetrone, Dr. Berry and Prof. Nunzi for your time, assessment and feedback on my thesis. I appreciate your valuable inputs.

Without my main collaborators, Dr. Ka, Dr. Gedamu, and Dr. Banerjee, this research would not have been this productive; all your scientific contributions and teamwork resulted in fruitful outcomes, a testament to the many collaborative publications.

To all other group members at the INRS (Lucas, Liliana, Ali, Julien, and Hossein) and ETS (Jaime, Felipe, Xiaohang, Paul, Francoise-Xavier, Soraya, Arjun, Suchismita, and Devika), you have all impacted me throughout this journey. Your friendship, academic supports, and collaborations helped in achieving a beautiful ending.

I would also like to recognize the invaluable assistance of the technicians, especially Mr. Chabanier and Dr. Harnagea at INRS, Dr. Saadati at ETS, and Mr. Masse. Also to all the staffs at INRS-EMT center (especially Hélène and Tatiana) and ETS electrical department.

A special appreciation to my funding agents MATECSS and FRQNT. Special thanks to the UNESCO chair Prof. Rosei for providing the platform for the MATECSS excellence scholarship and to Prof.

Vervoort, the then coordinator of the program, for his guidance. Without these enormous supports from both agencies, my dreams would not have been realized.

All my friends especially, Nimo, Sandrine, Ifeanyi, Aminat, Koffi, Nathaniel, Harriet, Sena, George, Joshua, Philip, Obed, Andrew, Mustapha, Nikki, and Linda etc., it would have been a boring journey without you. As they say, "*It takes the whole community to raise a child*", you have all indeed shaped my path to this accomplishment. Your constant encouragement, love, jokes, prayers, and motivation resulted in this beautiful outcome. I appreciate all your inputs in each unique way. Nimo, my 'personal person', thank you for always being there through it all. You believe in me and I'm grateful for your profound support.

To my family members, especially, Rogate, Godfried, Irene, Daniel, Albertha, Frederick, Esther, Rejoyce, Modester, Marius, my nieces, and nephews, I am overwhelmed with joy by your unconditional love and fervent prayers. I remember when you were at the airport to see me off on this adventure alone to a land where I knew no one. None of you ever forgot to check on me via text messages or a phone call. All your words of encouragement and prayers brought me this far. In particular, the two people to whom I am incredibly indebted are my mom and brother. Rogate: You called me almost every day to check on me and listen to all my challenges. Daniel: Your support, inspiration, and coaching since my childhood have made me a better person. These kind gestures kept me going and reminded me that I'm not only here for myself but also to make all of your proud whenever I feel down and homesick. As I have pushed through thick and thin to this end, I would forever be grateful to you all.

I am whole-heartedly indebted to my husband, Dr. N.Y Doumon, for his incredible support in my life. You were the pivotal point of this journey since we met in Abuja, and without your motivation, "push", and zealousness, I would not have come this far. The subject of my research work is something we have discussed since 2014, and I'm glad it became a reality. You have played an essential role in being my counselor, editor, comforter, and backup strength throughout this journey. Your unconditional love, patience, advice, emotional support, and determination brought me this far, and words are not enough to express my gratitude to you. Now that this chapter has ended, and on top of it, we have been blessed with a child (Elorm Karyss Doumon), I'm more excited about our future and other projects we have planned to accomplish together. In all, you are amazing!— *Mawu ne yra wo-*. Finally, to all others who have contributed in one way or another, I again say Akpe na mi!! Merci à tous!! Danke schön!! Thank you all!!

ABSTRACT

As the world energy consumption is expected to rise by 50% and plans for a drop in CO_2 emissions to net-zero around 2050 are made, we absolutely need to explore other renewable and sustainable energy resources and technologies to meet the challenge. The advent of halide perovskite materials has promoted incredible technological advances in the past years based on their device performance, flexibility, lightweight, and a vast range of device applications. Efficiency, stability, and cost are the three essential requirements for any technology to be commercially viable. Perovskite solar cells recorded a meteoric rise in efficiency to over 25% within only ten years of research and development. However, they are susceptible to degradation in the presence of moisture, ultraviolet light, and temperature. Due to the hygroscopic nature of the perovskite, they have been mostly processed in inert environments such as glove box which eventually increases fabrication costs and impedes their large-scale production. This thesis objective aimed to develop an affordable solution-based technology to fabricate high-quality perovskite thin-film with good efficiency and long-term stability under ambient conditions. Since the film fabrication method has a significant impact on the morphology of the film, its control proves to be an essential pathway in maximizing the performance of the devices. While critical, however, this is not sufficient. To obtain high-performing perovskite devices, the perovskite material stoichiometry, morphology, device architecture, and stability need to be optimized, which we were able to achieve entirely at the ambient conditions. We also highlighted the essential contribution of mixed-anions and moisture/humidity in the fabrication of perovskite films and their promising performance when integrated into solar cells.

The research presented here establishes a synthesis route for stable and reproducible halide perovskites by tailoring their microstructural properties via lead thiocyanate and solvent additives. Synergistic effects of solvent and solid additives on the morphology of the perovskite thin-film are also investigated. Various characterization tools are used to study the degradation mechanism of both the perovskite thin films and the related devices in which they are integrated, all fabricated and stored entirely under ambient conditions (25-55%RH).

The optimization of the crystallized perovskite layer to achieve superior solar cells efficiency and stability is further investigated using solvent-antisolvent treatment of mixed-cation halide

perovskite precursor materials during their deposition process. Solar cells have been fabricated, and the charge dynamics and the stability of the devices are studied. This approach results in reproducible, highly efficient solar cells with incredible stability in the ambient environment (25-55%RH) for more than ten months.

Furthermore, we explored other device applications of the perovskite by fabricating nanowires network-based photodetectors. A facile and low-cost method of preparing perovskite nanowires network via spin-coating atop both rigid and flexible pre-patterned substrates is presented. The microstructural and electrical properties of these novel nanowires-based optoelectronic devices, including photo-responsivity, detectivity, response time, and stability, are investigated.

Keywords: *Perovskite solar cells, photodetectors, stability, ambient processing, lead thiocyanate, pseudohalide, degradation, nanowires, trap density, additives.*

RÉSUMÉ

Alors que la consommation mondiale d'énergie devrait augmenter de 50 % et que des stratégies pour une réduction des émissions de CO_2 proche de zéro vers 2050 sont élaborés, nous devons absolument explorer d'autres technologies et d'autres ressources renouvelables et durables pour relever le défi. L'avènement des matériaux pérovskite hybrides organiques-inorganiques à base d'halogénure a permis des avancées technologiques incroyables au cours des dernières années en raison des performances, de la flexibilité, de la légèreté et de la vaste gamme d'applications des dispositifs fabriqués à base de ces nouveaux matériaux. L'efficacité, la stabilité et le coût sont les trois qualités essentielles requises pour qu'une technologie soit commercialement viable. Les cellules solaires à base de pérovskite ont enregistré une augmentation fulgurante de leur efficacité dépassant les 25 % après seulement dix ans de recherche et développement. Cependant, elles sont susceptibles de se dégrader en présence d'humidité, de rayonnement ultraviolet et de variations de température. En raison de la nature hygroscopique des pérovskites hybrides, elles ont été principalement synthétisées et traitées dans des environnements inertes tels que les boîtes à gants, ce qui augmente les coûts de fabrication et empêche leur production à grande échelle. L'objectif de cette thèse était de développer une technologie basée sur une solution abordable pour fabriquer des couches minces de pérovskites d'halogénure de haute qualité et les intégrer dans des dispositifs photovoltaïques avec une bonne efficacité de conversion et une stabilité à long terme (approchant les standards internationaux), tout cela dans les conditions ambiantes. Comme la méthode de synthèse des couches minces a un impact significatif sur la morphologie de celles-ci, le contrôle de la technique de fabrication s'avère être une voie essentielle pour maximiser les performances des dispositifs photovoltaïques. Ainsi, bien que critique, cela n'est pas suffisant dans notre cas. Pour obtenir des dispositifs à base de pérovskites d'halogénure performants, la stœchiométrie, la morphologie, l'architecture du dispositif et la stabilité du matériau pérovskite doivent être optimisées, ce que nous avons également pu réaliser, et cela entièrement dans les conditions ambiantes. De plus, notre recherche souligne la contribution essentielle des anions mixtes et le rôle de l'humidité dans la fabrication des couches de pérovskite ainsi que leurs performances prometteuses lorsqu'elles sont intégrées à des cellules solaires. Dans la recherche présentée ici, une approche de synthèse pour produire des couches minces pérovskites d'halogénure stables et reproductibles dans des conditions ambiantes a été établie, en adaptant

leurs propriétés microstructurales via des additifs de thiocyanate de plomb, d'eau et d'éthanol. Les effets synergiques des solvants et des additifs solides sur la morphologie des couches minces de pérovskite sont également étudiés. Divers outils de caractérisation sont utilisés pour étudier le mécanisme de dégradation à la fois des couches de pérovskite et des dispositifs dans lesquels elles sont intégrées, tous entièrement fabriqués et stockés dans des conditions ambiantes. L'optimisation de la couche de pérovskite cristallisée afin d'atteindre une efficacité et une très bonne stabilité des cellules solaires est étudiée en amont en utilisant un traitement solvant-antisolvant sur des précurseurs à cations multiples de pérovskite d'halogénure. Des cellules solaires ont été fabriquées, et la dynamique du transport des charges photogénérées, ainsi que la stabilité des dispositifs sont étudiées. Cette approche permet d'obtenir des cellules solaires reproductibles et hautement efficaces avec une très grande stabilité de plus de dix mois dans les conditions ambiantes (c.-à-d., 25-55% HR).

De plus, des photodétecteurs basés sur des réseaux de nanofils de pérovskites d'halogénure ont été fabriqués. Une méthode facile et peu coûteuse de synthèse de tels réseaux de nanofils de pérovskites via un revêtement par enduction centrifuge sur des substrats rigides et des substrats flexibles préalablement structurés est présentée. Les propriétés microstructurales et électriques de ces nouveaux dispositifs optoélectroniques à base de nanofils de pérovskite d'halogénure organiques-inorganiques à base d'halogénure, y compris leur photo-réactivité, leur détectivité, leur temps de réponse et leur stabilité, sont étudiées et présentées.

Mots-clés : *Cellules solaires pérovskite, photodétecteurs, stabilité, traitement ambiant, thiocyanate de plomb, pseudohalogénure, dégradation, nanofils, densité de piège, additifs.*

TABLE OF CONTENTS

LIST OF FIGURES

Chapter 1: General Introduction

1.1 Solar Energy

The increasing global energy demand is still one of the most critical challenges in the 21st century. Energy is needed in all aspects of life. And with the fast-growing global population, the demand for energy keeps rising exponentially. For centuries, most energy supplies have primarily relied on fossil fuels, such as oil, coal, and natural gas. These non-renewable resources account for about 85% of the current global energy consumption, as reported by the International Energy Agency (IEA).[1]

Moreover, the global energy demand is still on the rise. For instance, in 2018, this demand grew by 2.3%.[2] This growth is more than twice the yearly average growth since 2010, resulting in a 1.7% growth in energy-related carbon dioxide (CO_2) emissions compared to 2017.[2] Besides the growing concern about global warming due to greenhouse effects, these figures call for an urgent need to rethink energy conversion and use it responsibly as human activities are responsible for these effects. Thus, one needs to reduce the dependency and exploitation of non-renewable sources and adopt clean and sustainable alternative energy sources. For instance, during the first four months of the COVID-19 pandemic in 2020, the global energy demand dropped due to the lockdown in various parts of the world. Interestingly, this drop in demand resulted in lower global CO_2 emissions. CO_2 emissions in the first quarter of 2020 were over 5% lower than in the first quarter of 2019, according to reports by IEA.[3] The most staggering observation is that CO_2 emissions decreased more than the energy demand in the first quarter of 2020, leading to a predicted overall decrease of 8% in CO_2 emissions for 2020 compared to 2019.

Renewable energy sources, including wind, solar, geothermal, biofuels, and hydropower, can provide clean and sustainable resources with less adverse environmental impacts. Among these renewable energy resources, solar energy is among the most desirable. This is because the earth receives a massive amount of energy from the sun's irradiation, which is about 1.75×10^{17} W.[4] Thus, the sun's radiation reaching the earth's surface every hour would be sufficient to mitigate global energy usage for one year. Recently, the global energy generation from photovoltaic rose by 31.2% from 2017 to 2018.[2]. The question arises: '*Is solar energy then a suitable solution to*

our energy and global warming problems?' Although the sun radiation is free, we must be mindful that the cost of manufacturing devices to convert this energy into electricity and energy distribution is high. One other problem is that solar radiation, particularly for terrestrial utility, is intermittent and thus not available at all times of the day. Hence, it is essential to develop energy storage systems for such technologies to enable reliable power consumption and balance the electricity generation and demand. Fortunately, there are recent developments in the direction of manufacturing storage systems for renewable energy resources[5,6]. In parallel, we need to explore ways to make solar energy technology available and affordable to all and sundry.

1.1.1 Solar Technologies

Given that the world energy consumption will rise about 50% by 2050,[7] and the quest for balancing demand and supply, other sustainable and cheaper energy sources are explored. Renewable energy sources excluding hydro and traditional biomass – primarily wind and solar - remained low in primary global consumption. However, the world's attention has shifted to solar energy for electricity generation for various applications. Solar technologies can harness energy from the sun for a range of usages, such as generating electricity, drying food, lighting, and heating water for domestic, commercial, or industrial use. The three main ways to harness solar energy are solar thermal and cooling systems, solar concentrators, and photovoltaics (PVs). PV emerged on the energy scene with Silicon (Si) solar cells in the 1950s and was mainly used as an off-grid power supply for satellite applications[8]. Since then, there have been pronounced growths due to research and development (R&D) in the PV community.

A look at the global photovoltaic market shows a tremendous steady increase since 2009 from 23 GW to 627 GW in 2019 (**Figure 1.1**).[9] Thus, the continual recorded growth has presented an opportunity for a clean energy source by generating electricity from the sun. Although there are still some challenges regarding the integration and deployment of solar energy technologies, such as governmental policies and regulations in many countries, the solar cell market growth as of 2019 is incredibly promising compared to ten years ago. Moreover, over the recent years, some governments have subsidized the cost of solar panel installations and provided incentives that helped lower the cost of solar cells and make the technology competitive. It is imperative to highlight the incredible effort that Costa Rica in Central America has made efforts over the years

to achieve more than 90% dependence on renewables. It is understood that in the past half-decade, less than 2% of the country's electricity consumed by its inhabitants is generated from fossil fuels[10]. Costa Rica may even have a surplus of renewable energy[10], and the government has set an ambitious goal of 37,000 electric vehicles on the road by 2022.

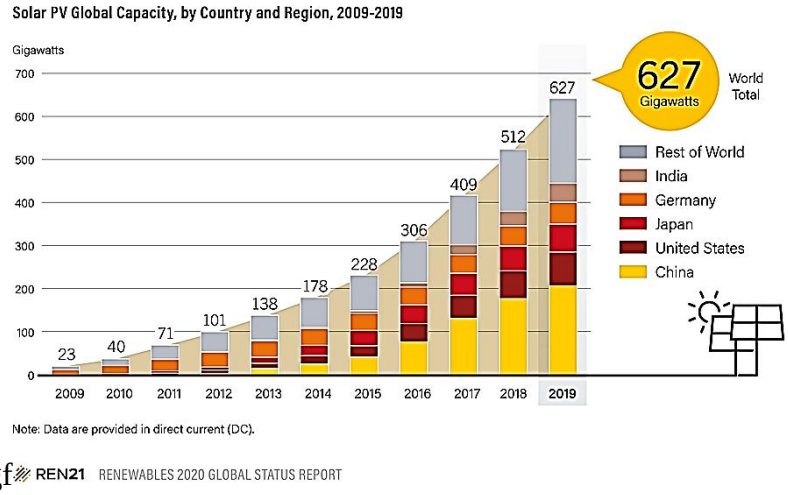

Figure 1. 1: Solar PV global Capacity by country and region from 2009-2019. It is copied from reference 9.

On these bases, the research for efficient, reliable, and cost-effective solar energy devices is of great importance towards their global energy supply and utilization. This drive for renewable energy sources saw the advent of solar cells and made possible the discovery of organic and inorganic semiconductors for such applications.

Solar cells have been used over the years as means for harvesting and converting solar energy to electricity for our day-to-day applications. Solar cells absorb energy from the sunlight and convert it directly into electricity through a semiconductor material. Currently, the global market for the photovoltaic industry is growing immensely. Even though many semiconductor compounds have been developed for solar conversion, silicon is still the most used material in the solar cell industry. For decades, it has been known to be one of the best materials for PV applications because of its optoelectrical properties and its availability for industrial processing and long-term stability. Also, silicon is non-toxic, and it is one of the most abundant elements on earth. Before silicon, as found in nature, can be used in the optoelectronic and photovoltaic industries, a comprehensive refining process must be applied. For applications in PV, the silicon must be purified. This can be achieved

by different modified methods to gain very high purity. The solar cells, made with such single crystalline silicon, have a larger share in the commercial market. However, the process involves high energy usage under high vacuum conditions and numerous lithographic steps, making it an expensive technology due to high manufacturing costs. Moreover, a large amount of pure silicon is lost during sawing into wafers. Thus, exploring ways to reduce processing and manufacturing costs and find other cost-effective alternate materials for PV applications is essential.

To this end, R&D has led to the discovery of other semiconductor materials used as absorbers in solar cells. They span from inorganic to organic through hybrid materials. Scientific studies have been exploring potential materials to achieve high-performance and durable PV devices. This has been made possible through novel processing methods, e.g., processing of thin films on substrates. Typical examples of inorganic materials for solar cells are Gallium Arsenide (GaAs), Cadmium Telluride (CdTe), and Copper Indium (Gallium) Selenide (CIGS). Organic materials are polymers, small molecules, etc., while hybrid materials are dye-sensitized, organic-inorganic halide perovskites. Depending on the material used, solar cells are categorized into three generations. The first generation is the silicon-based solar cells (single and poly-crystalline) with a record efficiency of 26.1% and 21.2%, respectively[11]. The second-generation solar cells use materials such as CdTe and CIGS as the absorber materials and have record efficiency of 22.1% and 23.4%, respectively, as shown in **Figure 1.2.**[11] The third (emerging) generation of solar cells is mainly based on organic and hybrid materials.

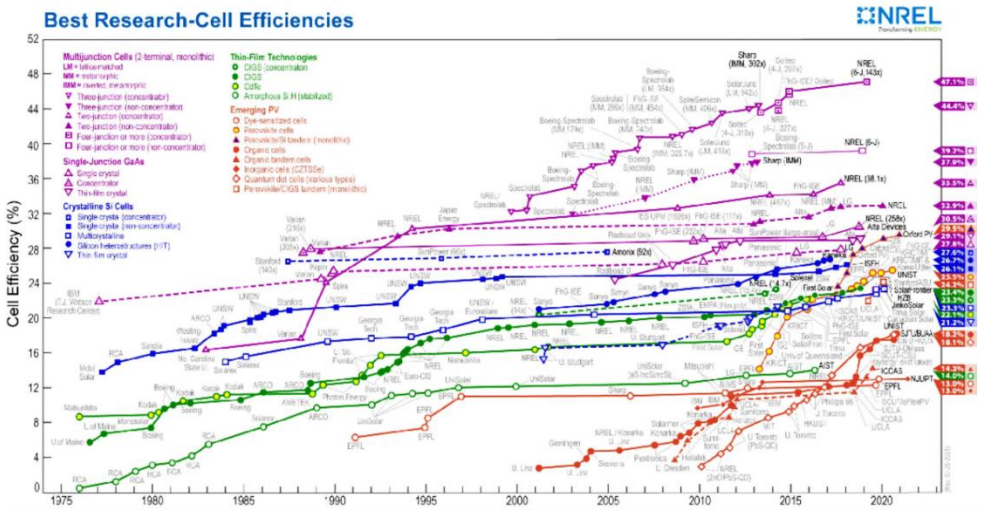

Figure 1. 2: NREL certified efficiencies of different solar cell technologies.[11]

Owing to the high production cost and complex fabrication processes associated with the first two generations, researchers have explored alternative materials for the third generation solar cells and advanced the PV field in a new direction. Thus, the third-generation solar cells are advantageous for the potential low-cost production of lightweight, thin-film, transparent, and flexible solar cells with low-temperature processing techniques. They also have a high potential for large-area production and building integrated applications. In this regard, organic molecules, quantum dots, and organic-inorganic halide perovskites are the materials that have stimulated substantial research interests in recent years. Moreover, the interest in these new materials is also driven by their solution processability (this guarantees fast manufacturing processes), remarkable and tunable optoelectronic properties, and ease of fabrication, which are all essential advantages for the production (ultimately the mass production) of novel optoelectronic and photovoltaic devices. Herein, this thesis focuses on an ambient fabrication of organic-inorganic halide perovskite materials for stable optoelectronic and photovoltaic device applications.

1.2 Perovskites: Short History

Perovskite refers to the crystal structure of the mineral $CaTiO_3$, discovered in 1839 by Gustav Rose and named after a Russian mineralogist, Count Lev A. Perovski[12]. Subsequently, any compound with an ABX_3 stoichiometry and the same crystal structure or a crystal structure resulting from a structural distortion of the ideal cubic perovskite structure is classified as perovskite-like and very often, even if improperly used, just as perovskite. In the ideal case, the A-cations are at the corners of the cubic or almost cubic unit cell, with the B-cations at the center of the unit cell, octahedrally coordinated with the X-anions (generally chalcogens - mainly oxygen- or halogens) occupying the face-centered positions. One exceptional characteristic of perovskites is their compositional and structural flexibility, which enables the tunability of their properties through the chemical substitution of A, B, or X site elements for various applications. Different perovskite materials, such as metal oxide-based and halide perovskites, have been extensively studied for several device applications. Examples of metal oxide-based perovskites include $PbTiO_3$, $PbZrO_3$, and $BaTiO_3$,[13–18] which have their X-sites occupied by oxygen. In some cases, the crystal structure is perovskite-like, as in the case of the double-perovskites $BiFeO_3$ and Bi_2FeCrO_6, or for $LiNbO_3$ and $LiTaO_3$. However, these highly distorted perovskites generally have a crystal structure too far away from the parent cubic perovskite to have an actual perovskite crystal structure. Indeed, unlike the

perovskites, their small A-cation has 6-fold coordination. In the case of organic-inorganic halide perovskites (OIHP), A is an organic cation, i.e., an ionized organic molecule such as methylammonium (MA) or formamidinium (FA) positively charged ($CH_3NH_3^+$ (MA^+) or $NH_2CHNH_2^+$(FA^+)), B is a divalent metal cation (such as Pb^{2+}, Sn^{2+}, Ge^{2+}) and X is a halogen/anions (I^-, Br^- or Cl^-)[19] as shown in **Figure 1.3**.

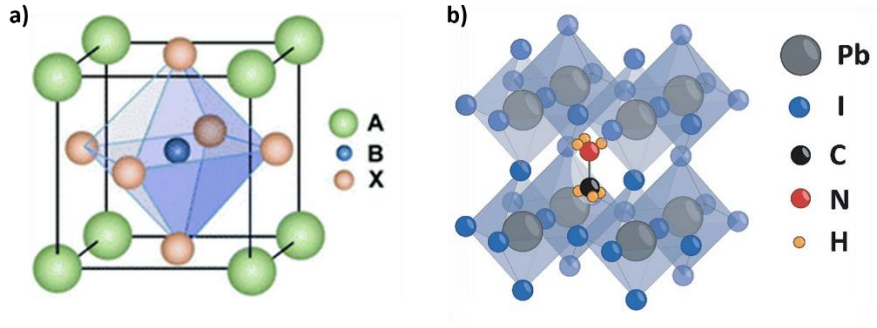

Figure 1. 3: a) A generic perovskite structure of the form ABX_3 and b) chemical structure of organic-inorganic halide perovskites showing the location of each element.

It has become common knowledge in the literature that just as perovskites adopt different crystal structures, they can equally form different phases, with some stable and others unstable. The Goldschmidt tolerance factor (*t*) is used to determine whether an ABX_3 composition forms a phase with a stable perovskite structure or not [20]. This tolerance factor *t* can be calculated from the ionic radius of the A, B, and X atoms using equation (1.1)[20]:

$$t = \frac{r_A + r_x}{\sqrt{2}(r_B + r_x)} \tag{1.1}$$

r_A, r_B, and r_X are effective ionic radii for *A, B,* and *X* ions, respectively. Perovskite structures could be formed when t is between 0.8-1.1. If *t* falls between 0.9-1, then cubic perovskite structures with high phase stability are formed. If $t > 1$, indicating a large A-cation, then a tetragonal or hexagonal crystal structure will be formed. If *t* is between 0.71-0.9, indicating a small A-cation, the structure will be orthorhombic or rhombohedral. Finally, $t < 0.71$ results in high distortion and leads to different structures, such as the ilmenite ($FeTiO_3$) crystal structure[20]. For example, in halide perovskites, the calculated ionic radii of FA^+, MA^+, Cs^+, Pb^{2+}, I^- and Br^- are 2.53, 2.16, 1.67, 1.19, 2.20, and 1.96 Å, respectively[21,22]. The *t*-factor helps to tune the perovskite composition for various applications. For $MAPbI_3$ is tetragonal at room temperature with a *t*-factor is close to 1,

and by adding $FA^{+,}$ which has a larger ionic radius, the stability is anticipated to be improved. Hence, adding or substituting cations/anions to the perovskite affects the optical, electrical, and microstructural properties.

1.2.1 Advances in Perovskite-Based Optoelectronic Devices

The distinct semiconductor properties of perovskite materials, including high-absorption coefficient, ambipolar charge transport, low exciton-binding energy, ferroelectric properties, etc., have ignited huge interest in this class of materials for optoelectronic and photovoltaic applications. For instance, recently, the ferroelectric and photovoltaic effects of $BiFeO_3$, $Bi_2FeCrO_{6,}$ and $BiMnO_3$ have been extensively studied[16,18,23,24]. These materials are ferroelectric; they possess a spontaneous polarization even in the absence of an electric field, and this polarization is switchable. Therefore, the internal electric field present within the material enables efficient charge carrier separation when implemented in PV cells. However, these metal oxide-based perovskite photovoltaic cells exhibit very low power conversion efficiency (PCE), due to their large bandgap and insulating properties, characteristic of ferroelectric materials[24].

In recent years, organic-inorganic halide perovskite (OIHP) materials have emerged as the ground-breaking class of materials in the field of thin-film photovoltaics. Mitzi et al.[19], back in the 1990s, premiered the studies of the structural properties of organic-inorganic hybrid perovskite material and engineered them for different thin-film devices, such as solar cells and transistors[25–28]. In 2009, Miyasaka's research group used OIHP in liquid electrolyte dye-sensitized solar cells (DSSCs) and reported a solar energy conversion efficiency of 3.8%.[29] However, the liquid electrolyte dissolved/degraded the perovskite material, making the solar cells highly unstable. Since then, little attention has been paid to perovskite solar cells (PSCs) due to the reported degradation and low power conversion efficiency. However, in 2012, organic-inorganic hybrid perovskite solar cells resurfaced on the PV chart with improved efficiency of 10.9%.[30] In order to address the degradation and low-efficiency problem, the liquid electrolyte was replaced with a stable solid-state version[31]. Solar cells were fabricated with an architecture similar to DSSCs where TiO_2 was used as the *n*-type electron transporting material and 2,2',7,7'-Tetrakis[N,N-di(4-methoxyphenyl)amino]-9,9'-spirobifluorene (Spiro-OMeTAD) as *p*-type hole transporting material, and the halide perovskite ($CH_3NH_3PbI_3$) as the active layer, was sandwiched between the

two charge-transporting layers[30]. Since this first report of all-solid-state halide perovskite-based solar cells, the power conversion efficiency (PCE) has skyrocketed from 3.8%[29] to a staggering 25.5 % [11] for single-junction architectures in 2020. This spectacular breakthrough has boosted the emerging PV field considerably, and the excitement for this novel class of material became widespread. As such, the last decade has seen PSCs gained a solid reputation as an impressively efficient and low-cost technology.

Notably, it has been shown that the bandgap of OIHP can be tuned between 1.55-2.3 eV by changing the cation or anion elements to access different parts of the solar spectrum[32–35]. Thanks to their excellent semiconducting properties[36–39], besides being used for solar cells[40–44], OIHP has been optimized and used for other optoelectronic devices such as photodetectors[45–51], light-emitting diodes (LEDs)[52–58], and transistors[59–61]. Nevertheless, the most significant limitation facing perovskite solar cells (PSCs) and optoelectronic devices are that they do not demonstrate sufficiently long-term stability in a wide range of environments. Importantly, for commercial viability and to compete with commercial solar cells, OIHP solar cells must last for at least ten year with little degradation while offering low-cost fabrication techniques. Whether or not PSCs are capable of such long-term stability under any operating conditions is still under investigation. In the early reports and under the laboratory environment, device stability of less than 500 hours has been reported for $CH_3NH_3PbI_3$[41,62]. However, recently, intensive R&D on perovskite materials has permitted striking advancement in the stability and PCE of PSCs[63,64]. This advancement is credited to many factors, such as improved processing of the active layer, i.e., the perovskite thin-films, crystallization, microstructure modification, and advanced device architectures, as well as selective charge-transport-layer modifications.

1.3 Operation of Solar Cells and Photodetectors

A solar cell should have the ability to absorb incident light, generate charge carriers and transport the charges to the electrodes. Generally, these purposes are achieved using a semiconductor material. Semiconductors are characterized by an energy bandgap, which is the gap that separates the valence band (VB), where electrons occupy the energy states, from the conduction band (CB), where no energy states are occupied. The light absorption is a characteristic and vital parameter of the active layer material used to make the solar cell, and it depends on its bandgap. Incident light with photon energy equal to or greater than the bandgap is absorbed while the excess energy is

dissipated as heat. However, the photon energy will not be absorbed if it is smaller than the bandgap of the absorber. Consequently, the absorption spectrum of the material is the fraction of incident radiation absorbed by the material over the range of wavelengths of the solar spectrum **(Figure 1.4a).** The light absorbed leads to the generation of charge carriers (electron-hole pairs), followed by their separation, transport and collection at the external electrodes. The built-in potential due to the difference in work functions of the electrodes causes diffusion or drift of the photo-generated charges with electrons to the cathode and the holes to the anode. Other mechanisms, such as recombination or annihilation of electron-hole pairs, can occur in different forms (radiative or non-radiative) and negatively affects the overall performance of the solar cell.

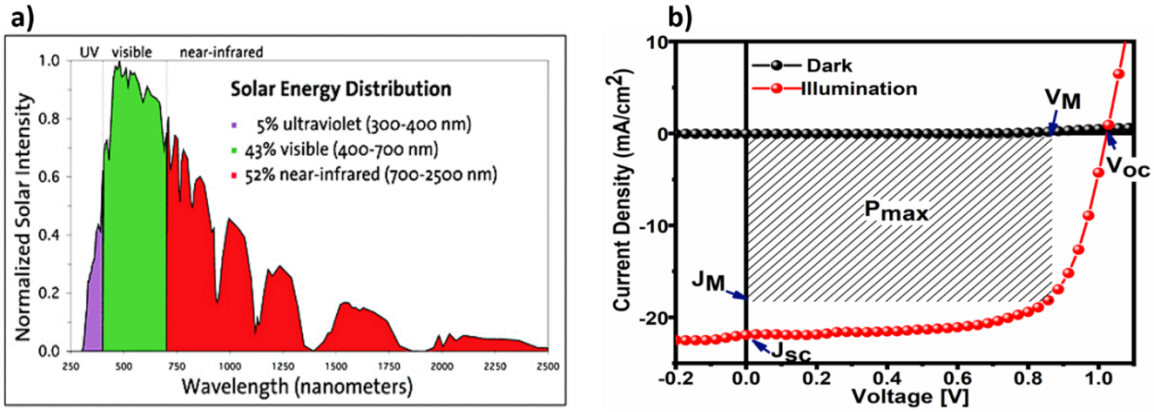

Figure 1. 4: a) Solar energy distribution diagram showing the ultra-violet, visible, and infrared radiation portions of the solar spectrum. b) An example of the *J-V* characteristic curve of a solar cell under dark (black) and illumination (red) conditions. P_{max}: maximum power, V_M: voltage at P_{max}, J_M: current density at P_{max}, V_{OC}: open-circuit voltage, and $J_{SC:}$ short-circuit current density.

Similarly, in a photodetector device, the creation of electron-hole pairs results from the absorption of light. Charge-carrier separation and migration give rise to a photocurrent, the portion of the photo-generated charge carriers collected by the electrodes. Photodetectors can be categorized into two types: (i) Photoconductors and (ii) Photovoltaic photodetectors. The photoconductor consists of a simple semiconductor layer, with two ohmic contacts at each end[65]. In contrast, the photovoltaic photodetectors operate based on the internal electric field of a *p-n* or Schottky (metal-semiconductor) junction to achieve charge separation and generate the asymmetry and diode behavior. In such configurations, an energy barrier height is established; hence the current generated is not linearly dependent on the applied electric field[65]. The main advantage of the photoconductors over photovoltaic photodetectors is their high gain, i.e., their high response

compared to photovoltaic detectors. In this thesis, our discussions will focus on the fabrication of photoconductors using OIHP materials as the active layer.

1.3.1 Mechanism of Charge Transfer Processes in Perovskite Solar Cells

The general working mechanism of a PSC[66] is illustrated in **Figure 1.5**. In a PSC, light is absorbed by the perovskite thin film to produce excitons (electron-hole pairs). Due to the high dielectric constant of the perovskite material, the excitons easily dissociate into free electrons and holes and are effectively transported and collected as photocurrent[67]. The electrons are then selectively injected into the CB of the electron transport layer (ETL) (1) and collected at the FTO electrode. The electron transport material is chosen such that the holes are blocked due to an unfavorable band alignment for holes. Likewise, the holes in the VB of the perovskite are injected into the hole-transporting layer (HTL) (2) while the electrons are blocked[68]. Then, at the two counter electrodes (FTO and gold), the charge carriers are efficiently collected and extracted as photocurrent in the external circuit.

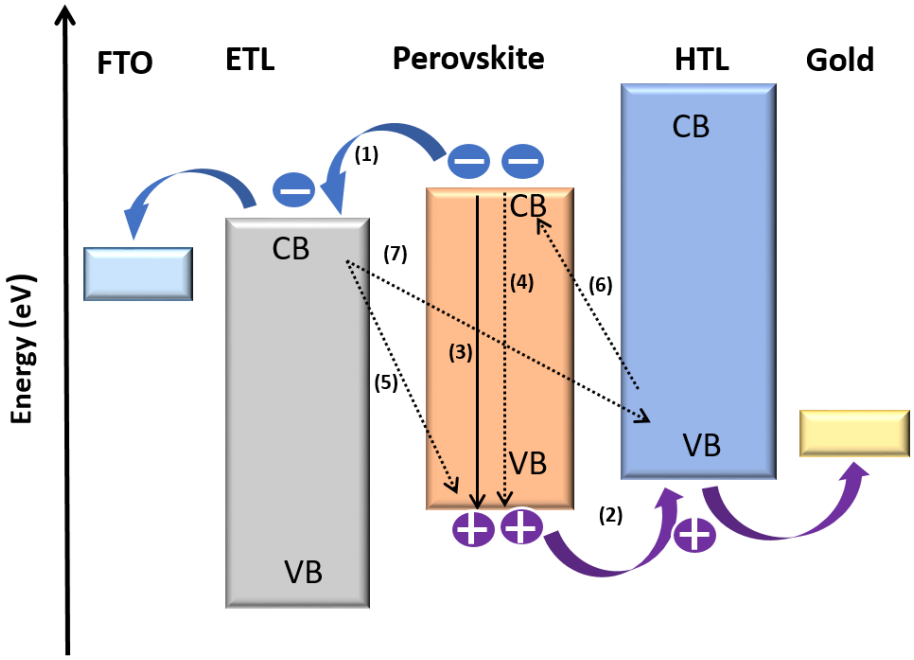

Figure 1. 5: Schematic diagram of energy band levels and charge transport processes of electrons and holes in perovskite solar cells. The arrows (1-7) indicate the direction of the charge transfer. The blue circle represents the electrons with a white minus sign, and the holes are the purple circles with a white plus sign. (FTO-Fluorine –doped Tin Oxide coated glass).

Other unwanted competing processes that affect the performance of the PSC include exciton annihilation resulting in photoluminescence(3), or non-radiative recombination (4), reverse transfer of electrons and holes, and recombination of the charges at the interfaces of ETL, HTL, and perovskite(5,6), and between the ETL and HTL (7). The surface recombination at the interfaces (5-7) could mostly occur due to pinholes/voids in the perovskite thin film. Therefore, these unwanted processes can be suppressed by tailoring the morphology of the perovskite thin film and device engineering by selectively choosing the contact materials and electrodes.

1.3.2 Solar cells and Photodetectors: Important parameters

Both solar cells and photodetectors are devices that convert an optical signal into an electrical signal. While solar cells are optimized for power conversion efficiency, photodetectors are optimized for light detection. Both devices have similarities in terms of operation, but there are some differences among them, such as the operating wavelengths and the optical source for which they are designed. A solar cell usually has a larger area, a higher spectral response over a larger range of wavelengths, a high PCE, and high external quantum efficiency under zero or moderate positive bias. While a photodetector has a smaller area, it operates in a narrower wavelength range corresponding to the wavelength of the optical signal to be detected. It also has high detectivity and high external quantum efficiency, low noise, and a fast response time[69]. Both devices, however, must be stable under their operating conditions.

Current density-voltage curves are used to evaluate the performance of the devices. The typical characteristic curve of a solar cell under dark and illumination is illustrated in **Figure 1.4b**. The critical parameters of a solar cell include the short-circuit current density (J_{SC}), the current density (*J)* where the voltage equals zero; the open-circuit voltage (V_{OC}) at $J = 0$; and the fill factor (FF). These parameters are used to determine the PCE and are determined directly from the *J-V* curve of solar cells under illumination. These four parameters: J_{sc}, V_{oc}, FF, and PCE, are key to the performance of a solar cell. The *J-V* characteristic curves of our solar cells are obtained by illuminating the cells using a solar simulator that replicates the solar spectrum (**Figure 1.4a**). The FF, which is a measure of the quality of the solar cell, is determined by:

$$FF = \frac{J_M V_M}{J_{sc} V_{oc}} = \frac{P_{\max}}{J_{sc} V_{oc}} \qquad (1.2)$$

where J_M is the current density at maximum power (P_{max}) and V_M voltage at P_{max}. Thus the P_{max} is defined as:

$$P_{\max} = J_M V_M = FF(J_{sc} V_{oc}) \quad (1.3)$$

And the PCE of the cell is given by:

$$PCE = \frac{P_{\max}}{P_{in}} = FF \frac{J_{sc} V_{oc}}{P_{in}} \quad (1.4)$$

where P_{in} is input power or the incident light power density of the solar simulator, equivalent to 100 $mW.cm^{-2}$.

Another critical parameter is the external quantum efficiency. The external quantum efficiency (EQE), also known as the incident photon conversion efficiency, is the measure of the number of electrons generated (n_e) per the number of the incident photon (n_{ph}) at a specific wavelength (λ):

$$\mathrm{EQE}\ (\lambda) = \frac{n_e}{n_{ph}} = \frac{hc}{q\lambda} \frac{J(\lambda)}{\mathrm{P_{in}}(\lambda)} \quad (1.5)$$

J(λ) is the photocurrent as a function of the wavelength, *h is* Plank's constant, *q* the electrical charge, *c* the speed of light, and P_{in} the power intensity of the incident light.

To confirm the values of J_{sc} measured under illumination with an AM1.5G (Air Mass 1.5 Global condition, defines 1 sun to be equal to 100 $mW.cm^{-2}$ of irradiance from a solar simulator), the integrated current density (J_{int}) is obtained by integrating the EQE per the equation:

$$J_{int} = q \int_{\lambda_1}^{\lambda_2} \mathrm{F}(\lambda)\mathrm{EQE}(\lambda) d\lambda \quad (1.6)$$

F(λ) is the photon flux as a function of the wavelength, and *q* is the electron charge. We used the photon flux of AM1.5G downloaded from (*http://rredc.nrel.gov/solar/spectra/am1.5/*).

In contrast, photodetectors are characterized by their ability to generate current under an applied bias and illumination. The electric field in the depletion region causes photo-generated carriers to separate and be collected across the junctions. This gives rise to the generation of photocurrent. Thus, the photocurrent is the difference between the dark current and the current under illumination ($I_{ph} = I_{light} - I_{dark}$).

Also, the spectral responsivity of a device, which describes the amount of generated photocurrent (J) per incident optical power at a given wavelength, is determined using the equation:

$$R(\lambda) = \frac{J(\lambda)}{\mathrm{P_{in}}(\lambda)} \tag{1.7}$$

The capability of a photodetector to detect the weakest optical signal is characterized by its specific detectivity (D*), which is the inverse of the noise-equivalent power (NEP) normalized by the square root of the area of the bandwidth. In general, the detectivity is defined by the equation:

$$D^* = \frac{\sqrt{\mathrm{A}}R}{\sqrt{2qI_d}} \tag{1.8}$$

where A is the active area, R is the responsivity, q is the elementary charge, and I_d is the dark current. The detectivity is evaluated by the spectral responsivity, the active area, and the dark current of the photodetector device at a desirable voltage. To achieve a high detectivity, the dark current should be very low, and this depends on the semiconductor material used to fabricate the device and the device architecture.

Finally, the response time of photodetectors, which depends on the surface area, and distance traveled by charge carriers in the depletion layer, is also a key parameter. To obtain a fast response speed, the width of the depletion layer should be very close to the active surface. Thus, the photo-detection response time is determined from the rise and the decay time constants, which are evaluated either using a bi-exponential curve fitting[70] or by the time interval during which the photocurrent rises from 10 to 90% and falls from 90 to 10%[71]. All the parameters mentioned above highly depend on the microstructural, optical, and electrical properties of the OIHP thin films.

1.4 Fabrication and Processing Techniques of Halide Perovskites Optoelectronic Devices

1.4.1 Device Architecture and Fabrication

In general, perovskite solar cell architectures are designed so that the OIHP active layer is located between two charge-selective layers and sandwiched between two electrodes. The top is a metal electrode, and the bottom is a transparent conductive oxide (TCO) electrode, allowing the photons to reach and be absorbed by the perovskite layer. The two charge selective layers are an electron transporting material (ETM) and a hole transporting material (HTM). Depending on the arrangement of the ETM and HTM, PSCs can be classified into three architectures: planar (**Figure**

1.6a), mesoporous (**Figure 1.6b**), and inverted (**Figure 1.6c**)[33–35]. The planar structure consists of TCO/ETM/perovskite/HTM/Au or Ag, with mostly TiO_2 compact layer as the ETM and Spiro-OMeTAD as HTM. The TiO_2 compact layer is deposited onto the TCO, such as indium tin oxide (ITO) and fluorine-doped tin oxide (FTO) glass substrates, as shown in **Figure 1.6a**. The mesoporous device structure is similar to the planar configuration. The only difference is the additional mesoporous ETM (mostly TiO_2 or Al_2O_3) atop the compact TiO_2 layer. Finally, in the inverted architecture, the ETM and the HTM are swapped with respect to the planar structure. In this case, a small molecule such as [6,6]-phenyl-C_{61}-butyric acid methyl ester (PCBM) is used as the ETM, and a transparent conductive polymer such as Poly(3,4-ethylenedioxythiophene) polystyrene sulfonate (PEDOT-PSS) is used as the HTM[33,72].

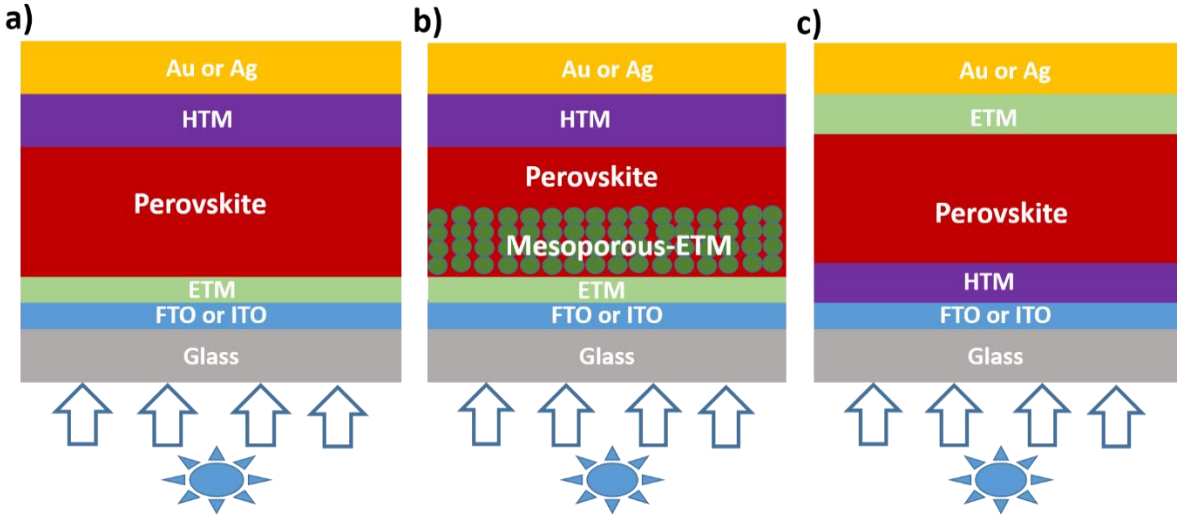

Figure 1. 6: Schematic of perovskite solar cells with a) planar, b) mesoporous, and c) inverted device architecture. (note: HTM: hole-transport material, ETM: electron transport material, FTO: Fluorine-Doped Tin Oxide, ITO: Indium Tin Oxide; ITO and FTO are both TCO electrodes).

Enormous progress has been made in optimizing the device performance by using various device architectures and organic-inorganic materials for the transport layers. Also, research has been done towards improving the morphology and crystallinity of the perovskite film by exploring different deposition methods, solvent treatments, and chemical composition substitution to fabricate efficient solar cells and optoelectronic devices.

Different methods, including vapor/vacuum deposition[73–77], inkjet printing[78,79], spray coating[80–82], etc., have been reported for fabricating perovskite thin film and related devices. Solution processing has also been widely employed for fabricating perovskite-based devices. This latter

method involves the dissolution of the precursor materials followed by its deposition via doctor blade coating, slot-die coating, or spin-coating. Among these deposition methods, spin-coating is a well-established technique used for solution-processed thin-film solar cells. We adopted the spin coating method throughout this thesis for solution-processing of perovskite-based PV and optoelectronic devices. This is because spin coating is an inexpensive technique that enables, to a great extent, the deposition from solutions of thin-film layers with relatively good control over the film uniformity and thickness, especially for small area devices.

1.4.2 Materials and Synthesis Methods

The perovskite precursor solution is prepared by dissolving the metal halide in an organic solvent via one-step or two-step solution processing. The metal halides used are all lead halides. They include lead iodide (PbI_2), lead chloride ($PbCl_2$), or lead bromide ($PbBr_2$). The organic component of the halide perovskite comprises materials such as methylammonium iodide (MAI), Formamidinium iodide (FAI), or Methylammonuim bromide (MABr). We utilized the commonly used organic solvents such as *N*,*N*-dimethylformamide (DMF), and Dimethyl sulfoxide (DMSO). Most of these materials are used under controlled environments to synthesize the organic halide films due to their sensitivity to humidity and their deterioration [63,83,84]. However, this thesis demonstrates a possible way to make thin films and nano-structured perovskite materials for solar cells and photodetectors under ambient conditions. More details on the halide perovskites preparations are provided in Chapter 2, and all other modifications are discussed in the subsequent chapters.

1.4.3 Processing Techniques: Morphological Control and Solvent Engineering

The requirement for achieving stable and high-performance PSCs is pinhole-free perovskite thin film with 'good' crystal structure and homogeneous morphology[85–87]. Obtaining these properties rely on reasonable control of the deposition method, the additives (solvents and solutes), device architecture, optimized precursor concentration, spin coating speed, post-annealing temperature, and processing conditions such as humidity and temperature[85–91]. Common pitfalls for the solution-processed perovskite thin films are inadequate coverage, 'poor' crystallinity, and the presence of many pinholes/voids. Non-compact perovskite film morphology is detrimental to the

device performance because it causes both electrical short circuits and the recombination of photo-generated carriers[92,93]. In line with these, various fabrication techniques have been explored to achieve the excellent performance of PSCs.

Through a one-step deposition method and chlorobenzene additive to aid fast recrystallization, Xiao et al. obtained a uniform and compact $CH_3NH_3PbI_3$ film with efficient solar cell performance[86]. Im et al. also reported the growth of $CH_3NH_3PbI_3$ cuboids with controlled size by varying the concentration of CH_3NH_3I and using a two-step deposition method[88]. Xiao et al. also found that solvent annealing, i.e., thermal annealing in the presence of solvent vapor, leads to the growth of large grains with increased crystallinity of perovskite films[94]. More specifically, they found that solvent annealing in DMF vapor enhanced both the microstructure and the electronic properties of the perovskite films. Despite the remarkable progress made in the device design and performance, establishing a suitable processing technique for controllable and scalable perovskite layers is highly desirable when considering their practical applications.

Thus, most investigations focused directly or indirectly on achieving high-quality perovskite films to increase the efficiency and stability of their devices.

The ambient environment accelerates degradation of OIHP by facilitating the rapid decomposition of the material into its constituents elements , such as PbI_2 [95]. In effect, most OIHP material synthesis, device fabrication, and testing are performed in an inert environment (eg. N_2-filled glove box) [63,96,97]. To operate in ambient, these devices are encapsulated to prevent such ambient-induced degradation. Thus, the fabrication under inert environment presents some level of complexity and increase production costs. To make low-cost OIHP devices, we will explore different methods spanning solvent-antisolvent treatments, pseudo-halides additive, mixed-cation-mixed-anion system, and two-step spin-coating deposition method to fabricate perovskite PV and optoelectronic devices.

1.5 Challenges of Perovskite-Based Technology

In general, for any optoelectronic technology to be commercially feasible, three critical parameters: namely, efficiency, cost, and lifetime need to be considered **(Figure 1.7a)**. Often, there could be a trade-off between them. The same is valid for perovskite optoelectronic technology[84]. Thus, OIHP-based devices must i) be of high efficiency, ii) low-cost, and iii) highly stable/reliable. PSCs are therefore competitive in terms of efficiency**,** as the PCE skyrocketed to a staggering

25.5% for single-junction and 29.5% for Si-perovskite tandem solar cells[11]. These PCEs are now comparable to the PCE values of the well-established silicon photovoltaic at 26.1%. However, there are identifiable challenges to the commercial viability of the technology.

1.5.1 Presence of Lead

Although these OIHP materials exhibit outstanding optical and electronic properties, the presence of lead (Pb) presents a potential environmental hazard and a challenge for the eventual commercialization of such solar cells. Several investigations have been carried out on the development of lead-free halide perovskites, attempting to replace or dope Pb with Tin (Sn), bismuth (Bi), or antimony (Sb)[98–105]. However, the performance and stability of these alternatives do not match that of lead-based devices due to differences in charge carrier transport, optical, and electric properties of the constituent elements. Nevertheless, in the recent lead-based perovskite solar cell, far less Pb is used than other technologies containing lead or other toxic substances. Moreover, this can be controlled by proper encapsulation and an appropriate method of disposal at the end of the device life[106–108].

1.5.2 Cost: Material and Fabrication Cost

Another vital parameter to consider that can set apart and favor a technology versus another is its availability and affordability in remote/deprived locations. The PSC technology thus needs to be low-cost in terms of production, maintenance, and material costs[109]. A method for synthesizing hybrid perovskites in ambient air, instead of the more complex and expensive controlled processing/production environment, will be a real breakthrough in this regard. However, there lies the challenge. The commercial viability of new energy-generating technologies, such as perovskite solar cells, ultimately relies on improving the costs per Watt peak (Wp) compared to existing competitions on the market[110]. Besides, in contrast to silicon, perovskite materials are soluble in a myriad of solvents. They can be easily sprayed or printed onto a surface, similar to inks or paints. This potentially makes PSCs much cheaper and simpler to manufacture on rigid and flexible substrates, which, in turn, opens up a wide range of new applications going beyond solar panels. Given this, we sort to fabricate perovskite-based devices in ambient air throughout this thesis to keep the cost of production even lower.

1.5.3 Stability

Stability measures the ability of the material or device to retain its properties over time. It usually translates into the lifetime of a material or device under different operational conditions/stressors as most materials or devices tend to degrade or deteriorate over time. The factors that affect the stability of the perovskite material and devices can be classified into two categories: intrinsic and extrinsic factors.

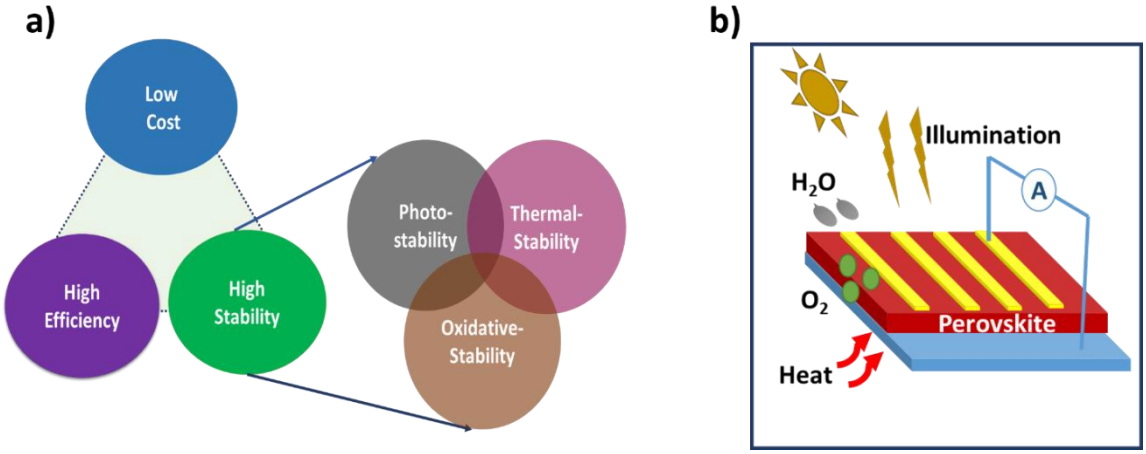

Figure 1. 7: a) The *golden triangle* for photovoltaic technology. The various types of stability or degradation mechanisms to be considered are as elaborated in the figure. b) Degradation factors (moisture, oxygen, heat, and illumination) that affect halide perovskite-based devices.

The intrinsic instability is related to the bulk perovskite material and the interface between the perovskite and the charge transport layers. In contrast, extrinsic instability is caused by external factors such as moisture, oxygen, and UV exposure[111], as illustrated in **Figure 1.7b**. We pay specific attention to the degradation of the perovskite active layer as it is the predominant part of the degradation of the device. That is, we mainly focus on explaining the mechanisms that govern the degradation of the perovskite thin films in the devices. Intrinsically, the degradation of the bulk perovskite is caused by thermal instability, photo-induced instability, ion migration, and hygroscopicity[112–115]. Thermal instability is caused by heat or elevated temperatures, resulting in thermal degradation. It can be suppressed by operating the cell at a constant temperature below or around the solar cell processing temperature, although this is difficult to achieve under real-life conditions. Recent works showed that thermal instability could be solved by tuning the chemical

composition of the perovskite to increase the decomposition energy, such as the use of cesium cation[63,116]. Also, continuous exposure to light can result in photo-induced degradation. This factor cannot be avoided as solar cells must be exposed to sunlight to generate electricity. However, filters, e.g., ultra-violet long-pass filters[117,118] and buffer inter-layers[112,113], have proven beneficial to reducing the impact of photo-degradation on solar cells.

Ion migration is almost inevitable in halide perovskites, and they manifest when external bias is applied across the perovskite device, resulting in hysteresis in the current-voltage curves[119–122]. Ion migration is mainly observed at defect sites, grain boundaries, and the interfaces between the perovskite and the transport layers[123–125]. However, this problem could be eliminated by grain boundary passivation[125–127] and ion substitution[128]. It is currently treated by cation/anion substitutions [126,129–131] and organic molecular additives[126].

The hygroscopicity of perovskites depends on the presence of moisture or humidity in the environment which results in oxidative degradation and morphological changes. Encapsulation[132] can more or less avoid it; however, since we synthesize our perovskite layers under ambient conditions, the effects of humidity/moisture and oxygen during their fabrication are inevitable. In the course of the perovskite synthesis, processing, and device measurements, oxygen and moisture in the atmosphere can directly affect the stability of the components (see the various reactions described in equations 1.9)[62,133]. First, due to the high sensitivity of halide perovskite, it tends to hydrolyze in the presence of moisture, leading to the degradation of perovskite, which occurs as follows:

$$CH_3NH_3PbI_3\ (s) \leftrightarrow PbI_2\ (s) + CH_3NH_3I\ (aq) \quad (1.9a)$$

$$CH_3NH_3I\ (aq) \leftrightarrow CH_3NH_2\ (aq) + HI\ (aq) \quad (1.9b)$$

$$4HI\ (aq) + O_2\ (g) \leftrightarrow 2I_2\ (s) + 2H_2O\ (l) \quad (1.9c)$$

$$2HI\ (aq) \leftrightarrow H_2\ (g) + I_2\ (s) \quad (1.9d)$$

Under the influence of moisture, oxygen, and UV radiation, reaction (1.9a) leads to the co-existence of CH_3NH_3I, CH_3NH_2, and HI in the film. There are two paths for HI to degrade in the next step. One path is a redox reaction in the presence of oxygen (1.9b); the other is a photochemical reaction, in which HI can decompose into H_2 and I_2 under UV radiation (1.9d).

According to reactions (1.9c) and (1.9d), the depletion of HI drives the whole degradation process of the perovskite layer[133].

Moreover, the perovskite thin-film directly interacts with the charge transporting layers in the bulk device structure, which could also be a degradation center. Hence a stable charge transport layer materials should be used to avoid inter-layer degradation. Consequently, non-hygroscopic materials such as carbon[129,134], inorganic transport layer materials[116,135], and metal oxide[83,136–139] have led to improved stability for PSCs.

In effect, under normal operation conditions, all degradation factors do occur. They can occur in pairs such as photo-oxidative degradation, thermo-oxidative degradation, and photo-thermal degradation **(Figure 1.7a)**. Usually, all three processes co-occur, making the study of degradation more complicated than anticipated. We only critically look at the oxidative degradation of our perovskite-based devices to streamline our work.

1.6 Scope of the Thesis

This thesis involves studies of the stability of halide perovskite materials for photovoltaic and optoelectronic devices. The main chemical elements in halide perovskite compounds with the best performance nowadays are lead (Pb) and iodine (I). Both are abundant materials and can be solution-processed. Thus, the material costs for the perovskite material are reasonably low. We seek to make PSC technology locally available and affordable around the globe especially, in rural/urban areas. Therefore, PSC technology needs to be low-cost in production, energy distribution, maintenance, and material costs. What we mean by low-cost is in terms of the fabrication methods we employ in this study. Devices are fabricated via spin-coating in ambient air. This aims to make perovskite optoelectronic research and technology accessible to developing countries. Besides, ambient conditions-processing of the perovskite materials will potentially lower the fabrication cost and pave the way for potential future local production of solar cells.

Herein, the main goal of this thesis is to find a low-cost synthesis route that enables a long-term stability of the perovskite materials. The first challenge is the synthesis of high-quality lead-based perovskite films via the solution process in ambient conditions. Synergistic effects of solvent additives on the morphology, stability, and efficiency of the perovskite thin films will be investigated. The aim here is also to reveal the advantages of tuning the morphology of the

perovskite films for their use in various optoelectronic applications, such as solar cells and photodetectors.

Also, the long-term stability of the materials has raised significant concerns for hybrid perovskite PV technology. In this context, the stability of the OIHP devices in ambient air is studied. We critically look at the ambient-induced (or oxidative) degradation of our perovskite-based devices. The goal is to understand the cause of the deterioration of the hybrid perovskite in a solar cell and develop innovative solutions to prevent or minimize the effects of such instabilities.

1.7 Thesis Outline

The organization of the thesis is outlined as follows:

Chapter 1 gives a brief background on solar technologies and halide perovskites for photovoltaic and optoelectronic applications and the scope of this work.

Chapter 2 presents the materials synthesis and characterization techniques used in this study.

Most of the results discussed in the following chapters are based on published articles from this research work. Chapters 3 and 4 relate perovskite thin film morphology to the stability and efficiency of their solar cells.

Chapter 3 describes the role of moisture and ethanol additives in the quality of the morphology and crystal structure of perovskite thin films for enhanced device performance.

Chapter 4 presents highly efficient and stable mixed-cation perovskite solar cells fabricated via thiocyanate doping and solvent-anti-solvent treatment.

Chapter 5 presents the synthesis and characterization of perovskite nanowires and their incorporation on rigid and flexible substrates for efficient, stable, and ultrafast photodetectors.

Chapter 6 accounts for perspectives towards lead-free perovskites and the outlook on the research work described in this thesis.

Finally, each of the main chapters, i.e., 3 to 5, is followed by an appendix. The appendix consists of some supporting but valuable information and figures.

Chapter 2: Materials Synthesis, Devices, and Characterization Techniques

This chapter discusses the materials used, synthesis, and processing of the films and nanowires of these materials, architecture, and fabrication of the devices. Finally, we will look at the characterization techniques used to probe the performance and stability of the materials and devices.

2.1 Materials

2.1.1 Perovskite Materials

In this study, we explored the application of halide perovskite materials as an active layer for solar cells and photodetectors. As previously described in **section 1.3**, the perovskite ABX_3 structure comprises of a monovalent organic cation [$CH_3NH_3^+$ = (MA^+) or $NH_2CHNH_2^+$ = (FA^+) or a combination thereof] at the A-site, B-site by a divalent metal cation (such as Pb^{2+}, Sn^{2+}, or Ge^{2+}) and X-site by a halogen/anions (I^-, Br^- or Cl^-)[19]. In our case, we developed a method for preparing methylammonium lead iodide ($CH_3NH_3PbI_3$) and its pseudohalide-based ($CH_3NH_3PbI_{3-x}(SCN)_x$) thin films entirely at the ambient conditions, i.e., without the need of a glove box for controlled atmosphere or humidity. We used lead iodide (PbI_2), methylammonium iodide (MAI) to prepare the $CH_3NH_3PbI_3$ perovskite precursor solution. All chemicals are of analytical grade and used without further purification.

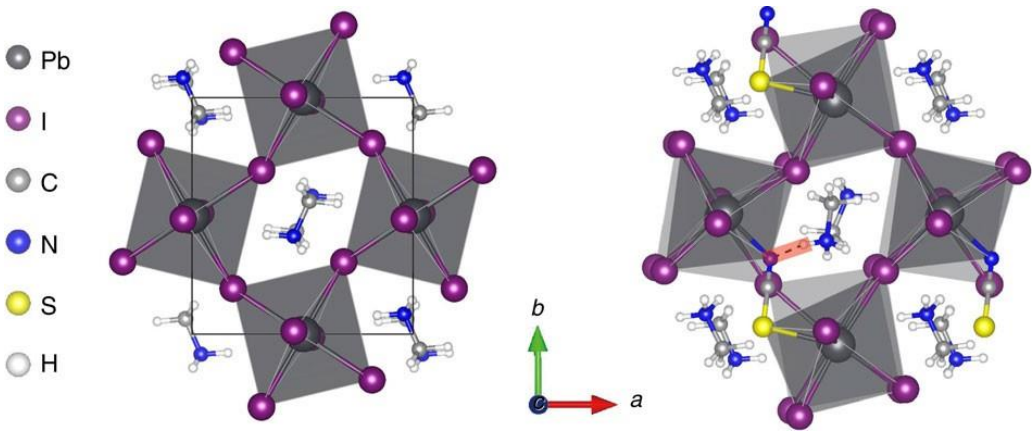

Figure 2. 1: Illustration of calculated crystal structures of a) $CH_3NH_3PbI_3$ and b) $CH_3NH_3PbI_{3-x}(SCN)_x$ with a hydrogen bond between SCN^- and CH_3NH_3 highlighted with red dash line[140].

$CH_3NH_3PbI_3$ perovskite is known to be unstable under operational conditions. Prior to this work, there was little literature about the experimental incorporation of monovalent anion in the X-site towards the synthesis of ambient-stable perovskites. Hence, we modified the composition of $CH_3NH_3PbI_3$ by incorporating pseudohalide, lead thiocyanate ($Pb(SCN)_2$), to stabilize the perovskite[42,48,141]. Pseudohalogens are molecules consisting of more than two electronegative atoms, which in a free state resemble the halogen. Thus, SCN^- is analogous to I^- hence its addition in the $CH_3NH_3PbI_3$ results in the substitution of I^- by SCN^- in the perovskite[48]. The calculated crystal structures of $CH_3NH_3PbI_3$ and $CH_3NH_3PbI_{3-x}(SCN)_x$ are shown in Figure 2.1[140]. This work was reported by Tai et al., and they found that the theoretical band structure of $CH_3NH_3PbI_{3-x}(SCN)_x$ is comparable to that of $CH_3NH_3PbI_3$. There are ionic interactions between SCN^- and adjacent Pb atoms and hydrogen bonds forming between SCN^- and $CH_3NH_3^+$ resulting in improved chemical stability of the perovskites[140,142]. Based on such reports, there is currently relatively more work on employing pseudohalides for perovskite-based devices[75,143–145].

2.1.2 Solvents and Solvent Additives

The organic and inorganic components, namely MAI, PbI_2, and $Pb(SCN)_2$ used for the preparation of the perovskite precursor solutions, were dissolved in polar aprotic solvents anhydrous N, N-dimethylformamide (DMF), and anhydrous dimethyl sulfoxide (DMSO). Both solvents have similar polarity and are versatile for dissolving many compounds. In most cases, we used only DMF for the precursor solutions, and in other cases, a combination of both solvents in volume ratios. MAI is also soluble in isopropanol (IPA), so we separately dissolve MAI in IPA in the case of two-step deposition. Solvent additives such as deionized water and ethanol were used as a moisture-assisted method to enhance the morphology and crystallinity of the perovskite thin films. All solvents are also used as received from Sigma-Aldrich without further purification.

2.1.3 Transport Materials

As mentioned in chapter 1, the general solar cell device structure (Figure 2.2 (a,b)) consists of the perovskite active layer sandwiched between an electron transport layer and a hole transport layer. We carefully selected the transport layer materials based on the literature since our focus is on synthesizing ambient-stable perovskite materials for device applications. The selection of the

transport materials is essential because it helps to effectively extract and transport electrons/holes to the counter electrodes in order to reduce carrier recombination and enhance the device performance.

The electron transporting material, ETM, is an essential component of PSCs and contributes to the performance of the device. The role of the ETM is to facilitate the extraction of the photo-generated electrons from the perovskite layer, transport them to the electrode, and block the photo-generated holes[33,66,146]. Thus, the energy level of the ETM should match that of the perovskite. The energy level of the bottom of its conduction band should be between that of the perovskite and the Fermi level of the electrodes to avoid losses and ensure efficient charge extraction (Figure 2.2c). To block the holes, the energy of the top of the valence band of ETM should also be lower than that of the perovskite. Therefore, the choice of ETM is crucial. The commonly used electron transport layer is titanium dioxide (TiO_2). TiO_2 has been extensively studied and shown to be an efficient ETM for PSCs[66,147–149]. Herein, we used commercially available TiO_2 as the ETM because it has good energy level alignment with the perovskite, a wide bandgap, and is transparent to visible light[149,150].

The hole transporting material, HTM, is another vital component in the solar cell. This layer helps extract the photo-generated holes from the perovskite layer, transport them to the electrode, and block the photo-generated electrons concurrently[33,66,146]. Likewise, the energy band alignment should be favorable to achieve this goal. The energy level of the top of the valence band of the HTM should be between that of the perovskite and the Fermi level of the electrode. And the bottom of the conduction band is higher than that of the perovskite (**Figure 2.2c**). As previously stated in **section 1.4.1**, we chose Spiro-OMeTAD as the HTM in our studies as it has relatively good mobility of 4×10^{-5} $cm^2.V^{-1}\cdot s$[151] and a better band match with the perovskite.

2.2 Device Architecture

In this thesis, we fabricated two different device architectures of solar cells, as shown in **Figure 2.2(a,b)**. These are planar configuration of FTO/ETM/perovskite/HTM/Au and FTO/ETM/mesoporous ETM/perovskite/HTM/Au. The mesoporous ETMs were used due to their high permeability and large surface-to-volume ratio, which helps to improve the performance of the device. These architectures consist of layered materials mainly deposited through the spin

coating technique (see **section 2.3**). The various steps of the fabrication process of the devices are described in detail in the coming sections.

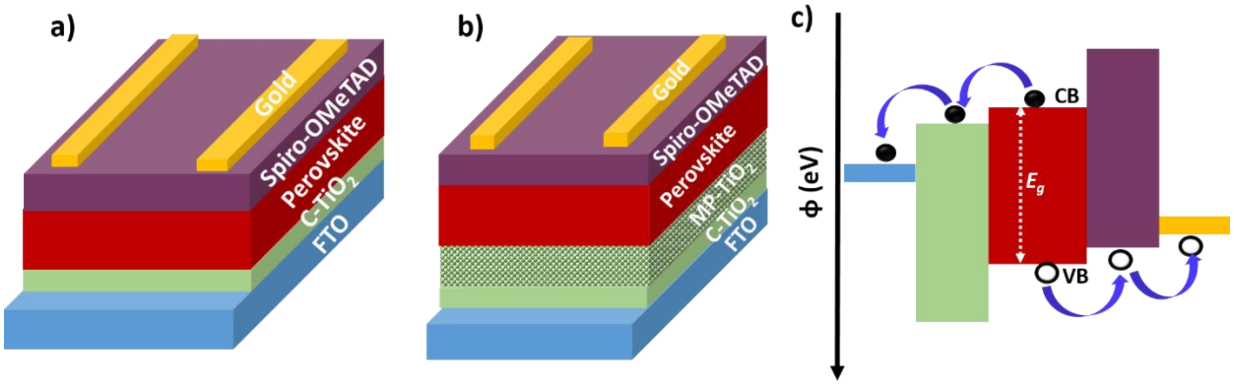

Figure 2. 2: Schematics of the final device architectures. a) in planar configuration with C-TiO_2 b) in planar-mesoporous structure with C-TiO_2 and mesoporous (MP)-TiO_2 and c) energy band alignment of charge extractors to energy levels of perovskite: The conduction band minimum is aligned for electron injection into TiO_2, and the valence band maximum is aligned for injection of holes into Spiro-OMeTAD, and the valence band maximum of TiO_2 is such that it prevents the transport of holes and the conduction band minimum of Spiro-OMeTAD such that it blocks electron transport.

Figure 2.2(c) illustrates a schematic of the energy band alignment of the solar cells, with the energy barriers at the interfaces between TiO_2/Perovskite/Spiro-OMeTAD. As shown from the figure, the perovskite has a favorable energy band alignment with the TiO_2 and Spiro-OMeTAD to extract electrons/block holes and extract holes/block electrons, respectively[33,42,44]. Under solar illumination, perovskite light absorbers generate charge carriers (electrons and holes). Then charge separation can occur. The electrons are transported through the ETM and holes through the HTM and collected at their respective electrodes[33,66,146]. For efficient charge extraction/transport, the thickness of the perovskite layer should be the order of the diffusion lengths of electrons and holes[33,36,146,152]. The latter has been measured to be longer than 1 μm for mixed halide perovskite light absorbers[33,153–155]. So the thickness of the absorber, ETM, and HTM should not exceed 1 μm. With their processing compatibility and facile deposition methods, these combined advantages make these extractors ideal candidates for PSCs.

2.3 Spin Coating Process

All through this thesis, we used the spin coating technique to deposit all the layers in the fabrication of our devices via several spin-coating deposition steps, as illustrated in Figure 2.3. Spin coating

is a technique that has been used for decades for the deposition of thin films for solar cells and optoelectronic devices[156,157]. It is a cost-effective, versatile, and simple technique that fits the purpose of our approach, which is the low-cost fabrication of perovskite-based devices. The working mechanism of spin coating is based on centripetal acceleration force applied to a precursor solution deposited on a flat substrate[156]. Two modes of spinning, static and dynamic, have been used in this work depending on the desirable outcome. Static mode is simply the deposition of a small amount (in microliters) of the precursor solution at the center of the substrate, followed by spinning at a desirable speed and rate. In the dynamic mode, the substrate is allowed to reach its desired rotational speed before the precursor solution is dropped onto it via a micro-pipette. This method helps us to obtain high-quality and consistent perovskite thin films.

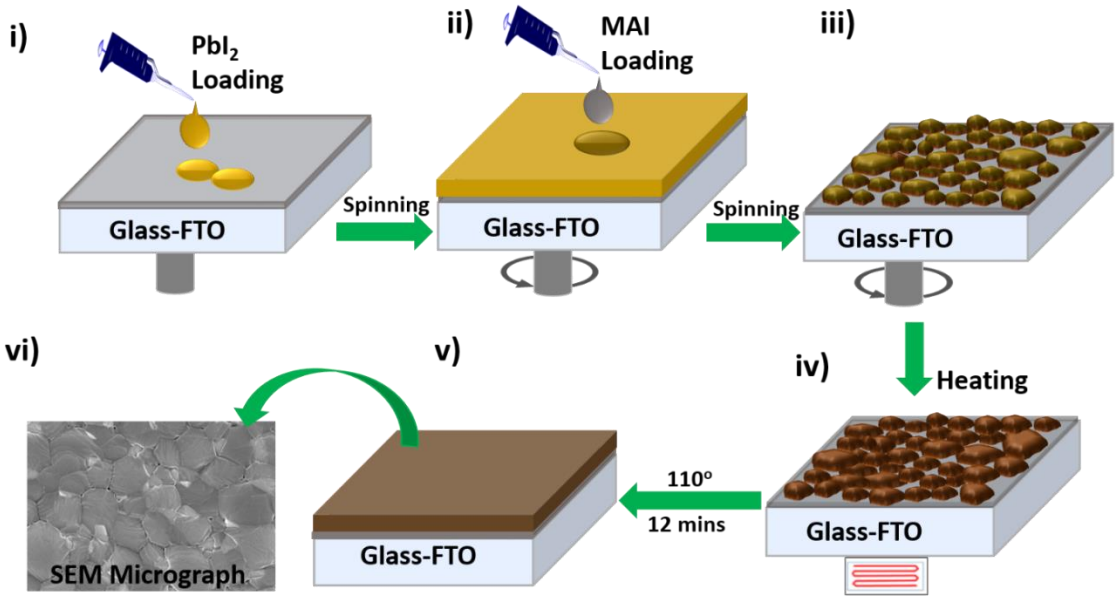

Figure 2. 3: Schematic of the perovskite thin film deposition steps. i) The process begins with PbI_2 precursor loading onto the FTO substrate followed by ii) loading of MAI precursor and iii) spinning steps to form a dark-yellow thin film. iv and v) Thermal annealing of the film for solvent removal and crystallization. vi) A typical scanning electron microscope image of the film is shown above.

Before the spin coating process, the precursor solutions must be prepared. The spin coating process begins by dropping the precursor solution at the center of a vacuum-clamped substrate (**Figure 2.3i**), which is rapidly rotated around an axis perpendicular to the coating area at a controlled speed. As a result, the coating material spreads towards the edge of the substrate, leaving a thin film coating on the substrate. For example, in a two-step deposition process, as depicted in **Figure 2.3**, the PbI_2 precursor solution was spin-coated first, followed by the MAI precursor solution.

Next, the solvent is partly removed during the evaporation process, simultaneously occurring throughout the spinning. Finally, the thin film is annealed on a hot plate (Figure **2.3 iv**) between 100-120 ^{o}C for 10-15 minutes to remove residual solvents and complete the crystallization process of the perovskite films[40,44,94].

The thickness and other properties of the thin film depend on the nature of the precursor solution (viscosity, drying rate, concentration, surface tension, etc.), the spinning parameters such as speed, acceleration and rate, annealing temperature, and time. For instance, high spin speed results in thinner films. Hence, these parameters are vital for controlling the formation of uniform thin films.

2.4 Solar Cell Device Fabrication

The various steps involved in the fabrication process of the solar cells discussed in the thesis are as follows in this precise order: i) cleaning of substrates; then spin coating of ii) TiO_2, iii) perovskite followed by solvent-anti-solvent treatment and annealing, iv) and Spiro-OMeTAD solutions; and finally v) thermal evaporation of gold. The particular details of each of the processes are subsequently described.

2.4.1 Cleaning of Substrates

The presence of contaminants such as dust particles can negatively affect the film formation and, eventually, the device's performance. Therefore, before the deposition of the various layers of the solar cells, it is imperative to thoroughly clean the Fluorine-doped tin oxide (FTO, (TEC 15, Ossila)) substrates. The cleaning involves a three-step ultrasonic cleaning procedure: (i) 15-20 minutes in a mixture of Extran 300 detergent and deionized water in a 1:10 volume ratio, followed by rinsing in deionized water, (ii) 10 minutes in acetone, and (iii) 10 minutes in isopropanol. After the ultrasonic cleaning steps, the FTO substrates were dried with compressed air. A UV-Ozone cleaner (UVO, Ossila Ltd) was then used to clean the surface for 20 minutes to remove other possible contaminants and improve the surface hydrophilicity.

2.4.2 Titanium Dioxide Layer Deposition

The compact TiO_2 layer was obtained by spin coating 60 µl of Ti-Nanoxide BL/SC solution (Solaronix SA) on the cleaned FTO substrate at 5000 rpm for 30 s followed by a heat treatment in

a furnace at 550 ºC for 45 minutes in a quartz tube[42,44]. Throughout the thesis, the compact TiO_2 layer is denoted by C-TiO_2. In the mesoporous configuration, we diluted mesoporous TiO_2 solution (Great cell 30 NR-D) with ethanol in a 1:6 volume ratio. We then spin-coated 100 µl of the mixture atop the as-deposited C-TiO_2 layer. Then the substrates were annealed on a hotplate at 500ºC for 30 minutes in ambient.

2.4.3 Preparation of the Perovskite Precursor Solution and Deposition

We prepared two different solutions to synthesize perovskite thin films: i) one with the inorganic material and ii) with the organic material. PbI_2 precursor solutions were prepared by dissolving 462 mg of PbI_2 powder in 1 mL of DMF. Similarly, to prepare PbI_2:$Pb(SCN)_2$ solutions, 370 mg of PbI_2 and 32 mg of $Pb(SCN)_2$ powders were mixed in 1 mL of DMF. The solutions were left under continuous stirring at 50ºC for 60 minutes to achieve complete dissolution. The second solution, 0.5 M MAI, was prepared by dissolving a 79.5 mg MAI in 1 mL of IPA and stirred for 30 minutes at room temperature. To obtain $CH_3NH_3PbI_3$ perovskite, we used the 1 M PbI_2 and 0.5 M MAI solutions. And for $CH_3NH_3PbI_{2.81}(SCN)_{0.19}$ perovskites, the PbI_2:$Pb(SCN)_2$ and 0.5 M MAI solutions were utilized. Solvent additives of volume fraction of deionized water (DI) and absolute ethanol (EtOH) were directly added to MAI: IPA precursor solution in separate vials. For instance, to prepare 2 vol% H_2O and 5 vol% EtOH–based $CH_3NH_3PbI_{2.81}(SCN)_{0.19}$ perovskite, 2 vol% of DI water and 5 vol% of EtOH were added to 1 mL of MAI in IPA. The perovskite precursor solutions were then spin-coated atop the FTO/TiO_2 layer at 2000 rpm for 15 s for the PbI_2 solution and 30 s for the MAI:IPA solution. The films were then annealed at 110ºC for 12 minutes to complete the crystallization process and evaporate any residual solvent (see **Figure 2.3**). After cooling to room temperature, the HTM precursor solution was deposited atop the perovskite layer. Thin films and solar cells fabricated using these precursor solutions are presented in chapter 3 of the thesis.

2.4.4 Solvent-Anti-Solvent Treatment

We employed solvent-anti-solvent treatment as an original procedure to achieve well-crystallized and compact perovskite films in this work. Chlorobenzene is used as an anti-solvent to induce rapid crystallization of the perovskite precursor solution, resulting in homogenous, pinhole-free perovskite thin films. While the solvent, absolute ethanol, contributes to the dissolution of the remnant solute since the organic counterparts of the perovskite, particularly methylammonium

iodide and methylammonium bromide, are soluble in ethanol. Thus, the use of combined volume ratios of ethanol and chlorobenzene is termed "solvent-antisolvent treatment". The solvent-antisolvent treatment process involves the addition of a combination of chlorobenzene and ethanol in different volume proportions. The addition of the mixture (chlorobenzene: ethanol) takes place during the last perovskite spinning step and a high spinning speed of 5000 rpm for 5-10 seconds, in dynamic spinning mode. Indeed, we optimized the method, and the findings are discussed in chapter 4.

2.4.5 Spiro-OMeTAD Preparation and Gold Depositions

The Spiro-OMeTAD solution was prepared by dissolving 144.6 mg of sublimed Spiro-OMeTAD (99.5%, purchased from Ossila) in 2 mL of chlorobenzene and stirred for 15 minutes. The following dopants were added: 56.6 μL of 4-tert-butyl pyridine; 35 μL lithium bis(trifluoromethane sulfonyl)imide, LiTSFI, solution, and 58 μL of tris(2-(1H-pyrazol-1-yl)-4-tertbutylpyridine) cobalt(III) bis(trifluoromethylsulphonyl)imide, FK209, solution, to improve the hole mobility[42,44] [158]. The LiTSFI and FK209 dopant solutions were prepared before adding them to the Spiro-OMeTAD solution by dissolving 520 mg of Li-TSFI and 300 mg of FK209 respectively in 1 mL acetonitrile, 99.8%. The mixture was stirred thoroughly using a magnetic stirrer in an ambient environment for 1 hour. The Spiro-OMeTAD precursor solution was then spin-coated at 4000 rpm for 30 s atop the FTO/TiO_2/perovskite layer. The devices were kept at room temperature for 24 hours to achieve complete oxidation of the Spiro-OMeTAD and increase its conductivity.

Finally, the solar cells were completed by thermal evaporation of 100 nm gold as the top contacts at a rate of 0.2 nm/s under vacuum at a pressure of $5x10^{-5}$ Torr. The active areas for all the solar cells are 0.025 and 0.067 $cm^{2,}$ as defined by the areas of the shadow mask. The fabrication and device measurements using an AM1.5G solar simulator occurred in ambient conditions: 22–25 ^{o}C and 25–55% relative humidity (RH).

2.5 Fabrication of Photodetector Device

2.5.1 Synthesis of Perovskite Nanowires

We present a method for preparing halide perovskite nanowires via solution processing. Four different concentrations of PbI_2 precursor solutions of 0.2 M, 0.4 M, 0.6 M, and 0.8 M were prepared to produce nanowires of various thicknesses. For instance, a 0.8 M PbI_2 solution was obtained by dissolving ~370 mg PbI_2 in a 9:1 volume ratio of DMF: DMSO mixed solvents. To stabilize each of the PbI_2 solutions, 90 mg of $Pb(SCN)_2$ was added and stirred until they dissolve completely. In effect, the mass of PbI_2 in the solution was varied to achieve the desired concentration. A second precursor solution of MAI was prepared by dissolving 25-30 mg of MAI in a mixed solvent containing 5 mL of IPA: 50 µL DMF[45,48]. As a result, the nanowires are formed by adding different volume ratios (30-100 µL) of DMF to the MAI: IPA solution until we obtained the optimum formation of nanowires with the reported 50 µL. Although PbI_2 dissolves well in both DMF and DMSO, the use of DMSO could not lead to the formation of well-defined nanowire networks compared to DMF. A possible explanation for the one-dimensional growth of perovskite is that the pre-deposited PbI_2 film slightly re-dissolves in the IPA: DMF solution during the second spin-coating step and mediates an anisotropic growth of the perovskite ($CH_3NH_3PbI_{3-x}(SCN)_x$). Therefore the addition of a substantial amount of DMF to IPA: MAI solution is the critical parameter in the growth of the perovskite nanowires.

2.5.2 Device Fabrication

The FTO substrates were pre-patterned by creating a 300 µm-wide channel by laser-etching and cleaned accordingly following the earlier steps. The fabrication of the photodetector is as follows. First, the perovskite nanowires were obtained by spin-coating the PbI_2: $Pb(SCN)_2$ precursor solution directly atop the cleaned FTO substrate at 3000 rpm for 15 seconds. Secondly, the MAI precursor solution is deposited on top of the PbI_2: $Pb(SCN)_2$ layer and spin-coated at 4000 rpm for 30 seconds after waiting 1 minute. The film was then dried on a hot plate at 110 $^{\circ}$C for 5 minutes to complete the perovskite formation process. Finally, 80 nm gold electrodes were thermally evaporated at 0.2 nm/s under vacuum at a pressure of $5x10^{-5}$ Torr through a shadow mask[45,48]. For the purposes of encapsulation, we deposited poly(methyl methacrylate) (PMMA) on top of the perovskite layer. The solution was prepared by dissolving 30 mg of PMMA in 1 mL of

chlorobenzene and spin-coated at 3000 rpm for 25s. The complete devices were then characterized, and the results are presented in chapter 5.

2.6 Thin-Film Characterization Techniques

The halide perovskite thin films and nanowires prepared in the framework of this thesis have been characterized by various structural, morphological, electrical, and optical characterization tools. In this section, we present a brief description of the techniques used.

2.6.1 X-ray Diffraction

The X-ray diffraction (XRD) technique was used to determine the crystal structure of the perovskite films and nanowires. In principle, when x-rays interact with a crystalline material, one gets a diffraction pattern with peaks directly related to the interatomic distance. For a given set of lattice planes with an inter-plane distance, *d*, the condition for diffraction to occur (and a peak to be present in the XRD pattern) can be simply written as:

$$2dsin\theta = n\lambda \tag{2.1}$$

which is known as Bragg's law, where λ is the wavelength of the X-ray, θ is the scattering angle, and *n* is an integer representing the order of the diffraction peak[159].

This technique enables crystalline phase identification, degree of crystallinity, and crystal orientation of the as-synthesized perovskite films and NWs. Characteristically, a diffraction pattern provides the fingerprint of the crystalline material, which is composed of peaks positioned at angles where the Bragg law is satisfied. Also, from the diffraction pattern, the size of the perovskite crystallites was estimated using Scherrer's equation:

$$D = 0.9\lambda/Bcos\theta \tag{2.2}$$

where *D* is the average crystallite size, λ is the wavelength of the X-ray (0.154 nm), *B* is the Full Width at Half Maximum (FWHM) and θ is the Bragg angle of the peak considered[160].

In this thesis, all the XRD patterns of the perovskite samples were acquired using a Bruker-AXS D8 Advance X-ray diffractometer with Cu Kα1 radiation (λ = 1.5406 Å) in the range of 10°–50° for 2θ, with a step size of 0.02°.

2.6.2 Scanning Electron Microscopy

A compact, pin-hole-free morphology of the perovskite layer is paramount to efficient thin-film device performance. Hence, a scanning electron microscope (SEM) was used to characterize the surface morphology of the perovskite samples. Through the SEM technique, topography and some chemical composition information can be obtained. The information about the surface morphology and chemical composition is obtained from the signal produced when a focused, high-energy beam of electrons scans the sample's surface under a vacuum. Through this interaction, three different signals are generated: (i) secondary electrons signal, which provides information on the surface morphology of the sample; (ii) backscattered electrons signal, which produces images with better chemical contrast relating to the differences in atomic number; and (iii) X-rays energy which is characteristic of the energy difference between these two atomic shells and can be used to identify the type of elements in a sample[161,162].

The SEM micrographs of the samples presented in this work were characterized using Hitachi SU 8230 ultra-high-resolution field emission SEM (FESEM) setup available at *École de Technologie Supérieure* (ETS). FESEM uses a cold field emission (CFE) gun for better-quality imaging and analytical performance. Typically, the accelerating voltage range is 0.5-30 kV, and we used 10 kV for imaging our samples[162]. Also, the thickness of the films and PeNWs were measured using cross-sectional SEM imaging of the samples deposited on the substrates. The elemental stoichiometric concentrations of the perovskite thin film were measured using the Energy Dispersive X-ray spectroscopy (EDS) technique with the same setup by limiting the scanning range of the electron beam energy (0-4 k eV).[42]

2.6.3 Transmission Electron Microscopy

We also carried out TEM characterization on the perovskite nanowires using a JEOL 2100 F TEM equipped with an EDX spectrometer to obtain more detailed information about the crystallinity of

the perovskite. In the setup, the electron source is a filament usually made of tungsten (W) or lanthanum hexaboride (LaB_6).[161,163] When the filament is heated, electrons are emitted. These electrons are accelerated towards the anode through a potential difference of ~200 kV.[161,163] Then this electron beam is condensed by an aperture and hits the sample. Below the sample, there is an objective lens that consists of an electromagnetic coil. This coil focuses the electron beam in the focal plane, and by using the projector lens, the electron beam is then focused on a screen. Thus in a TEM, a very thin sample is hit by an electron beam, and the transmitted electrons are observed. This way, it is possible to obtain a direct image of the sample with high resolution and an image of the diffracted electrons. We can extract information on the diffraction pattern, crystallinity, and chemical composition of our perovskite nanowires from the TEM characteristics.

2.6.4 UV-Visible-Near-Infrared (UV-vis-NIR) Spectroscopy

Furthermore, UV-vis-NIR Spectroscopy was used to measure the absorption spectrum of the perovskite samples. This tool gives evidence of the absorption of light by the sample. From the absorption spectrum of the sample, we can deduce, in particular, the bandgap of the perovskite material. The method employed throughout this thesis is the Tauc plot method. For a direct bandgap, as in the case of halide perovskite, we used the following formula:

$$(\alpha h\upsilon)^2 = A(h\upsilon - E_g) \tag{2.3}$$

where A is the measured absorption, h is Planck's constant, E_g is the bandgap of the material(E_g =1240/λ(nm)), α is the absorption coefficient (α = 2.303 A/t where t is the thickness for thin films). Thus, the absorption coefficient is experimentally calculated from the measured absorption and the thickness of the thin films. Then a plot of $(\alpha h\upsilon)^2$ (on the y-axis) versus $h\upsilon$ (on the x-axis) gives a straight-line regime, and the extrapolation of this straight line intercepts the x-axis to give the value of the bandgap E_g of the material. We acquired the absorption spectra of the perovskite films and PeNWs with a PerkinElmer Lamba 750 UV/VIS/NIR spectrophotometer by scanning within 300 to 800 nm range.

2.6.5 Photoluminescence (PL) Spectroscopy

The PL spectroscopy is similar to UV-Vis but involves an electronic transition from higher to lower energy levels. During this process, electron-hole recombination results in light emission.

The characteristic PL spectrum obtained is a plot of the intensity of emitted PL light (related to the electrical signal generated) as a function of the wavelength of emitted light for a fixed excitation wavelength[161]. In our experiments, we used a Torus 532 nm laser (Laser Quantum, Cheshire, UK) for excitation and a Jobin- Yvon iHR320 triple-grating spectrometer (Horiba Scientific, Kyoto, Japan) equipped with a Synapse TE-cooled CCD detector array to collect the photoemission. We also employ this technique to elucidate the charge transport mechanisms and identify surface defects in our perovskite materials.

2.7 Device Characterization

2.7.1 Current Density-Voltage Measurements

The current density-voltage (*J-V)* characteristics are used to determine the solar cell parameters (V_{oc}, J_{sc}, PCE, and FF), as presented in section 1.3.2. For all our experiments, the solar cell parameters are measured. The *J-V* characteristic curves were obtained for the PSCs under dark and simulated AM1.5G (Air Mass 1.5 Global) white light illumination at 100 $mW.cm^{-2}$ using a Newport solar simulator (Newport, model 91160-1000) through a computer-controlled Keithley 2400 source meter, under ambient condition. Before each measurement, the intensity of the light is calibrated using a single crystalline silicon reference cell.

2.7.2 External Quantum Efficiency of Devices

The external quantum efficiency (EQE) is a tool used to ascertain the efficiency of solar cells and photodetectors. The setup consists of a 150 W xenon lamp producing white incident light that passes through a monochromator with two arrays that can be used for both visible and ultraviolet wavelengths. This allows you to select a single wavelength. The light emerging from the TRIAX320 monochromator is modulated at a frequency and then focused on the device, placed where the light spot was projected. The lamp, the chopper, the lock-in amplifier, and the monochromator are controlled by a computer. Before each series of measurements, the power P (λ) of the incident light was measured for each wavelength (λ) with a step of 10 nm, between 300 nm and 800 nm, using a standard silicon detector. The use of the lock-in amplifier makes it possible to measure the generated photocurrent J(λ).[45,48] Finally, EQE (λ) is obtained by substituting the values of P_{in}(λ) and J (λ) in equation 1.5 and the integrated current is calculated from the EQE spectrum using equation 1.6.

2.7.3 Spectral Responsivity Measurement of Photodetectors

The spectral responsivity measurements were done with the same EQE setup. The excitation light is modulated between 50-100 Hz before illuminating the sample, which was biased between 1-10 V. The power of the incident light was first measured with a calibrated photodiode (Newport 918D)[45,48]. From equation 1.7, the spectral responsivity can be calculated from the measured photocurrent and incident power at each wavelength. The detectivity of the photodetectors was then calculated using equation 1.8 with values derived from the spectral responsivity and the measured dark current of the photodetector devices.

2.7.4 Determination of the Response Time of Photoconductive Devices

In order to compare our photodetector devices to reported works, we also determined their response times. The time-dependent photoresponse measurements were done by illuminating the device with a green (532 nm) laser or white light. The system used to determine the response times consists of a mechanical chopper modulating the light at the desired frequency, a function generator (Agilent DSO-X 3034 A) connected to the laser for sending voltage signals. An oscilloscope (Agilent DSO-X 3034 A) connected to the terminals of a resistor (1 GΩ) makes it possible to measure the photovoltage versus time induced by the illumination of the devices with the aid of the laser[45,48,49].

2.8 Evaluation of Device and Thin-Film Stabilities

A critical goal of the thesis is to prepare ambient-stable perovskite materials for optoelectronic device applications. As discussed in Section 1.5.3, halide perovskites are susceptible to moisture and oxygen, temperature, the solution process (additives and solvents), and UV light[92,133]. In the thesis, we focused on the effects of moisture and oxygen, solution process (additives and solvents), and illumination on the stability of the perovskite thin films and devices. We employ various characterization tools to probe the degradation of the perovskite thin films and the perovskite-based devices stored under ambient conditions. For the degradation of the as-prepared perovskite thin films, we utilized XRD, SEM and FTIR techniques to evaluate the degradation over several days of storage in air. An obvious way to assess this is the change in the color from dark-brown to yellow of the thin films.

A detailed example is discussed in Chapters 3 and 4. We monitored the behavior of the current-voltage parameters of the devices over some time by leaving the samples in the laboratory environment. Then, over time, the evolutions of the curves of the PV parameters, *Voc*, *Jsc*, PCE, and FF, are plotted. From the curves, an idea about the degradation mechanism, lifetime, and the main contributing factors to the loss in device performance is deduced. We also track the stability of the devices under continuous illumination using the solar simulator to evaluate the effect of photo-degradation for our unencapsulated devices. The shelf-lifetime of the devices is derived from the curve of the PCE vs. time using the T_{80} approach. T_{80} defines the time it takes a solar cell to lose 20% of its initial PCE. This method is widely used to determine the lifetime of organic solar cells and PSCs[64,118]. With the T_{80} method, the PCE decay curves typically show two distinct regions: an exponential-like or a pronounced rapid decay regime known as the '*burn-in'* followed by a slower decay part[164]. These two regimes of the decay curve are not always distinct; however, this method gives quite a reliable estimation of the lifetime of a solar cell. Accordingly, throughout this thesis, we estimate the lifetime of the devices from the PCE time-evolution curves after storage in air for at least one month unless otherwise stated.

Chapter 3: Moisture-Assisted Thiocyanate-Doped Single-Cation Perovskites for Stable Solar Cells

In this chapter, we present a method for fabricating perovskite solar cells under ambient conditions. The role of moisture/water and dopants on the formation and morphology of perovskite thin films on the one hand and the efficiency and stability of perovskite solar cells, on the other hand, is investigated. We introduce water and ethanol into the perovskite precursor solution to make it independent of the external fluctuations in relative humidity and demonstrate that pinhole-free halide perovskite films can be processed in the ambient.

The chapter is based on the following publication: *Asuo, I. M. et al. Tunable thiocyanate-doped perovskite microstructure via water-ethanol additives for stable solar cells at ambient conditions. Sol. Energy Mater. Sol. Cells* ***200****, 110029 (2019)*

3.1 Introduction

Organic-inorganic halide perovskite solar cells have shown rapid growth and stimulated enormous interest in the photovoltaic (PV) community. Halide perovskite materials have desirable semiconducting characteristics. These include direct bandgap, high absorption coefficient, low processing temperature, defect tolerance, and easy processability[29,34,72,165]. Device applications include light-emitting diodes (LEDs)[52–55], photodetectors[48,166,167], and solar cells[33,44,168]. Until recently, most reports focused on its application for solar cells. Perovskite solar cells (PSCs) can be fabricated via solution deposition of the perovskite precursor materials, allowing for a low-cost fabrication process.

Most research efforts have focused extensively on improving the efficiency of PSCs, while less work is reported on the stability of the devices over time under ambient conditions. One major challenge for halide perovskite is its hygroscopic nature. The organic part, methylammonium iodide (MAI), tends to decompose quickly in the presence of moisture. Hence, over the years, perovskite fabrication has been mainly carried out under inert environments. Devices fabricated under such controlled conditions exhibit high PV performance but increase the cost of production.

Moreover, the fabrication method significantly impacts the morphology, proving to be an essential parameter in maximizing the device's performance. Microstructural parameters such as crystal

structure, grain size, and grain boundaries have tremendous consequences on the charge carrier mobility[32,169] and the solar cell performance[40,76,158,170]. Therefore, it is crucial to obtain pinhole-free thin films before device fabrication. For instance, in a two-step process of thin film deposition, the first deposited layer of PbI_2 must have appropriate pores to enable efficient infiltration of MAI when subsequently deposited atop the PbI_2 layer[171].

In the last nine years, an unprecedented effort has been devoted to modifying the morphology and the microstructure to improve their efficiency under controlled conditions. However, an effective fabrication technique to synthesize and control the microstructure of the perovskite under ambient conditions has not been extensively studied[172]. Hence, a robust ambient-processing technique to tailor the crystallization process and reproducibility of pinhole-free perovskite thin films is required to produce efficient PSCs. The open question remaining to be answered, therefore: *"Can halide perovskites be synthesized under ambient conditions for stable and efficient solar cells?"*

This chapter presents a method for fabricating stable single-cation halide perovskite thin films under ambient conditions ($23^oC \pm 1^oC$, > 55% ± 5%RH). The objective here is to use chemical substitution and solvent additives to improve the perovskite films' microstructure, performance, and lifetime. To achieve the desired outcome, conventional $CH_3NH_3PbI_3$ (MAPI) films were fabricated without and with additives, and their device's performances were evaluated. Pseudo-halide, lead thiocyanate ($Pb(SCN)_2$), was added to the pristine (MAPI in this case) perovskite precursor solution, and its effects on performance have been investigated. The addition of $Pb(SCN)_2$ to the MAPI results in the partial substitution of I^- by SCN^- in the tetragonal sites to form $CH_3NH_3PbI_{3-x}(SCN)_x$. Thus, the incorporation of SCN^- into MAPI does not alter the crystallographic structure as it has a similar ionic radius (~0.217 nm) as iodine ions (~ 0. 220 nm)[173]. Also, Ganose *et al*. showed that SCN-based perovskite does not break down spontaneously based on their positive decomposition energy. Therefore, it exhibits higher thermodynamic stability than MAPI (which recorded negative decomposition energy), improving crystal quality and performance of perovskite solar cells[142].

Solvent additives are commonly used to aid the crystallization process of halide perovskite materials. Likewise, the effects of solvent additives on the properties of the perovskite film are studied by fabricating thin films with the addition of deionized water (H_2O) and ethanol (EtOH) to the main solvent (in our case, isopropanol (IPA)). It is reported that the growth of perovskite

thin films and their stability are affected by the presence of moisture and oxygen[111,133]. Owing to this, water plays a significant role in the synthesis of the perovskite in the ambient. On the one hand, it helps to slow down the crystallization process of the perovskite films and, thus, enhances the perovskite film microstructure[174–177].

On the other hand, it contributes to the degradation of the perovskite film[42,62,178]. Since we work under ambient, an uncontrolled environment, the perovskite is highly likely to deteriorate due to environmental moisture. We designed a way to stabilize the films, providing them the water content they require by introducing a moderate and controlled amount of H_2O in the precursor solution. In doing so, there is no need to extract water from the surrounding moisture. Also, the addition of ethanol achieves a further improvement of the crystal quality. Ethanol helps dissolve the remnant solutes such as PbI_2 and MAI, promoting nucleation and crystallization of grains of the halide perovskite[179].

Consequently, solar cells have been fabricated using the optimized precursor solutions, and their performance in terms of PV characteristics and stability has been studied. We highlight the essential contribution of morphology to the performance of the solar cells and perovskite thin films over time. We show that compact thin-film morphology is the key to obtaining effective charge carrier photo-generation, charge transport, and stable perovskite solar cells.

3.2 Results and Discussions

3.2.1 Synergistic Effects of SCN Ions, Water, and Ethanol on the Microstructure

Perovskite thin films are prepared and characterized before the fabrication of the solar cells. A detailed description of the perovskite precursor solution preparation is presented in **Section 2.4.3**. Briefly, the $CH_3NH_3PbI_{3-x}(SCN)_x$ (denoted as MPS) solution is prepared using PbI_2: $Pb(SCN)_2$:DMF and MAI: IPA precursors. The MAI solutions are obtained with different solvent additives (EtOH and H_2O in different ratios ranging from 1 to 10 vol%). The solvent additives EtOH and H_2O were added to the MAI in IPA precursor solution in different volume ratios before spin coating. Further studies are conducted on the optimized combination of 2 vol% H_2O and 5 vol% EtOH additives in the IPA solvent. The perovskite thin films are fabricated via a two-step-spin coating method where PbI_2 precursor solution is deposited first, followed by the deposition of MAI solution.

To confirm the composition of the thin films, we determine the elemental composition of the SCN-based perovskite film using energy-dispersive X-ray spectroscopy (EDS). The stoichiometric ratio of the inorganic components lead:iodine:sulfur (Pb:I:S) of the perovskite film is determined to be approximately 1:2.81:0.19, as shown in **Table A3.1**, indicating the evidence for successful SCN^- incorporation into the parent MAPI matrix.

The surface morphologies of the deposited thin films are characterized using the scanning electron microscope (SEM) technique. **Figure 3.1 (a,b)** shows the SEM micrographs of the $CH_3NH_3PbI_3$ and $CH_3NH_3PbI_{2.81}(SCN)_{0.19}$ thin films deposited onto FTO substrates. Notably, the surface morphology of the $CH_3NH_3PbI_3$ films (**Figure 3.1a**) is characterized by small crystal grains and numerous voids or holes, exposing the FTO/PbI_2 layer below (light grey). The big grains on the surface are composed of a collection of smaller grains of ~0.4 µm. Upon the $Pb(SCN)_2$ incorporation to form $CH_3NH_3PbI_{2.81}(SCN)_{0.19}$, there is an apparent change in the appearance of the films. As shown in **Figure 3.1b,** the grain size and morphology are enhanced, thus improving the coverage and reducing the area of the pinholes in the film. There was an almost eight-fold increase in grain size from ~0.4 µm to ~3 µm.

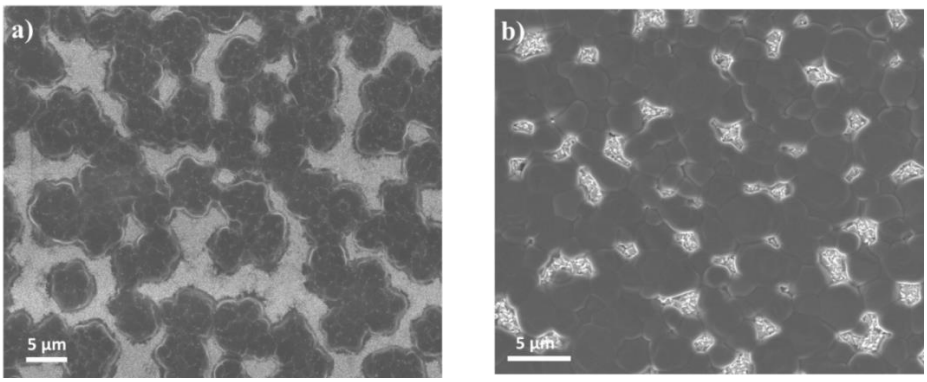

Figure 3. 1: a) SEM image of $CH_3NH_3PbI_3$ perovskite thin film. b) SEM images of $CH_3NH_3PbI_{2.81}(SCN)_{0.19}$ perovskite thin film.

Seeking to improve the morphology, we decided to add an optimized amount of 2 vol% H_2O to the $CH_3NH_3PbI_{2.81}(SCN)_{0.19}$ precursor solution. By so doing, a distinct change in morphology is observed, as shown in **Figure 3. 2 (a1,a2).** Full coverage and almost void-free films are obtained; however, there are still some pinholes and rough grain boundaries. Hence, we further improved the surface coverage by adding 5 vol% of EtOH to $CH_3NH_3PbI_{2.81}(SCN)_{0.19}$ in addition to the 2 vol% H_2O. Clearly, smooth, homogeneous, and larger grains of ~ 5 µm size are achieved (**Figure**

3.2 (b1,b2)). Thus, the addition of $Pb(SCN)_2$ and the solvent additives result in the formation of perovskite films with bigger grains and fewer pinholes. The increase in grain size implies that the total area of the grain boundaries in the film is reduced, emphasizing the critical role of the solvent additives in the nucleation and crystallization of the perovskite films. This could be explained by the additives contributing to slow crystallization of the perovskite by dissolving the remnant solutes of PbI_2, $Pb(SCN)_2$, and MAI yielding smooth and pinhole-free perovskite films[170,174,180]. Pinhole-free and large grains films are preferable for PV devices because they have a lower grain boundary density. Achieving these characteristics in thin films is crucial for working devices; particularly, they prevent shunting and short circuits and promote efficient charge transport under operational conditions.

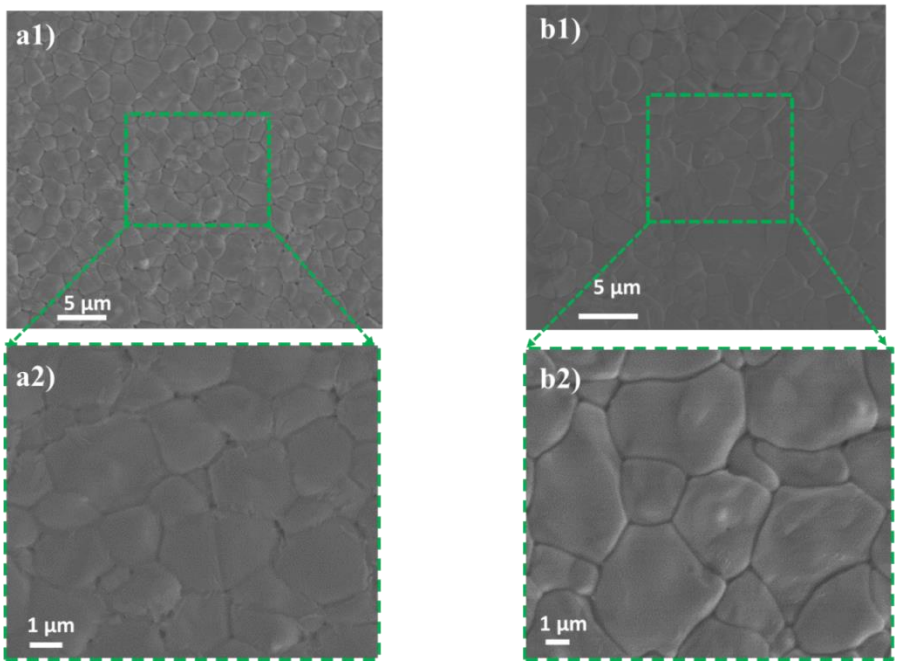

Figure 3. 2: a1) SEM images of $CH_3NH_3PbI_{2.81}(SCN)_{0.19}$ with 2 vol% H_2O and a2) at high magnification. b1) SEM images of $CH_3NH_3PbI_{2.81}(SCN)_{0.19}$ with 2 vol% H_2O and 5 vol% EtOH and b2) at high magnification.

Nonetheless, the quantity (vol%) of the solvent additives has to be controlled as an increased amount of H_2O in the solution results in poor morphology, as seen in **Figure A3.2** (*a*, *b*). We observe that the positive effect of H_2O on the morphology reaches saturation after 5 vol% (**Figure A3.1a**). Any excess water leads to poorer morphology, as seen in **Figure A3.1b**. The deterioration of the morphology beyond the 5 vol% is a complex chemistry-related matter and has not been

extensively explored in this thesis. We speculate that excess water makes the perovskite more susceptible to degradation due to the secondary PbI_2 phase.

It has been reported that the presence of H_2O in the perovskite leads to the formation of hydrate products[181,182]. H_2O integrates the perovskite crystal structure and occupies the same unit cell through the hydrogen bonds between iodine and methylammonium ions. The bonds between the ammonium (NH_3^+) group and the iodide are affected due to the sensitivity of the N-H stretch vibrations[182,183]. It is suggested that incorporating water could also lead to doping or filling of trap states, impacting the electronic and ionic conductivity of the perovskite without a change in the crystal structure[183]. This observation about the positive effect of H_2O on the perovskite without change in crystal structure has been supported by Mosconi et al.[184]. They demonstrated via ab initio molecular dynamics calculations that the addition of water to the MAPI shows insignificant changes in the tetragonal crystal structure of the perovskite[183,184]. Thus, the addition of H_2O increases the moisture resistance by strengthening the hydrogen-bond interaction in the $CH_3NH_3PbI_{3-x}(SCN)_x$ perovskite structure. Indeed, we demonstrate that the addition of H_2O and EtOH to the perovskite precursor solution promotes the growth of perovskite films with large grains and uniform coverage.

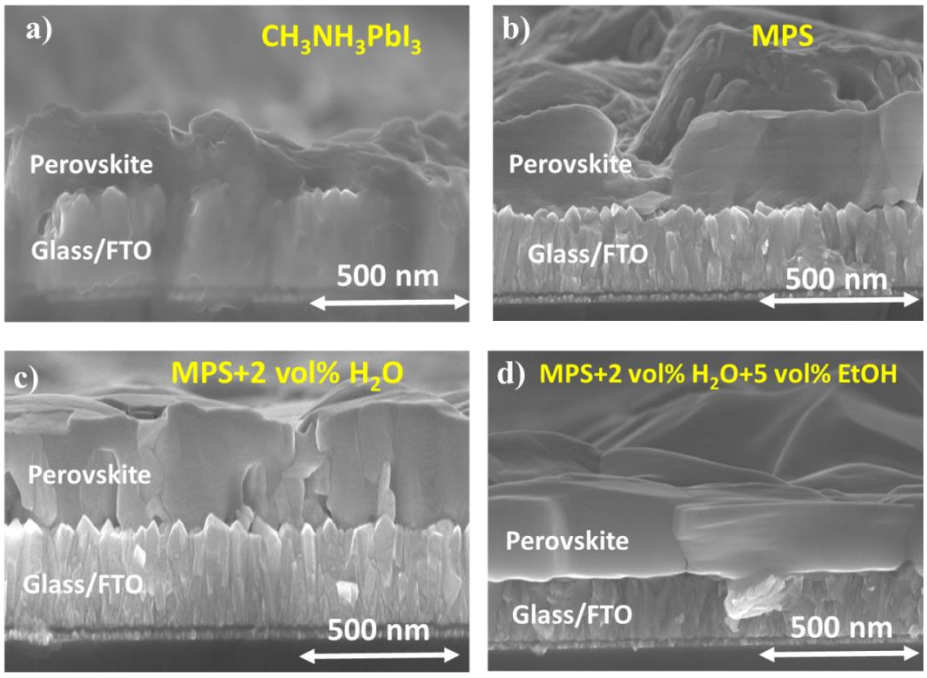

Figure 3. 3: Cross-sectional SEM micrographs of a) $CH_3NH_3PbI_3$, b) $CH_3NH_3PbI_{3-x}(SCN)_x$, c) $CH_3NH_3PbI_{3-x}(SCN)_x$ with 2 vol% H_2O d) $CH_3NH_3PbI_{3-x}(SCN)_x$ with 2 vol% H_2O and 5 vol% H_2O EtOH perovskite thin films deposited on FTO-glass substrates.

In **Figure 3.3,** we also show cross-sectional SEM micrographs of all perovskites films deposited on FTO substrates. Overall, the additives enhance smooth and compact depositions of the films, especially samples with MPS+2vol%H_2O+5vol% EtOH (Figure 3.3.d), which will ensure effective charge separation and increase the efficiency of the solar cells. The thicknesses of the perovskite thin films range from ~390 nm to 490 nm. We noted that the thickness of the perovskite films significantly increases as the additives are added. The thin films' thickness is in a favorable range for the absorption of photon, transport, and collection of generated charge carriers.

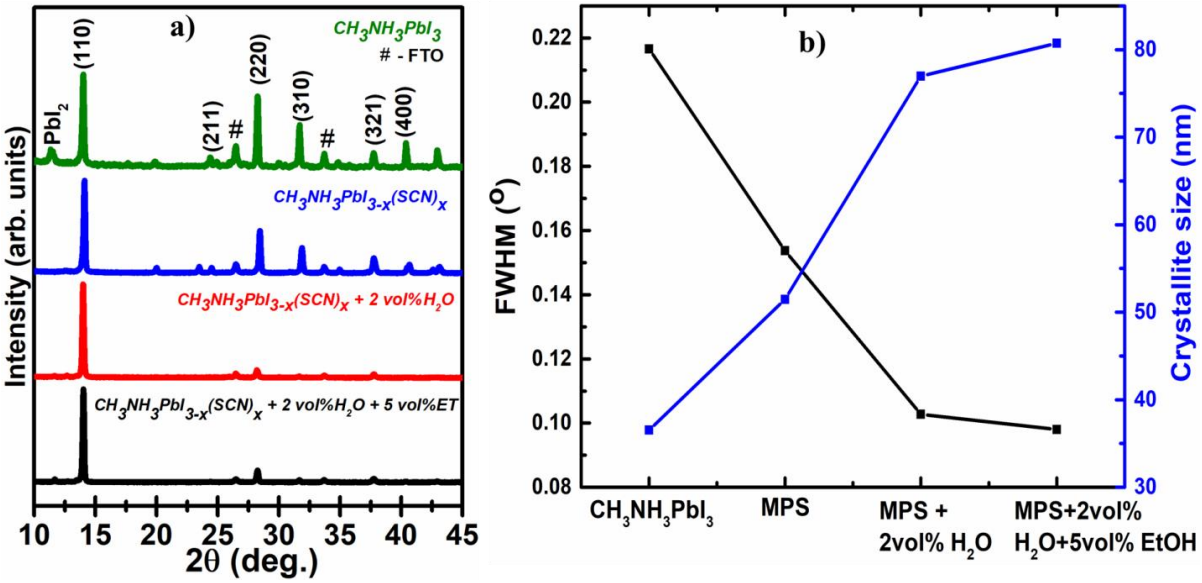

Figure 3. 4: a) XRD spectra of the films synthesized in different conditions indicated by the labels. From top to bottom is the pristine perovskite film followed by pure and solvent treated SCN-based perovskite films; b) The trends of calculated FWHM values (black curve) and crystallites size (blue curve) for the perovskite thin films.

The X-ray diffraction (XRD) pattern has been used further to identify the crystallinity of as-cast perovskite thin films. **Figure 3.4** shows the XRD patterns of the four different thin films, which exhibit characteristics similar to the reported tetragonal $MAPbI_3$ phase structure[34,185]. The characteristic diffraction peaks for the perovskites, evidenced at two-theta angles 14.10° and 28.20°, are ascribed to the (110) and (220) planes and indexed accordingly. These XRD patterns reveal that the additives did not alter the crystallographic properties of the pristine perovskite but somewhat helped to achieve highly oriented grains along the (110) plane. Also, the addition of water or ethanol or both suppresses other minor peaks while slightly increasing the (110) and (220) peak intensities, suggesting the improvement of the crystallinity of the MAPI phase. **Figure A3.1c** shows a small onset of the appearance of a PbI_2 phase at ~12.6° (indexed as (001) plane) for 5

vol% and 10 vol% H_2O. This implies there will be more PbI_2 in the solution if the amount of water increases, confirming the conflicting effects of water on halide perovskites. The samples with only EtOH formed a thin film with a surplus of PbI_2 components at the surface and grain boundaries. Thus, only EtOH tends to induce excess PbI_2, as evidenced on the XRD pattern in **Figure A3.2b2**, and could later speed up the degradation process of the perovskite films. Apparently, upon the addition of both H_2O and EtOH, the morphology of the film and crystal structure are tremendously enhanced (**Figure A3.2 (a1& a2**). Such compact morphologies are beneficial and basic requirements for working optoelectronic devices. For instance, they help prevent short circuits and reduce to some extent recombination in solar cells.

A closer look at the MAPI pattern reveals a peak at 12.62 °, corresponding to PbI_2 impurities. This PbI_2 peak is more pronounced in the MAPI patterns than in MPS patterns. This could originate from unreacted PbI_2 in the precursor solution or the degradation effect of humidity on the film during the fabrication process in ambient since MAI is hygroscopic[62,95,178]. However, the PbI_2 peak disappears upon adding SCN ions and mixed quantities of H_2O and EtOH to the precursor solution. The additives, therefore, improved the crystal quality while eliminating the PbI_2 peak by the dissolution of the remnant solutes.

Likewise, the change in peak intensity is accompanied by a difference in the full width at half-maximum (FWHM) of the peak. For instance, the FWHM of the (110) peak for MAPI narrows from 0.217° to 0.099° upon the addition of H_2O and EtOH. This behavior also confirms an increase in the crystallite size from 36.53 to 80 .74 nm estimated using Scherrer's equation[186] (**Figure 3.4b**). Consequently, the increase in the grain size observed in the surface morphology on the SEM micrographs is consistent with the evolution of the crystallite sizes. Crystallinity is a desirable feature in promoting charge dissociations and transport, leading to an increase in generated photocurrent in the solar cells. These microstructural characteristics point out that the presence of SCN^-, water and ethanol leads to a positive impact on the perovskite by enhancing the crystallinity of their thin films.

3.2.2 Performance of Perovskite Solar Cells: Efficiency

Based on the thin-film characteristics presented, we believe we have successfully prepared halide perovskite under ambient air, which possesses most of the basic requirements for a working device. Hence we decided to fabricate solar cells using these thin films to evaluate the performance under

operational conditions. Planar perovskite solar cells are fabricated with the sample without and with the dopant and solvent additives to study their effects on the device's performance, mainly efficiency and stability. The devices with $Pb(SCN)_2$ dopant, H_2O, and EtOH additives are considered device under test while device made with the pristine precursor perovskite solution is viewed as the reference ($CH_3NH_3PbI_3$ (MAPI)). The complete fabrication process is presented in **Section 2.4**. The solar cells are characterized using a solar simulator lamp of the AM1.5G (100 $mW.cm^{-2}$) spectrum at room temperature.

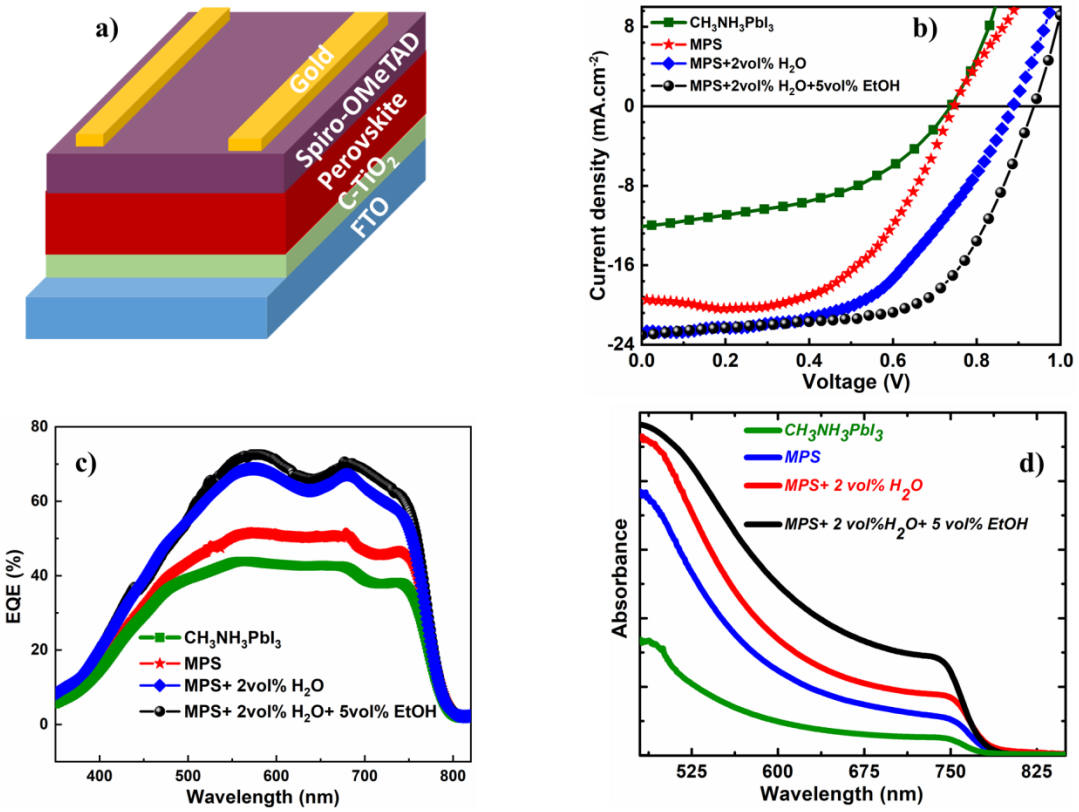

Figure 3. 5: a) Final device architecture for the planar perovskite solar cell. b) Current density versus voltage *(J-V)* characteristics of the different solar cell devices measured right after the fabrication under AM1.5G solar simulator in reverse scan mode. c) External quantum efficiency (EQE) spectra of the various solar cells. d) UV-vis absorption spectra for the films synthesized with and without additives.

Figure 3.5a displays the schematic of the device architecture used in this chapter; FTO/c-TiO_2/perovskite/Spiro-OMeTAD/Au. **Figure 3.5b** shows the *J-V* characteristic curves of the best-performing devices. The MAPI device under AM1.5G illumination exhibits a PCE of 4.12%, while the MPS-based solar cell shows a PCE of 8.35%, MPS+2 vol% H_2O a PCE of 10. 61% and MPS+2 vol% H_2O+5 vol% EtOH solar cell a PCE of 13.46%, which is more than three times higher than

the PCE obtained for the reference device. **Table 3.1** displays the summary of the PV parameters (open-circuit voltage (*Voc)*, short-circuit voltage (*Jsc)*, and fill factor (FF)) for the best-performing cells of each type of solar cell fabricated. The statistics of the individual devices (at least ten devices) fabricated under the same conditions show a reasonably reproducible device, as presented in **Figure A3.3** of the Appendix. It also shows that the additives make the statistical distribution much narrower. This means that the reproducibility of the devices is better with additives than without.

Table 3.1: Photovoltaic parameters for the best $CH_3NH_3PbI_3$ and $CH_3NH_3PbI_{2.81}(SCN)_{0.19}$ (indicated as MPS)-based solar cells.

Devices	J_{sc} **[mA.cm^{-2}]**	V_{oc} **[V]**	**FF [%]**	**PCE$_{best}$ [%]**	**PCE$_{avg.}$ [%]**
$CH_3NH_3PbI_3$	12.2	0.74	46	4.1	3.7±0.3
MPS	19.4	0.75	57	8.4	7.5±0.6
MPS + 2 vol% H_2O	22.7	0.89	53	10.6	9.5±0.6
MPS+2 vol% H_2O +5 vol% EtOH	23.0	0.94	62	13.5	12.8±0.5

We also present the measured external quantum efficiency (EQE) of the different devices **(Figure 3.5c)**. We observe that MPS+2 vol%H_2O+5 vol% EtOH showed the maximum EQE of ~73%, much higher than ~44% for the reference cell. The EQE increases with each added additive to the MPS, thereby indicating that the additives positively affect the photon absorption of the perovskite. This observation is in good agreement with the absorption spectra in **Figure 3.5d,** with the absorption thresholds of perovskite around ~780 nm (E_g of ~1.6 eV). The spectra elucidate the increasing trend observed in all the measured PV parameters of the solar cells. This increasing trend in absorption leading to better *J-V* performance can be related to several factors. First, compared to the reference sample MAPI, an increase in the absorption intensity with a slight red-shifted absorption edge is observed. This behavior could be due to the enhanced crystal quality and pin-hole-free thin-film morphology originating from the solvent additives[187–189]. Second, the *J-V* performance of thin-film solar cells depends on the morphology and crystallinity of the active layer. From our findings, the low PV parameters exhibited by the MAPI device compared to the MPS devices with additives could be attributed to the poor morphology; that is, the non-compactness (numerous voids) of the MAPI and MPS perovskite films. Finally, as reported in the

literature, morphological changes can impact charge transport, including recombination processes and photocurrent generation mechanisms in perovskite solar cells[190,191]. In the case of MAPI and MPS, the poor thin-film coverage could negatively i) affect photocurrent generation leading to low J_{sc} due to losses at the grain boundaries, and ii) affect charge transport and promote recombination loss resulting in the low V_{oc} and FF.

Consequently, from our investigations, we observe that adding ~5 wt% of $Pb(SCN)_2$ and the solvent additives increases the grain size, resulting in a direct effect on the PV performance. Thus, the obtained uniform films correlate with the observed enhancements in *Jsc*, V_{oc}, FF, and PCE. For instance, an increase of 89% in *Jsc* and 229% in the PCE are recorded for the MPS+2 vol% H_2O+5 vol% EtOH device compared to MAPI solar cells. Likewise, the low FF of MAPI could be attributed to low shunt resistance, which is closely related to the charge transport through the pores in the active layers.

3.2.3 Stability of the Perovskite Thin Films and Solar Cells

Knowing that the stability of the perovskite film is crucial, the effects of moisture and oxygen[95,176] on the as-cast perovskite films are evaluated. Perovskites can decompose into lead iodide (PbI_2), methylamine (CH_3NH_2), and hydrogen iodide (HI) in the presence of oxygen, moisture, temperature, and illumination[62,178,192]. For ambient processing, the effects of oxidative degradation of the film are inevitable. We, therefore, studied the oxidative degradation of the thin films. The samples were kept in ambient air (23ºC ± 1ºC, > 55% ± 5%RH) for more than 30 days. **Figure 3.6(a-d)** exhibits the evolution of the PV performance of the solar cells over time. The reduction in PV parameters goes through a rapid decline of the initial PCE, followed by a slow drop and a stabilization [193]. The 80% loss in PCE of the MAPI is ~26 hours (T_{80}) and complete degradation after 160 hours. In contrast, the total PCE loss of devices with MPS is 33%, and MPS+2 vol% H_2O (without EtOH) is 24% after storage. The MPS+2 vol% H_2O+5 vol% EtOH devices are most stable with operational lifetime, T_{80}, > 480 hours, and overall PCE loss of only 12% of its initial PCE. Thus, MPS+2 vol% H_2O and MPS+2 vol% H_2O+5 vol%EtOH films exhibit more stable characteristics due to their compact/pinhole-free morphology. Aside from the MAPI devices, which degraded entirely in a short time, the V_{oc} remained almost constant for the other cells. The J_{sc} and FF show some fluctuating behavior within the first 150 hours of storage and later

stabilized. We associate the poor device stability of MAPI and the limited stability of MPS devices to the reduction in J_{sc} and the non-uniform/porous morphology.

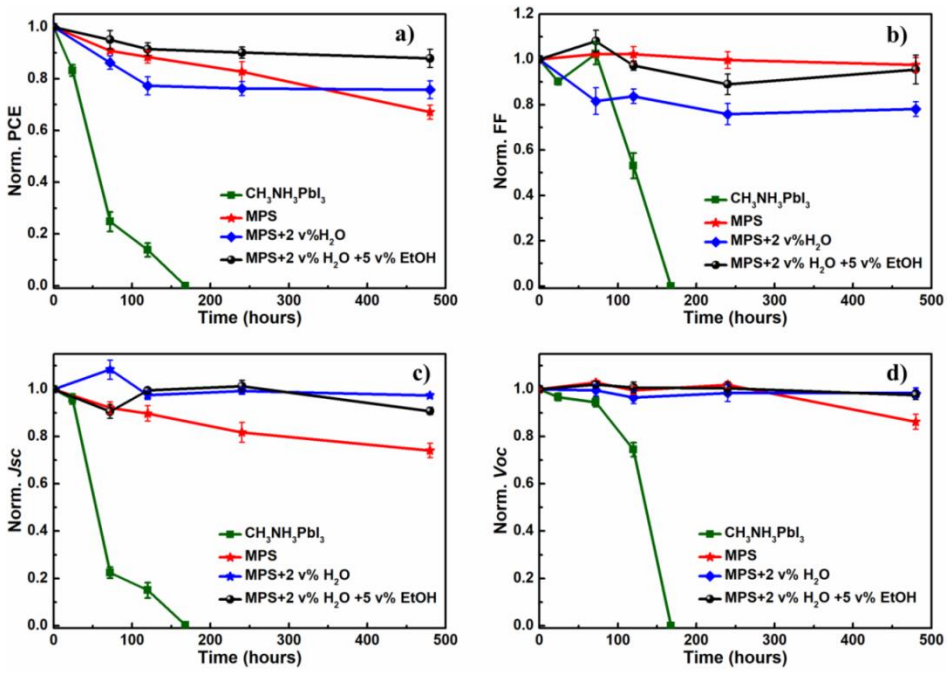

Figure 3. 6: The stability of the devices in the air is tested over 500 hours. a-d) The time evolution of the photovoltaic parameters, including PCE, FF, J_{sc}, and V_{oc}. (Note: The PV parameters for identical twelve devices are normalized using the initial PCE values and the standard error of the mean values are as indicated on the graphs).

We now observed the changes in the morphology and crystal structure of the films, which is believed to be a determinant factor of the loss in PV performance. A striking difference in the film morphology is evidenced in the SEM images taken before and after degradation, as shown in **Figure 3.7.** These observations suggest possible degradation of the perovskite materials. The degradation of the perovskite films is concomitant to the appearance of PbI_2 on the surface and at the grain boundaries. This is confirmed by the PbI_2 peak in the XRD patterns **Figure 3.8 (a-d),** where apparent changes are seen within the range of time of storage studied. Visually, the degradation is evidenced in the as-deposited films as the color changes from dark brown to yellow. Notably, MPS-based films maintained their initial dark-brown color over time, as seen in the insets of each XRD spectrum in **Figure 3.8,** showing a photograph of the films, taken on days 0, 10, 30, and 40, respectively. The thin films that did not degrade maintained the dark color until 40 days.

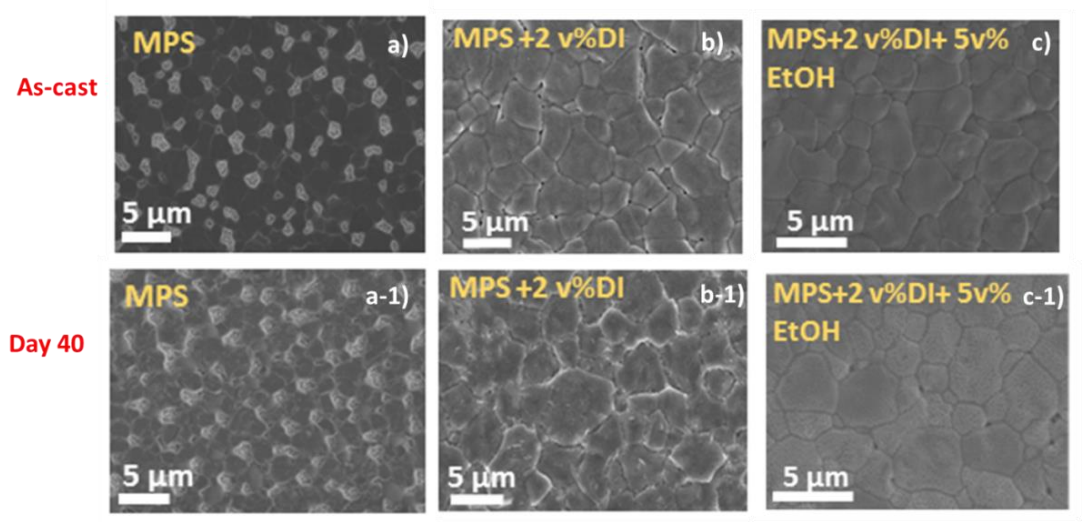

Figure 3. 7: SEM images of the top-view of as-cast and degraded perovskite thin films on FTO substrate. The first row shows the morphology of the films on the first day, and the second row shows the morphology after 40 days in ambient air. (a & a-1) $CH_3NH_3PbI_{2.81}(SCN)_{0.19}$ film (MPS). (b & b-1) MPS+ 2vol% H_2O and (c & c-1) MPS+2 vol% H_2O+5 vol% EtOH respectively.

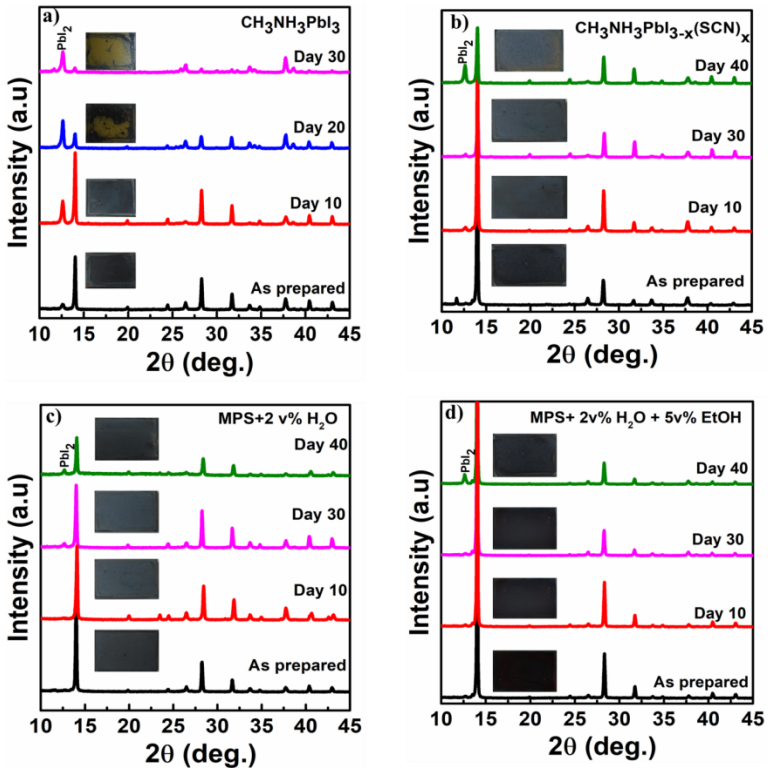

Figure 3. 8: (a-d) XRD patterns for the perovskite thin films studied over 40 days of exposure in the ambient environment (23°C ± 1°C, > 55% ± 5%RH). Insets are photographs showing the state of the film over time from fresh (bottom, as prepared, darker color) to degraded (top, 30 or 40 days, lighter color) perovskite thin films. These differences are more apparent in (a) and becoming less and less apparent from (b to d), with (d) the optimized blend showing little change in color from as-cast film to day 40 of the degradation.

The XRD pattern for MAPI films in **Figure 3.8a** shows the PbI_2 peak (at 12.6^o), whose intensity dramatically increased after storage in ambient air. Eventually, the prominent perovskite peaks almost disappeared after 30 days. Such an increase in the PbI_2 peak confirms that the perovskite completely decomposed. In **Figure 3.8b,** for MPS films, the PbI_2 peak is weakly noticeable after ten days and remains unchanged for more than 30 days before slightly increasing after 40 days. In contrast, the films with additives show a shallow PbI_2 peak after 30 days, as in the case of MPS+2 vol% H_2O and MPS+2 vol% H_2O+5 vol% EtOH films (**Figure 3.8(c, d)**). Thus, for MPS-based perovskite films, the use of the SCN dopant resulted in a more stable perovskite. This is associated with the strong ionic interactions between S-C-N and adjacent Pb and additional hydrogen bonding between SCN^- and $CH_3NH_3^+$.[142] The degradation of the perovskite films is initiated by morphological changes in the films due to the partial decomposition of constituent elements. Based on these observations, it can be established that the degradation process in MAPI films is much more rapid than that of SCN-doped films. We anticipate that such degradation is primarily due to the reaction of the film with moisture and oxygen present in their immediate environment leading to the gradual appearance and increase of the PbI_2 component, knowing that upon annealing of our samples at 110^{o}C, all excess solvents (including water) completely evaporated.

To determine whether SCN-ions remained in the perovskite films or not, we conducted Fourier transform Infrared Attenuated Total Reflectance (FTIR-ATR) spectroscopy on SCN-doped films for heated/annealed (HT), non-annealed (NHT), and degraded samples. The spectra in **Figure A3.4** reveal a peak of SCN- ion at 2064 cm^{-1} even after annealing the samples, which is in agreement with previous reports[194,195]. This ascertains that the SCN-ions did not completely evaporate during the annealing process as evidenced by the peak intensity at that characteristic wavenumber. From these observations, we believe that this could be another possible reason behind the good stability of the device with SCN additive. However, over time and in ambient condition, the perovskite films gradually degrade due to the presence of oxygen and moisture. The FTIR monitoring of the degraded samples also revealed the disappearance of the SCN-peaks, meaning that SCN-ions are lost or removed with time by other chemical mechanisms/reactions due to the variance in ambient environment. Therefore, our approach apparently played an essential role in the stabilization of the perovskite thin films.

Moreover, the benefits of incorporating both H_2O and EtOH into the MPS precursor solution do not only aid the crystallization process but also provide the necessary moisture needed and strengthens the hydrogen bonding in the crystal . This also makes our thin films more resistant to the surrounding environment moisture, hence more stable. In all, from the SEM and XRD results, we infer that the crystal quality and morphology, remarkably uniform pinhole-free perovskite thin film, have positively impacted the photovoltaic performance and stability of the fabricated devices.

3.3 Conclusions

This study was carried out to find a route to process and fabricate halide perovskite solar cells under ambient conditions, which had not been extensively studied in the available literature when this work was done. The effects of the fractional substitution of PbI_2 with $Pb(SCN)_2$ and solvent additives to the perovskite precursor solution on the morphology, crystallinity, PCE, and stability of ambient-processed perovskite solar cells were systematically investigated. Based on our investigations of the halide perovskite films obtained, it was found that the incorporation of SCN anions into single-cation $CH_3NH_3PbI_3$, precursor does not only improve film coverage but also prolongs the longevity of the perovskite films. From the findings, $CH_3NH_3PbI_{2.81}(SCN)_{0.19}$ with 2 vol% H_2O and 5 vol% EtOH additives presented pinhole-free, large grains, and well-crystallized perovskite film, which in turn enables a significant improvement in their PV performance and stability.

These findings boost our understanding of the critical role that the chemical composition and fabrication conditions of the perovskite precursor play in the performance of perovskite solar cells. It also constitutes one of the first steps to address the challenges moisture poses to the fabrication and stability of ambient-processed perovskite films. The results presented here suggest that stable and efficient perovskite solar cells can be achieved with perovskite films entirely processed under ambient conditions. Thus, our novel fabrication method paves the way towards efficient and moisture-immune perovskite-based devices suited for storage and operation in ambient conditions.

Chapter 4: Stable and Efficient Triple Cation Perovskite Solar Cells

We have presented, in chapter 3, a new solution of perovskite precursors for room-temperature fabrication of SCN-doped $MAPbI_3$-based solar cells that are reproducible, highly crystalline, efficient, and stable. To further improve the performance and especially the stability of these devices, we now present hybrid perovskite-based solar cells fabricated using halide precursors mixed with three different cations (Cs, MA, and FA) via a pseudohalide (SCN) additive and a solvent-antisolvent (ethanol and chlorobenzene) processing method instead of the previously used water and ethanol additives. We then investigate the effect of the additives on the i) microstructure, ii) device performance, iii) charge dynamics, and iv) stability of the perovskite material. In addition, the performance and degradation mechanisms are explained using the space-charge limited current (SCLC) method, trap-state density for charge carriers at the perovskite interfaces, and unbalanced charge carrier mobility in the device.

Most of the findings discussed in this chapter are based on the following publications:

1. *Asuo, I. M. et al. Ambient condition-processing strategy for improved air-stability and efficiency in mixed-cation perovskite solar cells. Mater. Adv.* ***1****, 1866 (2020).*
2. *International Patent number: WO/2020/248063, Published 17-12-2020*

4.1 Introduction

Over the past few years, several methods have been explored to address the short lifetime of perovskite solar cells (PSCs) through synthesis, structure, and device architectural optimization[140,196]. These modified syntheses were intended to achieve more stable and compact halide perovskite thin films. Most of these perovskite materials have been synthesized in a controlled or inert atmosphere. Besides, thin-film morphology plays a significant role in improving the stability and efficiency of the PSCs. Pinholes/voids will be present if the perovskite thin film is not uniformly formed on the substrate. These pinholes are means for recombination and short circuit in the device, leading to low efficiency or non-functional devices. Thus, the morphology of the thin film is greatly dependent on the fabrication processes and conditions. The process of obtaining compact thin films with large crystalline grains on a given substrate is challenging but

crucial for high-performance thin-film-based devices[158]. For optimum device performances, the ideal perovskite film should be pinhole-free, composed of large crystalline grains, with a smooth surface[197] and a few grain boundaries[198,199].

In addition, the long-term stability of PSCs is a core impediment that needs to be resolved for their viable deployment. In this context and to increase both efficiency and stability of the PSCs, recent studies focus directly or indirectly on achieving high-quality and compact morphology of perovskite films using either single[168], double[145], or mixed-cation[63] perovskite systems. In most single-cation systems such as $CH_3NH_3PbI_3$, the ambient environment accelerates their degradation, causing the rapid decomposition of the perovskite material into optically-inert constituents such as PbI_2.[95] A recent report, however, proposed a mixed-cation system that exhibits high and stable PV performance[63]. Nonetheless, in this report, as in most of the other reports so far, the films synthesis, device fabrication, and testing were performed in an inert atmosphere[63,116]. This, of course, is an expensive fabrication and testing process and not a true representation of the actual operating conditions as the solar cells will be used in the ambient environment. In chapter 3, we demonstrated that perovskite solar cells could be fabricated and tested entirely under ambient conditions. To achieve this, we incorporated lead thiocyanate into a single-cation perovskite which yielded stable thin films and devices. However, their performances (efficiency and stability) were still low compared to other benchmark solar technologies.

Meanwhile, mixed-cation showed potential for higher performance according to the literature. Thus, there is a strong interest in developing a method for fabricating mixed-cation perovskite solar cells with an equivalent or even better long-term stability under ambient conditions. Since this thesis aims to reduce fabrication costs, such a method that does not require an expensive controlled environment would likely be in high demand and readily adopted by any community. Based on the knowledge acquired and employed in chapter 3, we extended our investigation to triple-cation perovskites.

The chapter focuses on tailoring perovskite grain size and crystal quality by using an ionic additive, lead thiocyanate ($Pb(SCN)_2$), and a solvent–antisolvent (ethanol and chlorobenzene) treatment for the triple-cation perovskite films[141]. The combined impacts of solvent treatment and $Pb(SCN)_2$ integration on thin-film characteristics and the performance of devices fabricated were studied. Unlike in chapter 3 where the solvent additives were added into the precursor solution, here, the

solvent treatments are introduced during the spin coating process. The use of ethanol and chlorobenzene for solvent treatment promotes the nucleation of grains and crystallization of the perovskite[44,179]. Ethanol mainly contributes to the dissolution of the remnant solute of the perovskite[179]. Chlorobenzene, an anti-solvent for perovskite, is used to induce the fast precipitation of the perovskite film, resulting in the growth of smooth, well-crystallized, and large grain perovskite films. The literature and results presented in chapter 3 also advocate that $Pb(SCN)_2$ additive increases the moisture tolerance of perovskite thin films while conserving their microstructural properties[42,149,213]. It also reduces radiative and non-radiative losses, thereby improving the device's performance[144]. Henceforth, we incorporate $Pb(SCN)_2$ in different weight percentages into the perovskite entirely under ambient air and high relative humidity (~55±5 %RH).

Adopting such a strategy, we have successfully enhanced the morphology of triple-cation (or mixed-cation-mixed-halide) perovskite thin films and the charge transport properties of their photovoltaic devices. Using our optimized all-ambient processing method, we achieved pinhole-free, compact thin films with large crystalline grains and passivated grain boundaries. The perovskite thin films were used to fabricate solar cells. The best ones have an efficiency of approximately 20% with excellent stability for more than ten months. Our findings help establish that the performance of PSCs is related to their device architecture, grain morphology, trap-state density, and carrier mobility in the device before and after storage. These novel organic-inorganic halide perovskite films pave the way for industrial production of low-cost, efficient, and long-term stable solar cell modules.

4.2 Experimental Methods

4.2.1 Preparation and Deposition of Perovskite Precursor Materials

Mixed-cation-mixed halide perovskite of a similar form $Cs_y(MA_{0.17}FA_{0.83})Pb_{(1-x)}(I_{0.83}Br_{0.17})_3$ has been modified to prepare our precursor solution (DEV-0). For the perovskite to be resilient under ambient conditions, varying weight percentages of 2.9, 5.8, 9.4, and 11.1 wt% of $Pb(SCN)_2$ were added to the reference perovskite solution. To obtain the perovskite solution, we dissolved 0.6 M methylammonium iodide (MAI), 0.2 M methylammonium bromide (MABr), 1 M formamidinium iodide (FAI), 0.8 M lead (II) iodide (PbI_2) and 0.5 M lead (II) bromide ($PbBr_2$) in mixed solvent DMSO/DMF 1:4 volume ratio. Then, a volume ratio of cesium iodide (CsI) solution of 1.5 M in

DMSO was added to the perovskite solution and stirred gently for one hour. No pre-heating of the solutions was required before their depositions. The perovskite solution was then deposited onto the TiO_2 layer of the Glass/FTO/TiO_2 substrate and spin-coated at 2000 rpm for 20 s. A subsequent solvent-antisolvent treatment using different volume ratios (0-100 vol%) of chlorobenzene (CB) and ethanol (EtOH) was carried out in a dynamic spin-coating mode and spun at 5000 rpm for 10s (**see section 2.4.4**). After spin coating, the films were then annealed at 125 ^oC for 15 minutes to complete the perovskite crystallization process and evaporate the excess solvents. The fabrication steps took place under ambient conditions: 22^oC-25^oC and 25%-55%RH. *[International Patent number: WO/2020/248063, Published 17-12-2020]*

4.2.2 Solar Cell Fabrications

The perovskite solutions were deposited on the substrates and processed using the two-step spin coating method described above. The first step was casting the perovskite precursor solution onto the FTO/c-TiO_2/mp-TiO_2/ (section 2.4**),** followed by the solvent treatment. Then, the hole-transporting material, Spiro-OMeTAD, was subsequently deposited by spin-coating atop the FTO/c-TiO_2/mp-TiO_2/perovskite layer. The Spiro-OMeTAD solution was prepared following a process described in section 2.4.5. Finally, the devices were completed by thermal evaporation of a 100 nm gold layer to serve as a top electrode, deposited at 0.2 nm/s and pressure of $5x10^{-5}$ Torr. The active area for all the devices was 0.45 cm x 0.15 cm, defined by the size of the shadow mask used during the gold top electrode thermal evaporation.

4.2.3 Fabrication of Single-Carrier Devices

Single-carrier devices were also fabricated by spin-coating method to study the charge carrier dynamics in the perovskite. Hole-only devices were fabricated by depositing ~60 nm gold layer on top of FTO via thermal evaporation, followed by spin-coating the perovskite precursor solution at 2000 rpm for 25 s. A 100µl of the Spiro-OMeTAD solution was spin-coated at 3000 rpm for 30 s, and finally, ~80 nm of gold as a top electrode was deposited via thermal evaporation. Electron-only devices were fabricated by spin-coating the perovskite solution on FTO/TiO_2 layer at 2000 rpm for 25 s. This was then followed by spin-casting of [6,6]-Phenyl-C_{71}-butyric acid methyl Ester ($PC_{71}BM$) solution (15 mg/ml in chlorobenzene) at 1500 rpm for 30 s. Finally, the gold top

electrode was thermally evaporated. After each step of depositing the perovskite layers, they were annealed and cooled down to room temperature before spin-coating the following layers. For the stability measurement, the perovskite thin film was exposed to the ambient before the evaporation of the top electrodes.

4.3 Results and Discussions

4.3.1 Thin Film Morphology, Crystallinity, and Device Performance: The Role of Solvent-Anti Solvent Treatment

We have shown in the previous chapter that achieving efficient and stable perovskite solar cells is highly dependent on the grain morphology and the crystal quality of the thin-films. This section focuses on the influence of solvent-antisolvent treatment on the morphological, microstructural, and device parameters of the perovskite thin films. The mixed-cation-mixed-halide perovskite thin films were prepared by optimizing the composition of the precursor solutions and the solvent-antisolvent treatment process during film deposition. Perovskite thin films with varying volume percentages of chlorobenzene and ethanol were prepared to determine the best combination for achieving high-performance devices. The optimal volume fractions for combining CB and EtOH to achieve concurrently large grain and compact (pinhole-free) perovskite thin films have been determined. The surface morphologies are characterized using a scanning electron microscope (SEM) technique. **Figure 4.1** shows the top-view SEM images of the perovskite films treated with 0-100 vol % of CB and EtOH. Note that samples with no solvent treatment are labeled 0CB-0EtOH, and the ones with solvent treatment are labeled with respect to the vol% of chlorobenzene. For example, 10CB means 10 vol % of CB and 90 vol % EtOH were added.

A look at the SEM image reveals large grain, non-compact film for the pristine perovskite without solvent-anti-solvent treatment, as presented in **Figure 4.1a**. Although the grains are large, they are not interconnected, resulting in very poor surface coverage. The dark parts are the perovskite grains, and the white parts are mostly the exposed FTO substrate. Such porous morphology is not favorable for fabricating solar cells since it may lead to a short circuit, resulting in less efficient or unfunctional solar cells. In this regard, we employ the solvent-antisolvent treatment to aid fast precipitation and crystallization of the films, subsequently obtaining pinhole-free morphologies. Consequently, upon solvent treatment, the morphologies are significantly enhanced with more compact films with no visible pinholes/voids (**Figure 4.1(f-k)).** Notably, depending on the vol%

of solvent we add, the grain sizes improve, and the film coverage is greatly enhanced. We speculated that the observed grey/white grains (**Figure 4.1(b-d))** and layers at the grain boundaries (**Figure 4.1(e-h))** could be PbI_2-rich phases which eventually shrink as the vol% of CB is increased. These PbI_2-rich phases are evidenced by XRD patterns.

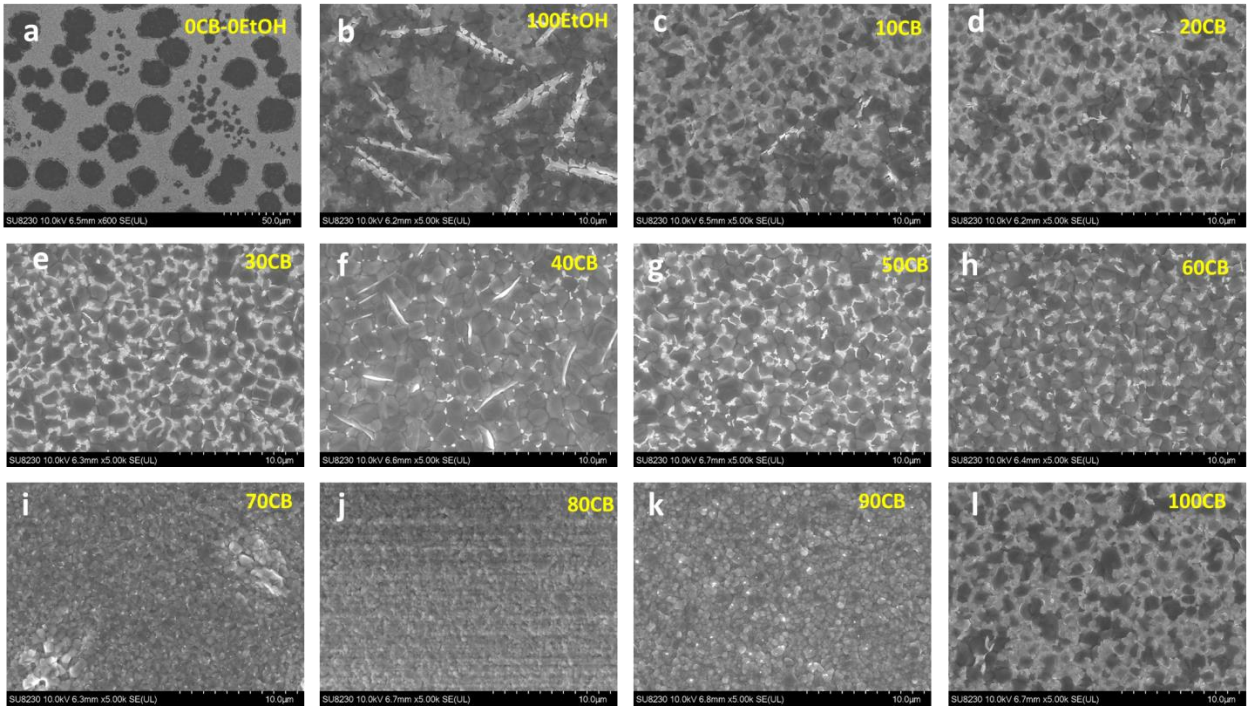

Figure 4. 1: Top view SEM images of the perovskite films with different volume ratio of chlorobenzene:ethanol (CB-EtOH) (a) 0:0 v/v %, (b) 0:100 v/v %, (c) 10:90 v/v %, (d) 20:80 v/v %, (e) 30:70 v/v %, (f) 40:60 v/v %, (g) 50:50 v/v %, (h) 60:40 v/v %, (i) 70:30 v/v %, (j) 80:20 v/v %, (k) 90:10 %v/v, and (l) 100:0 v/v %. The grey/white patches show thin films which are PbI_2-rich while the dark indicates well-crystalized perovskite films.

The XRD patterns of the perovskite films with the different volume ratios of CB:EtOH (0 to 100 vol%) displayed in **Figure 4.2** establish that with the increment in vol% of CB, the crystallization of the film improves. These patterns confirm highly crystallized films and tetragonal phase[44] of halide perovskite with two signature peaks indexed as (110) and (220) at 14.18º and 28.56º. By closely monitoring the two perovskite peaks, we can identify the influence of the solvent-antisolvent treatment on the crystallinity of the films. With solvent treatment from 70-90 vol% CB, we observe that the PbI_2 peak (at 12.7º) diminishes while the two prominent perovskite peaks become intense. For instance, the pattern for the 90CB sample (*in pink*) reveals a distinct crystal orientation along the (110) plane, suggesting highly-oriented crystals with preferential growth

direction along this plane[168]. In comparison, the 10CB sample (*in deep green*) exhibits the presence of the PbI_2 phase as well as the dominant perovskite peaks, which corroborate the grey features seen on the SEM characteristics. It is found that increasing the volume ratio of added ethanol (> 40 vol%) for the solvent treatment results in intense PbI_2 peaks while keeping it below that threshold show no sharp PbI_2 peaks. It is good not to have such a high presence of PbI_2 because it would result in fast degradation of the perovskite film. We, therefore, recommend that such a high degree of order in the perovskite films with high vol% of chlorobenzene (e.g. 90CB) originates from the pre-crystallization step during the solvent-antisolvent treatment.

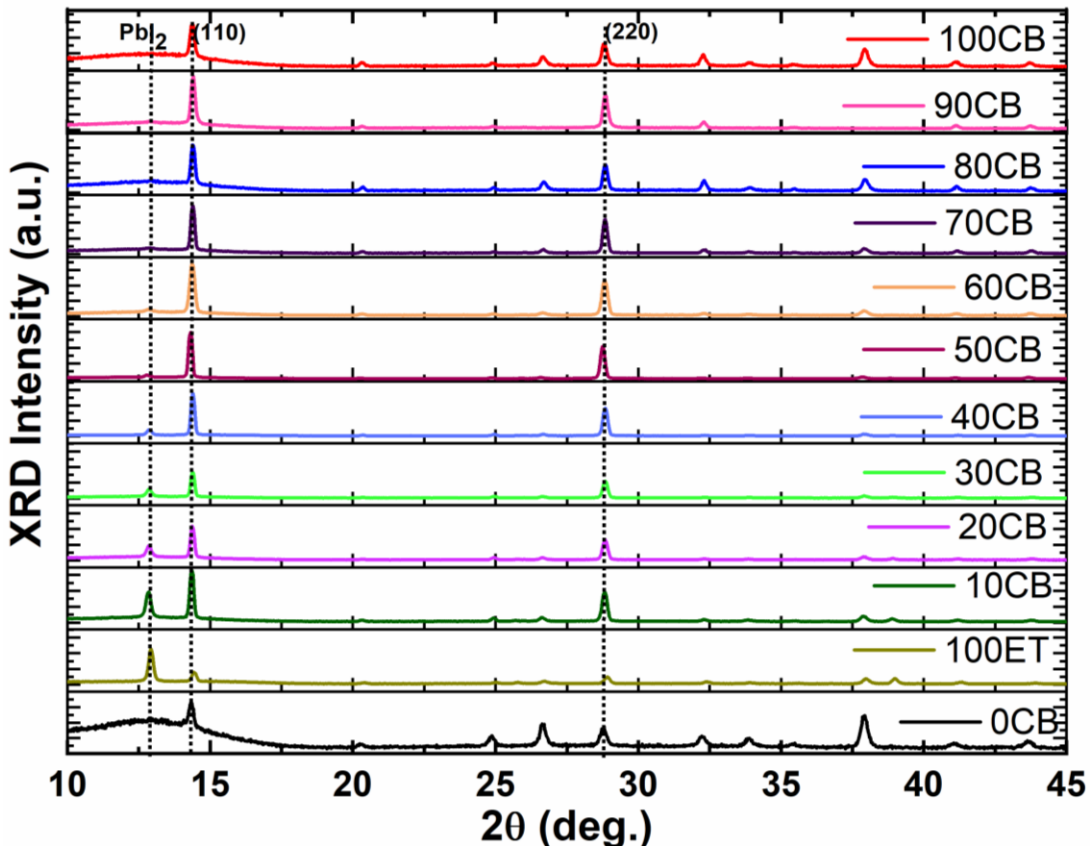

Figure 4. 2: XRD spectra of the perovskite films with the different volume ratios (0-100 vol%) of chlorobenzene: ethanol (CB-EtOH) as indicated on each pattern. The presence of PbI_2 is indicated at 12.7 º and diminished upon solvent treatment. The main tetragonal perovskite structures are at 14.18 º and 28.56º.

To confirm the correlation between film morphology, crystallinity, and device performance, we compared solar cells fabricated with 0 to 100 vol% of CB-EtOH solvent treatments. The cross-section SEM image presented in **Figure 4.3a** shows the device architecture (Glass/ FTO/C-TiO_2/mp-TiO_2/perovskite/spiro-OMeTAD/Au) of the solar cells with a typical film thickness of

about 500 nm. It is also found that the perovskite is infiltrated well into the mesoporous-TiO_2 film, which helps in effective charge transport and increases the device's efficiency. The *J-V* curves displayed in **Figure 4.3b** represent the performance of the solar cells under AM 1.5G illumination. The photovoltaic parameters; V_{oc}, J_{sc}, FF, and PCE are presented in **Table 4.1**. We observe a rise in PCE as the vol% of CB-EtOH increases. It is noted that the solvent treatment with 90CB shows the highest efficiency of 18.4% among the different fractions of CB-EtOH solvent. Most of the devices performed averagely well, and a significant improvement is observed as vol% of CB-EtOH increases.

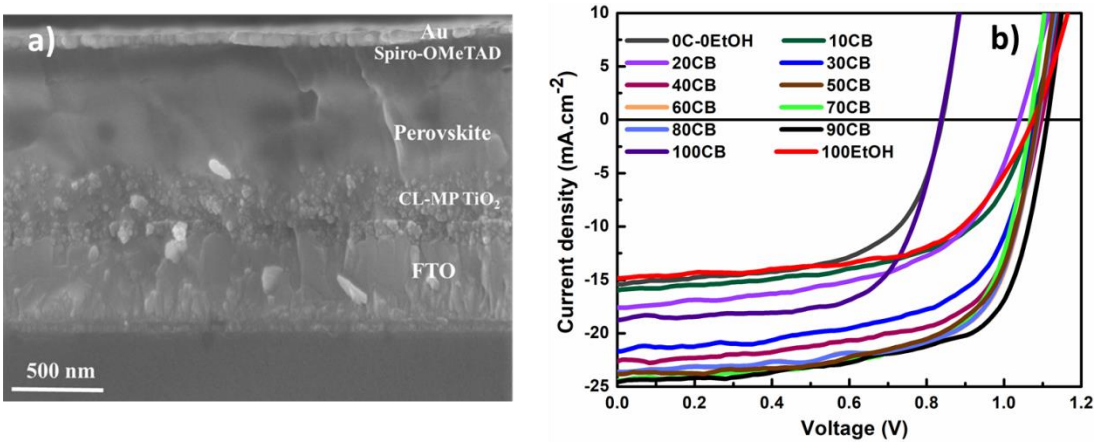

Figure 4.3: a) A cross-section SEM image of the fabricated mesoporous TiO_2-based solar cell. The solar cell device configuration is: Glass/FTO/CL-MP-TiO_2/perovskite/spiro-OMeTAD/gold. b) *J-V* characteristics curves showing the device performance of the solar cells fabricated with the different volume ratios of chlorobenzene and ethanol treatments from 0-100 vol%.

Indeed, the *J-V* characteristics confirm that the changes in grain morphology and crystallinity (shown in **Figures 4.1 & 4.2**) significantly affect the performance of the devices. Lower PCEs (<11%) are recorded when the samples are treated with 10CB, 20CB, 100CB, and 100ET. While the highest PCEs are achieved when the film is treated with 80 and 90 %vol CB. As indicated in **Table 4.1**, the improved cell efficiency is mainly driven by an improvement of J_{sc} and V_{oc} with FF reaching over 60%. Adding ethanol shifts the J_{sc} and V_{oc} to larger values, hence an increase in the PCE. Seemingly, the enhanced efficiency correlates with the evolution of the film morphology as depicted in the SEM images and the crystal quality from XRD patterns. The non-compact perovskite thin film for 0CB-0EtOH yielded lower PV parameters, while uniform films obtained

from the solvent-antisolvent treatment directly increased PV performance. Thus, the trend in the behavior of the solar cells is associated with the SEM and XRD findings and affirm that the performance of thin-film solar cell directly has a relationship with the film morphology. We have therefore succeeded in fabricating high-performance solar cells entirely under ambient.

Table 4.1: Evolution of solar cell performance with the different volume ratios of chlorobenzene and ethanol.

Samples	J_{sc} (mA.cm^{-2})	V_{oc} (V)	FF (%)	PCE (%)
0CB-0ET	15.4	0.837	60.0	8.0
100ET	14.8	1.076	61.0	9.7
10CB	15.9	1.071	58.3	10.0
20CB	17.5	1.040	56.2	10.3
30CB	21.7	1.082	61.9	14.5
40CB	22.6	1.097	64.9	16.1
50CB	23.8	1.086	65.3	16.9
60CB	24.3	1.084	66.4	17.5
70CB	24.4	1.068	66.9	17.4
80CB	23.6	1.088	70.0	18.0
90CB	24.5	1.112	67.7	18.4
100CB	18.7	0.840	66.6	10.5

4.3.2 Synergistic Effect of SCN Ions and Solvent-Anti Solvent on Morphology, Crystal Structure, and Optical Properties

To elucidate the synergistic effect of SCN^- and solvent anti-solvent treatment on the perovskite film, we narrow our investigations to 90CB samples. This decision is based on the morphology, crystal structure characterizations, and solar cell performances presented above. We believe the

90CB sample exhibits the best compact grains with no pinholes, fewest grain boundaries, and best crystal quality. Based on these qualities, samples were fabricated using varying weight percentages of $Pb(SCN)_2$ from 0-11 wt% to improve the film quality further and determine the optimum composition for the best performing solar cell under the same conditions. Then again, we seek to investigate this because it is directly related to the performance of PSCs in terms of efficiency, reproducibility, and stability. In this regard, the fabricated perovskite samples with and without the SCN-dopant are labeled DEV-*x* (where *x* is the weight percentage of the dopant from 0-11 wt%). To analyze the effect of SCN^- on film quality, we performed SEM, XRD, and absorption measurements.

Figure 4.4 shows the top-view SEM images of the as-deposited DEV-*0*, DEV-*5.8*, DEV-*9.4*, and DEV-*11.1* perovskite films, all solvent-treated, with 90 vol% CB:10 vol% EtOH. DEV-*0* film reveals compact morphology with interconnected fine grains of an average size of ~200 nm, while the addition of the SCN^- results in larger grains with no pinhole/voids. All the samples with SCN^- dopant exhibit complete surface coverage with large grains. The grain sizes are reduced slightly when the weight percentage of SCN^- is increased from 5.8 to 11.1 wt% while maintaining the compact morphology. Remarkably, the grain morphology of the DEV-5.8 films shows less and passivated grain boundaries with a grain size of ~3 microns, as shown in **Figure 4.4(b)**. Also, DEV-*9.4* and DEV-*11.1* films exhibit large and homogeneous grains with no apparent pinholes. SCN^- considerably modifies the crystallization process for achieving large grains and compact/uniform perovskite films, which are prerequisites for efficient thin-film solar cells.

The mechanisms for large grain growth have been suggested to originate from lower Gibbs free energy for nucleation due to the beneficial effect of incorporated SCN^- ion[143,201]. Also, during the perovskite film formation, there could be a reaction between $CH_3NH_3^+$ cations and SCN^- anions, leading to the formation of CH_3NH_2 gas[144,202]. The CH_3NH_2 gas is known to increase the grain size and crystalline quality of perovskite thin films. Besides, we have established that solvent–antisolvent treatment of perovskite films also results in larger grains[44]. These could be some of the reasons behind the grain enlargement of our thin films. Thus, the addition of $Pb(SCN)_2$ leads to increased crystallites size and reduced grain boundary density. The presence of fewer grain boundaries has been previously shown to reduce recombination, trap states, passivate the defects sites in perovskite films[125,203] and eventually promote charge transport in the solar cells.

Therefore, we believe the solar cells fabricated with these thin films will perform better since the films present fewer grain boundaries and compact grains, which helps avoid short circuits in the device under operational conditions.

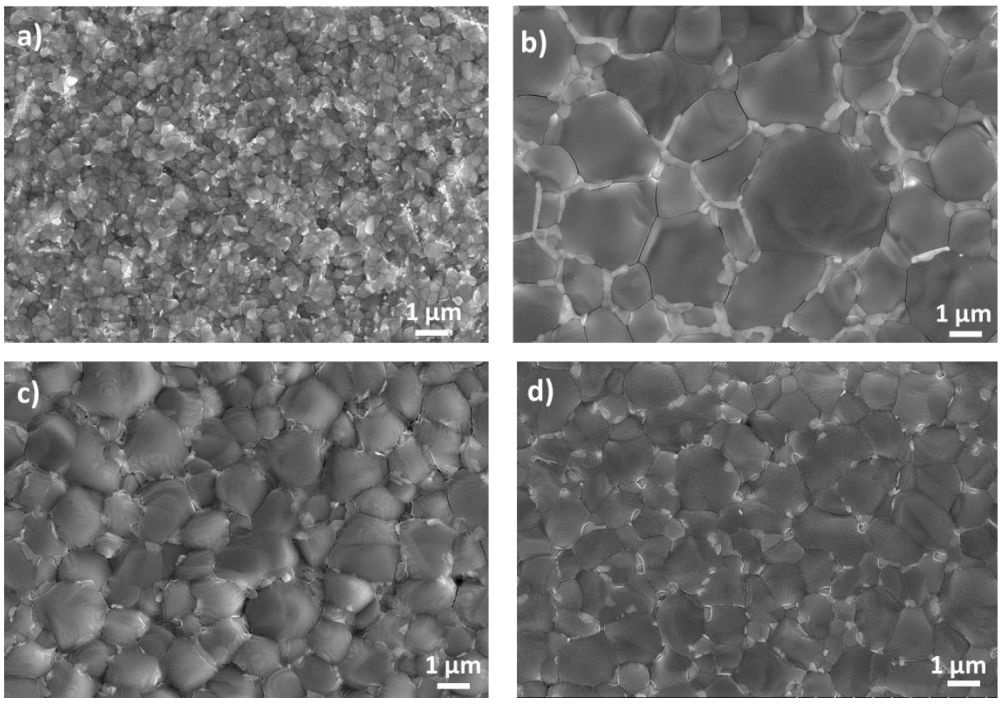

Figure 4.4: Top-view SEM images of the perovskite films for (a) DEV-*0*, (b) DEV-*5.8*, (c) DEV-*9.4*, and (d) DEV-11.1. The images in b, c, and d show grain boundaries passivation evidenced by the bright contrast as well as large grain sizes upon the addition of $Pb(SCN)_2$.

Next, we analyze the as-deposited films by XRD measurements (**Figure 4.5a**) to further consider the crystallinity of the perovskite depending on the wt% of SCN^- dopants. The XRD patterns exhibit strong and sharp peaks matching the tetragonal structure for halide perovskites, in agreement with previous reports[44,63]. The full width at half maximum (FWHM) values obtained from the (110) peaks show that the SCN-based films possess enhanced crystallinity with a value of 0.17±0.04º and a crystallite size of 47.4±3 nm determined from Scherrer's equation[186]. In comparison, the DEV-*0* films exhibit a FWHM value of 0.23±0.08º with a crystallite size of 34.6±4.1 nm. Thus, the inclusion of SCN^- helps achieve high-quality crystals of the perovskite thin films as confirmed from the sharp XRD peaks. These XRD spectra also demonstrate that there is no observable PbI_2 peak at ~12.6º for thin films.

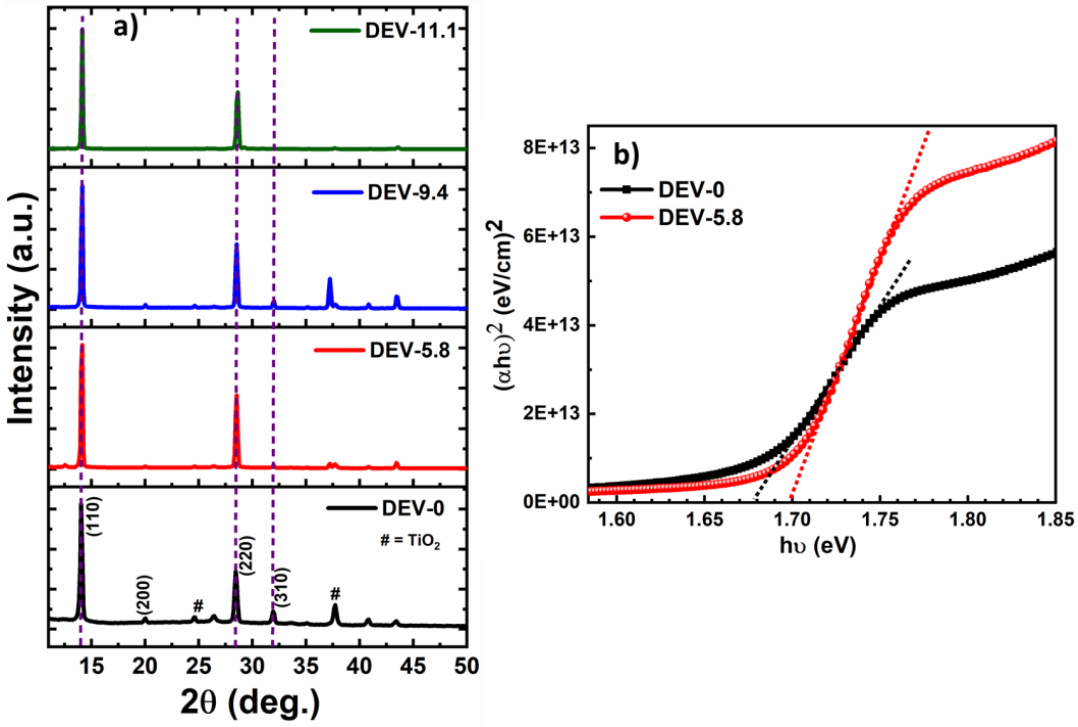

Figure 4. 5: (a) XRD spectra of the prepared perovskite films with and without the dopant as indicated on each spectrum: DEV-*0* (black), DEV-*5.8* (red), DEV-*9.4* (blue), and DEV-11.1 (green). (b) Tauc plot obtained from typical UV-Vis absorption spectra for DEV-*0* (black) and the DEV-*5.8* (red) samples.

We believe that the formations of the grey regions at the grain boundaries originate from the crystallization mechanism. The possible composition of the grey regions has been investigated and reported using energy-dispersive X-ray spectroscopy (EDS) and Auger spectra[141]. **Figure A4.1** depicts all the major elemental components such as Pb, I, S, and Cs in the perovskite material. From our Auger spectra (**Figure A4.2 (c-e)),** we found that there is a presence of sulfur at the grain boundaries with higher Pb intensities. These findings revealed that the grey regions observed in the SEM images are the Pb, I, and SCN-rich phases and explain why our best DEV-*5.8* films exhibited no PbI_2 peaks on the XRD pattern[141]. In general, the presence of excess Pb^{2+} at the grain boundaries is advantageous and impacts charge-carrier injection, hysteresis, and the overall device performance of PSCs[204]. Consequently, we demonstrate that the passivation of the grain boundaries through the systematic introduction of $Pb(SCN)_2$ and the solvent–antisolvent treatment effectively increase the grain size while avoiding the formation of excess pure PbI_2.

Furthermore, it is important to confirm that the perovskite films are optically active and can absorb light effectively. Given this, we examine the optical properties of the perovskite films through UV-

vis absorption measurements. The optical bandgaps of the perovskite films are determined from the Tauc plot of $(\alpha h\nu)^2$ versus $h\nu$. From **Figure 4.5b,** the bandgaps are estimated to be 1.68 eV and 1.7 eV for DEV-*0* and DEV-*5.8* perovskite films, respectively. The spectra show that our perovskite films can absorb light of ultraviolet, visible to near-infrared. This is also a vital parameter for an efficient thin-film-solar cell device[44,145]. Notably, SCN-dopant and the solvent treatment do not change the optical properties but rather synergistically result in broad spectral absorption of the perovskite films.

4.3.3 Photovoltaic Performance: Power Conversion Efficiency

To correlate the effect of the additives on the device performance, we compared solar cells fabricated with 0 to 11.1 wt% of SCN^- and 90CB-10EtOH solvent treatments. First, we compare the PCEs of the solar cells fabricated with varying wt% of SCN^- (0 to 11.1) and present the mean values to find the optimum performance, as shown in **Figure 4.6a**. The figure demonstrates the effect of the various weight percentages of SCN^- on the device performance. As the wt% of SCN^- increases, the PCE also improves, with 5.8 wt% registering the highest value, followed by a decrease in PCE up to 11 wt%. **Figure 4.6b** displays the best PV performances of the three main solar cells after further optimizations on the thin film deposition and device fabrication. The summary of the PV parameters is presented in **Table 4.2,** and it shows that DEV-*9.4* and DEV-*11.1* yielding more than 15% PCE with only a 6% increase in the PCE from DEV-*9.4* to DEV-*11.1*, while DEV-*2.9* has the lowest efficiency. At the same time, DEV-*5.8* recorded the best performance with a PCE of 19.3%, although the V_{oc} decreased a little. The major factor resulting in the higher PCE of the DEV-*5.8* sample is attributed to the enhanced J_{sc} and FF. Given the high PV performance of DEV-*5.8* solar cells and the similarities in the behavior of the other two SCN-based solar cells, we decided to simplify our studies in further investigations using only DEV-*5.8* solar cells and compare their performance to the one without SCN^- dopant.

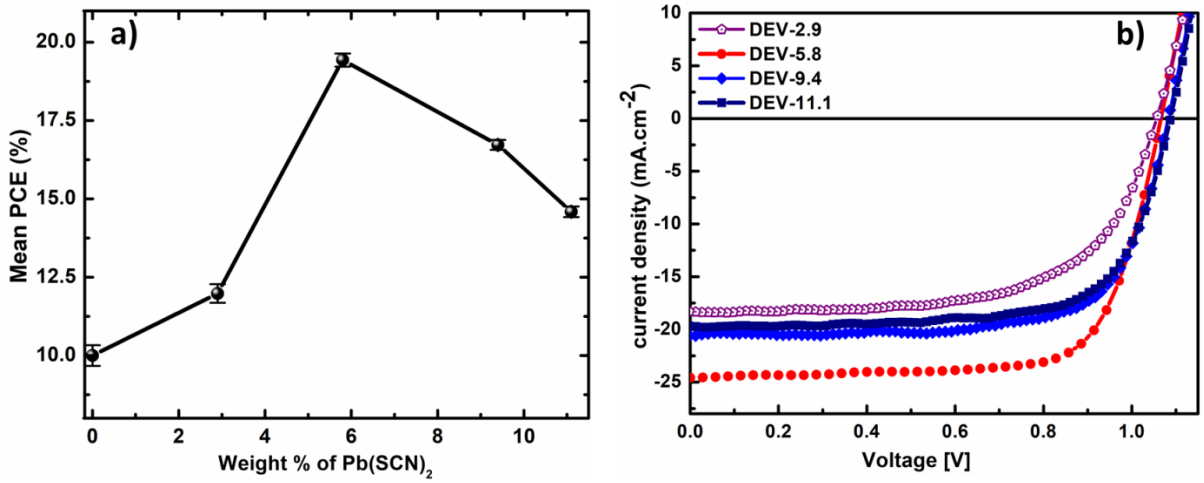

Figure 4. 6: a) The trend of the performance of the solar cell in terms of mean PCE versus the weight percentage of the $Pb(SCN)_2$ additive. b) *J–V* curves measured under AM1.5 illumination of optimized solar cell devices, fabricated using a perovskite with additives varying from 2.9 to 11.1 wt% $Pb(SCN)_2$ (DEV-*2.9*, DEV-*5.8*, DEV-*9.4*, and DEV-*11.1*) with 90CB solvent-antisolvent treatment.

Table 4.2: Device parameters of solar cells fabricated with varying weight percentages of $Pb(SCN)_2$.

J-V Parameters	**DEV-*2.9***	**DEV-*5.8***	**DEV-*9.4***	**DEV-*11.1***
V_{oc} (V)	1.056	1.066	1.083	1.088
J_{sc} (mA.cm^{-2})	18.3	24.5	20.6	19.7
FF (%)	63.1	73.8	71.7	70.5
PCE (%)	12.2	19.3	16.0	15.1

Figure 4.7(a) shows the typical current density-voltage (*J-V*) characteristics of the optimized DEV-*0* and DEV-*5.8* solar cells. The photovoltaic parameters of the solar cells fabricated under similar conditions are summarized in **Table 4.3**. The PCE results indicate that, in general, DEV-*5.8* solar cells outperformed the DEV-*0* devices (20.3% versus 11.0% for the best-performing solar cells). Thus, using SCN^- dopant resulted in an almost 55 % improvement in the PCE due to higher $J_{sc,}$ FF, and V_{oc}. The hysteresis behavior in PSC has been explored, as it is one of the critical parameters for PV performance[205–209]. The charge trapping at the interface and grain boundaries, iodine ion migration, and other factors have been proposed to be responsible for the hysteretic

behavior and lower extraction efficiencies[44,210] in PSCs. Hence, we determined the hysteresis index (HI) of our device by using the relation[211]:

$$Hysteresis\ Index = \frac{J_{rev}(0.8V_{oc}) - J_{fwd}(0.8V_{oc})}{J_{rev}(0.8V_{oc})} \quad (4.1)$$

with $J_{rev}(0.8V_{oc})$ the current-density at 80% of V_{OC} for the reverse scan and, $J_{fwd}(0.8V_{oc})$ the current density at 80% of V_{OC} for the forward scan. The measurements were obtained in forward and reverse scanning modes at a rate of 16 mV/s under illumination to evaluate the hysteresis.

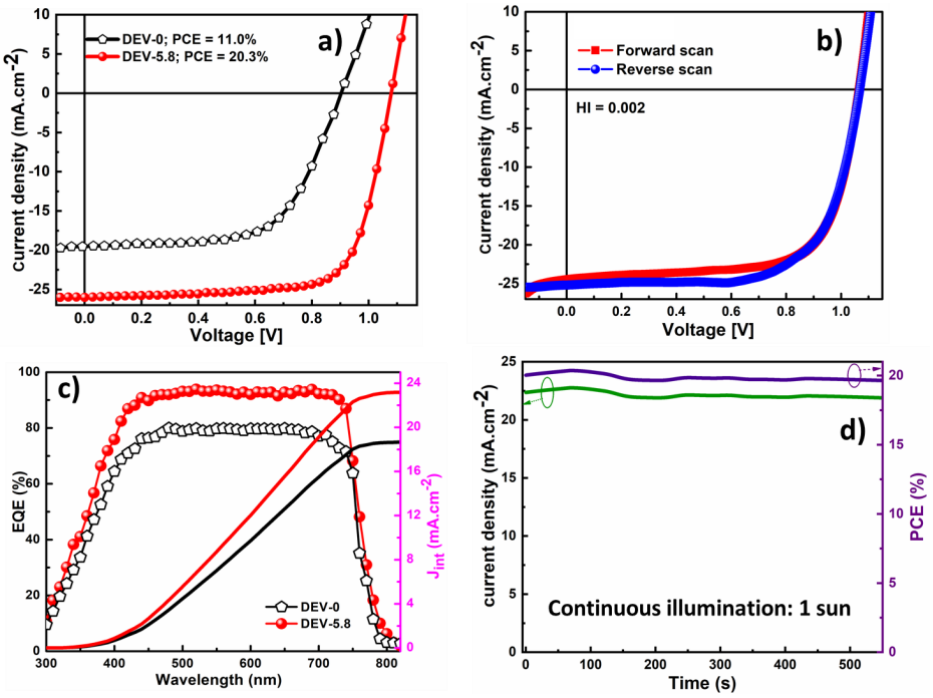

Figure 4. 7: a) Typical *J–V* curves obtained under AM1.5G illumination of solar cell devices, fabricated using a perovskite with and without additive (DEV-*0* and DEV-*5.8* with 90CB). b) *J-V* scan in both forward and reverse directions at a rate of 16 mV s^{-1} for DEV-*5.8* to evaluate the hysteresis. c) EQE spectra of the DEV-*0* and DEV-*5.8* solar cells. d) Steady-state current density and PCE outputs under maximum voltage (0.9 V) of the optimized device.

Table 4.3: Device parameters of DEV-*0* and DEV-*5.8* solar cells with the average values and standard deviation.

J-V Parameters	**DEV-*0*[a]**	**DEV-*5.8*[b]**
V_{oc} (V)	0.911(0.90 ± 0.01)	1.083 (1.06± 0.03)
J_{sc} (mA.cm^{-2})	19.5 (19.09 ±0.56)	25.8 (25.04 ±0.43)
FF (%)	61.9 (58.24 ± 4.85)	72.8 (71.46± 1.23)
PCE (%)	11.0 (9.73±0.65)	20.3 (19.05±0.95)

[a] 14 devices, and [b] 22 devices.

The solar cell exhibits almost no hysteresis effect in the *J-V*, as depicted in **Figure 4.7b**. The HI of 0.0022 is obtained for our optimized DEV-*5.8* device, indicating a negligible hysteresis effect in the *J-V* performance. The suppressed hysteresis is attributed to the incorporation of the SCN^- and the solvent treatment, resulting in the remarkable enhancements in the crystallinity and morphology of the DEV-*5.8* thin-film. Indeed, numerous grain boundaries could cause low device performances due to a large number of trap-assisted recombination centers for charge carrier trapping and reduced carrier mobilities[212]. Hence we suggest that the low efficiencies obtained for DEV-*0* and the other CB-EtOH devices with less than 30 v/v%CB (see **Table 4.1**) could be attributed to the numerous grain boundaries present in the film morphology[197,209]. However, *DEV-x* and > 30 v/v%CB samples exhibit large grains with fewer grain boundaries, resulting in superior PV performances.

Besides, the presence of the mesoporous TiO_2 layer reduces the possible direct contact between the perovskite layer and the FTO electrode, which could occur if there are voids in the compact TiO_2 layer. Therefore, the mesoporous TiO_2 layer is a barrier to leakage current, charge recombination, and limit shunt pathways from the perovskite to the FTO[213]. Compared to the best PCE of 13% obtained in chapter 3, it can be concluded that the device architecture also plays a role in the performance of PSCs. Given the high efficiency obtained for these solar cells with the mesoporous device structure, it is clear that obtaining uniform and compact thin films only do not warrant the very best performance if other parameters are not carefully optimized.

Further investigations on the solar cells are carried out by measuring the external quantum efficiency (EQE). **Figure 4.7c** confirms an excellent light-harvesting behavior of the solar cells reaching more than 90% for the DEV-*5.8* device between 450–730 nm. From the EQE spectra, we confirmed the values of J_{sc} obtained under illumination with an AM1.5G solar simulator by calculating the integrated current densities (J_{int}). The $J_{int,}$ as shown in **Figure 4.7c**, are 18.54 $mA.cm^{-2}$ and 23.18 $mA.cm^{-2}$ for DEV-*0* and DEV-*5.8*, respectively. In general, the EQE and J_{int} increase upon the incorporation of the additives and are in good agreement with the PV parameters. The J_{int} values are slightly lower than measured J_{sc}; though, these differences are within the acceptable measurement error margin[214,215]. The EQE spectra response demonstrates efficient charge carrier extraction and a low carrier recombination rate of our different devices due to a reduced density of grain boundary regions that act as carrier-trapping sites[190]. Thus, reducing the

density of grain boundaries and passivating them boosts charge carrier extraction with minimum losses at recombination sites within the perovskite films[216]. Moreover, grain boundaries are also known to be detrimental to the stability of perovskite-based solar cells, as they constitute an accessible channel for moisture (water molecules) in penetrating the perovskite film[123,217].

We also examined the stability of the PCE and J_{sc} outputs under continuous illumination. **Figure 4.7d** reveals a stable performance with no change in the parameters under constant exposure to 1 Sun. In addition, to check the reproducibility of our findings, we fabricated at least 14 devices for DEV-*0* and DEV-*5.8* under similar conditions and measured their PV parameters as presented in the statistical distribution in **Figure 4.8**. We find that the performance of the various solar cells is remarkably consistent.

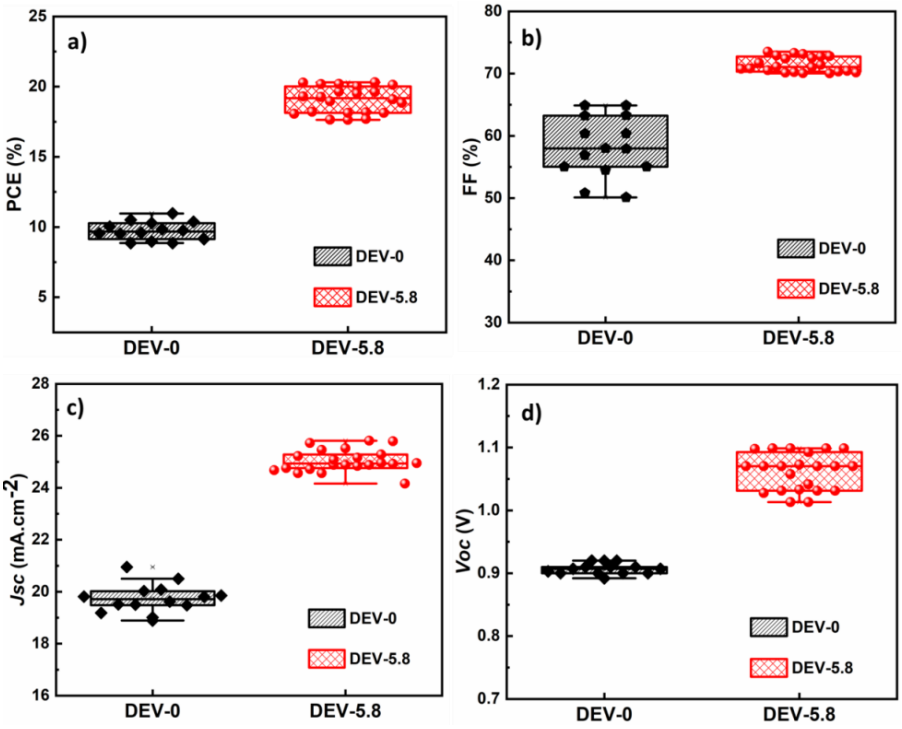

Figure 4. 8: The statistical distribution of a) PCE, b) V_{oc}, c) J_{sc}, and d) FF of the PV cells compared for more than twelve devices, each fabricated under ambient conditions.

4.4 Stability of the Photovoltaic Performance

One major problem with halide perovskite is its stability under different environments. We have investigated the stability of several batches of devices prepared under identical ambient conditions without any encapsulation. The devices are always kept in the ambient laboratory environment.

The photovoltaic parameters under AM 1.5G have been measured at different times over ten months, and the results are presented in **Figure 4.9**.

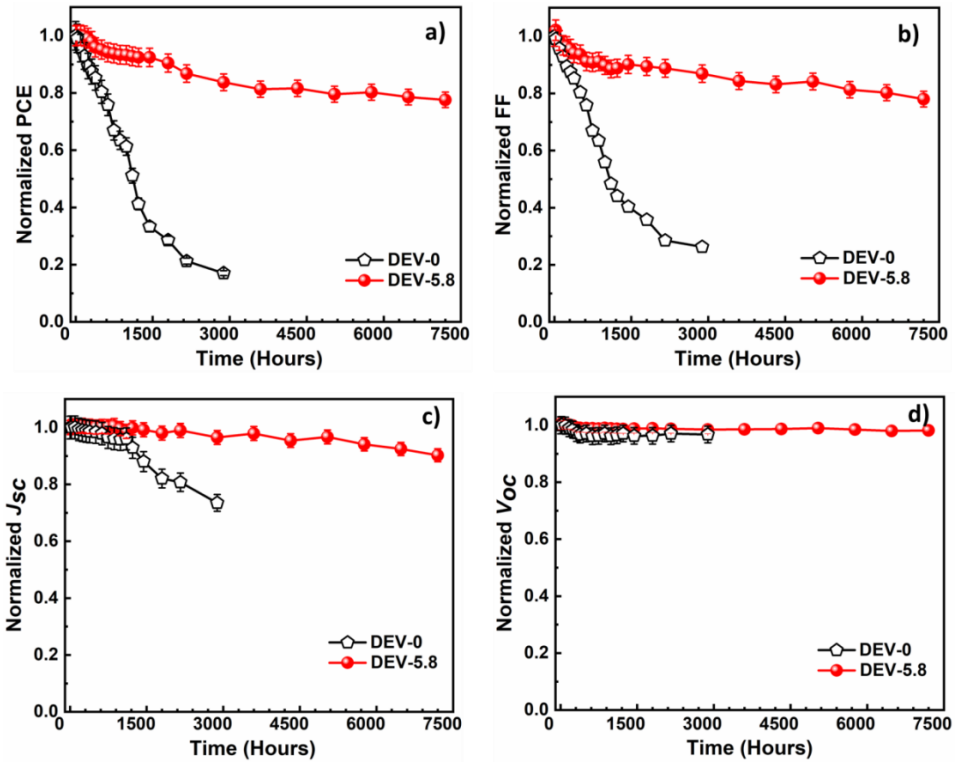

Figure 4. 9: Evolution of *J-V* parameters a) PCE b) FF c) *Jsc* and d) *Voc* for the different devices measured at different periods over ten months. Devices are always measured and stored in ambient laboratory conditions (T = 22 - 25ºC, RH = 25 - 55%RH).

As presented in **Figure 4.9a**, the DEV-*0* solar cells degrade the fastest, with more than 50% of the PCE loss after just 1200 hours. The device is almost completely degraded after 125 days of storage. This stability is somewhat reasonable and can be linked to the compact morphology resulting from the solvent treatment. In contrast, the DEV-*5.8* device shows remarkable resilience, with only about 21% loss in total PCE after ~312 days (10 months) of storage in ambient. The most significant finding is that the DEV-*5.8* solar cells are noticeably more stable than the DEV-0 based solar cells, as already anticipated from the grain boundaries and microstructure assessments. Consequently, the addition of SCN^- improves both the efficiency and stability of the perovskites by strong S-C-N intermolecular bonds in the perovskite lattice structure.[142,200] This resulted in an obtained long lifetime for the DEV-*5.8* solar cells as determined by the lifetime T_{80} parameter (the time at which the device losses 20% of its initial PCE).[64] Our solar cells exhibit a T_{80} of 523

hours for DEV-0 and 5036 hours (7 months) for DEV-5.8, respectively. Outstandingly, our recorded lifetime of >5000 hours is among the best-reported T_{80} so far for ambient-stable perovskite solar cells[64,218]. The degradation profiles of the other *J-V* parameters are displayed in **Figure 4.9(b-d)**. In general, the solar cells show relatively constant V_{oc} with minimal variation in the devices. However, the J_{sc} and especially FF show substantial degradation, which could be due to degradation of the perovskite thin film over the measurement of almost 7500 hours.

To further elucidate the device performance in terms of efficiency and stability, trap-state densities and charge transport[118,219,220] mechanisms have been evaluated in both fresh and degraded single-carrier devices assuming a space-charge-limited-current (SCLC) regime[118,221]. Hole-only devices suppress the injection of electrons at the electrodes, while electron-only devices limit the injection of holes. **Figure 4.10(a,b)** compares the logarithmic-scale *J–V* characteristics of the single-carrier devices, from which the trap density can be derived using equation[222] :

$$N_t = \frac{2\varepsilon\varepsilon_o V_{TFL}}{qL^2} \tag{4.2}$$

The voltage at which the trap states are filled with charge carriers is known as the trap-filled limit voltage (V_{TFL}). N_t is the trap density, q is the electronic charge (1.602 x 10^{-19} C), L is the thickness, ε is the dielectric constant of the material, and ε_o is the vacuum permittivity.

Figure 4.10(a,b) displays the logarithmic-scale *J-V* curves measured for the fresh and partially-degraded (after 240 hours or 10 days) single-carrier devices with the corresponding V_{TFL}. From the $V_{TFL,}$ the trap densities obtained using equation (4.2)[222] are displayed in **Table 4.4**. In the fresh state, we observe lower trap-state density (down to 10^{15} cm^{-3}) in our perovskite thin films, which slightly increase after exposure to humidity (35%±5 RH). This increment in N_t could help explain the observed degradation over time[219]. We also determined the SCLC mobilities[224,225] and the ratio of mobilities as previously described[226]. The observed degradation behavior may be explained by a change in charge transport (before and after exposure). To determine the mobilities, the *J-V* curves of the fresh and exposed devices in **Figure 4.10(c,d)** are fitted to the Mott-Gurney equation:[223]

$$J_{SCLC} = \frac{9}{8}\,\epsilon_o\epsilon_r\mu\frac{V^2}{L^3} \tag{4.3}$$

where J is SCLC density, ϵ_o and ϵ_r are the electric permittivities of free space and the relative dielectric constant of the active layer respectively, μ is the charge carrier mobility, V is the applied voltage, and L is the thickness of the device.

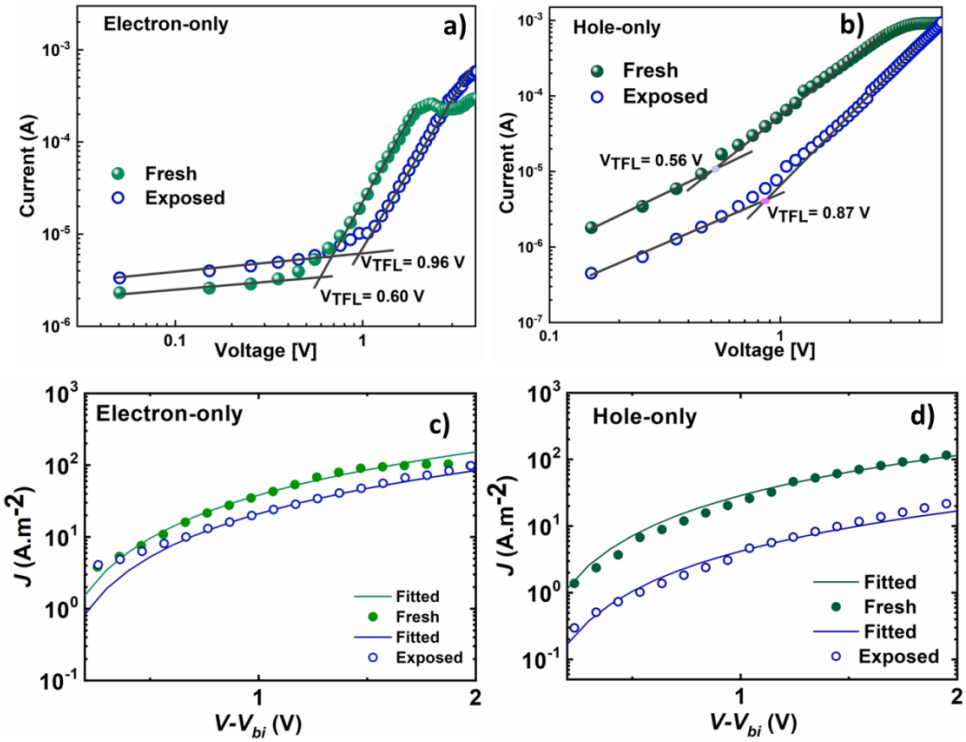

Figure 4. 10: DEV-5.8 devices. (a,b) Logarithmic-scale scale *J-V* curves in the dark indicating the trap-filling voltages (V_{TFL}) and showing fitted curves (c,d) with the Mott-Gurney equation[223] (SCLC regime) for mobilities for fresh and exposed (240 hours under ambient conditions): electron-only devices a,c) FTO/CL-MP-TiO_2/perovskite/$PC_{71}BM$/Au and hole-only devices b,d) FTO/Au/ perovskite/Spiro-OMeTAD/Au.

Table 4.4: Trap-state densities and mobilities of single-carrier devices. E-O: electron-only and H-O: hole-only inferred from the V_{TFL} measured on Fig 4.10 according to equation (4.2).

Devices	**Trap density Fresh (x 10^{16} cm^{-3})**	**Trap density Exposed (x 10^{16} cm^{-3})**	**Mobility (μ) Fresh (x 10^{-6} $cm^2V^{-1}s^{-1}$)**	**Mobility (μ) Exposed (x 10^{-6} $cm^2V^{-1}s^{-1}$)**
E-O	0.70	1.13	200	110
H-O	0.66	1.02	150	22
μ_{max}/μ_{min} (μ_e/μ_h)			1.33	5

Previous works indicated that imbalance in charge mobilities is suggested to be associated with the extraction rate, a reason behind the drop in FF.[226,227] When the ratio μ_{max}/μ_{min} (μ_e/μ_h or μ_h/μ_e) of the charge mobilities is close to unity, there is balanced charge transport, and if it is far greater than 1, then there is an imbalance in charge transport. μ_{max} or μ_{min} is used interchangeably depending on the type of charge carrier with higher or lower mobility. **Table 4.4** suggests the degree of mismatch of electron and hole mobilities in the fresh cells (with a ratio of 1.3) increases in the exposed cells (with a ratio of 5). Thus, a ratio of 1.3 in the fresh state implies a good charge balance in the device. However, there is an imbalance in charge transport after exposure resulting in drop of the FF, which points out to be the main contributor to the PCE degradation. It is reported that unbalanced mobilities induce build-up of space charge within the device, reduce charge extraction, and increase charge carrier densities[226]. Moreover, it is known that the FF is linked to the ratio of the extraction and recombination rates. The mobilities of electrons and holes affect both the extraction and recombination rates[228]. Consequently, the improved PV parameters for DEV-5.8 could be due to the low trap density, charge mobility and the charge balance in the device. Also, the constant decrease in the FF (**Figure 4.9b)** and the PCE narrow the cause of the degradation process down to the deterioration in electron and hole currents seen in **Figure 4.10(c,d),** the rise in trap-state densities, and an imbalance in charge carrier mobilities.

We, therefore, established that the SCN^- dopant and solvent-anti solvent treatment plays a critical passivation role, resulting in the formation of pinhole-free and large grains with fused GBs. This helps reduce the degradation of the perovskite material by preventing moisture accumulation and penetration into the device. It also minimizes the degradation related to the trap density and charges mobility in the perovskite devices stored under ambient air. These findings confirm what has been proven earlier that SCN^- doping produces stable perovskite solar cells due to enhanced chemical bonding.

4.5 Conclusions

We presented a novel perovskite ink for an all-ambient fabrication of highly crystalline, efficient, and stable solar cells. Perovskite solar cells were fabricated using mixed-cation-mixed-halide perovskite precursors via solvent-antisolvent treatment method. The collective effects of the additives on photovoltaic performances have been discussed in detail. The best performing device,

DEV-*5.8*, reaches a maximum efficiency of 20.3 % under standard AM 1.5G illumination with excellent reproducibility and stability in ambient. Remarkably, our champion device without encapsulation retained ~79% of its PCE after ten months of storage in ambient air. This outstanding performance of these solar cells is greatly attributed to their superior microstructural properties such as pinhole-free morphology, large grain size, and low-trap density. In addition, the mechanisms of degradation have been related to changes in the trap density and mobility, resulting in charge imbalance in the perovskite devices. Indeed, this work provides a breakthrough towards fabricating low-cost, high-efficiency, and stable perovskite solar cells.

Chapter 5: Photodetectors Based on Pseudohalide Perovskite Nanowire Network

In chapters 3 and 4, we investigated the synthesis of efficient and stable halide perovskites for solar cell applications. We demonstrated that incorporating thiocyanate ions and solvent-antisolvent treatment help to achieve large-grain thin films that are stable in ambient conditions. To show the versatility of perovskites for solution-processable optoelectronic devices, we extend the scope of device applications beyond solar cells by fabricating photodetectors. This chapter presents a route to modify the morphology of the halide perovskite material to form nanowires. The optical and microstructure properties of the nanowires have been investigated. Also, the performance of the photodetectors has been evaluated on rigid and flexible substrates.

Most of the results discussed in this chapter have been published as follows:

*Asuo, I. M. et al. High-performance pseudo-halide perovskite nanowire networks for stable and fast-response photodetector. Nano Energy **51**, 324–332 (2018).*

*Asuo, I. M. et al. Highly Efficient and Ultrasensitive Large-Area Flexible Photodetector Based on Perovskite Nanowires. Small **15**, 1804150 (2019).*

5.0 Introduction

5.1.1 Brief Description of Photodetectors

Photodetectors are devices, often based on semiconductors, used to detect optical signals and convert them to electrical signals through electronic processes. They can be tuned to detect light at a specific wavelength throughout the UV to infra-red spectral regions. Generally, three processes are identified in their mode of operation: carrier generation by the incident light, carrier transport, and extraction of the charge carrier at the terminal as current (or voltage) to provide an output signal. As presented in section 1.3, there are two categories of photodetectors: photoconductors and photodiodes.

In a photoconductive mode, an electric field is applied across a semiconductor layer through electrically biased ohmic contacts on either side, enabling the flow and collection of charge

carriers[65] (**Figure 5.1 a**). The conductivity in the device increases through the electron-hole generation, and the current flow is proportional to the optical power. Practically, the fabrication of a photoconductor is more straightforward than a photodiode because it is only made of the semiconductor material placed between the two electrodes.

Photodiodes are typically based on the reverse biased *p-n* junctions where only a tiny reverse current flows through the diode without illumination. When the *p-n* junction is illuminated, electron-hole pairs are created through the absorption of photons. In reverse bias, the electric field favors the flow of electrons toward the cathode, while holes travel to the anode. Because of the large built-in electric field, electrons and holes generated inside the depletion region or space-charge region are separated and contribute to the photocurrent[65]. This process results in the flow of current, which is proportional to the optical power. Though the basic device configuration can be simply a *p-n* junction, they can also be adapted to different designs such as *p-i-n* or *n-i-p* to enhance the performance. **Figure 5.1b** illustrates a device structure where the intrinsic semiconductor material is sandwiched between an electron transport material (or *n*-type material) and a hole transport material (or *p*-type material). Examples of photodiode applications include smoke detectors and remote controls.

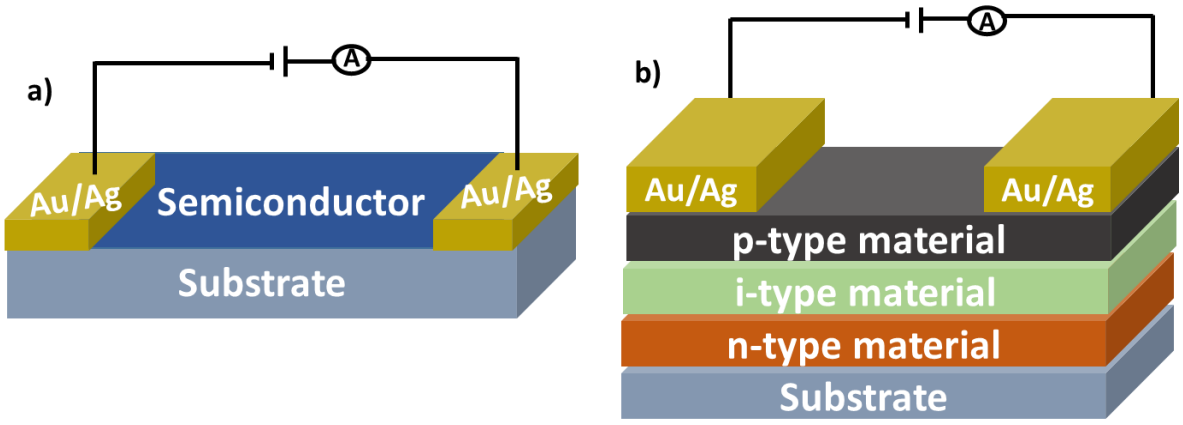

Figure 5. 1: Schematic of the vertical configuration of a) Photoconductor: Semiconductor sandwiched between two electrodes. b) Photodiode: The active layer sandwiched between electron and hole-transporting materials.

This chapter presents works on photoconductors made with perovskite nanowires network. The main parameters that characterize the performance of a photodetector include quantum efficiency, response time, dark current, gain, noise equivalent power, specific detectivity, and responsivity. We evaluate the photodetector performance based on these parameters that have been presented in **section 1.3.2** of the thesis. The photoresponse is characterized by a current-voltage (*I*-*V*) curve, which is the current variation as a function of the voltage. The photocurrent ($I_{ph} = I_{light} - I_{dark}$) generated at a given voltage corresponds to the difference between the dark current (I_{dark}) and the current generated under illumination (I_{light}). Above all, the dark current, possibly originating from thermally generated electron-hole pairs or ambient light, should be significantly low to obtain an excellent photodetector.

5.1.2 State-of-the-Art for Photodetectors

Photodetectors are widespread devices used for applications such as optical communications systems, wearable electronics, environmental monitoring, and internet-of-things (IoT) such as optical sensing devices[70,155,229]. The current market is mainly dominated by photodetectors based on silicon (Si), germanium (Ge), gallium nitride (GaN), and gallium arsenide (GaAs) [230,231]. In particular, Si and GaN are the most used photodetectors, and they are specially used for ultra-violet (UV) detection. Although some of these photodetectors are suited for high sensitivity and fast response time, they require complex fabrication methods, and the final cost of fabrication is high. For instance, Si and GaAs photodetectors require high-quality crystals that have to be prepared under a high vacuum. Also, due to the brittleness of these materials, it is challenging to use them in flexible electronics. Alternative materials have been explored for photodetectors, such as quantum dots, graphene, organic materials, and carbon nanotubes[232–235]. While they show promising performances, the majority still involve complex synthesis, high-cost fabrication and exhibit a low lifetime. For example, quantum dots such as PbS are synthesized using pulse laser deposition[236,237], while the roll-to-roll technique[238] is mostly explored for processing inorganic and organic semiconductors devices. Consequently, the drawbacks include expensive fabrication methods, limited detection range, and degradation over time. In addition, most of these materials are not readily adaptable on different surfaces for other applications such as wearable electronics. Given this, the fabrication of photodetectors with low-cost materials and methods is of interest to advancing the technology.

Halide perovskite materials are potential candidates. They possess excellent optoelectronic properties such as large carrier diffusion length, tunable bandgap, strong optical absorption, and carrier mobility suitable for photodetection[32,239,240]. In particular, halide perovskites have a small exciton binding energy of ~2 meV[241], implying that weakly bound excitons can be easily dissociated even without the aid of charge collector materials[242]. Their versatility, easy solution and low-temperature processing, adaptability to various substrates, and cost-effectiveness culminated in a tremendous advancement in their exploitation for optoelectronic devices. In the last decade, they have been massively explored for efficient solar cells; however, their potential application in photodetectors has only sparked interest in the research community in the past five years.

The use of the perovskite could help fabricate broadband photodetectors with good spectral response from ultra-violet to the near-infrared part of the electromagnetic spectrum. Recent studies seek to integrate solution-processed perovskite-based photodetectors on rigid substrates and low-temperature flexible substrates such as polyethylene terephthalate and polyimide[243–245]. Previous reports of such studies include a broadband device using a PbPc/$MAPbI_{3-x}Cl_x$ thin film,[246] a self-powered device using a $CH_3NH_3PbI_3$, and Spiro-OMeTAD composite film atop carbon cloth,[247] a $CH_3NH_3PbI_3$ thin-film device deposited by vapor solvent method,[71] and an intertwined fibrous perovskite–carbon devices[248]. Despite the enhanced device performances, the growth of the active layer is associated with two significant challenges: i) the non-uniform thin film coverage, which negatively impacts the device performance as it leads to reduced carrier mobility and collection[166], and ii) the degradation of the thin film caused by exposure to moisture, oxygen, and temperature[95]. The morphology control and degradation of the active layer remain to date a challenge. And as such, it is vital to achieve better morphology control and stability of perovskite-based photodetectors irrespective of the fabrication method. Conversely, taking fabrication cost into account, simple processing methods are highly desired.

Here, we utilize a simple method to fabricate pseudo-halide perovskite nanowire photodetectors. The choice of nanowires is based on our preliminary results comparing the thin film to nanowire-based perovskite photodetectors (see appendix **Figure A5.4**). The latter showed an overall better performance than the former. Thus, the discussions in this chapter are based on the nanowire photodetectors. The use of nanowires favors directional charge carrier transport owing to the large

surface-to-volume ratio. So, they help improve the confinement of the charge carriers in the device and limit loss mechanisms in the device, such as recombination. In the study, perovskite nanowires network (HPNW) are used as the active layer and are deposited directly atop a micro-patterned FTO and flexible Kapton substrates using a low-temperature solution-based process. This device fabrication process offers a low-cost route as compared to the conventional microelectronics processes. The performances of the photodetectors on both substrates are assessed using their photocurrents, response times, spectral responsivities, specific detectivities, and stabilities. The process developed and presented offers an opportunity for low-cost fabrication of reproducible ambient-stable nanostructured-halide-perovskite, providing fast response photodetector devices for a wide range of applications.

5.2 Synthesis of the Perovskite Nanowires and Device Fabrication

The precursor solution was prepared from commercially available chemicals purchased from Sigma Aldrich and Ossila unless otherwise stated. To prepare the nanowires network of $CH_3NH_3PbI_{3-x}(SCN)_x$ perovskite, two different solutions were prepared. First is the PbI_2: $Pb(SCN)_2$ solution, which was obtained by dissolving a 370 mg PbI_2 and 90 mg $Pb(SCN)_2$ in 9:1 volume ratio of anhydrous N,N-dimethylformamide (DMF), and Dimethyl sulfoxide (DMSO) solvents. The solution was stirred for about an hour at room temperature until a clear yellow solution was obtained. For the optimization, we varied the concentration of the PbI_2 precursor (i.e., 0.2 M, 0.4 M, 0.6 M, and 0.8 M) while keeping the other parameters constant. The second solution of 0.032 M methylammonium iodide (MAI) was prepared in a separate vial by dissolving 25 mg of MAI in 5 ml of isopropanol (IPA) [45,48,249]. An optimized amount of 50 µl of DMF was added to this solution as a modification, which was the catalyst for the nanostructure formation instead of the thin film. The mixture was stirred for about an hour until complete dissolution was achieved.

For the device fabrication, fluorine-doped tin oxide (FTO, TEC 15) glass substrates were pre-patterned with a channel width of 300 µm in width by laser etching. Subsequently, the FTO substrates were cleaned in deionized water, acetone, and isopropanol in an ultrasonic bath for 10 minutes each. While the Kapton substrates were cleaned in deionized water and isopropanol for 10 min and then dried with compressed air. Finally, the substrates were treated with UV- Ozone for about 10-15 minutes before the deposition of the precursor solutions. Then, the devices were fabricated on the cleaned pre-patterned FTO and Kapton substrates by a two-step spin coating

method to form the high-crystalline perovskite nanowires. In the first spin coating step, 50 µl of the PbI_2:$Pb(SCN)_2$ solution was dispersed onto the cleaned substrates and spin-coated at 3000 rpm for 15 s. Then, in the second step, a 250 µl of MAI:IPA: DMF solution was dispersed atop the PbI_2:$Pb(SCN)_2$ layer and laid to rest for 60 s. The system was then spun at 4000 rpm for 30 s, followed by drying on a hotplate at 110^{o}C for 5 minutes and also permitted to evaporate any excess solvent. This process results in a dark brown layer of perovskite on the substrates.

After cooling down to room temperature, we encapsulated some of the devices to avoid degradation: This was done by spin-coating a 30 mg/ml solution of PMMA in chlorobenzene at 3000 rpm for 25 s on top of the perovskite layer. Finally, for the flexible substrate devices, 80 nm gold top electrodes were thermally evaporated at a reduced pressure of $5x10^{-5}$ Torr through a shadow mask, resulting in a gold deposition rate of 0.2 nm/s.

5.3 Crystal Structure and Optical Characterization of the Perovskite Nanowire Networks

We investigated the crystalline structure and morphology of the as-deposited $CH_3NH_3PbI_{3-x}(SCN)_x$ perovskite nanowires (HPNWs) by using a scanning electron microscope (SEM), transmission electron microscopy (TEM), and X-ray diffraction (XRD) techniques. The surface morphologies of the nanowire networks deposited on the substrates using different molarities of the precursor solution are depicted in **Figure 5.2(a-d)**. It can be observed that the concentration of PbI_2 has significantly affected the surface coverage and density of the nanowire networks. The production of interconnected nanowires bridged the device's channel when precursor solutions with concentrations of 0.8 M, 0.6 M, and 0.4 M of PbI_2 **(Figure 5.2(a-c))** are used**,** whereas the precursor solutions containing 0.2 M of PbI_2 produced an incomplete coverage of the channel, as shown in **Figure 5.2d**. The high magnification SEM images exhibit nanowires of diameter ranging from 35-175 nm. Similarly, the thicknesses of the nanowire networks are determined from 3D imaging using an Olympus LEXT OLS4100 laser scanning digital microscope. The estimated thicknesses are 91 ± 5 nm, 207 ± 10 nm, 385 ±12 nm, and 487 ± 15 nm for the 0.2 M, 0.4 M, 0.6 M, and 0.8 M, respectively (**see Figure A5.1(a-d)**).

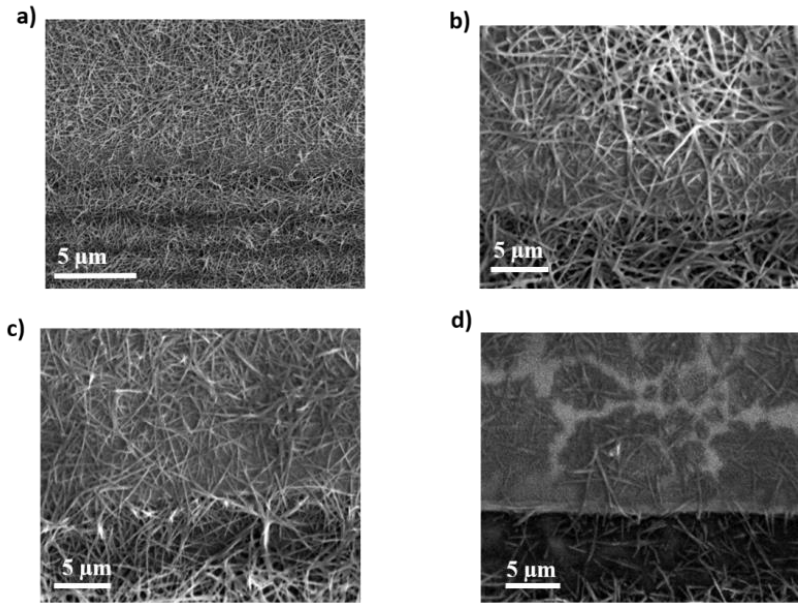

Figure 5. 2: SEM micrographs showing the top-view of the $CH_3NH_3PbI_{3-x}(SCN)_x$ perovskite nanowire networks on FTO substrate with the different molar concentration of PbI_2 in the precursor solutions, namely (a) 0.8 M (b) 0.6 M (c) 0.4 M (d) 0.2 M. (a–d) The nanowires network over the edge of the channel are seen in the lower part of the images, while the nanowires network over the FTO electrodes is seen in the upper part of the images.

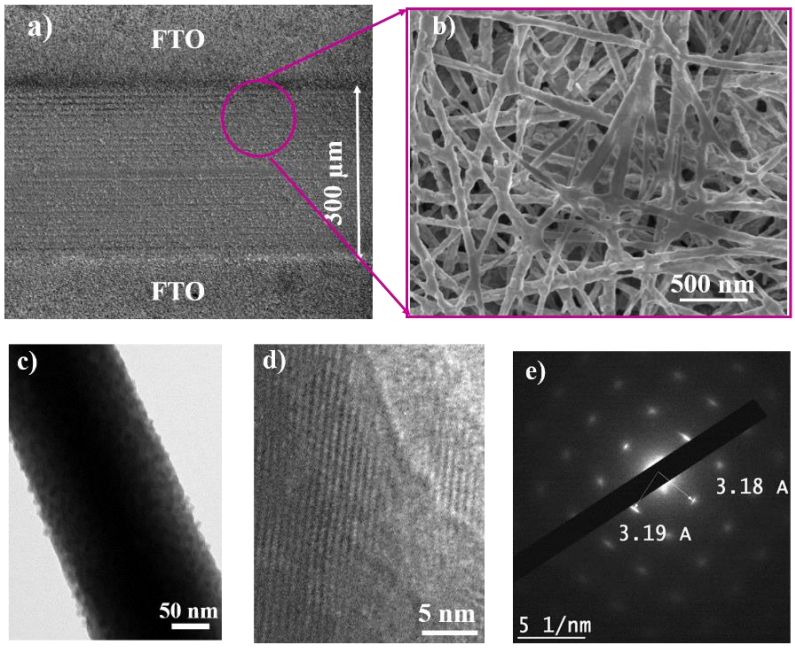

Figure 5. 3: (a) SEM micrographs of the deposited0.8 M perovskite precursor solution on FTO substrate with a gap of 300 µm. (b) High-resolution micrographs of the interconnected nanowires within in the channel. It indicates a granular nature of the nanowires. (c) TEM micrograph of a single nanowire showing randomly oriented small crystal grains. (d) HRTEM image of the nanowire. (e) SAED pattern and lattice spacing of a (220)-oriented grain of the HPNW tetragonal phase[250].

A closer look at the SEM image shows that the nanowire networks cover the gap and the active area completely (**Figure 5.3 (a)**), with the image revealing the detailed interconnected crystal grains in the microstructure of the perovskite nanowires, as displayed in **Figure 5.3(b)**. Likewise, the TEM image in **Figure 5.3(c)** reveals a ~150 nm-wide HPNW comprising numerous crystallites. The TEM results indicate that HPNWs are formed from single crystalline grains that are assembled with the presence of grain boundaries. Further investigation of the nanowire using high-resolution TEM (HRTEM) and selected area electron diffraction (SAED) are presented in **Figure 5.3(d, e)**. The presence of distortion in the lattice suggests irregularities in the stacking sequence of the atomic planes and the existence of planar defects in the NWs **(Figure 5.3(d))**. The SAED spots are elongated or have diffuse reflections, which can be ascribed to the finite crystal size of the perovskite nanowire[251]. As such, the SAED pattern in **Figure 5.4(e)** exhibits reflections corresponding to a tetragonal structure oriented along the [220] zone axis, suggesting a preferential growth of HPNWs along the in-plane [001] direction[48].

Although the underlying mechanism leading to the formation of the nanowires is not yet completely understood, it proves to be reproducible in our synthesis approach. Though we think it is more of a chemical effect, some plausible factors facilitated the formation of the nanowires. The main difference between the method presented here and the previous chapters is the addition of DMF as a solvent additive to the MAI precursor solution in isopropanol during the two-step solution processing stage. The volume ratio of DMF in IPA is the pivotal point to achieving nanowires. We added different volume ratios of DMF to 1 ml of the MAI: IPA solution, and we noticed that the best nanowires network was formed when about 50 µl of DMF was added. An alternative organic solvent like DMSO was also used for the same purpose. However, it did not yield well-defined nanostructures as compared to DMF. Hence, we believe that this could be because the boiling point of DMSO (189^{o}C) is higher than that of DMF (153^{o}C), resulting in slower evaporation of the solvent during the process. Another important parameter for obtaining the nanowires is the resting time of 60 seconds after the MAI:IPA:DMF solution is dropped atop the PbI_2 layers. During the resting stage, the pre-deposited PbI_2 layer re-dissolves in IPA: DMF and mediates the direction of the anisotropic growth of the perovskite. Lastly, the spinning speed also plays a vital role in the formation, and depending on the speed, the density and diameter of the nanowires can be controlled. After the resting stage, where the re-dissolution occurs, the samples are spin-coated at 4000 rpm, where rapid evaporation of solvents occurs. During this stage, the

perovskite's color changes from orange to white and then to light brown due to partial evaporation of the solvents. After annealing the samples, a final dark-brown color of the crystallized film is obtained. This proposed mechanism is supported by preferential growth along the in-plane [001] direction from the SAED and evidenced in the x-ray diffraction (XRD) patterns presented below.

The XRD patterns confirmed the crystalline phase of the $CH_3NH_3PbI_{3-x}(SCN)_x$ perovskite nanowires network. The typical XRD pattern is shown in **Figure 5.4(a)** reveals the main diffraction peaks at 14.12°, 28.46°, and 31.90°, which are indexed to (110), (220), and (310) planes of halide perovskite, respectively. All these planes are perpendicular to the [001] direction (consistent with the finding above), which is associated with PbI_2, suggesting that the growth direction of the nanowire axis is [001]. The (110), (220), and (310) planes again confirm that $CH_3NH_3PbI_{3-x}(SCN)_x$ HPNWs crystallize in the tetragonal perovskite phase[249], with lattice parameters a = b = 8.86 Å and c = 12.66 Å[34]. The lattice spacing of 3.19 Å measured in the SAED image (**Figure 5.3(e)**) corresponds to that of a diffraction plane (220) in agreement with the XRD pattern[199,252]. Thus, from our simple synthesis approach, high-quality crystals of halide perovskite can be produced in the form of nanowires network.

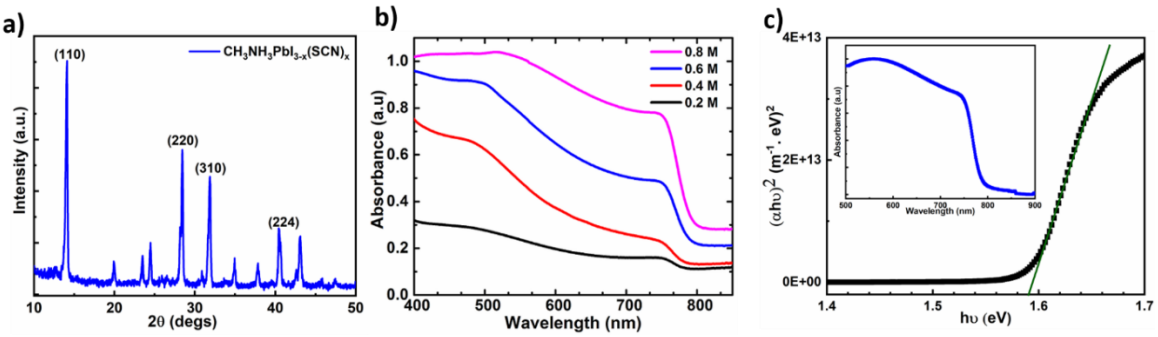

Figure 5. 4: (a) XRD spectrum of the $CH_3NH_3PbI_{3-x}(SCN)_x$ perovskite nanowire networks. b) UV-Vis absorption for 0.8 M, 0.6 M, 0.4 M, and 0.2 M perovskites, and (c) the corresponding bandgap determination from Tauc of the perovskite nanowires, assuming a direct-bandgap

The optical characterization of the $CH_3NH_3PbI_{3-x}(SCN)_x$ perovskite nanowires reveals a broadband absorption ranging from UV (300 nm) to the NIR (800 nm). **Figure 5.4 (b)** displays the UV-Vis-NIR absorbance spectra for the HPNWs with increasing absorbance as the molarity of PbI_2 is increased. The nanowires show a band edge located at 785 nm. The band edge value corresponds to a bandgap of ~1.59 eV, extrapolating from the Tauc plot (equation 2.8) of the

absorbance. The bandgap is found assuming the halide perovskites have a direct-band gap[154] (**Figure 5.4 (c))**. From the well-crystallized nanowires, fully bridging the channel, and the broadband optical properties of our HPNWs, we anticipate that photodetectors using $CH_3NH_3PbI_{3-x}(SCN)_x$ nanowires will exhibit good electronic properties.

5.4 Photodetector Performance on FTO (rigid) Substrate

The schematics of the device configuration and the band diagram of the photodetectors fabricated on the FTO substrate are shown in **Figure 5.5(a, b)**. The nanowires are deposited between the two electrodes in a channel of width 300 µm **(Figure 5.5a)**. In photoconductors, only one type of charge carrier flows by the induced built-in electric field while the other charge carrier gets trapped inside the active region of the device before their recombination[229,253]. Trap limits the movement of charge carriers, and they play an essential role in photoconduction since the generation of current depends on the flow of charge carriers through the semiconductor. Traps prolong the lifetime of the immobile charge carrier and delay its recombination, thereby increasing photoconductive gain[233,254,255]. From our band diagram **(Figure 5.5b)**, the electrons are mobile, and holes are mostly trapped[229]. These holes can remain trapped for a long time. However, in the presence of illumination, they can be released from the trap. In principle, upon illumination, the photocurrent generation mainly originates from the absorption of photons by the nanowires network where electron-hole pairs are generated, leading to an increase in conductivity. Thus, the photocurrent density is strongly dependant on the ability to collect charge carriers before their recombination.

As displayed in **Figure 5.5(b)**, the device is expected to operate in a photoconductive mode, where photocurrent is generated from an applied electric field across the perovskite layer through biased ohmic contacts on either side. The electric field favors the movement of the electrons toward the FTO side, while holes are trapped until they recombine. Such configuration exploits a favorable band alignment between the FTO and the perovskite nanowires. The conduction band maximum of the perovskite (3.8 eV) is close to the work function of the FTO (4.4 eV), resulting in a 0.6 eV barrier for the electrons and a 1.0 eV barrier for the holes. The 1.0 eV barrier is relatively high for the holes to quickly overcome, resulting in accumulation and subsequent trapping. On the other hand, the electrons can easily flow from perovskite to the electrodes for their extraction. Therefore,

it behaves like a single-carrier type of device. However, as the holes get de-trapped and the lifetime of the electrons shorten, they may recombine, which is unfavorable for photoconduction.

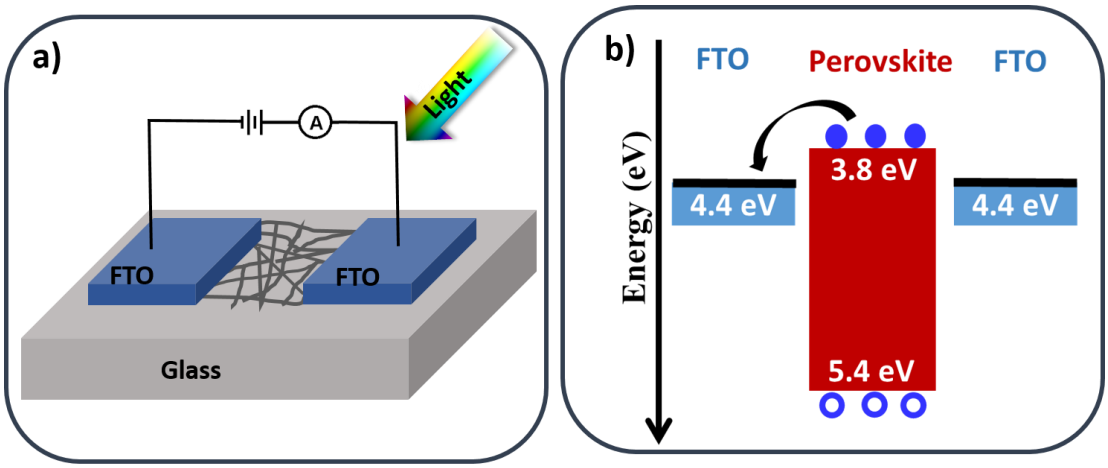

Figure 5. 5: (a) Illustration of the final photodetector device architecture on FTO substrate. (b) Band diagram illustrating the behavior of the photodetector showing the pathway of electrons and holes. In photoconductor mode, the electrons are mobile, and holes are trapped. In this case, the mobile electrons may recombine with the trapped holes which may increase the leakage current in the device.

We evaluate the optoelectronic performance of the perovskite photodetectors on FTO substrates using the current-voltage (*I-V*) characteristics, recorded by a Keithley-2400 source-measure unit (SMU) under AM 1.5G solar simulator. The critical parameters discussed here include photocurrent, spectral responsivity, specific detectivity, transient response times, and stability. **Figure 5.6(a,b)** present the *I-V* curves of the photodetectors fabricated using 0.2 M, 0.4 M, 0.6 M and 0.8 M-based HPNWs on linear scale **Figure 5.6 (a)** and on semi-logarithmic scale **Figure 5.6(b)**. From the *I-V* curves, the photocurrent ($I_{ph} = I_{light} - I_{dark}$) increases linearly with the applied voltage in both forward and reverse directions. The symmetric characteristic reveals a good ohmic contact, resulting in a small potential barrier at the HPNW/FTO interface. It is observed that increasing the concentration of the PbI_2 precursor solutions increases the general electrical conductivity of the photodetectors. For instance, the photocurrent increased 15-fold when the PbI_2 molarity is changed from 0.2 to 0.8 M. Indeed, the nanostructures offer a directional pathway for the flow of charge carriers throughout the device, and the interconnected nanowires possibly form nano-junctions within which aid the transport of the charge carriers resulting in the high generation of photocurrent.

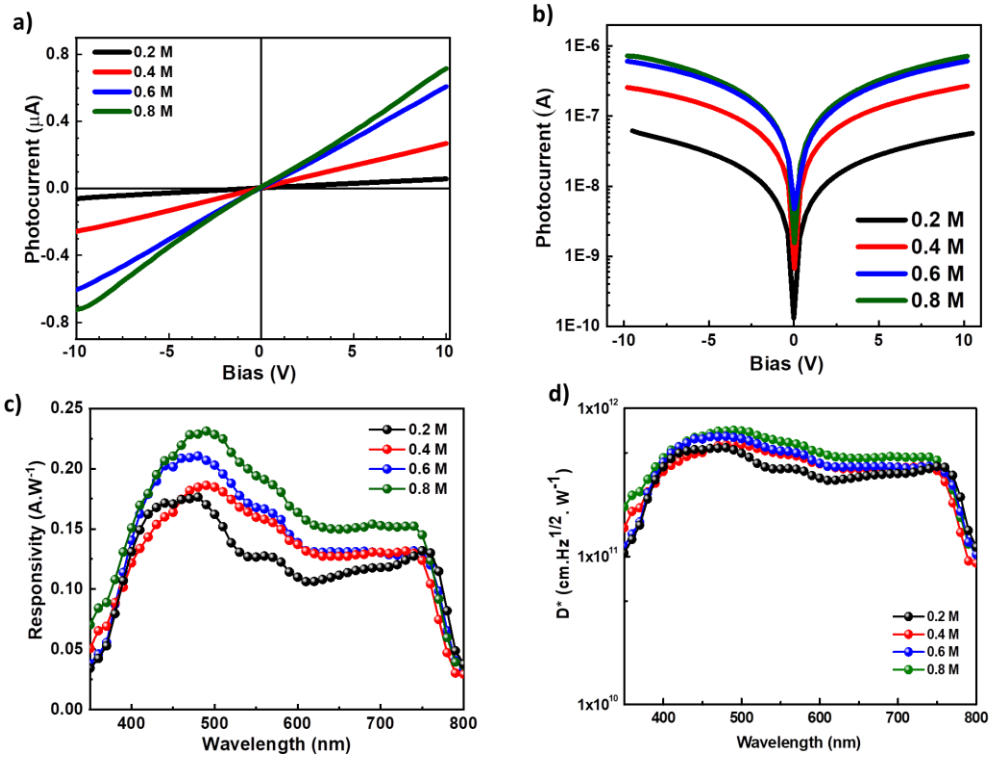

Figure 5. 6: Photo-response characteristic curves of HPNW-based photodetectors fabricated with PbI_2 molar concentration of 0.2 M, 0.4 M, 0.6 M, and 0.8 M on FTO substrates. (a) *I-V* characteristic curves of the devices on a linear scale. (b) The semi-logarithmic plot of the absolute values of *I* versus *V* plots for a better view of value distributions. (c) The spectral responsivity of the photodetectors measured at 2 V applied bias for various PbI_2 concentrations. (d) A plot of the Specific detectivity of the optimized photodetectors.

The responsivity is defined as the ratio of the electrical current output and the optical power input of the photodetector. The spectral responsivity measurements were done according to the procedure described in **section 2.7.3.** In the setup, light from the Xenon lamp first passes through the monochromator to perform a 10 nm-step scan from 300 nm to 850 nm. The excitation light is modulated at 50 Hz before the sample is illuminated. A 2 V bias is applied to the sample and placed right after a circular diaphragm of aperture 0.2 cm in diameter. The photocurrent is measured by means of a lock-in amplifier. To determine the responsivity, the photocurrent is divided by the power of the incident light at each wavelength, which is measured with a calibrated photodiode (Newport 918D). **Figure 5.6(c)** shows the measured spectral responsivity of the optimized photodetectors. We obtained a peak responsivity of 0.23 $A.W^{-1}$ at 490 nm for the fully covered nanowires with 0.8 M, while the less densed-nanowire with 0.2 M show a responsivity of about 0.17 $A.W^{-1}$.

The specific detectivity D* given by $\frac{\sqrt{A}R}{\sqrt{2qI_d}}$ in equation (1.8) is the ability of the photodetectors to detect weak light signals. **Figure 5.6 (d)** displays the specific detectivity of the optimized fully nanowire covered devices showing the moderate density 0.4 M and highest density 0.8 M photodetectors measured at 2 V applied bias. The photodetectors exhibit a broadband photodetection from UV-Vis to the NIR regime. At 490 nm, the 0.8 M photodetector showed a peak detectivity of $7.2x10^{11}$ cm.$Hz^{1/2}$.W^{-1} (i.e., $7.2x10^{11}$ Jones) and $4.7x10^{11}$ Jones at 700 nm. In contrast, the 0.2 M device recorded a peak detectivity of 5.3 x 10^{11} Jones at 490 nm and 3.7 $x10^{11}$ Jones at 700 nm.

In general, the improved performance of the photodetectors can be ascribed to the PbI_2 passivation at the grain boundaries[256]. Also, the solution with the highest concentration (0.8 M) showed enhanced performance due to the denser interconnected nanowires (see **Figure 5.3b**), which promotes more photo-carriers generation upon illumination. We observed that the peak positions in all the responsivity spectra do not change, indicating that the variation of the PbI_2 molarity does not negatively affect the optical properties of the perovskites. This agrees with the UV-Vis measurements, which show a broad absorption profile with a band edge located at ~785 nm for all the HPNW samples. Despite the overall simplicity of the device fabrication, material costs, and reproducibility, the optimized HPNWs photodetector device using the 0.8 M precursor solution achieves excellent performances with responsivities comparable to previous reports using more complex fabrication processes[257–260] (**Table 5.1**).

The final important critical parameter, response time, for the FTO-based photodetectors is determined using a 532 nm laser modulated at 830 Hz. **Figures 5.7(a-h)** show the time response characteristics of the 0.4 M and 0.8 M devices with and without PMMA encapsulation top layer, under a 10 V applied bias. We determined the rise and the decay time constants using two bi-exponential fitting equations[70]. Based on the curve fittings, the time constant for the 0.4 M device without encapsulation are $\tau_{d1} = \tau_{d2} = \tau_d$ = 102.2 µs for the decay time constant and τ_{r1} = 75 µs and τ_{r2} = 91.7 µs for the rising time constants. The same fitting performed on the 0.4 M devices encapsulated with PMMA showed shorter decay time constants of $\tau_{d1} = \tau_{d2}$ = 50.2 µs and rise time constants of τ_{r1} = 53.2 µs and τ_{r2} = 65 µs. Likewise, the time constants estimated for 0.8 M devices without encapsulation are $\tau_{d1} = \tau_{d2}$ = 57 µs and $\tau_{r1} = \tau_{r2} = \tau_r$ = 74 µs and with PMMA are $\tau_{d1} = \tau_{d2}$ = 62 µs and $\tau_{r1} = \tau_{r2}$ = 56 µs respectively. Comparably, the PMMA-based devices exhibited superior

photocurrent stability and transient response compared to pristine devices. These response times are among the fastest, based on the current literature (see Table 5.1).

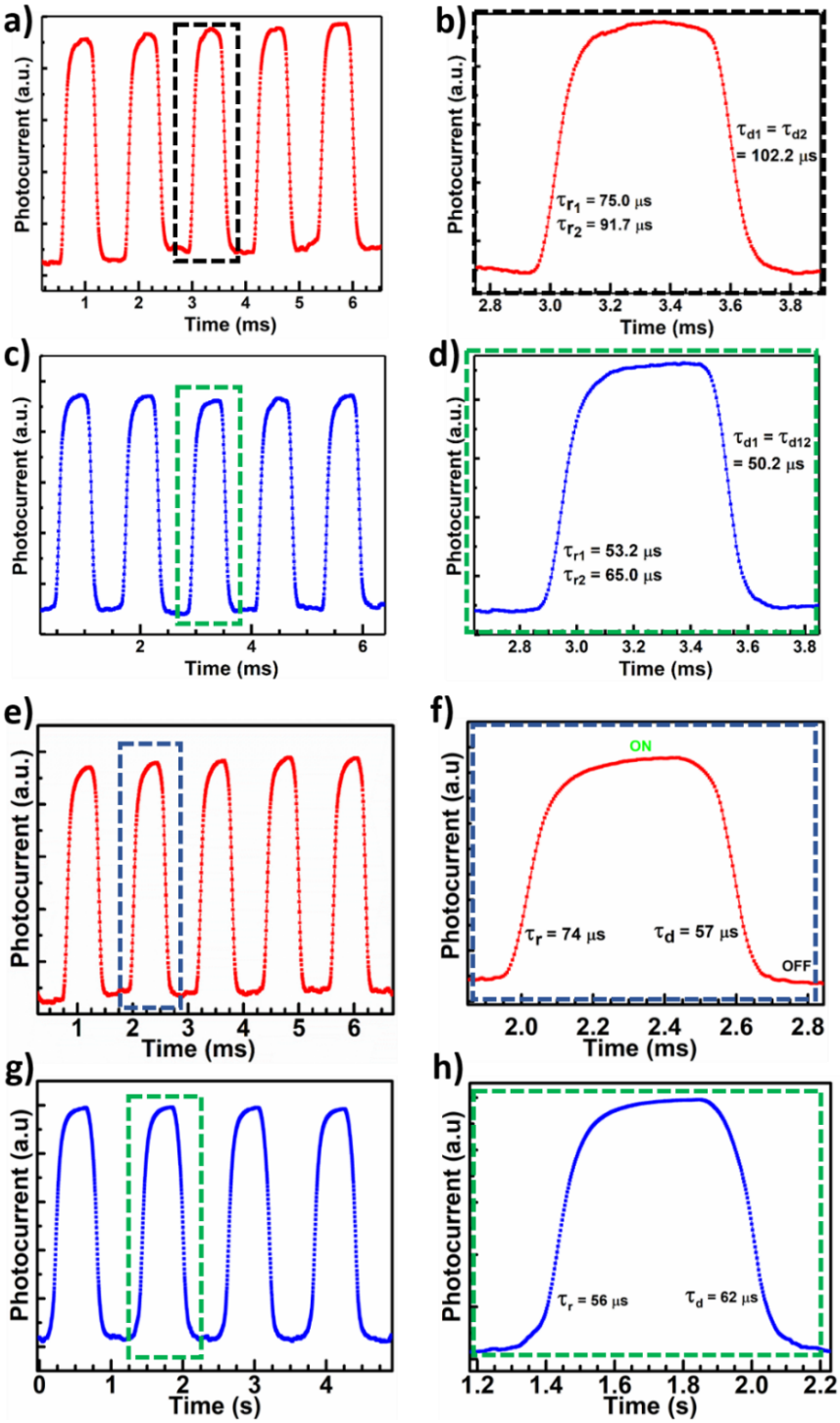

Figure 5. 7: Typical time-dependent response(*I-t*) behavior of reversible On/Off switching together with a zoom of a single pulse under 10 V applied bias for (a, b) 0.4 M device without PMMA encapsulation, (c,d) 0.4 M device encapsulated with PMMA, (e, f) 0.8M device without PMMA encapsulation, and (g,h) 0.8 M device encapsulated with PMMA.

This suggests that PMMA encapsulation helps to reduce losses originating from carrier recombination at the grain boundaries and surface states[123,261,262]. In halide perovskite devices, several studies revealed that grain boundaries are major recombination centers[123,262] which can result in longer response times. In this work, the utilization of PbI_2 and PMMA to minimize those negative impacts[123,256]. And the nanostructure of the perovskite facilitates the charge transport to the electrodes due to the large surface-to-volume ratio of the nanowires network, synergically resulting in a short response time.

To further elucidate the charge transport dynamics, time-resolved photoluminescence measurement was performed on the perovskite nanowires. The decay times are estimated by fitting the experimental data to the bi-exponential decay function. The 0.4 M based HPNWs exhibited a fast time constant (τ_f) of 0.72 ns and a slow time constant (τ_s) of 3.84 ns while a τ_f of 3.06 ns and τ_s of 24.1 ns are obtained for 0.8 M based HPNWs as shown in **Figure 5.8 (a)**. The fast and slow lifetime constants relate to surface and bulk defects in the perovskite material, respectively[263]. This implies that the photo-generated charge carriers have a prolonged lifetime before recombination and lead to the extraction of a higher number of charge carriers before they are annihilated. As a result, the 0.8 M-based HPNWs network exhibited a slower decay rate and higher steady-state photoluminescence because of the higher availability of active material[48]. This might also be explained by the presence of a lower defect density in the 0.8 M, resulting in a lower charge carrier recombination rate and a longer charge carrier diffusion length compared to the 0.4 M counterpart [199,264].

The trap or defect density is calculated using the space charge limited current method[50,265]. **Figure 5.8(b)** shows a regime transitioning from ohmic conduction to space-charge-limited conduction due to trap-filling at a point known as the trap filling voltage (V_{TFL}). Such transition behavior is consistent with defect-mediated charge carrier trapping. The trap density can be calculated from equation (4.2). From the logarithmic *I-V* curve in **Figure 5.8(b)**, we obtained a V_{TFL} of ~0.65 V, and the corresponding trap density N_t is then estimated to be 1.1 x 10^{16} cm^{-3}. The obtained N_t for the HPNWs is low[266,267], contributing to the effective extraction of photo-generated charge carriers in the device. To optimize the performance of a photodetector, the lifetimes of both the mobile charge carrier and the trapped one should be prolonged. Since oxidation is known to

increase the trap state lifetime[253], we believe that the ambient fabrication of the HPNWs aids in extending the lifetime of the trapped charge carriers as the perovskite can be simply oxidized.

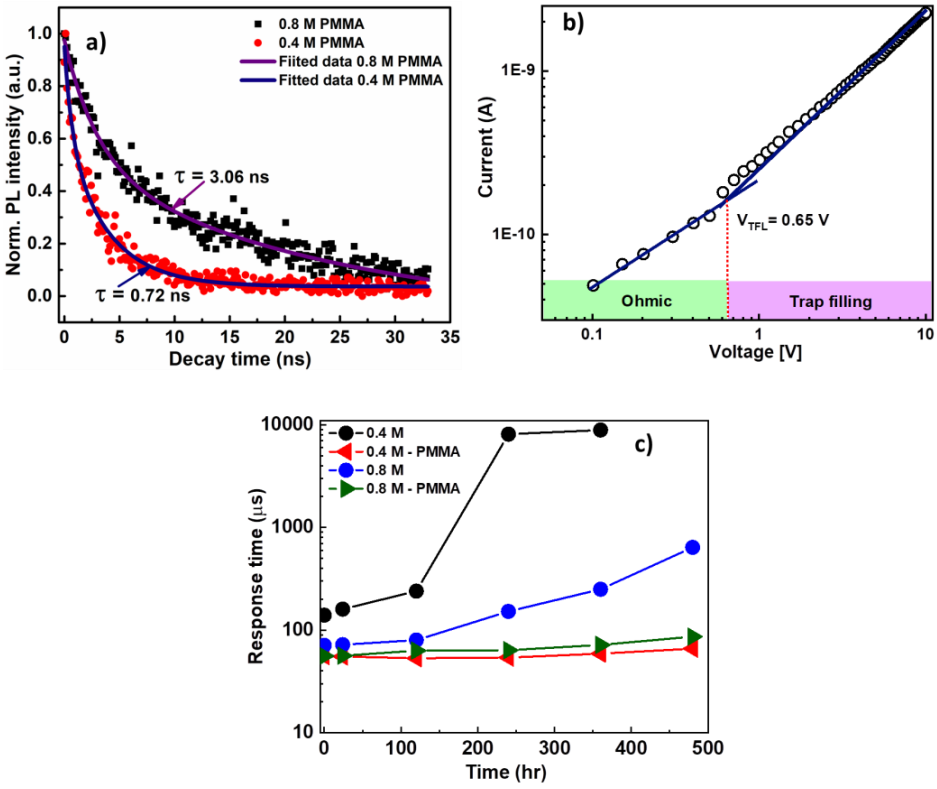

Figure 5. 8: (a) Time-resolved photoluminescence spectra with the bi-exponential fittings for 0.4 and 0.8 M perovskite nanowire networks deposited on glass substrates. (b) *I-V* plot on a logarithmic scale showing the trap filling voltage of the photodetector. (c) Photocurrent response time stability comparison for pristine and PMMA-encapsulated devices produced using 0.4 M and 0.8 M precursor solutions (test condition: 22-25 ^{o}C and 50±5 % RH).

Furthermore, the stability of devices is assessed by measuring the response times for devices stored in ambient environment (22-25 ^{o}C and 50±5 % RH) over the test period of about 20 days. As expected, devices with PMMA layer show reliable performance, as presented in **Figure 5.8(c)**. In comparison, the non-encapsulated devices exhibit a response time that is 26 times longer than the initial response time after 500 hrs due to photo-oxidative degradation. Although the stability of SCN-doped perovskites is known to be superior to undoped perovskites, encapsulation has also significantly improved their performance and stability. In addition, the PMMA layer protects the perovskites from degradation due to oxygen and humidity when the devices are exposed to ambient environmental conditions.

5.5 Photodetector Performance on Flexible Substrate

In this section, we discuss the performance of the photodetectors fabricated with perovskite nanowires made from 0.8 M PbI_2 precursor solution deposited on flexible Kapton substrates. The Kapton substrates were purchased from DuPont Company of thickness about 150 μm and the dimension of 3.5 cm × 2.4 cm. As presented in **Figure 5.9(a,b)**, the flexible device also operates in a photoconductive mode, but in this case, the holes are mobile, and electrons are trapped. The valence band of the perovskite (5.3 eV) is very close to the work function of the Au electrodes (5.1 eV), resulting in only a 0.2 eV barrier for the holes and a 1.35 eV barrier for the electrons. In this case, it is suggested that the photoconductors behave like a hole-dominant device. The holes can easily flow and be extracted at the electrodes. However, the 1.35 eV barrier is very high for the electrons to overcome, resulting in trapping and subsequent recombination with holes.

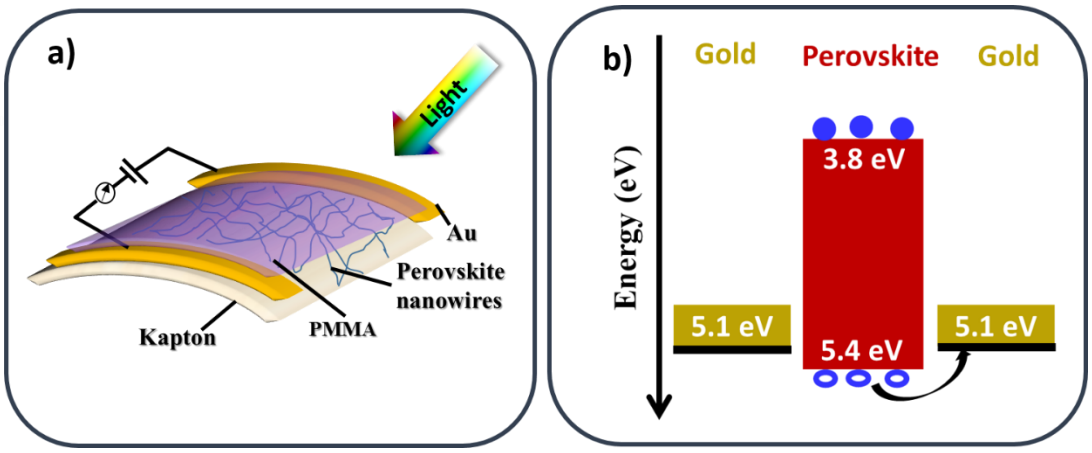

Figure 5. 9: (a) Device configuration of the flexible perovskite photodetector on Kapton substrate. (b) Band diagram illustrating the behavior of a photodetector showing the pathways of the electrons and holes. In photoconductor mode, the holes are mobile, and electrons are trapped. In this case, the mobile holes may recombine with the trapped electrons, which may increase the leakage current in the device.

The performance of the flexible photodetectors is evaluated from the electrical current measurements for flat substrates at room temperature. The area of the device is about 4.56 cm^2. **Figure 5.10(a)** exhibits the *I-V* characteristics of our flexible photodetector devices fabricated with and without PMMA layer, measured under A.M. 1.5G solar simulator. Like the FTO-based devices, we observe a symmetric and linear relationship between the current and voltage, demonstrating an ohmic photoconductive behavior. The devices (with and without PMMA layer) exhibit 1-2 orders of magnitude increase in current under illumination conditions. Likewise, the

device with PMMA layer outperformed the bare devices due to the reduction in recombination loss and surface defects of the perovskite nanowires[268,269].

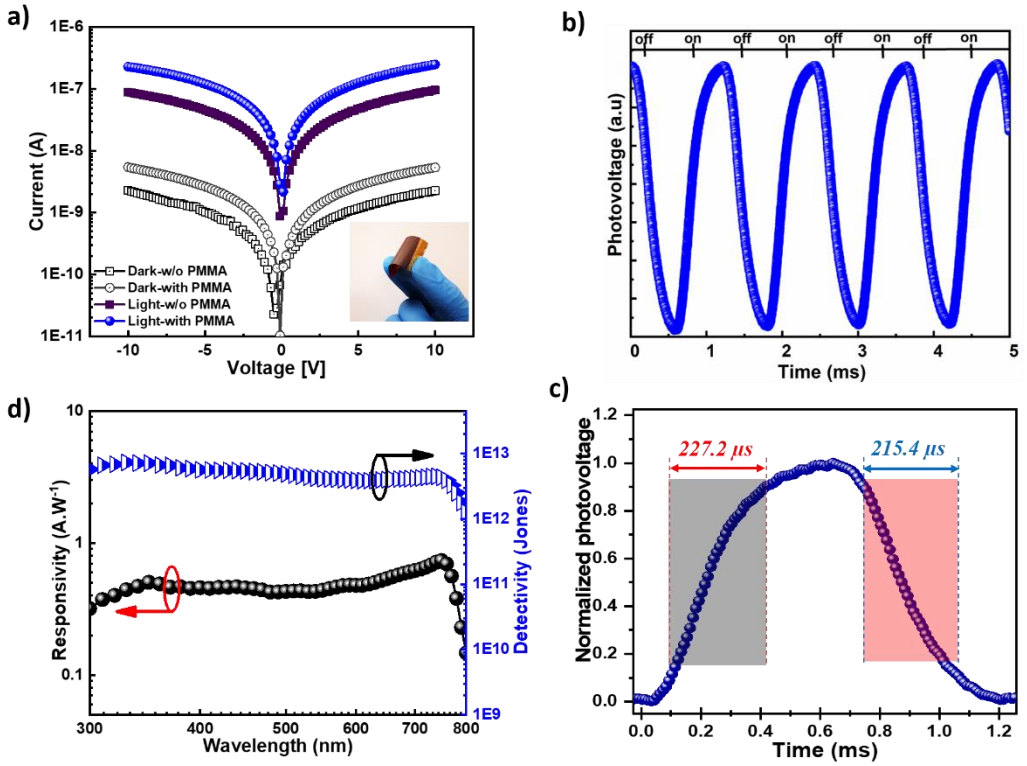

Figure 5. 10: (a) *I-V* curves of the 0.8 M perovskite flexible photodetectors made with and without PMMA layer under dark and illuminated conditions. The absolute values of the measured current are plotted versus the applied voltage on semi-logarithmic scale. (b) Transient response of the photodetectors at 10 V bias under constant illumination of A.M 1.5G and (c) a single pulse showing the rise and fall time constants. (d) Spectral responsivity and specific detectivity of the flexible HPNW photodetector. (The red arrow indicates the responsivity scale, and the black arrow indicates the specific detectivity scale).

Moreover, the response time can be estimated using a white light source modulated at 830 Hz with a chopper as described in Chapter 2, **section 2.7.4**. The transient response displays a steady and reproducible behavior, and the estimated rise and fall times are 227.2 µs and 216.4 µs, respectively, as shown in **Figure 5.10(b,c)**. **Figure A5.2(a, b)** indicates expectedly that the photocurrent increases with the power density, obtained using a 532 nm laser at different excitation powers. Also, the trend of the transient response with different applied voltages is measured at the maximum laser excitation power of 112.5 mW, as shown in **Figure A5.2(c)**. We observe that the peak-to-peak transient current response increases as the applied bias increases from 0 V to 20 V, demonstrating that these devices are responsive to light and sensitive at different voltages.

Additionally, we achieve a peak responsivity of 0.62 $A.W^{-1}$ at 10 V applied bias and a corresponding specific detectivity of 7.3 x 10^{12} Jones, as exhibited in **Figure 5.10(d)**. Overall, the photodetector shows fast response times and high detectivity.

These excellent performances may be attributed to the high crystalline quality of the perovskite nanowires resulting in reduced recombination losses, as well as to an efficient photon absorption, charge generation, and transport to the electrodes via the interconnected nanostructured perovskite film. Compared with the performance of the thin-film perovskite in appendix **Figure A5.4,** the photocurrent generated in the thin film is lower than that in the nanowires. Also, the measured responsivity of ~0.012 AW^{-1} (**Figure A5.4(d))** can be attributed to the morphology of the perovskites and losses due to numerous grain boundaries (cf. **Figure A5.4(b)**.

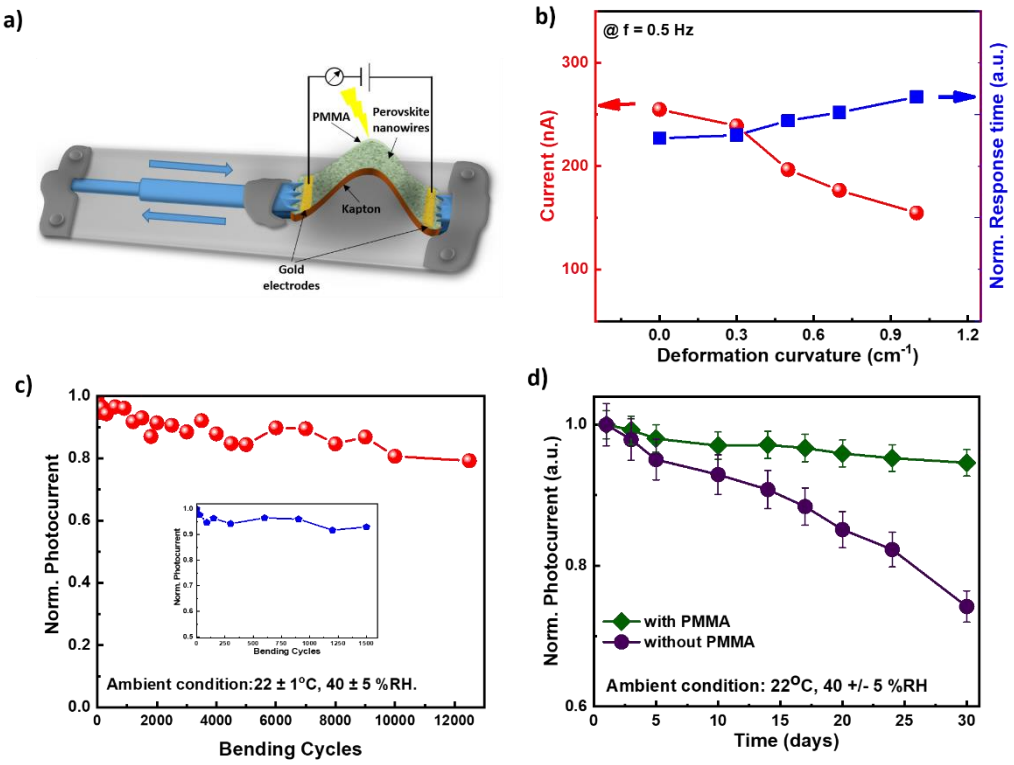

Figure 5. 11: (a) Schematic of the measurement setup under bending conditions. (b) Evolution of the current (*in red)* and the response time (*in blue*) as a function of the bending curvature (up to 1 cm^{-1}). (c) A plot of the evolution of photocurrent versus the number of bending cycles under white-light illumination (d) Photocurrent stability over 30 days period of the devices with (*in green*) and without PMMA (*in purple*) layer stored in ambient air.

The flexible photodetectors are characterized by studying the performance evolution under bending conditions. **Figure 5.11(a)** depicts the set-up used. All the tested devices were characterized using our homemade bending bench at a frequency of 0.5 Hz. The light was pulsed every 10 s, and the On-Off characteristic was registered. The current-voltage (*I*–*V*) measurements were performed in the dark and under illumination using a Keithley 2400 at room temperature. The bending cycles of the devices were performed at a 10 V bias under 100 $mW.cm^{-2}$ white-light illumination. Also, the photographs of the devices under different bending curvatures are presented in **Figure A5.3**. As shown in **Figure 5.11(b),** we observed a slight decrease in the current of the photodetector as bending increases at different curvatures (flat state to 1.0 cm^{-1}). The response speed for each curvature remains largely unchanged for all the devices. **Figure 5.11(c)** exhibits incredible stability of the photocurrent, retaining above 92% of its initial value during the first 1500 bending cycles (see the inset) and 80% for over 12000 bending cycles. This tremendous mechanical stability can be associated with the flexibility offered by both the halide perovskite structure and the Kapton substrate used in this study.

Finally, the stability of the flexible photodetectors is assessed under ambient conditions (23±1^{o}C, 40 ± 5 %RH) by observing the evolution of the photocurrent for 30 days for both encapsulated and non-encapsulated devices. **Figure 5.11(d)** illustrates the degradation behavior of the devices. As expected, PMMA encapsulated devices reveal superior stability since it passivates the surface defects and blocks moisture penetration into the perovskite layer. The encapsulated devices recorded merely 2% loss in the photocurrent after exposure to ambient air, showcasing their reliability for long-term operation. In contrast, the photodetectors without PMMA encapsulation recorded a 30% loss in the photocurrent over the same period. Thus, these attractive properties of the photodetectors make them ideal and suitable for applications in flexible and wearable electronics.

Overall, the performances of our photodetectors on both rigid and flexible substrates are comparable with previous reports (**Table 5.1**), with our devices being among the best perovskite-based photodetectors in the literature with a very short response time.

Table 5.1: Comparison of the critical parameters of different photodetectors fabricated using organo-metal halide perovskite (OMP) as the active layer on both rigid and flexible substrates.

Device materials	**Spectrum (nm)**	**Detectivity (Jones)**	**Responsivity ($A.W^{-1}$)**	**Rise time**	**Decay time**	**Ref.**
FTO-OMP-NW network	532	$7.1x10^{11}$	0.23	53.2 µs	50.2 µs	This work
Kapton/OMP-NWs/PMMA	White light	7.3×10^{12}	0.62	227 µs	215 µs	This work
OMP-Microwire arrays	420	$5.25x10^{12}$	13.5	80 µs	240 µs	[257]
Cs-doped OMP-thin film	White light	$2.7x10^{13}$	5.7	45 ns	91 ns	[258]
OMP-NW network	650	$1.02x10^{12}$	0.1	0.3 ms	0.4 ms	[260]
PET/OMP nanoflakes	265	10^{11}	12.0	2.2 ms	4 ms	[243]
Single Crystal OMP/Au	532	--	2.55	74 µs	58 µs	[270]
C/TiO_2/OMP-Spiro	550	2.60×10^{10}	0.10	<200 ms	<200 ms	[247]
PET/OMP-NWs	532	-	-	120 ms	210 ms	[245]
PET/OMP/$NAYF_4$:Yb/Er	980	0.76×10^{12}	0.27	52 ms	67 ms	[271]
PET/ ITO/OMP	680	2×10^{11}	81	0.38 ms	0.23 ms	[71]

5.6 Conclusions

In conclusion, we present a simple, fast, and low-cost all-solution-based fabrication technique to produce rigid and flexible halide perovskite nanowire-based photodetectors in ambient air. The devices are made up of interconnected nanowire networks bridging two electrodes on FTO and Kapton substrates. The thiocyanate doping improved the quality of the perovskite nanowires, as confirmed by the structural analysis and optical measurements. The PMMA-encapsulated photodetectors exhibit a fast response and recovery times of 53.2 µs and 50.2 µs (227.2 µs and 216.4 µs for flexible devices), respectively. They also show a high specific detectivity of $7.1x10^{11}$ Jones ($7.3x10^{12}$ Jones for flexible device), together with excellent moisture resistance and stability for more than 500 hours. We also demonstrate that a layer of PMMA improves both the performance and stability of the devices through passivation and protection of the perovskite nanowires from moisture. Hence, these quickly and simply fabricated perovskite nanowire-based photodetectors in ambient conditions are cost-effective, making them suitable candidates for upscaling and mass fabrication of highly efficient optoelectronic devices with the most promising applications in wearable electronics, biosensors, and fiber optics technologies.

Chapter 6: Conclusions and Perspectives

6.1 Conclusions

Reports have suggested that it would take hundreds of years to manufacture and install enough silicon PV panels to meet the world's rapidly growing energy demand and achieve the global de-carbonization objectives that would slow the impact of climate change. Given the limited time window during which it is possible to prevent catastrophic climate change, alternative energy sources need to be established urgently. For years, scientists have experimented with alternative material candidates that would allow solar panels to harvest energy at a lower cost than crystalline silicon. Until now, a few solution-processable designs based on thin films have emerged with the potential for high power efficiency devices[272].

Halide perovskite is an example of such material that has attracted significant attention in the last decade due to its vast applications in optoelectronic devices. However, as most technologies face challenges in their early stages, halide perovskites are no exception. The three primary players for any technology to be commercially viable are efficiency, stability over time (determining their useful lifetime), and cost. The main question of interest we asked ourselves during this research is, *"can efficient and stable halide perovskite-based devices be fabricated under ambient conditions?"* In this thesis, we have successfully done so and established a route to synthesize halide perovskite materials for photovoltaic and optoelectronic applications, mainly solar cells and photodetectors. Notably, we worked on a fabrication process in ambient air instead of the usual expensive process in a controlled environment such as a glove box. We first prepared single-cation organic-inorganic halide perovskite precursor solutions by adding pseudo-halide additives and a mixture of solvents. Our studies revealed that relative moisture/humidity plays a vital role during the precursor preparation and affects the microstructural and optoelectronic properties of the perovskite thin films prepared through a two-step spin-coating deposition technique. Since humidity can cause rapid degradation of the perovskite, we prepared mixed-cation perovskites and further our investigations by incorporating ionic additives and solvent engineering into the fabrication process of the solar cells. The devices fabricated using our novel synthesis process in ambient have shown very high power conversion efficiencies and remarkable ambient stability. Subsequently, by replacing the hole-transporting material Spiro-OMeTAD in the solar cells heterostructure with copper thiocyanate (CuSCN), we improved the cost-effectiveness of the

laboratory fabricated devices further while keeping good photovoltaic performances[273] as shown in Figure A6.1, A6.2 and Table A6 (refer to *Appendix II* for details).

Finally, we explored the versatility of the halide perovskite materials by making nanowire networks via a solution process to fabricate photodetectors. After introducing some fundamentals on solar energy and photovoltaic devices, as well as on perovskite materials and devices, their architecture, and synthesis techniques in chapters 1 and 2, the findings of the thesis are discussed in detail in chapters 3, 4, and 5. They are briefly summarized here, followed by some perspectives that arise from this research.

Chapter 3: An alternative way to fabricate perovskite solar cells entirely in ambient conditions with reasonable efficiency and stability has been developed and is presented. The effects of $Pb(SCN)_2$, water, and ethanol on the morphology of single-cation perovskite thin films have been explored using different characterization methods. Highly crystallized large grains over 4 µm are achieved by spin-coating a solution of $CH_3NH_3PbI_3$ doped with 5 wt% of $Pb(SCN)_2$, 2 vol% of deionized water, and 5 vol% of ethanol. The stability of the perovskite thin films obtained was investigated. We compared the long-term stability of the optimized films to that of pristine $CH_3NH_3PbI_3$ perovskite thin films and found it was significantly improved. Motivated by our findings, solar cells are fabricated using the optimized recipe, and their stability is studied for over 30 days. We attain a solar cell's efficiency of 13.5% for the best performing cell with a lifetime, $T_{80,}$ of over 480 hours, resulting in low degradation loss in the device. Our ability to synthesize high-quality crystalline halide perovskite thin-films in ambient is in itself a significant achievement in the field of halide perovskite technology, as it allows integrating them into efficient and stable solar cells without the need for controlled and inert environmental conditions. Therefore, our simple, low-temperature method presents a promising cost-effective route for preparing ambient-processed halide perovskites for optoelectronic devices.

Chapter 4: The findings described in chapter 3 improved our understanding of the role of the morphology, chemical structure, and humidity in the stability of halide perovskite solar cells. Inspired by that novel knowledge and good results, we further our studies by investigating the effect of modifying the elemental composition of the perovskite materials on both the efficiency and stability of the performance of the PSC. We highlight further improvements resulting from modifying and optimizing the synthesis and processing technique using solvent-anti solvent

engineering for triple-cation perovskite. Since a high-quality perovskite film is believed to be the prerequisite for high efficiency and stability, we achieved pinhole-free films by utilizing chlorobenzene and ethanol. These solvent additives help the nucleation and precipitation of grains, resulting in well-crystallized perovskite films with large grains. As a result, perovskite solar cells with remarkable efficiency of 20.3% and excellent stability have been realized. Indeed, the solvent-treated and $Pb(SCN)_2$ incorporated devices show good long-term stability with less than 20% loss in PCE for over ten months of exposure at ambient conditions. Finally, we highlight the physical mechanism of the degradation process by employing trap-state densities and charge transport evaluation for fresh and degraded devices. The results show the inter-dependency between the incredible enhancement in PCE and the material and the correlation between microstructure and stability of halide perovskites.

Chapter 5: Finally, we present a comprehensive study reporting photodetectors with fast response using networks of pseudo-halide perovskite nanowires as building blocks. The nanowire photodetectors exhibit well-defined and promising operation characteristics such as rapid response, excellent reproducibilities, and relatively high detectivities. Next, we demonstrated large-area broadband flexible photodetectors based on these perovskite nanowire networks on flexible Kapton substrates by a cost-effective low-temperature fabrication technique with excellent stability that can be further improved after encapsulation. The devices show high detectivity of 10^{12} Jones and short response times in the order of micro-seconds with remarkable stability under different bending conditions without the bending state altering the photoresponse.

6.2 Perspectives

Despite the challenges encountered during this work, we achieved our goal of fabricating stable and efficient perovskite photovoltaic and optoelectronic devices under ambient conditions. At the beginning of this research about five years ago, halide perovskite devices could only survive a few hours under operational conditions. Moreover, most of the reported literature was geared towards improving the efficiency of devices fabricated under controlled and inert conditions. Only a few reports were considering ambient processing, and the devices synthesized under ambient conditions exhibited low performance. In general, compared with efforts in the scientific community to increase efficiency, there were only a few stability studies. We, therefore, consider that the research work made a significant contribution to the field. Although we have been able to

fabricate suitable devices with good performance, there are still some open challenges that need the attention of the scientific community:

The stability studies in this work are limited to moisture effects and continuous illumination on non-encapsulated solar cells. Although the stability achieved is quite remarkable, losses are primarily due to oxidative degradation and mechanical load. We suspect that other harsh environmental conditions, such as heat and/or UV-illumination (such a conditions a device would be subjected to in space, for instance), could deteriorate the devices much faster. Hence, further studies of the stability of our devices should be extended to investigate their behavior under the actual operation conditions (starting simply with outdoor measurements, for instance). A setup could be designed to study the in-situ degradation of halide perovskite solar cells and simultaneously point out UV light, moisture, oxygen, and heat effects on the device. Finally, XPS and FTIR analysis of freshly prepared and a sample of different ages can be performed to give further information about the degradation mechanism.

In chapter 5, the preparation of the perovskite nanowires was done through a simple spin-coating technique, and it was speculated that the nanowires network originated from some sort of crystallization process. The detailed and complete mechanism behind the growth of the nanowires and nanowire network, as interesting as it is, is still unknown and has not been thoroughly addressed in this work. Thus, a further interesting research topic would be a detailed study of the nanowires growth mechanism by an in-situ characterization tool and/or possibly by simulating the process using available crystal growth software. This would provide a much-needed insight into the growth mechanism of the halide perovskites nanowires and nanowire networks and pave to way for their large-scale production by low-temperature solution process.

Although we can successfully fabricate solar cells that meet the viable technological requirements: high efficiency, long lifetime, and low cost, one remaining issue with the halide perovskite technology is the toxicity due to the presence of lead. At present, there are two schools of thought on lead toxicity in the field. Some argue that the amount or toxicity level of lead present in these devices is immaterial compared to some existing technologies like lithium-ion batteries. The others hold the view that anything toxic is not suitable for a “so-called” renewable energy source.

For instance, the disposal and long-term safety of cadmium telluride (CdTe) solar cells is a known issue for large-scale commercialization. Though the cadmium is toxic, challenging to synthesize

in large quantities, and tellurium is rare and can limit the number of panels that can be manufactured, their record laboratory efficiency is as high as 22.1%. They represent the second-largest PV technology commercialized in the market after crystalline silicon PV. Thus, developing recycling protocols to limit the environmental impact of such technologies is possible, and PSCs are not exclusive. Currently, researchers are actively working on developing non-toxic substitutes, and developing recycling protocols to limit the environmental impact of such technologies[106]. Nevertheless, PSCs are still regarded as the photovoltaic technology of the future. Considerable efforts are being deployed to increase the efficiency and stability of PSCs, prolong their lifetime and make this technology as "green" as possible with limited environmental and health impacts.

In this regard, we carried out some preliminary experiments by using an alternative to lead-based perovskites, namely bismuth-halide PSC. We investigated methylammonium bismuth iodide $(CH_3NH_3)_3Bi_2I_9$ (MBI) for solar cell fabrication in an attempt towards' lead-free' halide perovskite. To obtain high-quality and uniform film coverage, we explored different deposition techniques: one-step spin-coating, two-step spin-coating, and dip-coating of the precursors. Our most successful approach was one-step spin-coating, which yielded big hexagonal-shaped grains. The efficiency of the cells was extremely low, however, but they did show excellent long-term stability. We anticipate that the low efficiency is due to the large bandgap of the MBI around 2.2 eV, the non-uniformity of the film on the substrates, and the many predicted defects in the MBI[274–279].

Further work in this direction with some computational analysis using tools such as DFT would help to understand their electronic structure and properties. Based on my Ph.D. thesis work results, a fabrication route could be engineered toward high-performance bismuth-based halide perovskite devices. Additionally, other divalent elements can be explored in place of lead, and if successful, the toxicity problem could be resolved.

References

[1] US EIA, "EIA: International Energy Outlook 2019 Presentation," **2019**.

[2] R. J. Zedalis, *Global Energy & CO_2 Status Report 2018*, **2019**.

[3] "IEA (2020), Global Energy Review 2020, IEA, Paris," can be found under https://www.iea.org/reports/global-energy-review-2020/global-energy-and-co2-emissions-in-2020.

[4] S. A. Kalogirou, *Prog. Energy Combust. Sci.* **2004**, *30*, 231.

[5] A. J. Lamadrid, *Int. J. Electr. Power Energy Syst.* **2015**, *71*, 101.

[6] O. Bolufawi, in *Spec. Top. Renew. Energy Syst.*, InTech, **2018**.

[7] U. Energy Information Administration, *International Energy Outlook 2020 (IEO2020).*

[8] D. M. Chapin, C. S. Fuller, G. L. Pearson, *J. Appl. Phys.* **1954**, *25*, 676.

[9] R. Adib, A. Zervos, M. Eckhart, M. E.-A. David, H. Kirsty, H. P. Rae, F. Bariloche, *REN21, Renewables 2020 Global Status Report*, **2020**.

[10] "Costa Rica Is On The Brink Of An EVolution — #CleanTechnica Exclusive | CleanTechnica," can be found under https://cleantechnica.com/2018/12/31/costa-rica-is-on-the-brink-of-an-evolution-cleantechnica-exclusive/.

[11] NREL, **2019**.

[12] M. Hu, D. S. Hans-Rudolf Wenk, *Am. Mineral.* **1992**, *77*, 359.

[13] A. M. Glass, D. Von Der Linde, T. J. Negran, *Appl. Phys. Lett.* **1974**, *25*, 233.

[14] L. Pintilie, I. Vrejoiu, G. Le Rhun, M. Alexe, *J. Appl. Phys.* **2007**, *101*, DOI 10.1063/1.2560217.

[15] Y. S. Yang, S. J. Lee, S. Yi, B. G. Chae, S. H. Lee, H. J. Joo, M. S. Jang, *Appl. Phys. Lett.* **2000**, *76*, 774.

[16] R. Nechache, C. Harnagea, S. Licoccia, E. Traversa, A. Ruediger, A. Pignolet, F. Rosei,

Appl. Phys. Lett. **2011**, *98*, DOI 10.1063/1.3590270.

[17] R. Nechache, C. Harnagea, S. Li, L. Cardenas, W. Huang, J. Chakrabartty, F. Rosei, *Nat. Photonics* **2014**, *9*, 61.

[18] S. Y. Yang, L. W. Martin, S. J. Byrnes, T. E. Conry, S. R. Basu, D. Paran, L. Reichertz, J. Ihlefeld, C. Adamo, A. Melville, Y. H. Chu, C. H. Yang, J. L. Musfeldt, D. G. Schlom, J. W. Ager, R. Ramesh, *Appl. Phys. Lett.* **2009**, *95*, DOI 10.1063/1.3204695.

[19] Mitzi David B., *Progress in Inorganic Chemistry. Volume 48*, Wiley, **1999**.

[20] Z. Li, M. Yang, J.-S. S. Park, S.-H. H. Wei, J. J. Berry, K. Zhu, *Chem. Mater. 28*, 284.

[21] G. P. Nagabhushana, R. Shivaramaiah, A. Navrotsky, *Proc. Natl. Acad. Sci. U. S. A.* **2016**, *113*, 7717.

[22] W. Travis, E. N. K. Glover, H. Bronstein, D. O. Scanlon, R. G. Palgrave, *Chem. Sci.* **2016**, *7*, 4548.

[23] W. Ji, K. Yao, Y. C. Liang, *Adv. Mater.* **2010**, *22*, 1763.

[24] J. P. Chakrabartty, R. Nechache, C. Harnagea, F. Rosei, *Opt. Express* **2014**, *22*, A80.

[25] D. B. Mitzi, P. Brock, *Inorg. Chem.* **2001**, *40*, 2096.

[26] D. B. Mitzi, *Inorg. Chem.* **2000**, *39*, 6107.

[27] D. B. Mitzi, *Chem. Mater.* **2001**, *13*, 3283.

[28] D. B. Mitzi, *Chem. Mater.* **1996**, *8*, 791.

[29] A. Kojima, K. Teshima, Y. Shirai, T. Miyasaka, *J. Am. Chem. Soc.* **2009**, DOI 10.1021/ja809598r.

[30] M. M. Lee, J. Teuscher, T. Miyasaka, T. N. Murakami, H. J. Snaith, *Science (80-.).* **2012**, *338*, 643.

[31] J. H. Im, C. R. Lee, J. W. Lee, S. W. Park, N. G. Park, *Nanoscale* **2011**, *3*, 4088.

[32] S. D. Stranks, G. E. Eperon, G. Grancini, C. Menelaou, M. J. P. Alcocer, T. Leijtens, L. M. Herz, A. Petrozza, H. J. Snaith, *Science (80-.).* **2013**, *342*, 341.

[33] H. S. Jung, N.-G. G. Park, *Small* **2015**, *11*, 10.

[34] H.-S. Kim, S. H. Im, N.-G. Park, *J. Phys. Chem. C* **2014**, *118*, 5615.

[35] M. Grätzel, *Nat. Mater.* **2014**, *13*, 838.

[36] C. Wehrenfennig, G. E. Eperon, M. B. Johnston, H. J. Snaith, L. M. Herz, *Adv. Mater.* **2014**, *26*, 1584.

[37] G. E. Eperon, S. D. Stranks, C. Menelaou, M. B. Johnston, L. M. Herz, H. J. Snaith, *Energy Environ. Sci.* **2014**, *7*, 982.

[38] C. C. Stoumpos, C. D. Malliakas, M. G. Kanatzidis, *Inorg. Chem.* **2013**, *52*, 9019.

[39] F. Zheng, L. Z. Tan, S. Liu, A. M. Rappe, *Nano Lett.* **2015**, *15*, 7794.

[40] J.-H. Im, I.-H. Jang, N. Pellet, M. Grätzel, N.-G. Park, *Nat. Nanotechnol.* **2014**, *9*, 927.

[41] N. J. Jeon, J. H. Noh, Y. C. Kim, W. S. Yang, S. Ryu, S. Il Seok, *Nat. Mater.* **2014**, *13*, 897.

[42] I. M. Asuo, I. Ka, D. Gedamu, A. Pignolet, R. Nechache, S. G. Cloutier, *Sol. Energy Mater. Sol. Cells* **2019**, *200*, 110029.

[43] I. Ka, I. M. Asuo, S. Basu, P. Fourmont, D. M. Gedamu, A. Pignolet, S. G. Cloutier, R. Nechache, *Small* **2018**, *14*, 1802319.

[44] D. Gedamu, I. M. Asuo, D. Benetti, M. Basti, I. Ka, S. G. Cloutier, F. Rosei, R. Nechache, *Sci. Rep.* **2018**, *8*, 12885.

[45] I. M. Asuo, P. Fourmont, I. Ka, D. Gedamu, S. Bouzidi, A. Pignolet, R. Nechache, S. G. Cloutier, *Small* **2019**, *15*, 1804150.

[46] H. Zhou, J. Mei, M. Xue, Z. Song, H. Wang, *J. Phys. Chem. C* **2017**, *121*, 21541.

[47] L. Dou, Y. (Micheal) Yang, J. You, Z. Hong, W.-H. Chang, G. Li, Y. (Micheal) Yang, *Nat. Commun.* **2014**, *5*, 5404.

[48] I. M. Asuo, D. Gedamu, I. Ka, L. F. L. F. Gerlein, F.-X. Fortier, A. Pignolet, S. G. S. G. Cloutier, R. Nechache, *Nano Energy* **2018**, *51*, 324.

[49] I. Ka, L. F. Gerlein, I. M. Asuo, R. Nechache, S. G. Cloutier, *Nanoscale* **2018**, *10*, 9044.

[50] M. I. Saidaminov, V. Adinolfi, R. Comin, A. L. Abdelhady, W. Peng, I. Dursun, M. Yuan, S. Hoogland, E. H. Sargent, O. M. Bakr, *Nat. Commun.* **2015**, *6*, 1.

[51] W. Deng, L. Huang, X. Xu, X. Zhang, X. Jin, S.-T. Lee, J. Jie, *Nano Lett.* **2017**, *17*, 2482.

[52] K. Lin, J. Xing, L. N. Quan, F. P. G. de Arquer, X. Gong, J. Lu, L. Xie, W. Zhao, D. Zhang, C. Yan, W. Li, X. Liu, Y. Lu, J. Kirman, E. H. Sargent, Q. Xiong, Z. Wei, *Nature* **2018**, *562*, 245.

[53] Y. Cao, N. Wang, H. Tian, J. Guo, Y. Wei, H. Chen, Y. Miao, W. Zou, K. Pan, Y. He, H. Cao, Y. Ke, M. Xu, Y. Wang, M. Yang, K. Du, Z. Fu, D. Kong, D. Dai, Y. Jin, G. Li, H. Li, Q. Peng, J. Wang, W. Huang, *Nature* **2018**, *562*, 249.

[54] X. Zhang, H. Liu, W. Wang, J. Zhang, B. Xu, K. L. Karen, Y. Zheng, S. Liu, S. Chen, K. Wang, X. W. Sun, *Adv. Mater.* **2017**, *29*, DOI 10.1002/adma.201606405.

[55] L. Zhang, X. Yang, Q. Jiang, P. Wang, Z. Yin, X. Zhang, H. Tan, Y. M. Yang, M. Wei, B. R. Sutherland, E. H. Sargent, J. You, *Nat. Commun.* **2017**, *8*, DOI 10.1038/ncomms15640.

[56] H. Cho, S. H. Jeong, M. H. Park, Y. H. Kim, C. Wolf, C. L. Lee, J. H. Heo, A. Sadhanala, N. S. Myoung, S. Yoo, S. H. Im, R. H. Friend, T. W. Lee, *Science (80-.).* **2015**, *350*, 1222.

[57] N. Wang, L. Cheng, R. Ge, S. Zhang, Y. Miao, W. Zou, C. Yi, Y. Sun, Y. Cao, R. Yang, Y. Wei, Q. Guo, Y. Ke, M. Yu, Y. Jin, Y. Liu, Q. Ding, D. Di, L. Yang, G. Xing, H. Tian, C. Jin, F. Gao, R. H. Friend, J. Wang, W. Huang, *Nat. Photonics* **2016**, *10*, 699.

[58] Z. Xiao, R. A. Kerner, L. Zhao, N. L. Tran, K. M. Lee, T.-W. W. Koh, G. D. Scholes, B. P. Rand, *Nat. Photonics* **2017**, *11*, 108.

[59] W. Yu, F. Li, L. Yu, M. R. Niazi, Y. Zou, D. Corzo, A. Basu, C. Ma, S. Dey, M. L. Tietze, U. Buttner, X. Wang, Z. Wang, M. N. Hedhili, C. Guo, T. Wu, A. Amassian, *Nat. Commun.* **2018**, *9*, DOI 10.1038/s41467-018-07706-9.

[60] X. Liu, D. Yu, X. Song, H. Zeng, *Small* **2018**, *14*, DOI 10.1002/smll.201801460.

[61] S. P. Senanayak, B. Yang, T. H. Thomas, N. Giesbrecht, W. Huang, E. Gann, B. Nair, K.

Goedel, S. Guha, X. Moya, C. R. McNeill, P. Docampo, A. Sadhanala, R. H. Friend, H. Sirringhaus, *Sci. Adv.* **2017**, *3*, e1601935.

[62] B. Li, Y. Li, C. Zheng, D. Gao, W. Huang, D. Sabba, M. Grätzel, S. Mhaisalkar, T. C. Sum, H. P. He, Z. Z. Ye, M. L. Lai, R. H. Friend, W. Huang, U. Steiner, *RSC Adv.* **2016**, *6*, 38079.

[63] M. Saliba, T. Matsui, J.-Y. Seo, K. Domanski, J.-P. Correa-Baena, M. K. Nazeeruddin, S. M. Zakeeruddin, W. Tress, A. Abate, A. Hagfeldt, M. Grätzel, *Energy Environ. Sci.* **2016**, *9*, 1989.

[64] L. K. Ono, Y. Qi, S. (Frank) Liu, *Joule* **2018**, *2*, 1961.

[65] D. Decoster, J. Harari, *Optoelectronic Sensors*, ISTE, **2009**.

[66] A. Marchioro, J. Teuscher, D. Friedrich, M. Kunst, R. Van De Krol, T. Moehl, M. Grätzel, J. E. Moser, *Nat. Photonics* **2014**, *8*, 250.

[67] D. Zhou, T. Zhou, Y. Tian, X. Zhu, Y. Tu, *J. Nanomater.* **2018**, *2018*, DOI 10.1155/2018/8148072.

[68] I. N. Mora-Seró, *Joule* **2018**, *2*, 585.

[69] S. M. Sze, *DEVICES Physics and Technology 2nd Edition*, **1985**.

[70] D. Gedamu, I. Paulowicz, S. Kaps, O. Lupan, S. Wille, G. Haidarschin, Y. K. Y. K. Mishra, R. Adelung, Y. Kumar, R. Adelung, Y. K. Y. K. Mishra, R. Adelung, *Adv. Mater.* **2014**, *26*, 1541.

[71] W. Hu, W. Huang, S. Yang, X. Wang, Z. Jiang, X. Zhu, H. Zhou, H. Liu, Q. Zhang, X. Zhuang, J. Yang, D. H. Kim, A. Pan, *Adv. Mater.* **2017**, *29*, 1703256.

[72] M. A. Green, A. Ho-Baillie, H. J. Snaith, *Nat. Photonics* **2014**, *8*, 506.

[73] C.-W. Chen, H.-W. Kang, S.-Y. Hsiao, P.-F. Yang, K.-M. Chiang, H.-W. Lin, *Adv. Mater.* **2014**, *26*, 6647.

[74] X. Li, D. Bi, C. Yi, J.-D. Décoppet, J. Luo, S. M. Zakeeruddin, A. Hagfeldt, M. Grätzel, *Science* **2016**, *353*, 58.

[75] Y.-H. H. Chiang, H.-M. M. Cheng, M.-H. H. Li, T.-F. F. Guo, P. Chen, *ChemSusChem* **2016**, *9*, 2620.

[76] M. Liu, M. B. Johnston, H. J. Snaith, *Nature* **2013**, *501*, 395.

[77] Q. Chen, H. Zhou, Z. Hong, S. Luo, H.-S. S. Duan, H.-H. H. Wang, Y. Liu, G. Li, Y. Yang, *J. Am. Chem. Soc.* **2014**, *136*, 622.

[78] S. G. Li, K. J. Jiang, M. J. Su, X. P. Cui, J. H. Huang, Q. Q. Zhang, X. Q. Zhou, L. M. Yang, Y. L. Song, *J. Mater. Chem. A* **2015**, *3*, 9092.

[79] C. Trudeau, M. Bolduc, P. Beaupre, I. Ka, I. M. Asuo, S. G. Cloutier, **2018**, pp. 1–6.

[80] A. T. Barrows, A. J. Pearson, C. K. Kwak, A. D. F. Dunbar, A. R. Buckley, D. G. Lidzey, *Energy Environ. Sci.* **2014**, *7*, 2944.

[81] S. Ulična, B. Dou, D. H. Kim, K. Zhu, J. M. Walls, J. W. Bowers, M. F. A. M. Van Hest, *ACS Appl. Energy Mater.* **2018**, *1*, 1853.

[82] J. E. Bishop, T. J. Routledge, D. G. Lidzey, *J. Phys. Chem. Lett.* **2018**, *9*, 1977.

[83] W. Chen, Y. Wu, Y. Yue, J. Liu, W. Zhang, X. Yang, H. Chen, E. Bi, I. Ashraful, M. Grätzel, L. Han, *Science (80-.).* **2015**, *350*, 944.

[84] Y. Rong, Y. Hu, A. Mei, H. Tan, M. I. Saidaminov, S. Il Seok, M. D. McGehee, E. H. Sargent, H. Han, *Science (80-.).* **2018**, *361*, DOI 10.1126/science.aat8235.

[85] J. S. Shaikh, N. S. Shaikh, A. D. Sheikh, S. S. Mali, A. J. Kale, P. Kanjanaboos, C. K. Hong, J. H. Kim, P. S. Patil, *Mater. Des.* **2017**, *136*, 54.

[86] M. Xiao, F. Huang, W. Huang, Y. Dkhissi, Y. Zhu, J. Etheridge, A. Gray-Weale, U. Bach, Y.-B. Cheng, L. Spiccia, *Angew. Chemie* **2014**, *126*, 10056.

[87] J. H. Im, H. S. Kim, N. G. Park, *APL Mater.* **2014**, *2*, DOI 10.1063/1.4891275.

[88] J. H. Im, I. H. Jang, N. Pellet, M. Grätzel, N. G. Park, *Nat. Nanotechnol.* **2014**, *9*, 927.

[89] J. H. Heo, H. J. Han, D. Kim, T. K. Ahn, S. H. Im, *Energy Environ. Sci.* **2015**, *8*, 1602.

[90] J. Xiao, Y. Yang, X. Xu, J. Shi, L. Zhu, S. Lv, H. Wu, Y. Luo, D. Li, Q. Meng, *J. Mater.*

Chem. A **2015**, *3*, 5289.

[91] M. M. Tavakoli, L. Gu, Y. Gao, C. Reckmeier, J. He, A. L. Rogach, Y. Yao, Z. Fan, *Sci. Rep.* **2015**, *5*, DOI 10.1038/srep14083.

[92] X. Qin, Z. Zhao, Y. Wang, J. Wu, Q. Jiang, J. You, *J. Semicond.* **2017**, *38*, 011002.

[93] M. Lira-Cantú, *Nat. Energy* **2017**, *2*, DOI 10.1038/nenergy.2017.115.

[94] Z. Xiao, Q. Dong, C. Bi, Y. Shao, Y. Yuan, J. Huang, *Adv. Mater.* **2014**, *26*, 6503.

[95] T. A. Berhe, W.-N. Su, C.-H. Chen, C.-J. Pan, J.-H. Cheng, H.-M. Chen, M.-C. Tsai, L.-Y. Chen, A. A. Dubale, B.-J. Hwang, *Energy Environ. Sci.* **2016**, *9*, 323.

[96] J. Troughton, K. Hooper, T. M. Watson, *Nano Energy* **2017**, *39*, 60.

[97] M. Saliba, T. Matsui, K. Domanski, J.-Y. Seo, A. Ummadisingu, S. M. Zakeeruddin, J.-P. Correa-Baena, W. R. Tress, A. Abate, A. Hagfeldt, M. Gratzel, *Science (80-.).* **2016**, *5557*, DOI 10.1126/science.aah5557.

[98] T. Leijtens, R. Prasanna, A. Gold-Parker, M. F. Toney, M. D. McGehee, *ACS Energy Lett.* **2017**, *2*, 2159.

[99] F. Hao, C. C. Stoumpos, D. H. Cao, R. P. H. Chang, M. G. Kanatzidis, *Nat. Photonics* **2014**, *8*, 489.

[100] A. L. Abdelhady, M. I. Saidaminov, B. Murali, V. Adinolfi, O. Voznyy, K. Katsiev, E. Alarousu, R. Comin, I. Dursun, L. Sinatra, E. H. Sargent, O. F. Mohammed, O. M. Bakr, *J. Phys. Chem. Lett.* **2016**, *7*, 295.

[101] E. Mosconi, B. Merabet, D. Meggiolaro, A. Zaoui, F. De Angelis, *J. Phys. Chem. C* **2018**, *122*, 14107.

[102] A. K. Baranwal, H. Masutani, H. Sugita, H. Kanda, S. Kanaya, N. Shibayama, Y. Sanehira, M. Ikegami, Y. Numata, K. Yamada, T. Miyasaka, T. Umeyama, H. Imahori, S. Ito, *Nano Converg.* **2017**, *4*, DOI 10.1186/s40580-017-0120-3.

[103] F. Jiang, D. Yang, Y. Jiang, T. Liu, X. Zhao, Y. Ming, B. Luo, F. Qin, J. Fan, H. Han, L. Zhang, Y. Zhou, *J. Am. Chem. Soc.* **2018**, *140*, 1019.

[104] F. Giustino, H. J. Snaith, *ACS Energy Lett.* **2016**, *1*, 1233.

[105] A. Abate, *Joule* **2017**, *1*, 659.

[106] A. Binek, M. L. Petrus, N. Huber, H. Bristow, Y. Hu, T. Bein, P. Docampo, *ACS Appl. Mater. Interfaces* **2016**, *8*, 12881.

[107] W. Ke, M. G. Kanatzidis, *Nat. Commun.* **2019**, *10*, DOI 10.1038/s41467-019-08918-3.

[108] J. M. Kadro, A. Hagfeldt, *Joule* **2017**, *1*, 29.

[109] M. Cai, Y. Wu, H. Chen, X. Yang, Y. Qiang, L. Han, *Adv. Sci.* **2017**, *4*, 1600269.

[110] J. H. Noh, S. H. Im, J. H. Heo, T. N. Mandal, S. Il Seok, *Nano Lett.* **2013**, *13*, 1764.

[111] L. Meng, J. You, Y. Yang, *Nat. Commun.* **2018**, *9*, 5265.

[112] Guangda Niu, Xudong Guo, Liduo Wang, *J. Mater. Chem. A* **2015**, *3*, 8970.

[113] Y. Y. Zhang, S. Chen, P. Xu, H. Xiang, X. G. Gong, A. Walsh, S. H. Wei, *Chinese Phys. Lett.* **2018**, *35*, 036104.

[114] N. Arora, M. I. Dar, M. Abdi-Jalebi, F. Giordano, N. Pellet, G. Jacopin, R. H. Friend, S. M. Zakeeruddin, M. Grätzel, *Nano Lett.* **2016**, *16*, 7155.

[115] Z. Ahmad, M. A. Najeeb, R. A. Shakoor, A. Alashraf, S. A. Al-Muhtaseb, A. Soliman, M. K. Nazeeruddin, *Sci. Rep.* **2017**, *7*, 15406.

[116] N. Arora, M. I. Dar, A. Hinderhofer, N. Pellet, F. Schreiber, S. M. Zakeeruddin, M. Grätzel, *Science (80-.).* **2017**, *358*, 768.

[117] N. Y. Doumon, G. Wang, X. Qiu, A. J. Minnaard, R. C. Chiechi, L. J. A. Koster, *Sci. Rep.* **2019**, *9*, 4350.

[118] N. Y. Doumon, G. Wang, R. C. Chiechi, L. J. A. Koster, *J. Mater. Chem. C* **2017**, *5*, 6611.

[119] H. J. Snaith, A. Abate, J. M. Ball, G. E. Eperon, T. Leijtens, N. K. Noel, S. D. Stranks, J. T. W. Wang, K. Wojciechowski, W. Zhang, *J. Phys. Chem. Lett.* **2014**, *5*, 1511.

[120] W. Tress, N. Marinova, T. Moehl, S. M. Zakeeruddin, M. K. Nazeeruddin, M. Grätzel, *Energy Environ. Sci.* **2015**, *8*, 995.

[121] A. A. Bakulin, O. Selig, H. J. Bakker, Y. L. A. Rezus, C. Müller, T. Glaser, R. Lovrincic, Z. Sun, Z. Chen, A. Walsh, J. M. Frost, T. L. C. Jansen, *J. Phys. Chem. Lett.* **2015**, *6*, 3663.

[122] E. L. Unger, E. T. Hoke, C. D. Bailie, W. H. Nguyen, A. R. Bowring, T. Heumüller, M. G. Christoforo, M. D. McGehee, *Energy Environ. Sci.* **2014**, *7*, 3690.

[123] Z. Chu, M. Yang, P. Schulz, D. Wu, X. Ma, E. Seifert, L. Sun, X. Li, K. Zhu, K. Lai, *Nat. Commun.* **2017**, *8*, 2230.

[124] D. W. DeQuilettes, S. M. Vorpahl, S. D. Stranks, H. Nagaoka, G. E. Eperon, M. E. Ziffer, H. J. Snaith, D. S. Ginger, *Science (80-.).* **2015**, *348*, 683.

[125] T. S. Sherkar, C. Momblona, M. Sessolo, H. J. Bolink, L. Jan Anton Koster, **2017**, *2*, 21.

[126] Y. Zong, Y. Zhou, Y. Zhang, Z. Li, L. Zhang, M. G. Ju, M. Chen, S. Pang, X. C. Zeng, N. P. Padture, *Chem* **2018**, *4*, 1404.

[127] Z. Wang, Z. Shi, T. Li, Y. Chen, W. Huang, *Angew. Chemie - Int. Ed.* **2017**, *56*, 1190.

[128] M. I. Saidaminov, J. Kim, A. Jain, R. Quintero-Bermudez, H. Tan, G. Long, F. Tan, A. Johnston, Y. Zhao, O. Voznyy, E. H. Sargent, *Nat. Energy* **2018**, *3*, 648.

[129] G. Grancini, C. Roldán-Carmona, I. Zimmermann, E. Mosconi, X. Lee, D. Martineau, S. Narbey, F. Oswald, F. De Angelis, M. Graetzel, M. K. Nazeeruddin, *Nat. Commun.* **2017**, *8*, 15684.

[130] P. Wang, X. Zhang, Y. Zhou, Q. Jiang, Q. Ye, Z. Chu, X. Li, X. Yang, Z. Yin, J. You, *Nat. Commun.* **2018**, *9*, 2225.

[131] W. Zhou, Y. Zhao, X. Zhou, R. Fu, Q. Li, Y. Zhao, K. Liu, D. Yu, Q. Zhao, *J. Phys. Chem. Lett.* **2017**, *8*, 4122.

[132] Z. Wang, Q. Lin, F. P. Chmiel, N. Sakai, L. M. Herz, H. J. Snaith, *Nat. Energy* **2017**, *2*, 17135.

[133] G. Niu, X. Guo, L. Wang, *J. Mater. Chem. A* **2015**, *3*, 8970.

[134] A. Mei, X. Li, L. Liu, Z. Ku, T. Liu, Y. Rong, M. M. Xu, M. Hu, J. Chen, Y. Yang, M.

Grätzel, H. Han, M. Gratzel, H. Han, M. Grätzel, H. Han, *Science* **2014**, *345*, 295.

[135] P. Qin, S. Tanaka, S. Ito, N. Tetreault, K. Manabe, H. Nishino, M. K. Nazeeruddin, M. Grätzel, *Nat. Commun.* **2014**, *5*, 3834.

[136] Y. Hou, X. Du, S. Scheiner, D. P. McMeekin, Z. Wang, N. Li, M. S. Killian, H. Chen, M. Richter, I. Levchuk, N. Schrenker, E. Spiecker, T. Stubhan, N. A. Luechinger, A. Hirsch, P. Schmuki, H. P. Steinrück, R. H. Fink, M. Halik, H. J. Snaith, C. J. Brabec, *Science (80-.).* **2017**, *358*, 1192.

[137] S. Chatterjee, A. J. Pal, *J. Phys. Chem. C* **2016**, *120*, 1428.

[138] Z.-K. Yu, W.-F. Fu, W.-Q. Liu, Z.-Q. Zhang, Y.-J. Liu, J.-L. Yan, T. Ye, W.-T. Yang, H.-Y. Li, H.-Z. Chen, *Chinese Chem. Lett.* **2017**, *28*, 13.

[139] S. Weber, T. Rath, J. Mangalam, B. Kunert, A. M. Coclite, M. Bauch, T. Dimopoulos, G. Trimmel, *J. Mater. Sci. Mater. Electron.* **2018**, *29*, 1847.

[140] Q. Tai, P. You, H. Sang, Z. Liu, C. Hu, H. L. W. W. Chan, F. Yan, *Nat. Commun.* **2016**, *7*, 11105.

[141] I. M. Asuo, D. Gedamu, N. Y. Doumon, I. Ka, A. Pignolet, S. G. Cloutier, R. Nechache, *Mater. Adv.* **2020**, *1*, 1866.

[142] A. M. Ganose, C. N. Savory, D. O. Scanlon, *J. Phys. Chem. Lett.* **2015**, *6*, 4594.

[143] Y.-H. Chiang, M.-H. Li, H.-M. Cheng, P.-S. Shen, P. Chen, *ACS Appl. Mater. Interfaces* **2017**, *9*, 2403.

[144] W. Ke, C. Xiao, C. Wang, B. Saparov, H.-S. S. Duan, D. Zhao, Z. Xiao, P. Schulz, S. P. Harvey, W. Liao, W. Meng, Y. Yu, A. J. Cimaroli, C.-S. S. Jiang, K. Zhu, M. Al-Jassim, G. Fang, D. B. Mitzi, Y. Yan, *Adv. Mater.* **2016**, *28*, 5214.

[145] Y. Yu, C. Wang, C. R. Grice, N. Shrestha, D. Zhao, W. Liao, L. Guan, R. A. Awni, W. Meng, A. J. Cimaroli, K. Zhu, R. J. Ellingson, Y. Yan, *ACS Energy Lett.* **2017**, *2*, 1177.

[146] V. Gonzalez-Pedro, E. J. Juarez-Perez, W. S. Arsyad, E. M. Barea, F. Fabregat-Santiago, I. Mora-Sero, J. Bisquert, *Nano Lett.* **2014**, *14*, 888.

[147] Y. Zhao, H. Zhang, X. Ren, H. L. Zhu, Z. Huang, F. Ye, D. Ouyang, K. W. Cheah, A. K. Y. Jen, W. C. H. Choy, *ACS Energy Lett.* **2018**, *3*, 2891.

[148] D. Y. Son, J. W. Lee, Y. J. Choi, I. H. Jang, S. Lee, P. J. Yoo, H. Shin, N. Ahn, M. Choi, D. Kim, N. G. Park, *Nat. Energy* **2016**, *1*, DOI 10.1038/nenergy.2016.81.

[149] H. Tan, A. Jain, O. Voznyy, X. Lan, F. P. G. De Arquer, J. Z. Fan, R. Quintero-Bermudez, M. Yuan, B. Zhang, Y. Y. Zhao, F. Fan, P. Li, L. N. Quan, Y. Y. Zhao, Z. H. Lu, Z. Yang, S. Hoogland, E. H. Sargent, *Science (80-.).* **2017**, *355*, 722.

[150] Z. Xu, J. Wu, T. Wu, Q. Bao, X. He, Z. Lan, J. Lin, M. Huang, Y. Huang, L. Fan, *Energy Technol.* **2017**, *5*, 1820.

[151] P. Qin, S. Tanaka, S. Ito, N. Tetreault, K. Manabe, H. Nishino, M. K. Nazeeruddin, M. Grätzel, Y.-J. Jeon, S. S.-H. Lee, R. Kang, J.-E. Kim, J.-S. Yeo, S. S.-H. Lee, S.-S. Kim, J.-M. Yun, D.-Y. Kim, *Nat. Commun.* **2014**, *5*, 3834.

[152] G. Xing, N. Mathews, S. Sun, S. S. Lim, Y. M. Lam, M. Graẗzel, S. Mhaisalkar, T. C. Sum, *Science (80-.).* **2013**, *342*, 344.

[153] M. Xiao, F. Huang, W. Huang, Y. Dkhissi, Y. Zhu, J. Etheridge, A. Gray-Weale, U. Bach, Y. B. Cheng, L. Spiccia, *Angew. Chemie - Int. Ed.* **2014**, *53*, 9898.

[154] Y. Zhao, K. Zhu, *J. Phys. Chem. Lett.* **2013**, *4*, 2880−2884.

[155] G. Xing, N. Mathews, S. Sun, S. S. Lim, Y. M. Lam, M. Gratzel, S. Mhaisalkar, T. C. Sum, *Science (80-.).* **2013**, *342*, 344.

[156] A. Kumar, D. Nanda, in *Superhydrophobic Polym. Coatings*, Elsevier, **2019**, pp. 43–75.

[157] J. X. J. Zhang, K. Hoshino, in *Mol. Sensors Nanodevices*, Elsevier, **2019**, pp. 43–111.

[158] J. Burschka, N. Pellet, S.-J. Moon, R. Humphry-Baker, P. Gao, M. K. Nazeeruddin, M. Grätzel, *Nature* **2013**, *499*, 316.

[159] "X-ray Powder Diffraction (XRD)," can be found under https://serc.carleton.edu/research_education/geochemsheets/techniques/XRD.html.

[160] Y. Sun, Y. Wu, X. Fang, L. Xu, Z. Ma, Y. Lu, W.-H. Zhang, Q. Yu, N. Yuan, J. Ding, H.

L. Wang, A. D. Mohite, *J. Mater. Chem. A* **2017**, *5*, 1374.

[161] J. Z. Zhang, *Optical Properties and Spectroscopy of Nanomaterials*, World Scientific Publishing Co., **2009**.

[162] *Ultra-High Resolution Scanning Electron Microscope*.

[163] "JEM-2100 Electron Microscope | Products | JEOL Ltd.," can be found under https://www.jeol.co.jp/en/products/detail/JEM-2100.html.

[164] N. Y. Doumon, The Degradation of Organic Solar Cells: From Chemistry to Device Physics through Materials, University of Groningen, **2019**.

[165] S. Luo, W. A. Daoud, *J. Mater. Chem. A* **2015**, *3*, 8992.

[166] X. Hu, X. Zhang, L. Liang, J. Bao, S. Li, W. Yang, Y. Xie, *Adv. Funct. Mater.* **2014**, *24*, 7373.

[167] R. Dong, Y. Fang, J. Chae, J. Dai, Z. Xiao, Q. Dong, Y. Yuan, A. Centrone, X. C. Zeng, J. Huang, *Adv. Mater.* **2015**, *27*, 1912.

[168] D. Liu, T. L. Kelly, *Nat. Photonics* **2014**, *8*, 133.

[169] G. Grancini, S. Marras, M. Prato, C. Giannini, C. Quarti, F. De Angelis, M. De Bastiani, G. E. Eperon, H. J. Snaith, L. Manna, A. Petrozza, *J. Phys. Chem. Lett.* **2014**, *5*, 3836.

[170] N. Adhikari, A. Dubey, E. A. Gaml, B. Vaagensmith, K. M. Reza, S. A. A. Mabrouk, S. Gu, J. Zai, X. Qian, Q. Qiao, *Nanoscale* **2016**, *8*, 2693.

[171] D. Bae, A. Palmstrom, K. Roelofs, B. Mei, I. Chorkendorff, S. F. Bent, P. C. K. Vesborg, *ACS Appl. Mater. Interfaces* **2016**, *8*, 14301.

[172] F. Hao, C. C. Stoumpos, Z. Liu, R. P. H. Chang, M. G. Kanatzidis, *J. Am. Chem. Soc.* **2014**, *136*, 16411.

[173] A. Halder, R. Chulliyil, A. S. Subbiah, T. Khan, S. Chattoraj, A. Chowdhury, S. K. Sarkar, *J. Phys. Chem. Lett.* **2015**, *6*, 3483.

[174] C.-H. Chiang, M. K. Nazeeruddin, M. Grä Tzel, C.-G. Wu, *Energy Environ. Sci. Energy Environ. Sci* **2017**, *808*, 808.

[175] X. Gong, M. Li, X.-B. B. Shi, H. Ma, Z.-K. K. Wang, L.-S. S. Liao, *Adv. Funct. Mater.* **2015**, *25*, 6671.

[176] J. You, Y. Yang, Z. Hong, T.-B. Song, L. Meng, Y. Liu, C. Jiang, H. Zhou, W.-H. Chang, G. Li, *Appl. Phys. Lett.* **2014**, *105*, 183902.

[177] C.-G. Wu, C.-H. Chiang, Z.-L. Tseng, M. K. Nazeeruddin, A. Hagfeldt, M. Grätzel, M. K. Nazeeruddin, M. Grätzel, J. Huang, G. Li, Y. Yang, M. Grä, *Energy Environ. Sci.* **2015**, *8*, 2725.

[178] G. Niu, X. Guo, L. Wang, Guangda Niu, Xudong Guo, Liduo Wang, G. Niu, X. Guo, L. Wang, *J. Mater. Chem. A* **2015**, *3*, 8970.

[179] J. M. Kadro, N. Pellet, F. Giordano, A. Ulianov, O. Müntener, J. Maier, M. Grätzel, A. Hagfeldt, O. Mü, J. Maier, M. Grä, A. Hagfeldt, *Energy Environ. Sci.* **2016**, *3172*, 3172.

[180] M. K. Gangishetty, R. W. J. Scott, T. L. Kelly, *Nanoscale* **2016**, *8*, 6300.

[181] J. A. Christians, P. A. Miranda Herrera, P. V. Kamat, *J. Am. Chem. Soc.* **2015**, *137*, 1530.

[182] Z. Zhu, V. G. Hadjiev, Y. Rong, R. Guo, B. Cao, Z. Tang, F. Qin, Y. Li, Y. Wang, F. Hao, S. Venkatesan, W. Li, S. Baldelli, A. M. Guloy, H. Fang, Y. Hu, Y. Yao, Z. Wang, J. Bao, *Chem. Mater.* **2016**, *28*, 7385.

[183] C. Müller, T. Glaser, M. Plogmeyer, M. Sendner, S. Döring, A. A. Bakulin, C. Brzuska, R. Scheer, M. S. Pshenichnikov, W. Kowalsky, A. Pucci, R. Lovrinčić, *Chem. Mater.* **2015**, *27*, 7835.

[184] E. Mosconi, J. M. Azpiroz, F. De Angelis, *Chem. Mater.* **2015**, *27*, 4885.

[185] C. C. Stoumpos, C. D. Malliakas, M. G. Kanatzidis, *Inorg. Chem.* **2013**, *52*, 9019.

[186] P. Scherrer, *Nachrichten von der Gesellschaft der Wissenschaften zu Göttingen, Math. Klasse* **n.d.**, *1918*, 98.

[187] P.-H. Huang, Y.-H. Wang, J.-C. Ke, C.-J. Huang, P.-H. Huang, Y.-H. Wang, J.-C. Ke, C.-J. Huang, *Energies* **2017**, *10*, 599.

[188] Y.-C. Huang, C.-S. Tsao, Y.-J. Cho, K.-C. Chen, K.-M. Chiang, S.-Y. Hsiao, C.-W. Chen,

C.-J. Su, U.-S. Jeng, H.-W. Lin, *Sci. Rep.* **2015**, *5*, 13657.

[189] J. J. Kim, T. Hwang, S. Lee, B. Lee, J. J. Kim, G. S. Jang, S. Nam, B. Park, *Sci. Rep.* **2016**, *6*, 25648.

[190] G.-J. A. H. Wetzelaer, M. Scheepers, A. M. Sempere, C. Momblona, J. Ávila, H. J. Bolink, *Adv. Mater.* **2015**, *27*, 1837.

[191] J. M. Azpiroz, E. Mosconi, J. Bisquert, F. De Angelis, *Energy Environ. Sci.* **2015**, *8*, 2118.

[192] G. Niu, W. Li, F. Meng, L. Wang, H. Dong, Y. Qiu, *J. Mater. Chem. A* **2014**, *2*, 705.

[193] M. Corazza, F. C. Krebs, S. A. Gevorgyan, *Sol. Energy Mater. Sol. Cells* **2014**, *130*, 99.

[194] Y. Chen, B. Li, W. Huang, D. Gao, Z. Liang, *Chem. Commun. Chem. Commun* **2015**, *51*, 11997.

[195] M. Peng, Y. Liu, A. Yu, Y. Zhang, C. Liu, J. Liu, W. Wu, K. Zhang, X. Shi, J. Kou, J. Zhai, Z. Lin Wang, *ACS Nano* **2016**, *10*, 1572.

[196] S. Trilok, Ö. Senol, S. Alexander, F. Robert, M. Sanjay, M. Tsutomu, *Adv. Funct. Mater.* **2018**, *28*, 1706287.

[197] W. Nie, H. Tsai, R. Asadpour, J.-C. Blancon, A. J. Neukirch, G. Gupta, J. J. Crochet, M. Chhowalla, S. Tretiak, M. A. Alam, H.-L. Wang, A. D. Mohite, *Science (80-.).* **2015**, *347*, 522.

[198] N. Tianqi, L. Jing, M. Rahim, L. Jianbo, B. Dounya, Z. Xu, H. Hanlin, Y. Zhou, A. Aram, Z. Kui, L. S. (Frank), *Adv. Mater.* **2018**, *30*, 1706576.

[199] B. Wang, K. Y. Wong, S. Yang, T. Chen, *J. Mater. Chem. A Mater. energy Sustain.* **2016**, *4*, 3806.

[200] Q. Jiang, D. Rebollar, J. Gong, E. L. Piacentino, C. Zheng, T. Xu, *Angew. Chemie Int. Ed.* **2015**, *54*, 7617.

[201] M. K. Kim, T. Jeon, H. Il Park, J. M. Lee, S. A. Nam, S. O. Kim, *CrystEngComm* **2016**, *18*, 6090.

[202] Y. Zhou, O. S. Game, S. Pang, N. P. Padture, *J. Phys. Chem. Lett.* **2015**, *6*, 4827.

[203] N. Liu, Q. Du, G. Yin, P. Liu, L. Li, H. Xie, C. Zhu, Y. Li, H. Zhou, W.-B. Zhang, Q. Chen, *J. Mater. Chem. A* **2018**, *6*, 6806.

[204] T. J. Jacobsson, J. P. Correa-Baena, E. Halvani Anaraki, B. Philippe, S. D. Stranks, M. E. F. Bouduban, W. Tress, K. Schenk, J. Teuscher, J. E. Moser, H. Rensmo, A. Hagfeldt, *J. Am. Chem. Soc.* **2016**, *138*, 10331.

[205] Y. Shao, Y. Fang, T. Li, Q. Wang, Q. Dong, Y. Deng, Y. Yuan, H. Wei, M. Wang, A. Gruverman, J. Shield, J. Huang, *Energy Environ. Sci.* **2016**, *9*, 1752.

[206] C. Li, S. Tscheuschner, F. Paulus, P. E. Hopkinson, J. Kießling, A. Köhler, Y. Vaynzof, S. Huettner, *Adv. Mater.* **2016**, *28*, 2446.

[207] J. M. Frost, K. T. Butler, F. Brivio, C. H. Hendon, M. van Schilfgaarde, A. Walsh, *Nano Lett.* **2014**, *14*, 2584.

[208] B. Chen, M. Yang, S. Priya, K. Zhu, *J. Phys. Chem. Lett.* **2016**, *7*, 905.

[209] B. Chen, M. Yang, X. Zheng, C. Wu, W. Li, Y. Yan, J. Bisquert, G. Garcia-Belmonte, K. Zhu, S. Priya, *J. Phys. Chem. Lett.* **2015**, *6*, 4693.

[210] O. Almora, C. Aranda, I. Zarazua, A. Guerrero, G. Garcia-Belmonte, *ACS Energy Lett.* **2016**, *1*, 209.

[211] H.-S. Kim, N.-G. Park, *J. Phys. Chem. Lett.* **2014**, *5*, 2927.

[212] Z. Liang, S. Zhang, X. Xu, N. Wang, J. Wang, X. Wang, Z. Bi, G. Xu, N. Yuan, J. Ding, *RSC Adv.* **2015**, *5*, 60562.

[213] F. Giordano, A. Abate, J. P. Correa Baena, M. Saliba, T. Matsui, S. H. Im, S. M. Zakeeruddin, M. K. Nazeeruddin, A. Hagfeldt, M. Graetzel, *Nat. Commun.* **2016**, *7*, 10379.

[214] E. Zimmermann, P. Ehrenreich, T. Pfadler, J. A. Dorman, J. Weickert, L. Schmidt-Mende, *Nat. Photonics* **2014**, *8*, 669.

[215] A. Nakane, H. Tampo, M. Tamakoshi, S. Fujimoto, K. M. Kim, S. Kim, H. Shibata, S. Niki, H. Fujiwara, *J. Appl. Phys.* **2016**, *120*, 064505.

[216] D. Bi, W. Tress, M. I. Dar, P. Gao, J. Luo, C. Renevier, K. Schenk, A. Abate, F. Giordano, J.-P. Correa Baena, J.-D. Decoppet, S. M. Zakeeruddin, M. K. Nazeeruddin, M. Grätzel, A. Hagfeldt, *Sci. Adv.* **2016**, *2*, e1501170.

[217] R. Long, J. Liu, O. V. Prezhdo, *J. Am. Chem. Soc.* **2016**, *138*, 3884.

[218] Z. Wang, D. P. McMeekin, N. Sakai, S. van Reenen, K. Wojciechowski, J. B. Patel, M. B. Johnston, H. J. Snaith, *Adv. Mater.* **2017**, *29*, 1604186.

[219] X. Du, T. Heumueller, W. Gruber, A. Classen, T. Unruh, N. Li, C. J. Brabec, *Joule* **2019**, *3*, 215.

[220] J. A. Röhr, X. Shi, S. A. Haque, T. Kirchartz, J. Nelson, *Phys. Rev. Appl.* **2018**, *9*, 044017.

[221] R. H. Bube, *J. Appl. Phys.* **1962**, *33*, 1733.

[222] K. Poorkazem, T. L. Kelly, *Sustain. Energy Fuels* **2018**, *2*, 1332.

[223] P. N. Murgatroyd, *J. Phys. D. Appl. Phys.* **1970**, *3*, 308.

[224] C. Chiang, C. Wu, *Nat. Photonics* **2016**, *10*, 196.

[225] W. Zhou, P. Zhou, X. Lei, Z. Fang, M. Zhang, Q. Liu, T. Chen, H. Zeng, L. Ding, J. Zhu, S. Dai, S. Yang, *ACS Appl. Mater. Interfaces* **2018**, *10*, 1897.

[226] N. Y. Doumon, F. V. Houard, J. Dong, H. Yao, G. Portale, J. Hou, L. J. A. Koster, *Org. Electron.* **2019**, *69*, 255.

[227] N. Y. Doumon, M. V Dryzhov, F. V Houard, V. M. Le Corre, A. Rahimi Chatri, P. Christodoulis, L. J. A. Koster, *ACS Appl. Mater. Interfaces* **2019**, *11*, 8310.

[228] D. Bartesaghi, I. D. C. Pérez, J. Kniepert, S. Roland, M. Turbiez, D. Neher, L. J. A. Koster, *Nat. Commun.* **2015**, *6*, 7083.

[229] G. Konstantatos, E. H. Sargent, *Nanostructured Materials for Photon Detection*, Nature Publishing Group, **2010**.

[230] F. Akhtar, J. Dabrowski, M. Lisker, Y. Yamamoto, A. Mai, C. Wenger, M. Lukosius, *ACS Appl. Mater. Interfaces* **2020**, *12*, 3188.

[231] S. Pal, S. Mukherjee, M. Nand, H. Srivastava, C. Mukherjee, S. N. Jha, S. K. Ray, *Appl. Surf. Sci.* **2020**, *502*, 144196.

[232] Y. Liu, F. Wang, X. X. X. Wang, X. X. X. Wang, E. Flahaut, X. Liu, Y. Li, X. X. X. Wang, Y. Xu, Y. Shi, R. Zhang, *Nat. Commun. 2015 61* **2015**, *6*, 1.

[233] S. A. McDonald, G. Konstantatos, S. Zhang, P. W. Cyr, E. J. D. Klem, L. Levina, E. H. Sargent, *Nat. Mater. 2005 42* **2005**, *4*, 138.

[234] C. Livache, B. Martinez, N. Goubet, C. Gréboval, J. Qu, A. Chu, S. Royer, S. Ithurria, M. G. Silly, B. Dubertret, E. Lhuillier, *Nat. Commun. 2019 101* **2019**, *10*, 1.

[235] T. An, Y. Wang, J. Xue, *Opt. Quantum Electron. 2019 521* **2019**, *52*, 1.

[236] J. D. Yao, Z. Q. Zheng, G. W. Yang, *Prog. Mater. Sci.* **2019**, *106*, 100573.

[237] I. Ka, V. Le Borgne, K. Fujisawa, T. Hayashi, Y. A. Kim, M. Endo, D. Ma, M. A. El Khakani, *Sci. Rep.* **2016**, *6*, 20083.

[238] Q. Hu, H. Wu, J. Sun, D. Yan, Y. Gao, J. Yang, *Nanoscale* **2016**, *8*, 5350.

[239] S. D. Stranks, G. E. Eperon, G. Grancini, C. Menelaou, M. J. P. Alcocer, T. Leijtens, L. M. Herz, A. Petrozza, H. J. Snaith, **2013**, *342*, 341.

[240] F. Hao, C. C. Stoumpos, D. H. Cao, R. P. H. Chang, M. G. Kanatzidis, *Nat. Photonics* **2014**, *8*, 489.

[241] F. P. García De Arquer, A. Armin, P. Meredith, E. H. Sargent, *Nat. Rev. Mater.* **2017**, *2*, DOI 10.1038/natrevmats.2016.100.

[242] M. Hu, C. Bi, Y. Yuan, Z. Xiao, Q. Dong, Y. Shao, J. Huang, *Small* **2015**, *11*, 2164.

[243] W. Zheng, R. Lin, Z. Zhang, Q. Liao, J. Liu, F. Huang, *Nanoscale* **2017**, *9*, 12718.

[244] T. Vinh Quang Dang, Gill-Sang Han, N.-E. L. Quang Trung, Le Thai Duy, Young-Un Jin, Byeong-Ung Hwang, Hyun-Suk Jung, *Carbon N. Y.* **2016**, *105*, 353.

[245] P. Zhu, S. Gu, X. Shen, N. Xu, Y. Tan, S. Zhuang, Y. Deng, Z. Lu, Z. Wang, J. Zhu, *Nano Lett.* **2016**, *16*, 871.

[246] X. Luo, F. Zhao, L. Du, W. Lv, K. Xu, Y. Peng, Y. Wang, F. Lu, *npj Flex. Electron.* **2017**, *1*, 6.

[247] H. Sun, T. Lei, W. Tian, F. Cao, J. Xiong, L. Li, *Small* **2017**, *13*, 1701042.

[248] H. Sun, W. Tian, F. Cao, J. Xiong, L. Li, *Adv. Mater.* **2018**, *30*, 1706986.

[249] J. Im, J. Luo, M. Franckevičius, N. Pellet, P. Gao, T. Moehl, S. M. Zakeeruddin, M. K. Nazeeruddin, M. Grätzel, N. Park, *Nano Lett.* **2015**, *15*, 2120.

[250] M. Xiao, F. Huang, W. Huang, Y. Dkhissi, Y. Zhu, J. Etheridge, A. Gray-Weale, U. Bach, Y. B. Cheng, L. Spiccia, *Angew. Chemie - Int. Ed.* **2014**, *53*, 9898.

[251] J. Yu, H. Wen, M. Shafiei, M. R. Field, Z. F. Liu, W. Wlodarski, N. Motta, Y. X. Li, K. Kalantar-zadeh, P. T. Lai, *Sensors Actuators B* **2013**, *184*, 118.

[252] Y. Chen, S. Yang, X. Chen, Y. C. Zheng, Y. Hou, Y. H. Li, H. D. Zeng, H. G. Yang, *J. Mater. Chem. A* **2015**, *3*, 15854.

[253] G. Konstantatos, I. Howard, A. Fischer, S. Hoogland, J. Clifford, E. Klem, L. Levina, E. H. Sargent, *Nature* **2006**, *442*, 180.

[254] G. Konstantatos, L. Levina, A. Fischer, E. H. Sargent, *Nano Lett.* **2008**, *8*, 1446.

[255] C. HY, L. MK, Y. G, M. HG, Y. Y, *Nat. Nanotechnol.* **2008**, *3*, 543.

[256] G. Tong, X. Geng, Y. Yu, L. Yu, J. Xu, Y. Jiang, Y. Sheng, Y. Shi, K. Chen, *RSC Adv.* **2017**, *7*, 18224.

[257] D. Wei, Z. Xiujuan, H. Liming, X. Xiuzhen, W. Liang, W. Jincheng, S. Qixun, L. Shuit-Tong, J. Jiansheng, *Adv. Mater.* **2016**, *28*, 2201.

[258] L. Feng-Xia, W. Jiu-Zhen, Z. Zhi-Xiang, W. You-Yi, G. Yang, L. Lin-Bao, *Adv. Opt. Mater.* **2017**, *5*, 1700654.

[259] H. Deng, D. Dong, K. Qiao, L. Bu, B. Li, D. Yang, H.-E. Wang, Y. Cheng, Z. Zhao, J. Tang, H. Song, *Nanoscale* **2015**, *7*, 4163.

[260] H. Deng, X. Yang, D. Dong, B. Li, D. Yang, S. Yuan, K. Qiao, Y.-B. B. Cheng, J. Tang, H. Song, *Nano Lett.* **2015**, *15*, 7963.

[261] Q. Wang, Q. Dong, T. Li, A. Gruverman, J. Huang, *Adv. Mater.* **2016**, *28*, 6734.

[262] B. Yang, O. Dyck, J. Poplawsky, J. Keum, A. Puretzky, S. Das, I. Ivanov, C. Rouleau, G. Duscher, D. Geohegan, K. Xiao, *J. Am. Chem. Soc.* **2015**, *137*, 9210.

[263] D. Shi, V. Adinolfi, R. Comin, M. Yuan, E. Alarousu, A. Buin, Y. Chen, S. Hoogland, A. Rothenberger, K. Katsiev, Y. Losovyj, X. Zhang, P. A. Dowben, O. F. Mohammed, E. H. Sargent, O. M. Bakr, *Science (80-.).* **2015**, *347*, 519.

[264] T. S. Sherkar, C. Momblona, M. Sessolo, H. J. Bolink, L. Jan Anton Koster, L. Gil-Escrig, J. Ávila, M. Sessolo, H. J. Bolink, L. J. A. Koster, *ACS Energy Lett.* **2017**, *2*, 21.

[265] A. Rose, *Phys. Rev.* **1955**, *97*, 1538.

[266] Z. Liu, J. Hu, H. Jiao, L. Li, G. Zheng, Y. Chen, Y. Huang, Q. Zhang, C. Shen, Q. Chen, H. Zhou, *Adv. Mater.* **2017**, *29*, 1606774.

[267] J. Chen, J. Xu, S. Zhang, S. Zhou, K. Zhou, B. Zhang, X. Xia, Y. Liu, S. Dai, J. Yao, *J. Phys. Chem. C* **2017**, *7*, 44.

[268] X. Wen, J. Wu, M. Ye, D. Gao, C. Lin, *Chem. Commun.* **2016**, *52*, 11355.

[269] F. Wang, A. Shimazaki, F. Yang, K. Kanahashi, K. Matsuki, Y. Miyauchi, T. Takenobu, A. Wakamiya, Y. Murata, K. Matsuda, *J. Phys. Chem. C* **2017**, *121*, 1562.

[270] Z. Lian, Q. Yan, Q. Lv, Y. Wang, L. Liu, L. Zhang, S. Pan, Q. Li, L. Wang, J.-L. Sun, *Sci. Rep.* **2015**, *5*, 16563.

[271] J. Li, Y. Shen, Y. Liu, F. Shi, X. Ren, T. Niu, K. Zhao, S. (Frank) Liu, *ACS Appl. Mater. Interfaces* **2017**, *9*, 19176.

[272] L. J. A. Koster, S. E. Shaheen, J. C. Hummelen, *Adv. Energy Mater.* **2012**, *2*, 1246.

[273] I. M. Asuo, S. Bouzidi, I. Ka, F. Rosei, A. Pignolet, R. Nechache, S. G. Cloutier, *Energy Technol.* **2021**, *9*, DOI 10.1002/ente.202000791.

[274] A. H. Slavney, T. Hu, A. M. Lindenberg, H. I. Karunadasa, *J. Am. Chem. Soc.* **2016**, *138*, 2138.

[275] M. Pazoki, M. B. Johansson, H. Zhu, P. Broqvist, T. Edvinsson, G. Boschloo, E. M. J.

Johansson, *J. Phys. Chem. C* **2016**, *120*, 29039.

[276] R. L. Z. Hoye, R. E. Brandt, A. Osherov, V. Stevanovic, S. D. Stranks, M. W. B. Wilson, H. Kim, A. J. Akey, J. D. Perkins, R. C. Kurchin, J. R. Poindexter, E. N. Wang, M. G. Bawendi, V. Bulovic, T. Buonassisi, *Chem. - A Eur. J.* **2016**, *22*, 2605.

[277] B. W. Park, B. Philippe, X. Zhang, H. Rensmo, G. Boschloo, E. M. J. Johansson, *Adv. Mater.* **2015**, *27*, 6806.

[278] S. F. Hoefler, G. Trimmel, T. Rath, *Monatshefte fur Chemie* **2017**, *148*, 795.

[279] F. Bai, Y. Hu, Y. Hu, T. Qiu, X. Miao, S. Zhang, *Sol. Energy Mater. Sol. Cells* **2018**, *184*, 15.

APPENDIX I

Supporting Information for Chapter 3

Table A3.1 SEM-EDS analysis for $CH_3NH_3PbI_{3-x}(SCN)_x$ film.

Normalized Stoichiometric concentration [%]			
Spot location	**Sulfur (S)**	**Iodine (I)**	**Lead (Pb)**
1	4.44	70.74	24.82
2	4.96	68.92	26.12
3	4.75	70.99	24.26
4	4.65	70.40	24.94
Mean	**4.70**	**70.26**	**25.04**
SigmaMean	0.11	0.46	0.39

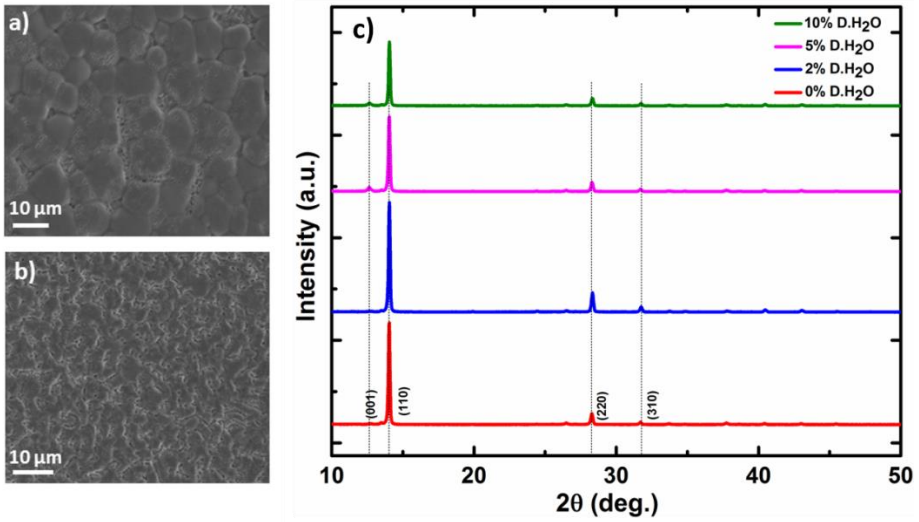

Figure A3.1: SEM images and XRD spectra of the deposited perovskite on FTO substrate. a) $CH_3NH_3PbI_{3-x}(SCN)_x$ + 5 vol% H_2O, b) $CH_3NH_3PbI_{3-x}(SCN)_x$ +10 vol% H_2O (c) Shows the XRD spectra for all the samples prepared with and without water additive.

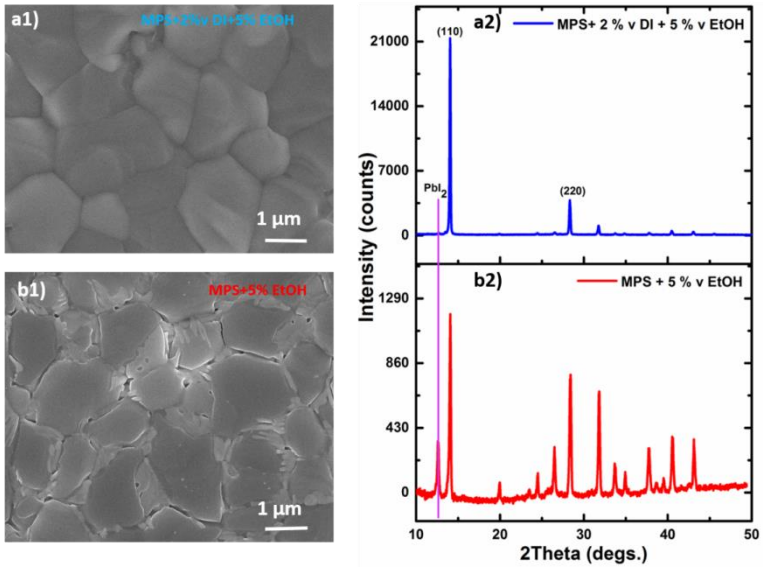

Figure A3.2: Effect of water and ethanol on the microstructure of $CH_3NH_3PbI_{3-x}(SCN)_x$ films. a1) XRD pattern of MPS +2 vol % H_2O+5 vol % EtOH film. a2) SEM micrograph of MPS+2 vol % H_2O +5 vol % EtOH film. b1) XRD pattern of MPS+5 vol % EtOH film. b2) SEM micrograph of MPS+5 vol% EtOH film. The perovskite films were processed under the same ambient conditions.

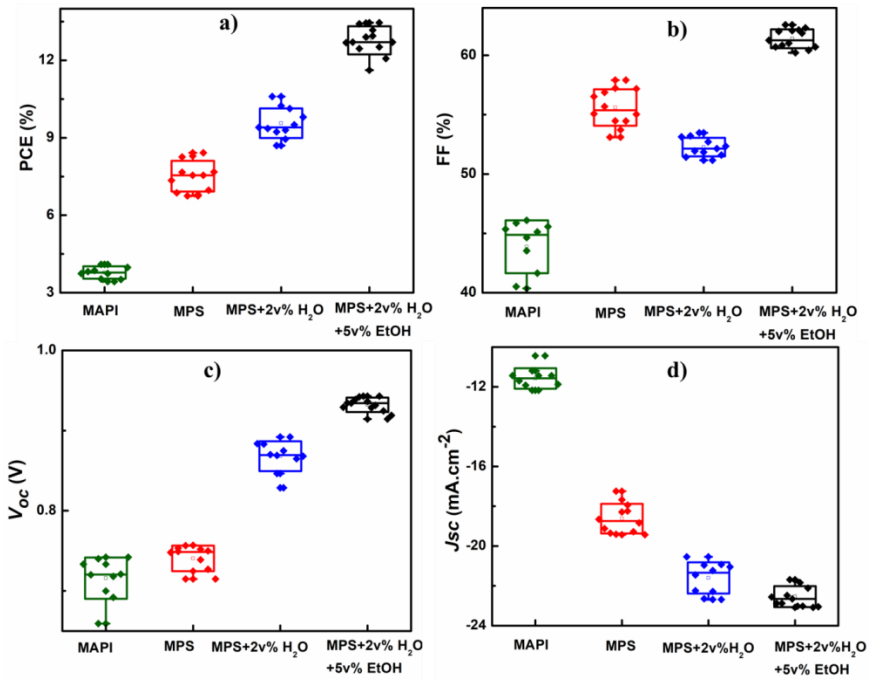

Figure A3.3 The statistical distribution graphs for the *J-V* parameters for each device fabrication under the same ambient conditions.

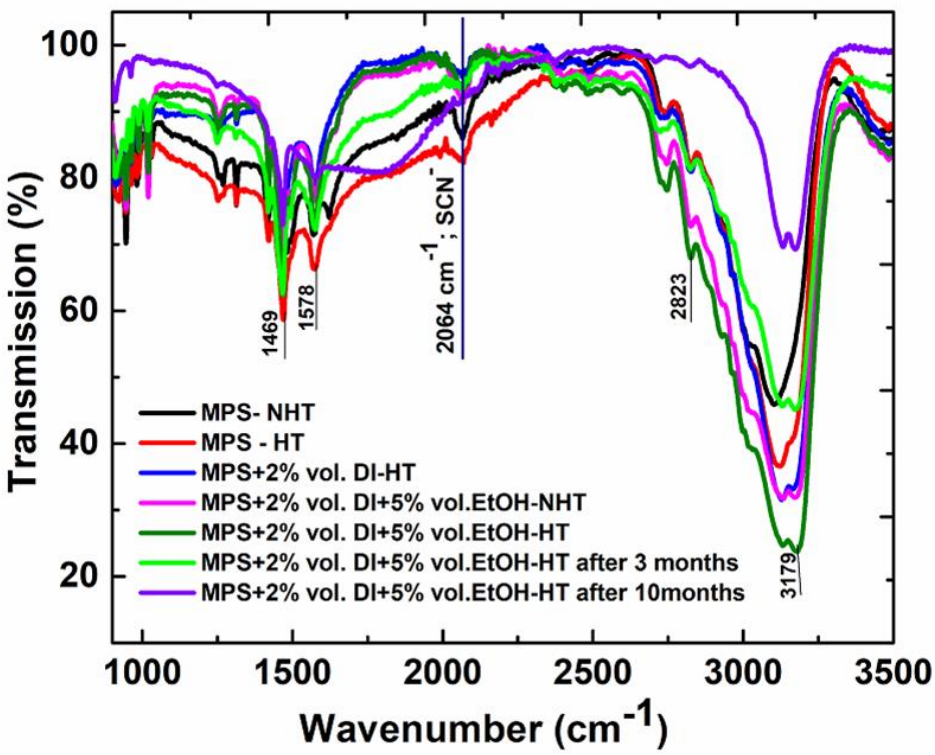

Figure A3.4 The FTIR spectra for $CH_3NH_3PbI_{3-x}(SCN)_x$ (MPS) films with and without water and ethanol additives. Some of the thin films were measured before annealing and after annealing to confirm the presence of SCN-ions. After complete annealing, the films were measure periodically, fresh state, at 3 months and 10 months respectively.

Supporting Information for Chapter 4

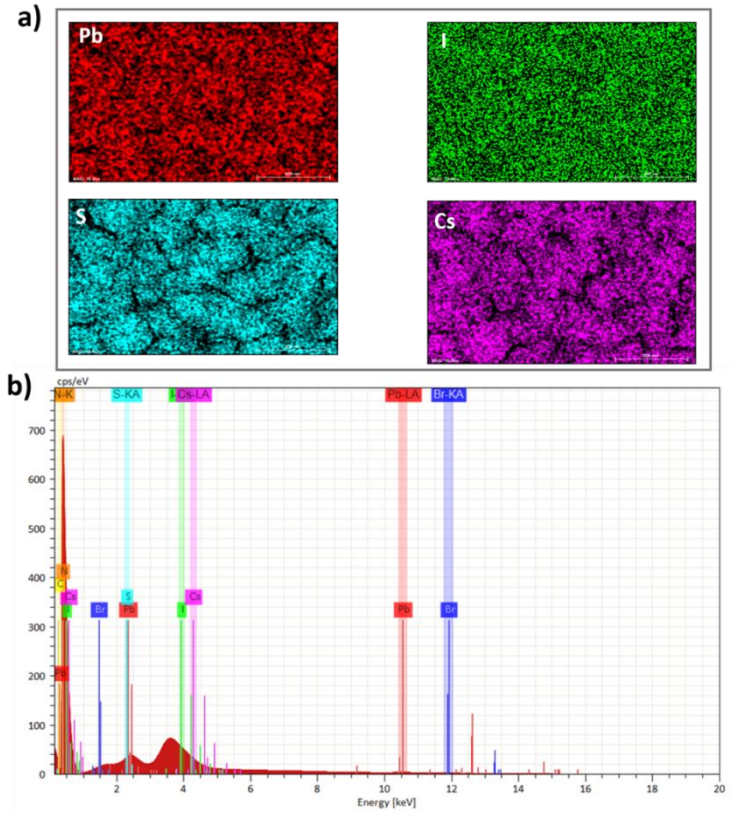

Figure A4.1 a) EDS mapping images of DEV-5.8 perovskite films for Pb, I, S, and Cs, respectively. b) The corresponding EDS spectra, indicating all the chemical composition in the perovskite film.

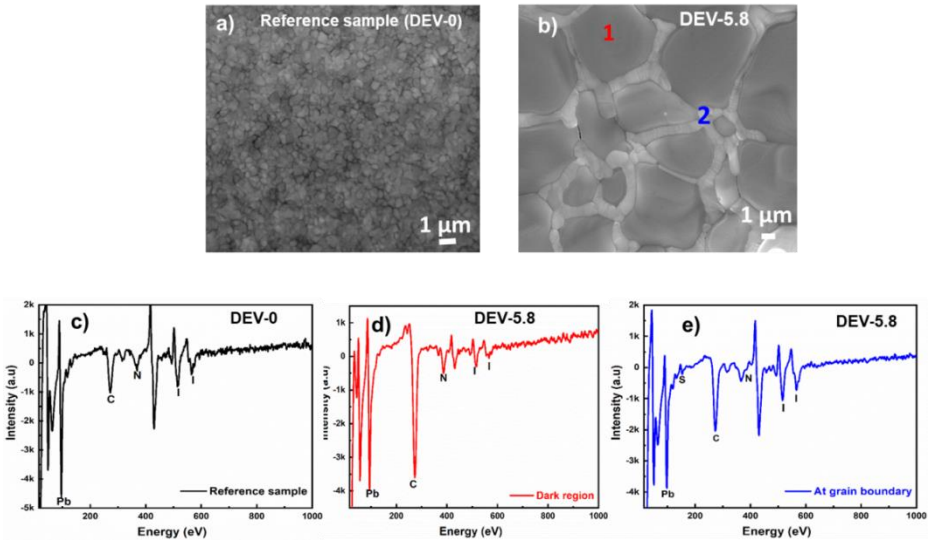

Figure A4.2: SEM images of the morphology of the perovskite films for a) DEV-0 and b) DEV-5.8 showing dark grains regions (1) and bright regions at the grain boundaries (2). (c) Auger spectra for the reference sample, DEV-0 (d) Auger spectra for a dark region (1 in Fig. A4.2b) on DEV-5.8, and (e) Auger spectra for a bright region (2 in Fig. A4.2b) (grain boundary) of DEV-5.8 perovskite film.

Supporting Information for Chapter 5

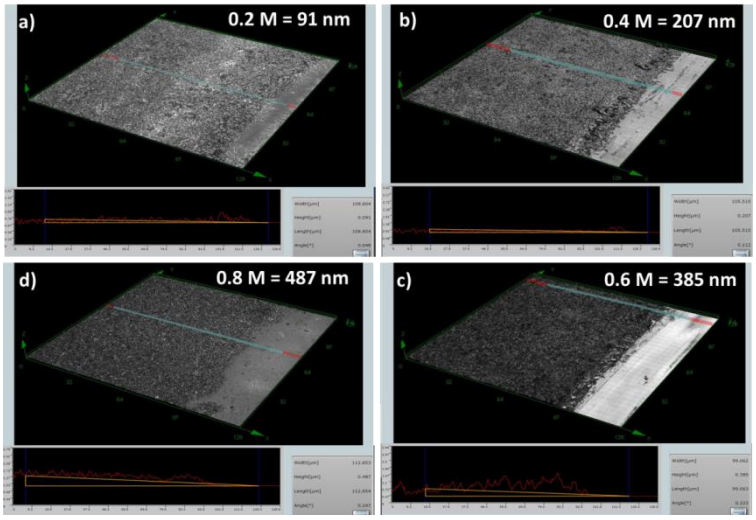

Figure A5.1 Optical image of the perovskite nanowires made with different PbI_2 molarity (0.2- 0.8 M) taken with an Olympus LEXT OLS4100 laser scanning digital microscope. The thicknesses are estimated from the 3D images and measurements of surface profile.

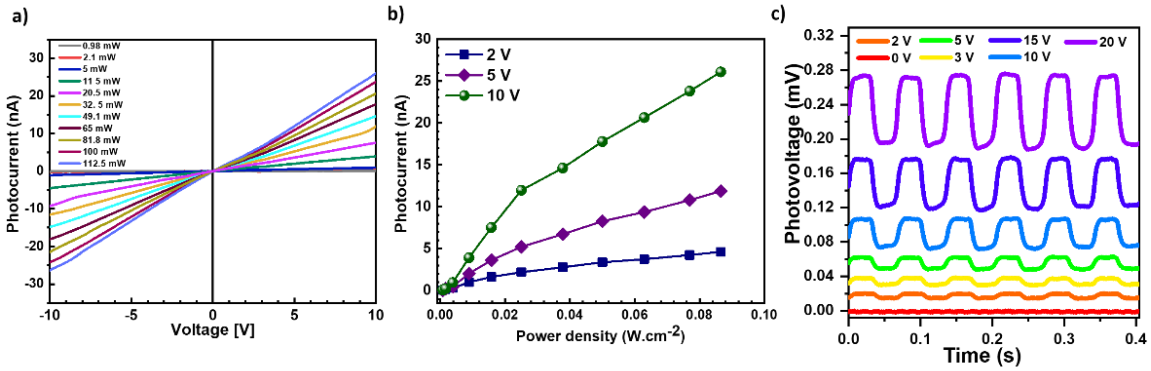

Figure A5.2: a) *I-V* curves of the measured photocurrent as a function of the light power density. b) The photocurrent-power density dependency plot extracted from a). c) *I-T* measured as a function of applied voltage for the photodetectors.

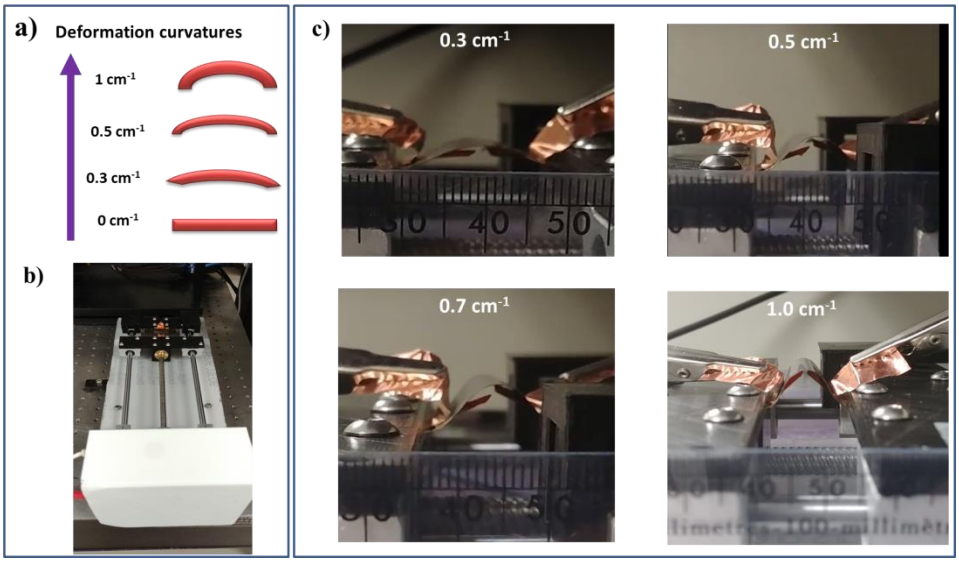

Figure A5.3 (a) Schematics of the deformation curvatures for flexibility test showing the evolution of the bending curvatures (cm^{-1}) from the flat surface. (b) A picture of the setup for the bending tests measurements. (c) Photographs of the devices under different bending curvatures (0.3 to 1 cm^{-1}) of the flexible perovskite photodetectors.

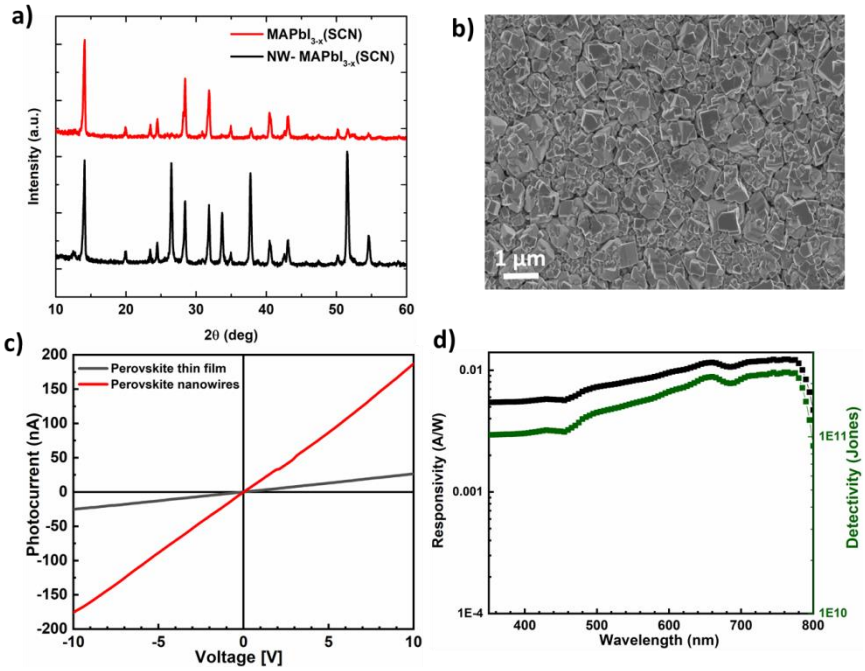

Figure A5.4 a) XRD pattern of $CH_3NH_3PbI_{3-x}(SCN)_x$ perovskite film and nanowires b) SEM image of the $CH_3NH_3PbI_{3-x}(SCN)_x$ film. c) I-V characteristic of the perovskite film and nanowires. d) Spectral responsivity and detectivity of the perovskite film-based photodetectors.

APPENDIX II

All-ambient processed CuSCN as an inexpensive alternative to Spiro-OMeTAD for perovskite-based devices

Ivy M. Asuo[1,2], Soraya Bouzidi[2], Ibrahima Ka[1], Federico Rosei[1], Alain Pignolet[1], Riad Nechache[1] and Sylvain G. Cloutier[2].**

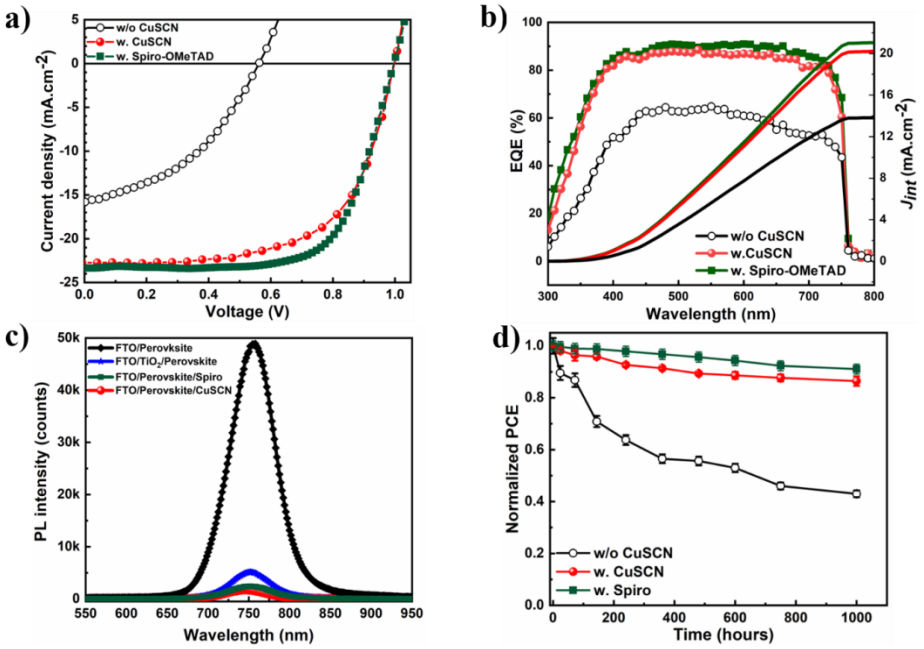

Figure A6.1: Comparison of the optoelectronic characteristics: a) Current density-Voltage *(J-V)* curves; b) EQE spectra and the corresponding calculated integrated current; c) Photoluminescence spectra of the perovskite film deposited on FTO (in black) and then covered by CuSCN HTL (in red) or Spiro-OMeTAD HTL (in green). Also shown is the perovskite layer deposited on the TiO_2 layer (in blue). d) Evolution of PCE value versus time, of the solar cells made with CuSCN HTL (in red), with Spiro-OMeTAD HTL (in green) and without any HTL (in black). Devices are stored under ambient air of relative humidity 45±10% RH for the study of stability.

Cost Estimation for Perovskite Solar Cells with Spiro-OMeTAD and CuSCN Hole Transport Layers

For the commercialization of any optoelectronic technology, three main requirements need to be satisfied: (i) high efficiency, (ii) high stability, and (iii) low cost (**Figure A6.2a**). As shown earlier, the processing of our devices in ambient instead of a glove-box environment helps to reduce the

production cost of the solar cells, while maintaining a satisfactory performance and an acceptable level of stability without encapsulation. Previous works have argued that inorganic HTL materials are cheaper than organic materials[6,10,11], without, however, provided a quantitative estimation of the cost. Hence, we estimated the cost of materials used for a PSC with Spiro-OMeTAD as HTL and compared it to that of a PSC using CuSCN as HTL. In order to provide a cost estimate, the calculations are based on the price of the raw materials as purchased only, the cost of a wafer with several PSCs being estimated from the cost of an individual cell. Since the cost of fabrication of both devices, either with Spiro-OMeTAD or with CuSCN as HTL fabrication, facilities, and utility costs are the same, and since it is the same planar device architecture used for both, the main difference is only in the respective HTL materials and costs such as labor, procurement, utility, and use of facility have not been considered. The summary of the cost of the raw materials used is presented in **Table A6**.

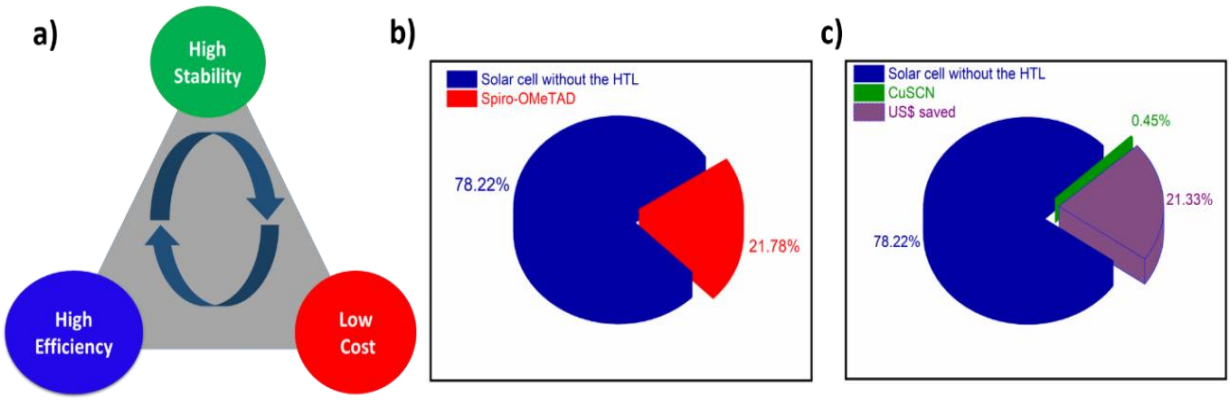

Figure A6.2: a) Requirements for the commercialization of any technology. Material costs breakout (in percentage) for b) a typical Spiro-OMeTAD HTL-based perovskite solar cell, with Spiro-OMeTAD accounting for about 22 % of the total cost (portion in red); and c) a CuSCN HTL-based perovskite solar cell with CuSCN HTL accounting for ~0.5 % of the total cost of a Spiro-OMeTAD -based PSC (in green), demonstrating the cost-effectiveness of CuSCN HTL for PSCs.

The total raw material cost for Spiro-OMeTAD-based PSCs is significantly higher than that of CuSCN-based PSCs. The cost of the raw materials estimated to fabricate Spiro-OMeTAD-based solar cells amounts to 4.994 US$/per substrate (each substrate holding 12 cells, each with an active area 2.5 mm^2), Spiro-OMeTAD constituting ~22 % of the total material cost, as shown in **Figure A6.2b**. If Spiro-OMeTAD is replaced with CuSCN, the substrate holding 12 cells with the same active area costs 3.929 US$/per substrate, with CuSCN accounting for only 0.46 % of the total

material cost of a Spiro-OMeTAD-based solar cell (or 0.59 % of the total material cost of a CuSCN-based solar cell). Thus, using CuSCN as HTL in PSC saves about 1.065 US$/per substrate, or a whopping 21.3 % of the total cost per device. Considering the mass-production of millions of devices/modules, this 1.065 US$/per substrate saving becomes significant.

Table A6: Materials cost for perovskite solar cells.

Replacing Spiro-OMeTAD HTL by CuSCN HTL, while providing a similar performance of the PSCs, saves about 21% of the total cost of the halide perovskite-based solar cell.

Materials	**Cost (US $)***	**Total cost (US $)**	**Percentage (%)**
Glass/FTO substrate	1.553		
TiO_2	0.690		**78.22**
Perovskite	0.840		
Gold	0.823		
Spiro-OMeTAD	1.088	**4. 994**	**21.78**
CuSCN	0.023	**3.929**	**0.46**

* Each price is per FTO substrate (with 12 solar cells) used for the deposition of the thin films.

SOMMAIRE RECAPITULATIF

Pérovskites d'halogénure pour les dispositifs photovoltaïques et optoélectroniques synthétisées et traitées à l'air libre

1. Introduction

L'augmentation de la demande énergétique globale reste l'un des défis majeurs du 21e siècle. L'énergie est nécessaire dans tous les aspects de la vie. Et avec la croissance rapide de la population mondiale, la demande énergétique ne cesse de croître de façon exponentielle. Depuis des siècles, les réserves énergétiques dans lesquelles notre société technologique a puisé sans retenue sont principalement des combustibles fossiles tels que le pétrole, le charbon et le gaz naturel. Selon l'agence internationale de l'énergie (IEA)[1], ces ressources non renouvelables représentent environ 85 % de la consommation énergétique mondiale actuelle.

De plus, la demande énergétique mondiale est toujours à la hausse. Par exemple, en 2018, cette demande a augmenté de 2,3 %.[2] Cette croissance est plus de deux fois supérieure à la croissance annuelle moyenne depuis 2010. Cette croissance effrénée de la demande se traduit par une croissance de 1,7% des émissions de dioxyde de carbone (CO_2) liées à l'énergie par rapport aux émissions de 2017.[2] Outre l'inquiétude grandissante concernant le réchauffement climatique dû aux effets de serre, ces chiffres appellent à une prise de conscience urgente de la gravité et l'urgence du problème et à repenser la production d'énergie et son utilisation responsable, car les activités humaines sont la principale cause de ces effets. Outre une baisse souhaitable de la demande énergétique, obtenue par exemple par des mesures d'économie et de réduction des pertes, il faut aussi réduire la dépendance et l'exploitation des sources énergétiques non renouvelables et adopter des sources d'énergie propres et durables. Par exemple, pendant les quatre premiers mois de la pandémie de COVID-19 en 2020, la demande mondiale d'énergie a chuté en raison de l'immobilisation des populations due au confinement partout dans le monde. Cette baisse de la demande énergétique a entraîné une réduction des émissions mondiales de CO_2. Ainsi, les émissions de CO_2 au premier trimestre de 2020 étaient de plus de 5% inférieures à celles du premier trimestre de 2019 selon les rapports de l'IEA.[3] L'observation la plus surprenante est que les

émissions de CO_2 ont diminué plus que la demande d'énergie au premier trimestre de 2020, entraînant une chute globale projetée de 8% des émissions de CO_2 pour 2020 par rapport à 2019.

Les sources d'énergie renouvelable, y compris l'éolien, le solaire, la géothermie, les biocarburants et l'hydroélectricité, peuvent fournir des ressources propres et durables avec moins d'effets nocifs que les sources d'énergie fossile sur l'environnement. Parmi ces ressources énergétiques renouvelables, l'énergie solaire est l'une des plus recherchées, car la terre reçoit une énorme quantité d'énergie de l'irradiation du soleil, soit environ $1{,}75 \times 10^{17}$ W.[4] Ainsi, si cette énergie pouvait être entièrement collectée, le rayonnement solaire atteignant la surface de la terre toutes les heures serait suffisant pour approvisionner la consommation/demande mondiale d'énergie pendant un an. Récemment, la production mondiale d'énergie à partir du photovoltaïque a augmenté de 31,2 % de 2017 à 2018.[2] Une question se pose: «*L'énergie solaire est-elle alors une solution adaptée à nos problèmes énergétiques et de réchauffement climatique*?» Bien que le rayonnement solaire soit gratuit, il faut être conscient que le coût de fabrication des dispositifs pour convertir cette énergie en électricité ainsi que pour garantir sa distribution est élevé. Une autre difficulté est que le rayonnement solaire est intermittent et n'est donc pas accessible toute la journée. Par conséquent, il est essentiel de développer des systèmes de stockage d'énergie pour ces technologies afin de permettre un approvisionnement d'énergie fiable et équilibrer la production et la demande d'électricité. Heureusement, des avancées récentes ont été enregistrées dans la fabrication de systèmes de stockage pour les ressources énergétiques renouvelables.[5,6] En parallèle, nous devons explorer les moyens de rendre la technologie de l'énergie solaire disponible et accessible à tous.

Étant donné que la consommation mondiale d'énergie augmentera d'environ 50 % d'ici 2050 [7] et que la quête d'un équilibre entre l'offre et la demande est une lutte constante, d'autres sources d'énergie durables et moins chères sont aussi explorées. Les énergies renouvelables hors hydraulique et biomasse traditionnelle – principalement éolienne et solaire – sont restées minoritaire dans la production et la consommation primaire mondiale de l'énergie. Cependant, à cause de sa disponibilité et de sa facilité d'accès presque partout sur la planète, l'attention du monde s'est tournée vers l'énergie solaire pour la production d'électricité pour des utilisations diverses. Les technologies solaires peuvent exploiter l'énergie du soleil pour une gamme d'utilisations, telles que la production d'électricité, le séchage des aliments, l'éclairage et le

chauffage de l'eau à des fins domestiques, commerciales ou industrielles. Les trois principaux moyens d'exploiter l'énergie solaire sont les systèmes solaires thermiques pour le chauffage ou le refroidissement, les concentrateurs solaires et le photovoltaïque (PV). Le PV est apparu sur la scène énergétique avec les cellules solaires au silicium (Si) dans les années 1950 et était principalement utilisé pour alimentation électrique des satellites.[8] Depuis lors, il y a eu des avancés remarquables dans le domaine de la génération d'électricité solaire notamment en raison de la recherche et du développement (R&D) dans la communauté des chercheurs en photovoltaïque. Donc, la recherche de dispositifs collectant l'énergie solaire et la convertissant en électricité de manière efficace, fiable et rentable est d'une grande importance pour l'approvisionnement et l'utilisation mondiale de l'énergie. Cet élan pour les sources d'énergie renouvelables a favorisé l'avènement des cellules solaires et a rendu possible la découverte de semi-conducteurs organiques et inorganiques pour de telles applications.

Les pérovskites d'halogénure organiques-inorganiques (OIHP) de la forme ABX_3 (où A = $CH_3NH_3^+$ (MA^+) ou $NH_2CHNH_2^+$ (FA^+)), B = Pb^{2+}, Sn^{2+} ou Ge^{2+}, et X= I^-, Br^- ou Cl^-) sont récemment apparus comme des systèmes de matériaux prometteurs en raison de leur synthèse simple et peu coûteuse et leur gamme d'applications optoélectroniques. Grâce à leurs excellentes propriétés semi-conductrices et à leur fabrication aisée, les OIHP ont été optimisées et utilisées pour d'autres dispositifs optoélectroniques tels que les photodétecteurs[45-51], les diodes électroluminescentes (LED)[52-58] et les transistors [59-61], en plus d'être utilisé pour les cellules solaires.[40-44]

Malgré leur potentiel d'application élevé, les cellules solaires à pérovskite (PSC) en sont à leurs premiers stades de commercialisation en raison d'un certain nombre de défis. Pour que toute technologie optoélectronique soit commercialisée, trois paramètres critiques doivent être pris en compte à savoir, l'efficacité, le coût et la durée de vie. Les dispositifs basés sur les OIHPs doivent utiliser des techniques de production à haut rendement et à faible coût avec des composants stables. Des progrès énormes ont été réalisés et après quelques années de recherche et de développement, les PSC montrent des valeurs record d'efficacité. En termes d'efficacité, les PSC sont compétitifs avec les cellules photovoltaïques à base de silicium, puisqu'elles ont actuellement une efficacité de 25,5 % pour les cellules solaires à simple jonction et de 29,5 % pour les cellules solaires tandem

Si-pérovskite[11]. Ces efficacités sont maintenant comparables aux valeurs (26,1%) de la technologie bien établie du photovoltaïque au silicium.

Contrairement au silicium, les pérovskites sont solubles dans plusieurs solvants. Elles peuvent donc être facilement pulvérisées ou imprimées sous forme de couches minces sur une surface tout comme les encres ou les peintures. Cela rend potentiellement les PSC moins chères et plus simples à fabriquer sur toutes sortes de substrats rigides et flexibles. Ceci occasionne de nouvelles applications telles que l'utilisation du photovoltaïque à l'intérieur ou intégré à la structure des bâtiments et véhicules, pour l'électronique et l'Internet des objets (IoT), ainsi que pour les panneaux solaires traditionnels.

Néanmoins, la plus grande limitation des PSC est qu'elles n'ont pas une stabilité suffisante à long terme dans les environnements opérationnels. Les changements de température, d'humidité et la portion ultraviolette de l'irradiation solaire provoquent une détérioration des PSC. Les réactions avec l'humidité/l'eau forment des hydrates qui modifient la structure des matériaux pérovskites et affaiblissent leur capacité d'absorption de la lumière. Les premiers rapports de laboratoire ont rapporté une stabilité du dispositif inférieure à 500 heures pour $CH_3NH_3PbI_3$.[41,62] Cependant, récemment, une R&D intensive sur les matériaux pérovskites a permis un progrès remarquable dans la stabilité et l'efficacité des PSC.[63,64] Cette amélioration de la stabilité est attribuée à de nombreux facteurs, tels que le processus de synthèse et le traitement subséquent de la pérovskite, la cristallisation, la modification de la microstructure, les architectures avancées des dispositifs récents, ainsi que les modifications sélectives de la couche de transport de charge. Ici, l'objectif de cette dissertation est de trouver ou établir une méthode de synthèse ***ambiante*** de matériaux de pérovskite aux halogénures organiques-inorganiques pour des applications dans des dispositifs optoélectroniques ayant à la fois de bonnes performances et une bonne stabilité.

2. Etendue de la Dissertation

Cette thèse porte sur l'étude et l'amélioration de la stabilité des matériaux pérovskites d'halogénure pour les dispositifs photovoltaïques et optoélectroniques. Actuellement, les principaux éléments chimiques des composés pérovskites d'halogénure les plus performants sont le plomb (Pb) et l'iode (I). Ces deux matériaux sont abondants et peuvent être traités en solution,

rendant les coûts des matériaux de pérovskite comparativement peu élevés. Ainsi, la technologie PSC est prévue pour être accessible et disponible localement, en particulier dans les zones rurales et isolées. Par conséquent, la technologie PSC doit être moins la moins coûteuse possible, considérant les coûts de production, de distribution d'énergie, de maintenance ainsi que le coût des matériaux eux-mêmes. La synthèse et le traitement de ces matériaux sous conditions ambiantes permettront de réduire considérablement à la foi la complexité et le coût de leur fabrication permettant ainsi une production locale d'électricité proche du site de son utilisation.

Ici, l'objectif principal de cette thèse est d'établir une voie de synthèse à faible coût tout en réalisant une bonne stabilité à long terme des matériaux pérovskites. Le premier défi est la synthèse en solution et par enduction centrifuge ('spin coating') en conditions ambiantes de couches minces de pérovskite à base de plomb de haute qualité. Les effets synergiques des additifs ajoutés aux solvants sur la morphologie, la stabilité et l'efficacité des couches minces de pérovskite ont été étudiés. Le but ici a été de révéler les avantages de l'ajustement de la microstructure des films de pérovskite pour leur utilisation dans diverses applications optoélectroniques, telles que les cellules solaires ou les photodétecteurs.

La stabilité à long terme des matériaux constituant les dispositifs PSC est cruciale pour le bon fonctionnement et le déploiement de la technologie photovoltaïque à pérovskite d'halogénure. Dans ce cadre, la stabilité des dispositifs OIHP dans l'air ambiant a été étudiée. Sous conditions ambiantes, nous examinons de manière critique la dégradation de nos dispositifs à base de pérovskite d'halogénure induite par leur irradiation par des photons. L'idée est de comprendre la cause de la détérioration de la pérovskite d'halogénure dans une cellule solaire et de développer des solutions innovantes pour prévenir ou minimiser ces instabilités.

3. Pérovskites Monocationiques Dopées au Thiocyanate Assistées par l'humidité pour des Cellules Solaires Stables

La plupart des efforts de recherche à ce jour se sont largement concentrés sur l'amélioration de l'efficacité des PSC. Moins de travaux se sont intéressés à la stabilité des dispositifs, surtout dans des conditions ambiantes. Un défi majeur pour la pérovskite d'halogénure est sa nature hygroscopique. La partie organique, l'iodure de méthylammonium (MAI), a tendance à se

décomposer rapidement en présence d'humidité. Ainsi, la fabrication de pérovskite a été longtemps principalement réalisée dans des environnements inertes et secs. Malgré les performances photovoltaïques élevées de ces dispositifs fabriqués dans des conditions bien contrôlées, celles-ci entraînent une augmentation significative de la complexité et du coût de production. Au cours des neuf dernières années, un effort sans précédent a été consacré à la modification de la morphologie et de la microstructure des couches minces de pérovskite pour améliorer leur efficacité dans des conditions contrôlées. Cependant, une technique de fabrication efficace pour synthétiser et contrôler la microstructure de la pérovskite dans les conditions ambiantes n'a pas été suffisamment étudiée[172]. Pourtant, une telle technique robuste et à l'ambiante permettant de maîtriser les processus de cristallisation, et la reproductibilité des couches minces de pérovskite d'halogénure continues sans aucun trou traversant la couche est nécessaire pour produire des PSC efficaces. Une question ouverte reste donc: «*Peut-on synthétiser des pérovskites d'halogénure dans des conditions ambiantes pour des cellules solaires stables et efficaces?*»

Ce chapitre présente une méthode de fabrication à l'ambiante de couches minces de pérovskite aux halogénures stables (23^{o}C ± 1^{o}C, > 55% ± 5%RH). Cet objectif a été atteint en d'utilisant des additifs (i) modifiant le solvant et (ii) dopant la couche minces de perovskite pour améliorer la microstructure, les performances et la durée de vie des couches minces de pérovskite d'halogénure. Pour obtenir le résultat souhaité, des films conventionnels $CH_3NH_3PbI_3$ (MAPI) avec et sans les additifs ont été fabriqués et les performances de leur dispositif ont été évaluées. Un pseudo-halogénure, le thiocyanate de plomb ($Pb(SCN)_2$), a été ajouté à la solution originale du précurseur de pérovskite (MAPI dans ce cas), et ses effets sur les performances ont été étudiés en détail. L'incorporation de $Pb(SCN)_2$ dans MAPI entraîne la substitution partielle de I^- par SCN^- en sites tétragonaux pour former $CH_3NH_3PbI_{3-x}(SCN)_x$. L'ajout de SCN^- ne modifie pas la structure cristallographique de MAPI car SCN^- a un rayon ionique (~ 0,217 nm) similaire à celui (~ 0,220 nm) des ions iode.[191] De plus, Ganose et al. ont montré qu'en fonction de leur énergie de décomposition positive la pérovskite hybride modifiée à l'aide de SCN ne se décompose pas spontanément. Par conséquent, la perovskite dopée/modifiée présente une stabilité thermodynamique plus élevée que le MAPI (qui a une énergie de décomposition négative), améliorant la qualité des cristaux et les performances des cellules solaires fabriquées avec ces pérovskites hybrides dopées au thiocyanate.[142]

Les additifs de solvants sont souvent utilisés pour faciliter le processus de cristallisation des matériaux pérovskites d'halogénure. Ainsi, en ajoutant de l'eau (H_2O) déionisée et de l'éthanol (EtOH) au solvant principal (dans notre cas l'isopropanol, IPA), les effets de ces additifs de solvants sur les propriétés des couches minces de pérovskite sont étudiés. Il est souvent rapporté dans la littérature que la croissance des couches minces de pérovskite et leur stabilité sont affectées par la présence de l'humidité et de l'oxygène.[111,133] Par conséquent, l'humidité joue un rôle prépondérant dans la synthèse des pérovskites en milieu ambiant. D'une part, elle contribue à ralentir le processus de cristallisation des couches de pérovskite, améliorant ainsi leurs microstructures[174-177], d'autre part, elle contribue à la dégradation des couches de pérovskite.[42,62,178] Étant donné que nous travaillons à l'ambiante dans un environnement non contrôlé, le risque de détérioration des pérovskites est élevé en raison de l'humidité ambiante. Nous avons conçu un moyen de stabiliser les couches. On leur fournit l'essentiel en H_2O dont elles ont besoin en introduisant une quantité modérée et contrôlée de H_2O dans la solution de précurseur. Ce faisant, il n'est plus nécessaire pour les couches d'extraire l'eau de l'humidité environnante. De plus, l'ajout de l'éthanol permet d'améliorer encore plus la qualité des cristaux. L'éthanol aide à dissoudre les solutés restants tels que PbI_2 et MAI, et favorise la nucléation et la cristallisation des grains de pérovskites d'halogénure.[179]

Par conséquent, des cellules solaires ont été fabriquées à l'aide des solutions de précurseurs optimisées et leurs performances en termes des paramètres photovoltaïques et de stabilité ont été étudiées en détail. Nous avons mis en évidence la contribution essentielle de la morphologie aux performances des cellules solaires et des couches minces de pérovskite. Nous avons clairement montré que la morphologie compacte des couches minces est incontournable pour obtenir une photo-génération efficace de porteurs de charge, ainsi qu'un transport de charge et des cellules solaires à base de pérovskite d'halogénure stables.

Effet Synergique des Ions SCN, de l'eau et de l'ethanol sur la Microstructure et les Performances du Dispositif

Les micrographies de microscopie électronique à balayage (MEB) des couches minces $CH_3NH_3PbI_3$ (MAPI) et $CH_3NH_3PbI_{3-x}(SCN)_x$ (ou MPS) déposées sur substrats d'oxyde d'étain dopé au fluor (FTO) sont illustrées dans la Figure 3.1(a&b). Notamment, la morphologie des couches minces MAPI (Figure 3.1a) est caractérisée par de petits grains cristallins et de nombreux

trous, à travers lesquels on entrevoit la couche de FTO/PbI_2 (les parties blanches) en dessous. Comme espéré, avec un raffinement supplémentaire de la solution de précurseur par l'ajout d'ions SCN, 5 % en volume d'EtOH plus 2 % en volume de H_2O, la taille des grains et la microstructure sont améliorées, réduisant ainsi le nombre de trous dans la morphologie de la couche (Figure 3.1b). L'augmentation de la taille des grains implique que la surface totale couverte par les joints de grains dans la couche, ayant des propriétés d'absorption différente du volume, est réduite, indiquant ainsi le rôle primordial des additifs dans la nucléation et la cristallisation des couches de pérovskite. Cela pourrait s'expliquer par le fait que ces additifs, combinés, contribuent à obtenir une cristallisation progressive lors de la formation de la couche de pérovskite en dissolvant les solutés restants de PbI_2, $Pb(SCN)_2$ et MAI pour obtenir des couches de pérovskite lisses, sans trous, et bien cristallisées.[170,174,180]

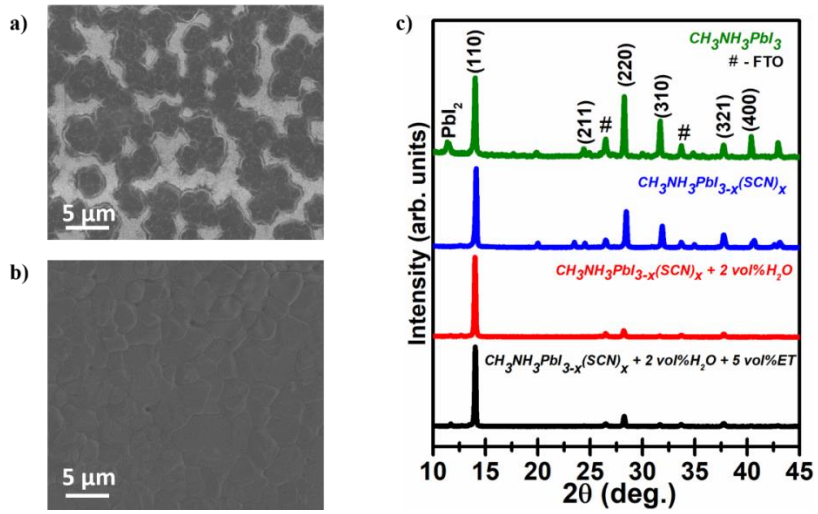

Figure 3.2: a) Image MEB d'une couche mince de pérovskite $CH_3NH_3PbI_3$. b) Images MEB de $CH_3NH_3PbI_{3-x}(SCN)_x$ avec 2 % en volume d'H_2O et 5 % en volume d'EtOH. c) Spectres XRD des couches minces synthétisées sous différentes conditions indiquées sur l'image.

La qualité cristalline des couches minces de pérovskite est étudiée par la technique de la diffraction de rayons X ou DRX. La Figure 3.1c montre les spectres DRX des différents couches minces, qui présentent des caractéristiques similaires à la structure de phase tétragonale de $CH_3NH_3PbI_3$ rapportée dans la littérature.[34,185] Les pics de diffraction caractéristiques des pérovskites, mis en évidence aux angles 2-thêta 14,10° et 28,20°, sont attribués aux plans (110) et (220) et indexés en conséquence. Ces caractéristiques DRX révèlent que les additifs n'ont pas modifié les propriétés cristallographiques du matériau pérovskite mais ont en partie aidé à obtenir des grains hautement

orientés ayant leurs plans cristallins (110) parallèles à la surface du substrat. Un examen plus attentif du modèle MAPI révèle un pic à 12,62°, ce qui correspond aux impuretés PbI_2. Ce pic PbI_2 est plus prononcé dans le spectre de MAPI que dans celui du MPS. Cependant, le pic PbI_2 a disparu lors de l'ajout simultané d'ions SCN et de quantités mélangées de H_2O et EtOH à la solution de précurseur. Cet ajout de SCN, H_2O et EtOH améliore ainsi la qualité cristalline des pérovskites tout en éliminant le pic PbI_2 par la dissolution des solutés restants.

Performances des Dispositifs: Efficacité et Stabilité

Des cellules solaires planaires à base de pérovskite hybride, avec l'architecture FTO/c-TiO_2/perovskite/Spiro-OMeTAD/Au, sont alors fabriquées en ajoutant les additifs à la solution de précurseur de pérovskite pour étudier les effets synergiques sur les performances des dispositifs de cellules solaires, notamment leur efficacité et leur stabilité.

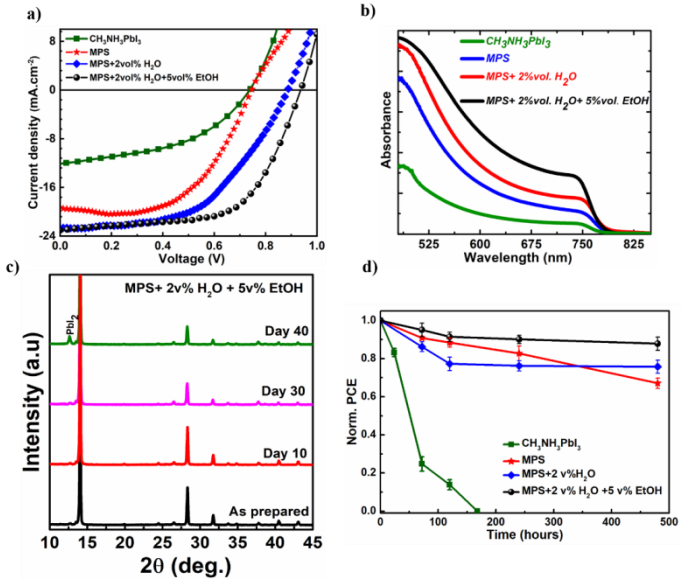

Figure 3.2 a) Caractéristiques de densité de courant en fonction de la tension (*j-V*) des différentes cellules solaires mesurées juste après leur fabrication. b) Spectres d'absorption des couches minces. c) Diagrammes DRX pour les couches minces de pérovskite exposées à l'environnement ambiant (23°C ± 1°C, > 55% ± 5%RH) étudiées sur 40 jours. d) Stabilité des dispositifs de cellules solaires exposés à l'air ambiant et testée pour 500 heures.

La Figure 3.2a montre les courbes caractéristiques *j-V* des dispositifs les plus performants. Le dispositif MAPI présente une efficacité de 4,12 %, tandis que la cellule solaire MPS affiche une efficacité de 8,35 %, le MPS + 2 v% H_2O une efficacité de 10, 61 % tandis que le MPS + 2 v% H_2O + 5 v% EtOH présente une efficacité de 13,46 %, ce qui est nettement supérieur à l'efficacité

obtenue pour le dispositif de référence (MAPI). La tendance à la hausse des performances *j-V* peut être liée à plusieurs facteurs. Tout d'abord, par rapport à l'échantillon de référence MAPI, une augmentation de l'intensité de l'absorption avec un léger décalage du bord d'absorption vers le rouge est observée (Figure 3.1b). Ce comportement pourrait être dû à la qualité cristalline améliorée et à la morphologie des couches minces sans trous.[187-189] Les performances *j-V* des cellules solaires à couche minces dépendent de la microstructure et de la cristallinité de la couche mince active. Ainsi, d'après nos résultats, les faibles paramètres PV présentés par le dispositif MAPI par rapport aux autres dispositifs avec additifs pourraient être attribués à la non-compacité des couches minces de pérovskite MAPI. En outre, sous irradiation à la lumière solaire, les mécanismes de transport de charge et de génération de photo-courant dans les cellules solaires à pérovskite d'halogénure sont fortement affectés par la morphologie, les défauts et les processus de recombinaison dans les couches minces.[190,191]

Pour des dispositifs soumis aux conditions ambiantes, les effets de la dégradation oxydative du film sont inévitables. Nous avons donc étudié la dégradation oxydative des couches minces déposées. Les échantillons ont été conservés à l'air ambiant ($23^oC \pm 1^oC$, > 55% ± 5% HR) pendant plus de 30 jours.

La dégradation des couches minces de pérovskite d'halogénure est concomitante à l'apparition de PbI_2 dans les couches et aux joints de grains. Ceci est confirmé par le pic PbI_2 dans les spectres DRX où des changements apparents sont observés durant le stockage à l'ambiante. Avec notre film optimisé de MPS+2 v% H_2O+5 v% EtOH, aucun pic de PbI_2 n'est observé avant 30 jours (Figure 3.2c). La figure 3.2d montre l'évolution de l'efficacité au fil du temps. Nous avons observé que les dispositifs MPS+2 v% H_2O+5 v% EtOH sont les plus stables avec une durée de vie, T_{80}, > 480 heures et une perte d'efficacité de seulement 12% de son efficacité originale. Ainsi, l'utilisation du dopant SCN a abouti à un matériau pérovskite hybride plus stable avec une liaison chimique améliorée. Cela est dû à de fortes interactions ioniques entre le S-C-N et le Pb adjacent et à des liaisons hydrogène supplémentaires entre SCN^- et $CH_3NH_3^+$.[142] Sur la base de ces observations, il n'est pas étonnant que le processus de dégradation dans les couches minces MAPI soit plus rapide par rapport à celui des couches minces dopées SCN. Ces résultats renforcent notre compréhension du rôle essentiel que jouent la composition chimique et les conditions de fabrication du précurseur de pérovskite dans les performances des cellules solaires à base de pérovskite d'halogénure. Il constitue également l'une des premières étapes pour relever les défis

que pose l'humidité à la fabrication et à la stabilité des couches minces de pérovskite d'halogénure fabriquées et traitées à pression et température ambiante. En effet, nos résultats suggèrent que des cellules solaires à base de pérovskite d'halogénure stables et efficaces peuvent être obtenues même si pour les couches minces de pérovskite sont synthétisées et traitées à température ambiante.

4. Cellules Solaires à Pérovskites à Triple Cation Stables et Efficaces

Nous avons présenté ci-dessus une nouvelle solution de précurseurs de pérovskite pour une fabrication à l'ambiante de cellules solaires à base de $MAPbI_3$ dopées avec SCN qui sont reproductibles, hautement cristallines, efficaces et plus stables. Afin d'améliorer encore les performances et surtout la stabilité de ces dispositifs, nous présentons maintenant, des cellules solaires à base de pérovskite hybrides fabriquées en utilisant des précurseurs aux halogénures mélangés à trois cations différents (Cs^-, MA^- et FA^-) via un additif de pseudohalogénure (SCN) et une méthode de traitement solvant-antisolvant (éthanol et chlorobenzène) au lieu des additifs eau et éthanol utilisés pécédemment.[141] Il a en effet été montré que l'utilisation d'éthanol et de chlorobenzène pour le traitement par solvant–antisolvant favorise la nucléation des grains et la cristallisation de couches minces de pérovskite.[44,179] Les effets synergiques des additifs sur les performances photovoltaïques, y compris la détermination du dopage de SCN optimal, ont été étudiés et sont présentés. Nous avons modifié la morphologie de couches minces de pérovskite à cations mixtes ainsi que les propriétés de transport de charge des dispositifs fabriqués avec ces couches. Les échantillons de pérovskite avec et sans addition de thiocyanate de plomb ($Pb(SCN)_2$) sont respectivement désignés DEV-x et DEV-0 (où x est le pourcentage en poids de l'additif). Une gamme de pourcentages entre 0 et 11,1 % en poids de l'additif a été utilisée pour déterminer le dopage optimisant les performances des cellules solaires. Grâce à notre méthode de traitement optimisée et brevetée, des grains cristallins compacts, sans trous, et de grande taille avec des joints de grains passivés sont obtenus. Les couches minces de pérovskite hybrides à triple cations ont été utilisées pour fabriquer des cellules solaires à hétérostructure n-i-p qui ont atteint un très bon rendement de 20,3 % sous un éclairage AM 1.5G standard et une excellente reproductibilité. Ces cellules solaires ont également démontré une excellente stabilité dans l'environnement ambiant (25-55% HR) sur une période de plus de dix mois. Les performances exceptionnelles de ces cellules solaires sont largement attribuées à leurs propriétés microstructurales supérieures, telles qu'une morphologie compacte, une grande taille de grain et une faible densité de piège. Cette

dernière propriété ainsi que la bonne mobilité des charges explique également leur faible dégradation lorsque les dispositifs sont stockés à l'ambiante, le mécanisme de dégradation ayant été lié à la densité des pièges et à la mobilité des charges.[228] En effet, ce travail ouvre véritablement la voie vers la fabrication de cellules solaires à pérovskite hybride et cations mixtes entièrement synthétisées à partir d'une solution de précurseurs et traitées à température ambiante, possédant à la fois un haut rendement et une bonne stabilité.

Résultats

Les performances photovoltaïques des cellules solaires à pérovskite (PSC) dépendent fortement de la morphologie des grains et de la qualité cristalline des couches minces de pérovskite. Les pérovskites d'halogénure cationiques mixtes sont modifiées par dopage avec $Pb(SCN)_2$ pour être stables dans les conditions ambiantes et ensuite utilisés pour préparer notre solution de référence (DEV-0, sans SCN) et nos solution DEV-x, avec 2,9, 5,8, 9,4 et 11,1 % en poids d'ions SCN qui sont ajoutés à la solution de pérovskite de référence. Pour élucider l'effet combiné des anions SCN et des additifs anti-solvants sur les couches minces de pérovskite, des échantillons sont fabriqués en utilisant 0 à 11,1% en poids de SCN- dans les mêmes conditions. La figure 4.1a montre la vue typique de dessus de l'image MEB d'une couche mince de pérovskite optimisée DEV-5.8. La couche mince révèle une morphologie de grain compacte avec des joints de grains (GB) moins nombreux et passivés et d'une taille de grain d'environ 2 microns. Il a été proposé que les mécanismes permettant la croissance de grains plus grands provient de l'énergie libre de Gibbs inférieure pour la nucléation en raison de l'effet bénéfique d'ion pseudo-halogénure SCN incorporé. En outre, il a déjà été démontré que la présence de joints de grains moins nombreux réduisait la recombinaison, diminuait la présence d'états de piège et passivait les sites de défauts dans les couches de pérovskite.[125,203] Par conséquent, les grandes tailles de grains dans les couches de pérovskite hybrides DEV-5.8 favorisent et expliquent le rendement élevé obtenu pour les cellules solaires fabriquées avec ces couches car les porteurs photogénérés voient des barrières réduites et moins nombreuses en termes de sites de défauts et de GB.

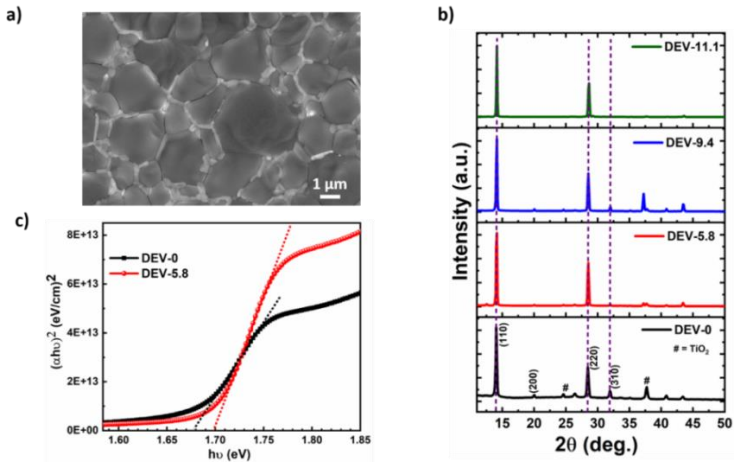

Figure 4.1. (a) Images MEB en vue de dessus d'une couche de pérovskite DEV-5.8. (b) Spectres DRX des couches de pérovskite préparées avec et sans dopant comme indiqué sur chaque spectre. (c) Diagramme de Tauc obtenu à partir des spectres d'absorption UV-Vis pour les échantillons DEV-0 et DEV-5.8.

De plus, les spectres modèles DRX acquis (Figure 4.1b) présentent des pics intenses et étroits correspondant à la structure tétragonale des pérovskites hybride aux halogénures, en accord avec les rapports précédents.[44,63] Les valeurs de largeur à mi-hauteur (FWHM) obtenues à partir du pic (110) montrent que les couches DEV-5,8 possèdent une meilleure cristallinité que les couches DEV-0 avec une valeur de 0,17º et une taille de cristallite de 47,4 nm obtenue à partir de l'équation de Scherrer[186], tandis que les couches DEV-0 présentent une valeur FWHM de 0,23º avec une taille de cristallite de 34,6 nm. À partir du diagramme de Tauc $(\alpha h\nu)^2$ en fonction de $h\nu$ sur la figure 4.1c, les bandes interdites sont estimées à 1,68 eV et 1,7 eV pour les couches de pérovskite DEV-0 et DEV-5,8 respectivement. L'utilisation d'un dopant SCN et d'un traitement au solvant améliore de manière synergique les propriétés microstructurales avec une large absorption spectrale des pérovskites à cations mixtes, qui sont des paramètres cruciaux pour un dispositif de cellule solaire à couche mince efficace.

Pour confirmer la corrélation entre la morphologie de la couche mince, la cristallinité et les performances du dispositif, nous avons comparé des cellules solaires (configuration du dispositif: Verre/FTO/compact-mesoporous-TiO_2 layer (CL-MP-TiO_2)/Perovskite/Spiro-OMeTAD/Or) fabriquées avec 0 à 11,1 % en poids de SCN (Figure 4.2a) et en utilisant des traitements au solvant à l'éthanol et au chlorobenzène (90 % en volume CB et 10 % en volume EtOH). Sur la figure 4.2a, on observe une augmentation de l'efficacité à mesure que la quantité de dopant SCN augmente jusqu'à 5,8 % en poids, après quoi il y a une diminution de l'efficacité. La figure 4.2b montre les

caractéristiques de densité de courant-tension (*J-V*) des cellules solaires optimisées DEV-0 et DEV-5.8. Les paramètres photovoltaïques des cellules solaires, y compris le *Jsc*, le *Voc*, le FF et l'efficacité, sont résumés dans le tableau 4.1. Les résultats de l'efficacité indiquent qu'en général, les cellules solaires à cations mixtes avec dopant (DEV-5.8) ont surpassé les dispositifs DEV-0 (20,3% contre 11,0% pour les cellules solaires les plus performantes). Ainsi, l'utilisation du dopant SCN a entraîné une amélioration de près de 55 % de l'efficacité en raison de FF et de *Voc* plus élevés. De plus, la mesure de l'efficacité quantique externe (EQE) confirme une excellente qualité de l'absorption de la lumière des cellules solaires atteignant plus de 90 % (Figure 4.2c). La réponse spectrale EQE démontre une extraction efficace des porteurs de charge et le taux faible de recombinaison des porteurs de nos différents dispositifs en raison de la densité réduite de joints de grains qui agissent comme des sites de piégeage des porteurs de charge.[26] En outre, les joints de grains sont préjudiciables à la stabilité des cellules solaires à base de pérovskite d'halogénure car ils constituent un canal facile permettant à l'humidité (molécules d'eau) de s'infiltrer dans la couche mince de pérovskite.[123,217]

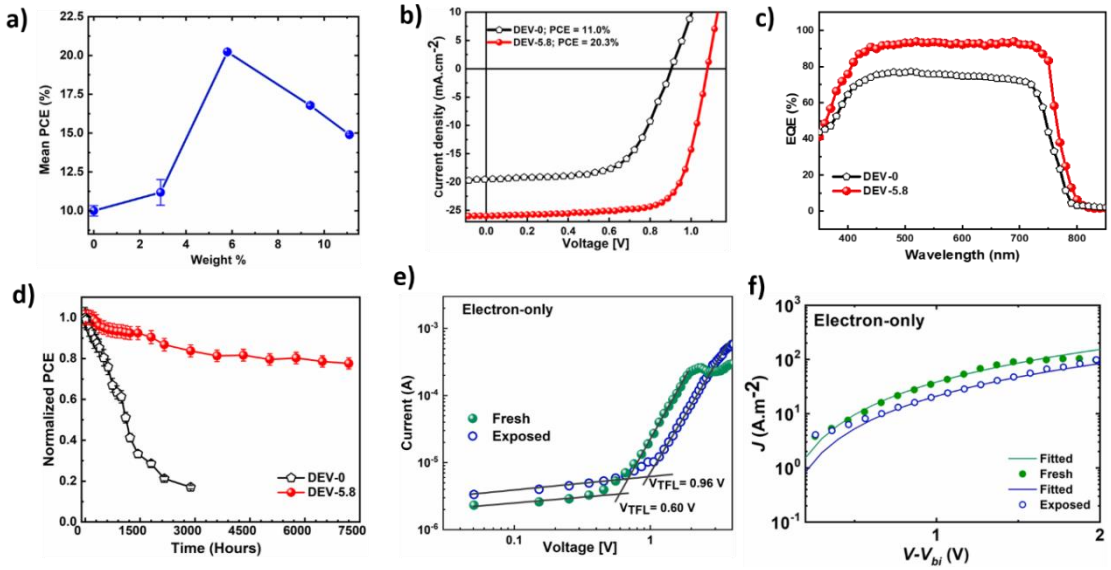

Figure 4.2. a) Evolution des performances du dispositif avec le pourcentage massique de l'additif $Pb(SCN)_2$ et le traitement 90%vol CB et 10%vol EtOH. b) Courbes *J-V* typiques obtenues sous éclairage AM1.5 de dispositifs à cellules solaires, fabriqués à l'aide d'une pérovskite avec et sans additif (DEV-0 et DEV-5.8). Les caractéristiques *J–V* ont toutes été mesurées dans des directions de balayage inversées à un taux de 16 mVs^{-1}. c) Spectres EQE des cellules solaires. d) Evolution des PCE normalisés pour les différents dispositifs mesurés à différentes périodes sur dix mois. Les appareils sont toujours mesurés et stockés dans des conditions ambiantes de laboratoire (T=22-25ºC, RH=25-55% RH. e) Courbes *J-V* de dispositifs DEV-5.8 dans l'obscurité à échelle logarithmique indiquant les tensions de remplissage du piège (V_{TFL}) et montrant les courbes ajustées (f) avec l'équation de Mott-Gurney[47] pour les mobilités lorsque fraichement déposé et exposés à l'atmosphère (240 heures aux conditions ambiantes): dispositifs à électrons seuls : FTO/CL-MP-TiO_2/perovskite/$PC_{71}BM$/Au.

Tableau 4.1: Paramètres des cellules solaires avec les valeurs moyennes et l'écart type.

Paramètres j-V	**DEV-0[a]**	**DEV-5.8[b]**
V_{oc} **(V)**	0.911 (0.90 ± 0.01)	1.083 (1.06± 0.03)
J_{sc} **(mA.cm^{-2})**	19.5 (19.09 ±0.56)	25.8 (25.04 ±0.43)
FF (%)	61.9 (58.24 ± 4.85)	72.8 (71.46± 1.23)
PCE (%)	11.0 (9.73±0.65)	20.31(9.05±0.95)

[a] 14 dispositifs et [b] 22 dispositifs.

En termes de stabilité, les cellules solaires DEV-5.8 sont sensiblement plus stables que les cellules solaires DEV-0, comme prévu à partir des résultats concernant la densité des joints de grains et la microstructure. En effet, l'ajout de SCN- améliore l'efficacité et la stabilité des pérovskites par de fortes liaisons intermoléculaires entre SCN dans la structure du réseau pérovskite.[142,200] Nous avons également obtenu une longue durée de vie pour les cellules solaires DEV-5.8 telle que déterminée par le T_{80} (le temps auquel le dispositif perd 20 % de son efficacité initial)[64] soit 523 heures pour DEV-0, et 5036 heures pour DEV-5.8 (Figure 4.2d).

Pour comprendre davantage les performances du dispositif en termes d'efficacité et de stabilité, les densités d'état de piège et les mécanismes de transport de charge[118,219,220] ont été évalués dans des dispositifs à porteurs de charge unique (ici des électrons) fraichement déposées et dégradés par la méthode limitation du courant par charge d'espace.[118,221] Lorsque fraichement déposés, nous avons observé une densité d'état de piège faible (jusqu'à 10^{15} cm^{-3}) dans les couches minces de pérovskite hybrides optimisées (Figure 4.2e), qui augmente légèrement après exposition à l'humidité (35%±5RH) en raison de la dégradation de la couche mince au fil du temps. En outre, un déséquilibre dans le transport des charges positives et négatives est constaté, entrainant une diminution du facteur de remplissage, ce qui selon nous est le principal contributeur à la dégradation de l'efficacité. Ainsi, la perte de courant électronique pourrait expliquer la dégradation observée. Nous sommes également certains que le traitement dopant SCN et solvant-anti-solvant joue un rôle de passivation très significatif et même critique, entraînant la formation de couches denses et sans trous, avec des grains de grandes tailles, ce qui contribue à réduire le taux de dégradation du dispositif de pérovskite DEV-5.8 en empêchant l'accumulation et la pénétration de l'humidité dans le dispositif et donc améliore sa stabilité à l'ambiante. Nos résultats contribuent à

établir que les performances des cellules solaires à base de pérovskite hybride sont liées à la fois à l'architecture des dispositifs, à la morphologie de la couche et la taille des grains la composant, à la densité des états piège et à l'équilibre ente les courants des porteurs de charge positifs et négatifs dans le dispositif avant et après le stockage. Ce nouveau procédé de synthèse et de traitement de couches minces de pérovskites hybrides à cations mixtes et dopée au SCN entièrement aux conditions ambiantes ouvre la voie à la production industrielle à faible coût de modules de cellules solaires efficaces et stables à long terme.

5. Photodétecteurs Basés sur le Réseau de Nanofils de Pseudohalogénure de Pérovskite

Dans les chapitres 3 et 4, nous avons étudié la synthèse de pérovskites d'halogénure efficaces et stables pour leurs applications aux cellules solaires. Nous avons démontré que l'incorporation d'ions thiocyanate et le traitement solvant-antisolvant aident à obtenir des couches minces denses avec de gros grains et qui sont stables sous conditions ambiantes. Pour montrer la polyvalence des couches minces de pérovskite d'halogénure traitables en solution pour les dispositifs optoélectroniques, nous avons étendu la portée de leur application à des dispositifs au-delà des cellules solaires en fabriquant aussi des photodétecteurs utilisant ces couches. Ce chapitre présente une procédure pour modifier la morphologie du matériau pérovskite aux halogénures afin de former des nanofils. Les propriétés optiques et microstructurales des nanofils ainsi créés ont été étudiées. De plus, les performances des photodétecteurs ont été évaluées à la fois sur des substrats rigides et flexibles.

Les photodétecteurs sont des dispositifs, souvent à base de matériaux semi-conducteurs, utilisés pour détecter des signaux optiques et le convertir en signaux électriques par le biais d'un processus électronique. Ils peuvent être réglés pour détecter la lumière à une longueur d'onde spécifique allant de l'ultraviolet à l'infrarouge. Généralement, trois processus sont identifiés dans leur mode de fonctionnement: la génération de porteurs de charges par la lumière incidente, leur transport et leur extraction sous forme de courant (ou de tension) pour fournir un signal de sortie électrique.

Si beaucoup de recherches et de progrès ont été réalisés dans l'exploitation des pérovskites d'halogénure (HP) pour des cellules solaires efficaces, moins de recherches ont étudié et exploré leur potentiel pour les photodétecteurs. Les photodétecteurs sont pourtant des dispositifs omniprésents utilisés dans diverses applications telles que les systèmes de communication, les

dispositifs portables, la surveillance environnementale et les dispositifs de détection de l'internet des objets.[70,155,229] Le marché actuel est principalement dominé par les photodétecteurs semi-conducteurs à base de silicium (Si), de germanium (Ge), de nitrure de gallium (GaN) et d'arséniure de gallium (GaAs).[230,231] En particulier, le Si et le GaN sont les matériaux les plus utilisés pour les photodétecteurs, spécialement pour la détection des ultraviolets. Bien que certains de ces photodétecteurs soient adaptés pour des mesures exigeant une sensibilité élevée et un temps de réponse rapide, ils nécessitent des méthodes de fabrication complexes et le coût final de leur fabrication est élevé.

Les matériaux pérovskites d'halogénure sont des candidats potentiels pour remplir cette niche. Ils possèdent d'excellentes propriétés optoélectroniques telles qu'une grande longueur de diffusion des porteurs de charges, une bande interdite qui peut être choisie dans une certaine gamme d'énergie, une forte absorption optique et une mobilité des porteurs bien adaptée à la photodétection.[32,258,259] En particulier, les pérovskites d'halogénure ont une faible énergie de liaison des excitons d'environ 2 meV,[241] ce qui implique que ces excitons faiblement liés peuvent être facilement dissociés même sans l'aide de matériaux collecteurs de charge.[261] La polyvalence des perovskites d'halogénure, leur facile traitement en solution et à basse température, leur adaptabilité aisée aux divers substrats et leurs bonnes performances malgré leur faible coûts, ont mené à un nombre considérable d'études et de recherches pour leur exploitation dans des applications photovoltaïques et optoélectroniques. En particulier, les perovskites d'halogénure ont été massivement explorées pour la fabrication de cellules solaires efficaces au cours de la dernière décennie. Leur application potentielle dans les photodétecteurs n'a cependant commencé susciter l'intérêt de la communauté des chercheurs qu'au cours des cinq dernières années.

L'utilisation de pérovskites d'halogénure pourrait par exemple aider à la fabrication de photodétecteurs à large bande avec une bonne réponse spectrale sur toute la gamme de fréquences du spectre électromagnétique allant de l'ultraviolet au proche infrarouge. Des études récentes cherchent à intégrer des photodétecteurs à base de pérovskite d'halogénure traitées en solution à basse température sur des substrats rigides et flexibles tels que le polyéthylène téréphtalate et le polyimide.[243-245]

Ici, nous utilisons une méthode simple pour fabriquer des photodétecteurs à nanofils de perovskite pseudo-halogénure. Le choix de photodétecteur à nanofils de perovskites d'halogénure est basé

sur nos résultats préliminaires comparant les photodétecteurs pérovskites à base de couches minces à ceux à base de nanofils (voir annexe Figure A5.4). Ce dernier a montré, en général, une meilleure performance que le photodétecteur couche mince. Ainsi, tous les résultats et les discussions dans ce chapitre concernent uniquement les photodétecteurs à nanofils. L'utilisation de nanofils favorise le transport directionnel des porteurs de charges en raison du haut rapport surface/volume. Ainsi, ils permettent d'améliorer le confinement des porteurs de charges et de limiter les mécanismes de pertes dans le dispositif, tels que la recombinaison. Dans cette étude, le réseau de nanofils de pérovskite (HPNW) est utilisé comme couche active et est déposé directement sur FTO microstructuré et de substrats flexibles en Kapton à l'aide d'un processus de dépôt en solution à basse température. Ce processus de fabrication de dispositifs de photodétection offre une voie économique et rentable comparée aux processus micro-électroniques conventionnels. Les performances des photodétecteurs sur les substrats FTO et flexibles sont évaluées à l'aide des paramètres suivants : photocourant, temps de réponse, sensibilité spectrale, détectivité spécifique et stabilité. Le processus développé et présenté ci-dessous révèle une opportunité pour la fabrication à faible coût de pérovskite d'halogénure nanostructurée qui est reproductible et stable à l'environnement, et qui fournit des dispositifs photodétecteurs avec une réponse suffisamment rapide pour une large gamme d'applications.

Caractérisation des Matériaux des Réseaux de Nanofils Pérovskites

La structure cristalline et la morphologie des HPNW de $CH_3NH_3PbI_{3-x}(SCN)_x$ tels que déposés sont étudiées en utilisant des techniques de microscopie électronique à balayage (MEB), de microscopie électronique à transmission (MET) et de diffraction des rayons X (DRX). Les morphologies de surface des réseaux de nanofils p**é**rovskites d'halogénure déposés sur les substrats en utilisant différentes molarités des solutions précurseurs ont ainsi été étudiées. Nous avons observé la production de nanofils interconnectés reliant le canal du dispositif à l'aide de solutions précurseurs de MAI et de PbI_2 dopé SCN, la concentration de cette dernière solution de précurseur étant de 0,8 M, 0,6 M et 0,4 M. La couche constituée du réseau de nanofils a une épaisseur allant de 91 à 487 nm et les images agrandies de MEB présentent des nanofils interconnectés d'un diamètre allant de 35 à 175 nm pour les échantillons de 0,8 M.

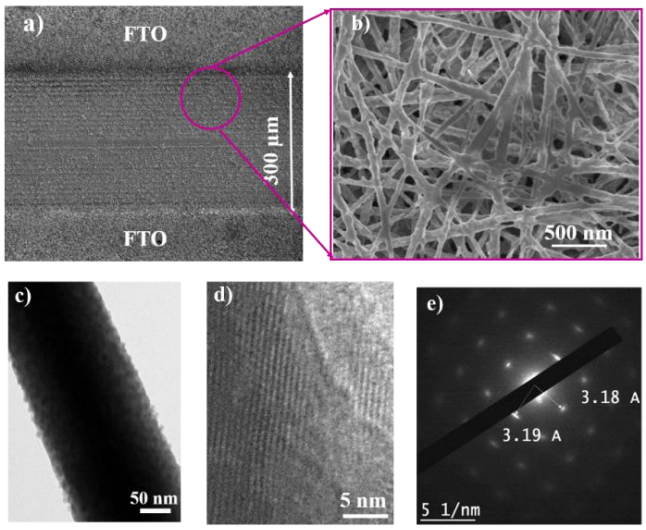

Figure 6.1: (a) Micrographies MEB de la solution de précurseur de pérovskite 0,8 M déposée sur un substrat FTO avec un canal large de 300 µm. (b) Micrographies à haute résolution des nanofils interconnectés dans le canal, indiquant la nature granulaire des nanofils. (c) Micrographie MET d'un seul nanofil montrant de petits grains de cristal orientés au hasard. (d) Image HRTEM du nanofil. (e) Modèle SAED et espacement du réseau de HP indexé à (220) de la phase tétragonale[250].

De même, l'image MET de la figure 6.1c révèle un HPNW d'environ 150 nm de large comprenant de nombreuses cristallites interconnectées. Les résultats de MET indiquent que les HPNW sont formés à partir de grains monocristallins rassemblés par leurs joints de grains. La présence de distorsion dans le réseau suggère des irrégularités dans la séquence d'empilement des plans atomiques et l'existence de défauts planaires dans les nanofils (Figure 6.1d). Les spots SAED sont allongés ou ont des réflexions diffuses qui peuvent être attribuées à la taille finie du nanofil de pérovskite d'halogénure.[251] En tant que tel, le motif SAED de la figure 6.1e présente des réflexions correspondant à la structure tétragonale orientée le long de l'axe de zone [220], suggérant une croissance préférentielle des HPNW le long de la direction [001][48] avec une constante de réseau de 3,19 Å.

Performance des Photodétecteurs à Base de Réseaux de Nanofils de Pérovskites

Les principaux paramètres qui caractérisent les performances d'un photodétecteur comprennent l'efficacité quantique, le temps de réponse, le courant d'obscurité, le gain, la puissance équivalente de bruit, la détectivité et la sensibilité spectrale. Nous avons évalué les performances du photodétecteur sur la base de ces paramètres qui sont présentés dans la section 1.3.2 de la thèse.

La photoréponse d'un photodétecteur est caractérisée par une courbe courant-tension (*I-V*), qui est la variation du photocourant en fonction de la tension. Le photocourant ($I_{ph} = I_{light} - I_{dark}$) généré à une tension donnée correspond à la différence entre le courant généré sous éclairage (I_{light}) et le courant d'obscurité (I_{dark}) .

Nous avons évalué les performances optoélectroniques des photodétecteurs à base de HPNW de $CH_3NH_3PbI_{3-x}(SCN)_x$ sur des substrats de FTO et de Kapton flexibles en utilisant les caractéristiques courant-tension (*I-V*), enregistrées par une unité source-mesure (SMU) Keithley-2400 sous une irradiation AM 1.5G d'un simulateur solaire. Les paramètres critiques discutés ici incluent le photocourant, la sensibilité spectrale, la détectivité spécifique, les temps de réponse transitoires et la stabilité.

D'après les courbes *I-V* présentées à la Figure 6.2a, le photocourant ($I_{ph} = I_{light} - I_{dark}$) augmente avec la tension appliquée aussi avec une polarité positive que négative de la tension. La caractéristique symétrique révèle un bon contact ohmique suggérant une petite barrière de potentiel à l'interface HPNW/FTO. La Figure 6.2b montre la sensibilité spectrale mesurée à une polarisation appliquée de 2 V pour les photodétecteurs optimisés avec une sensibilité maximale de 0,23 AW^{-1} pour le dispositif de 0,8 M, tandis que le dispositif le moins réactif (0,2 M) a une sensibilité de 0,17 AW^{-1} à 490 nm. De plus, la capacité des photodétecteurs à détecter des signaux lumineux faibles est caractérisée par la détectivité spécifique D*. À 490 nm, le photodétecteur 0,8 M a montré une détectivité maximale de 7,2 x 10^{11} cm. $Hz^{1/2}W^{-1}$ (Jones) et 4,7 x10^{11} Jones à 700 nm (Figure 6.2c). Le dispositif 0,2 M, lui, enregistrait 5,3 x 10^{11} Jones à 490 nm et 3,7 x10^{11} Jones à 700 nm. Les temps de réponse transitoire des photodétecteurs sont déterminés à l'aide d'un laser à 532 nm modulé à 830 Hz. Nous déterminons les constantes de temps de montée et de décroissance à l'aide de deux équations d'ajustement bi-exponentielles. Sur la base des ajustements de courbe, la constante de temps de notre dispositif le plus rapide fabriqué avec 0,4 M et en PMMA, comme le montre la Figure 6.2d, a enregistré une constante de temps de décroissance de $\tau_{d1} = \tau_{d2} = 50{,}2$ s et des constantes de temps de montée de $\tau_{r1} = 53{,}2$ µs et $\tau_{r2} = 65$ µs.

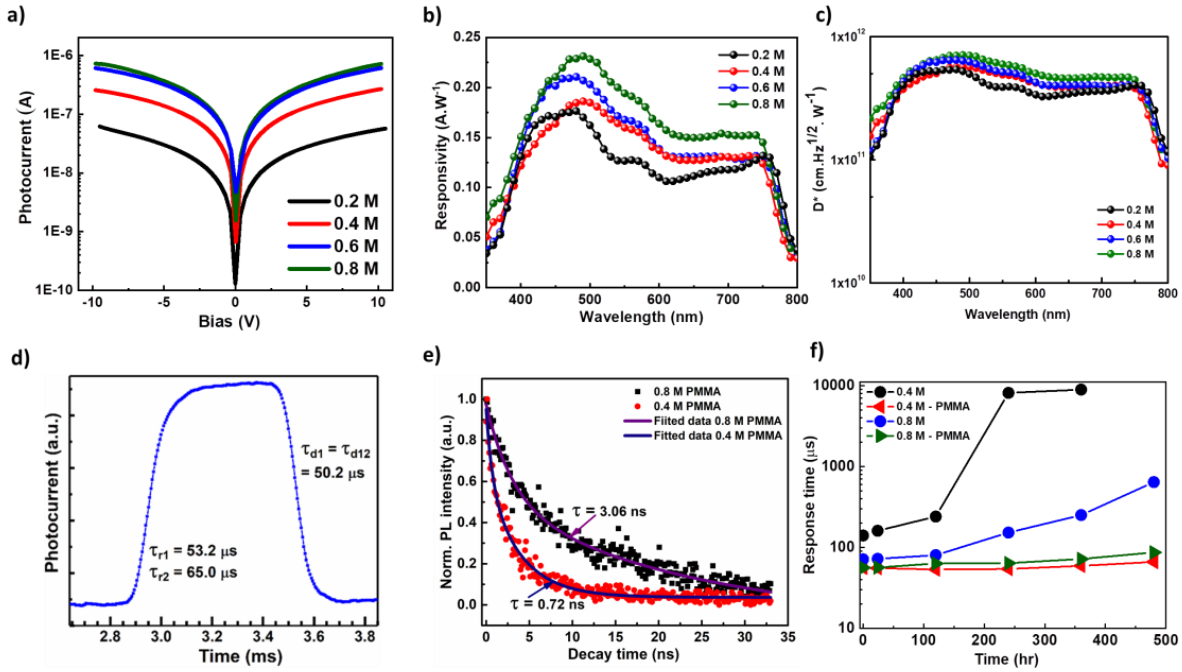

Figure 6.2: (a) Courbes caractéristiques *I-V* des photodétecteurs HPNW fabriqués avec des rapports molaires de PbI_2 dopé au SCN de 0,2 M, 0,4 M, 0,6 M et 0,8 M sur des substrats de FTO. (b) La sensibilité spectrale des photodétecteurs est mesurée à 2 V de polarisation appliquée. (c) Courbe de la détectivité spécifique des photodétecteurs. (d) Comportement de la photoréponse en fonction du temps (*I-t*) de la commutation ON/OFF réversible pour le dispositif 0,4 M avec encapsulation PMMA. (e) Spectres de photoluminescence résolus en temps avec les courbes d'ajustement bi-exponentiels pour les réseaux de nanofils de pérovskite d'halogénure de 0,4 M et 0,8 M déposés sur des substrats de verre. (f) Stabilité de la réponse au photocourant pour les dispositifs de référence et encapsulés dans du PMMA produits à l'aide de solutions de précurseurs 0,4 M et 0,8 M (conditions d'essai : 22-25 ^{o}C et 50±5 % HR).

Afin d'élucider davantage la dynamique de transport de charge, une photoluminescence résolue en temps a aussi été effectuée sur les nanofils de pérovskite. Le temps de décroissance est estimé sur la base d'une fonction de décroissance bi-exponentielle. Les HPNW basés sur 0,4 M présentaient une constante de temps rapide (τ_f) de 0,72 ns et une constante de temps lente (τ_s) de 3,84 ns tandis qu'un τ_f de 3,06 ns et τ_s de 24,1 ns sont obtenus pour des HPNW basés sur 0,8 M, comme le montre la figure 6.2.e. Les constantes de durée de vie rapide et lente sont reliées respectivement aux défauts de surface et de masse du matériau pérovskite.[263]

La stabilité des dispositifs est évaluée en mesurant l'évolution avec le temps des constantes de temps de réponse pour les dispositifs stockés dans un environnement ambiant (22-25 ^{o}C et 50±5 % HR) sur une période de mesure d'environ 20 jours. De manière peu surprenante, les dispositifs

dotés d'une couche PMMA affichent des performances fiables avec seulement 2% de perte de leur réponse initiale, comme affiché dans la Figure 6.2f. Bien que la stabilité des pérovskites dopées SCN soit connue pour être supérieure aux pérovskites non dopées, l'encapsulation a toujours également considérablement amélioré leurs performances et leur stabilité.

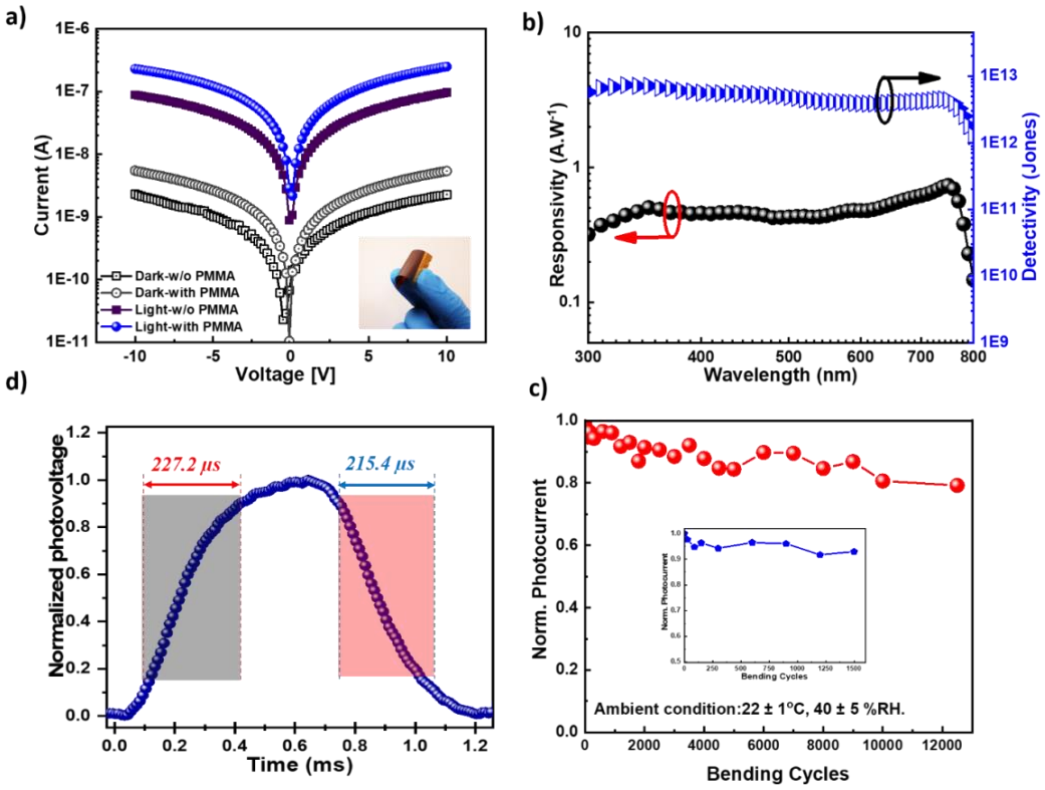

Figure 6.3: (a) Courbes *I-V* des photodétecteurs flexibles réalisés avec et sans couche de PMMA dans des conditions d'obscurité et sous éclairage en lumière blanche. (b) Sensibilité spectrale et détectivité spécifique du photodétecteur flexible HPNW. (La flèche rouge indique l'échelle de sensibilité et la flèche noire indique l'échelle de détectivité spécifique). (c) Une seule impulsion montrant les constantes de temps de montée et de descente. (d) Courbe de l'évolution du photocourant en fonction du nombre de cycles de flexion mécanique sous un éclairage en lumière blanche.

La Figure 6.3a présente les caractéristiques *I-V* des photodétecteurs flexibles fabriqués avec et sans couche de PMMA. Comme les dispositifs basés sur FTO, nous avons observé une relation symétrique et linéaire entre le courant et la tension, démontrant un comportement photoconducteur ohmique. Ainsi, lors de la photo-absorption par les HPNW, des paires électron-trou sont générées, entraînant une augmentation de la conductivité dans le matériau actif. En outre, nous avons obtenu une sensibilité maximale de 0,62 AW^{-1} à une polarisation appliquée de 10 V et une détectivité

spécifique correspondante de 7,3 x 10^{12} Jones comme montré sur la Figure 6.3b. La réponse transitoire affiche un comportement du photodétecteur stable et reproductible et les temps de montée et de descente estimés sont respectivement de 227,2 µs et 216,4 µs, comme affichés dans la Figure 6.3c. Dans l'ensemble, le photodétecteur affiche des vitesses de réponse rapides et une détectivité élevée.

La flexibilité des photodétecteurs est caractérisée en utilisant l'évolution des performances dans des conditions de flexion. La figure 6.3d montre une stabilité incroyable du photocourant, conservant plus de 92 % de sa valeur initiale pendant les 1500 premiers cycles de flexion (voir image insérée) et 80 % pour plus de 12000 cycles de flexion. Cette formidable stabilité mécanique peut être associée à la flexibilité offerte à la fois par la structure du dispositif à base de HPNW de pérovskite d'halogénure et par le substrat de Kapton utilisé dans cette étude.

Compte tenu de la simplicité de la fabrication du dispositif, des coûts des matériaux et de la reproductibilité des résultats, le dispositif photodétecteur optimisé HPNWs utilisant une solution de précurseur de 0,8 M a atteint d'excellentes performances avec des sensibilités comparables à celle rapportée dans la littérature utilisant des processus de fabrication plus complexes. De plus, les dispositifs encapsulés en PMMA ont présenté une stabilité de réponse transitoire supérieure par rapport aux dispositifs vierges. Cela suggère que l'encapsulation de PMMA aide à réduire les pertes provenant de la recombinaison des porteurs aux joints de grains et aux états de surface. De plus, la couche de PMMA aide à passiver et protéger les nanofils de pérovskite de la dégradation due à l'oxygène et à l'humidité, améliorant ainsi à la fois les performances et la stabilité des dispositifs. Nous attribuons également les temps de réponse rapides obtenus à la contribution synergique de la passivation des joints de grains avec le PMMA et le PbI_2 dopé SCN, qui minimisent leurs impacts négatifs, ainsi qu'à la nature 1-D du nanofil de pérovskite d'halogénure qui facilite le transport de charge vers les électrodes. Par conséquent, ces photodétecteurs économiques à base de nanofils de pérovskite d'halogénure sont fabriqués de manière rapide et simple entièrement dans un environnement ambiant. Ceci en fait des candidats appropriés pour la mise à l'échelle et la fabrication de masse de dispositifs optoélectroniques hautement efficaces avec des applications viables dans l'électronique portable, les biocapteurs et les technologies de fibre optique.

6. Conclusions et Perspectives

Conclusions

Des experts ont suggéré qu'il faudrait des centaines d'années pour fabriquer et installer suffisamment de panneaux photovoltaïques en silicium pour répondre à la croissance continue et incessante de la demande énergétique mondiale et atteindre les objectifs mondiaux de décarbonisation qui ralentiraient l'impact du changement climatique. Compte tenu du temps limité pendant lequel il serait possible de prévenir un changement climatique catastrophique, des sources d'énergie alternatives doivent être mises en place de toute urgence. Pendant des années, les scientifiques ont expérimenté des matériaux candidats alternatifs qui permettraient aux panneaux solaires de récolter de l'énergie à un coût inférieur à celui du silicium cristallin. De nos jours, Il existe quelques concepts et dispositifs basés sur des couches minces via un processus de synthèse en solution qui ont émergé et qui ont le potentiel de pouvoir produire des dispositifs énergétique à haute efficacité.[272]

Les pérovskites d'halogénure sont des exemples de tels matériaux qui ont attiré une attention considérable au cours de la dernière décennie en raison de ses multiples propriétés et de sa vaste gamme d'application dans des dispositifs optoélectroniques. Comme toutes les autres technologies à leur stade initial, les pérovskites d'halogénure ont été et sont toujours confrontées à des défis. Les trois principaux éléments pour qu'une technologie soit commercialement viable sont l'efficacité, la stabilité au fil du temps (déterminant leur durée de vie utile) et le coût. La principale question d'intérêt que nous nous sommes posée au cours de cette recherche est la suivante : «Peut-on fabriquer des dispositifs à base de pérovskites d'halogénure efficaces et stables sous conditions ambiantes?» Dans cette thèse, nous avons démontré que c'était le cas et nous avons établi une voie pour synthétiser des matériaux pérovskites d'halogénure entièrement à l'ambiante pour des applications photovoltaïques et optoélectroniques, principalement des cellules solaires et des photodétecteurs. Nous avons notamment travaillé sur un procédé de fabrication à l'air ambiant au lieu du procédé couteux habituel qui se déroule dans un environnement contrôlé. Nous avons d'abord préparé des solutions précurseurs de pérovskite d'halogénure organique-inorganique à un seul cation en ajoutant des additifs pseudo-halogénures et un mélange de solvants. Nos études ont révélé que l'humidité joue un rôle fondamental lors de la préparation du précurseur et affecte les propriétés microstructurales et optoélectroniques des couches minces de pérovskite d'halogénure

préparés par une technique de dépôt par enduction centrifuge ou «spin coating» en deux étapes. Étant donné que l'humidité peut provoquer une détérioration rapide des pérovskites, nous avons préparé des pérovskites à cations mixtes et approfondi nos investigations en incorporant l'ingénierie des solvants ainsi que des additifs ioniques dans le processus de fabrication des cellules solaires. Les dispositifs fabriqués à l'aide de notre nouveau procédé de synthèse à température ambiante ont montré des efficacités très élevés et une stabilité à l'ambiante remarquable. Par la suite, en remplaçant le matériau de transport de trous Spiro-OMeTAD dans l'hétérostructure des cellules solaires par du thiocyanate de cuivre (CuSCN), nous avons pu améliorer encore le processus de synthèse des dispositifs fabriqués tout en conservant de bonnes performances photovoltaïques[273] (voir *l'annexe II* pour plus de détails). Enfin, nous avons exploré la polyvalence des matériaux pérovskites d'halogénure en remplaçant les couches continues de pérovskites hybrides par des réseaux de nanofils de perovskite d'halogénure via un processus de synthèse en solution modifié et utilisé pour la fabrication de photodétecteurs. Après l'introduction de quelques principes fondamentaux sur l'énergie solaire et les dispositifs photovoltaïques, ainsi que sur les matériaux et dispositifs à base de pérovskites d'halogénure, leur architecture et les techniques de synthèse dans les chapitres 1 et 2, les résultats de la thèse sont discutés en détail dans les chapitres 3, 4 et 5 et 6.

Perspectives

Malgré les défis rencontrés au cours de ce travail, nous avons atteint notre objectif : la fabrication de dispositifs photovoltaïques et optoélectroniques à pérovskite d'halogénure stables et efficaces sous conditions ambiantes. En début de recherche, il y a environ cinq ans, les dispositifs à pérovskites d'halogénure ne survivaient que quelques heures sous conditions opérationnelles. De plus, la plupart des rapports dans la littérature visaient à améliorer l'efficacité des dispositifs fabriqués dans des conditions très bien contrôlées, par exemple sous atmosphère inerte. Seuls quelques rapports envisageaient un traitement à l'ambiante. Mais ces dispositifs synthétisés sous conditions ambiantes présentaient de faibles performances. En général, il n'y avait que quelques études de stabilité, par rapport aux efforts de la communauté scientifique pour augmenter l'efficacité. Nous considérons donc que nos travaux de recherches ont apporté une contribution significative dans ce domaine. Bien que nous ayons pu fabriquer des dispositifs de bonne qualité

avec de bonnes performances sous conditions ambiantes, il reste encore des défis ouverts qui nécessitent l'attention de la communauté scientifique:

Les études de stabilité dans ce travail sont limitées aux effets de l'humidité continue et à l'éclairage sur des cellules solaires non encapsulées. Bien que la stabilité atteinte soit assez remarquable, les pertes sont principalement dues à la dégradation oxydative et au poids mécanique. Nous soupçonnons que d'autres conditions environnementales ardues, telles que la chaleur et/ou une forte illumination UV (par exemple dans des telles que celles auxquelles seraient soumis un dispositif dans l'espace), pourraient détériorer les dispositifs très rapidement. Par conséquent, les travaux sur la stabilité de nos dispositifs devraient être étendus pour étudier leur comportement dans des conditions de fonctionnement réelles (par exemple en commençant tout simplement par des études à l'extérieur du laboratoire). Un banc d'essais pourrait être conçu pour étudier la dégradation des cellules solaires à pérovskites d'halogénure *in situ* et permettant d'étudier simultanément les effets de la lumière UV, de l'humidité, de l'oxygène et de la chaleur sur les dispositifs. Enfin, des analyses XPS et FTIR d'échantillons fraîchement préparés ainsi que de différents échantillons détériorés pourraient aussi être effectuées pour donner de plus amples informations sur les mécanismes de dégradation.

Dans le chapitre 5, la préparation des nanofils de pérovskite a été réalisée grâce à une simple technique de «spin coating», et il est supposé que le réseau de nanofils provient d'un processus de cristallisation. Le mécanisme détaillé et complet de cette croissance des nanofils et du réseau de nanofils, aussi intéressant soit-il, est encore inconnu et n'a pas été complètement abordé dans ce travail. Ainsi, un autre sujet important de recherche serait une étude détaillée du mécanisme de croissance des nanofils par un outil de caractérisation in-situ et/ou éventuellement en simulant le processus à l'aide des logiciels de croissance cristalline disponibles. Cela fournirait un aperçu indispensable du mécanisme de croissance des nanofils de pérovskites d'halogénure et des réseaux de nanofils et ouvrirait la voie à leur production à grande échelle à travers un processus de synthèse en solution et de traitement à basse température.

Bien que nous puissions fabriquer avec succès des cellules solaires qui répondent aux exigences technologiques viables : haute efficacité, longue durée de vie et faible coût, un problème persistant avec la technologie de pérovskites d'halogénure est la toxicité due à la présence de plomb. À l'heure actuelle, il y a deux opinions sur la toxicité du plomb. Certains soutiennent que la quantité

ou le niveau de toxicité du plomb présent dans ces dispositifs est relativement faible et sans comparaison avec certaines autres technologies existantes comme les batteries aux ions lithium. Les autres sont d'avis que tout ce qui est toxique ne convient pas à une source d'énergie dite propre.

Par exemple, l'élimination et la sécurité à long terme des cellules solaires au tellurure de cadmium (CdTe) est un problème connu, mais qui ne semble pas affecter trop leur commercialisation à grande échelle. Bien que le cadmium soit toxique, difficile à synthétiser en grande quantité et que le tellure soit lui aussi rare et que cela puisse limiter le nombre de panneaux pouvant être fabriqués, leur efficacité record en laboratoire atteint 22,1 %. Ils représentent la deuxième technologie photovoltaïque commercialisée sur le marché après le silicium cristallin photovoltaïque. Ainsi, le développement de protocoles de recyclage est indispensable pour limiter l'impact environnemental de telles technologies, et ce problème n'est de loin pas exclusif aux pérovskites d'halogénure de plomb. Actuellement, les chercheurs travaillent activement sur le développement de substituts au plomb non toxiques, tels que l'étain, et au développement de protocoles de recyclage pour limiter l'impact environnemental de ces technologies.[106] Néanmoins, les cellules solaires pérovskites d'halogénure sont toujours considérées par la plupart des experts comme la technologie photovoltaïque du futur. Des efforts considérables sont déployés pour augmenter l'efficacité et la stabilité des cellules solaires à base de pérovskites d'halogénure, pour prolonger leur durée de vie et pour rendre cette technologie aussi propre ou «verte» que possible afin de limiter au maximum les impacts environnementaux et sanitaires.

À cet égard, nous avons réalisé quelques expériences préliminaires en utilisant une alternative aux pérovskites d'halogénure de plomb, à savoir les pérovskites d'halogénure de bismuth, pour fabriquer des cellules solaires. Dans cette tentative de pérovskite d'halogénure «sans plomb», nous avons étudié l'iodure de méthylammonium bismuth $(CH_3NH_3)_3Bi_2I_9$ (MBI) pour la fabrication de cellules solaires. Nous avons exploré différentes techniques de dépôt : «spin coating» en une étape ou en deux étapes et dépôt par immersion dans les solutions de précurseurs pour obtenir une couverture uniforme et de haute qualité des couches minces. Notre approche la plus réussie a été le «spin coating» en une étape, qui a donné de gros grains de forme hexagonale. Cependant, l'efficacité des cellules était extrêmement faible. Mais elles ont par contre montré une excellente stabilité à long terme. Nous prévoyons que la faible efficacité est due à la large bande interdite du MBI, autour de 2,2 eV, à la non-uniformité de la couche mince et aux nombreux défauts prédits

pour le MBI.[274-279] Des travaux supplémentaires dans cette direction avec une analyse à l'aide de l'informatique, utilisant des outils tels que la DFT, aideraient à comprendre la structure électronique détaillées de ces matériaux et leurs propriétés. Sur la base des résultats du travail de ma thèse, une voie de fabrication pourrait être conçue vers des dispositifs de pérovskite d'halogénure à hautes performances à base de bismuth. En outre, d'autres éléments divalents peuvent encore être explorés pour remplacer le plomb, avec en cas de succès, le potentiel de voir le problème de toxicité des cellules solaires à base de perovskites d'halogénure résolu.

APPENDIX III

List of Publications

First-authored publications related to the work presented in this thesis.

Contribution: I was fully in charge and managing most of these projects, conceived and developed the perovskite materials' various preparations and syntheses, while their subsequent integration into various devices was a team effort. I performed most of the experiments and measurements presented in the thesis and reached out to collaborators to obtain additional measurements. I also carried out the data analysis and the interpretations of the results with notable and valuable inputs from all my co-authors. I wrote the first version of the manuscripts and participated in the revision with inputs from my co-authors.

1. **Asuo, I. M.**; Bouzidi, S.; Ka, I.; Rosei, F.; Pignolet, A.; Nechache, R.; Cloutier, S. G. All-Ambient-Processed CuSCN as an Inexpensive Alternative to Spiro-OMeTAD for Perovskite-Based Devices. *Energy Technol.* **2021**, *9* (1). https://doi.org/10.1002/ente.202000791.

2. **Asuo, I. M.**; Gedamu, D.; Doumon, N. Y.; Ka, I.; Pignolet, A.; Cloutier, S. G.; Nechache, R. Ambient Condition-Processing Strategy for Improved Air-Stability and Efficiency in Mixed-Cation Perovskite Solar Cells. *Mater. Adv.* **2020**, *1* (6), 1866–1876. https://doi.org/10.1039/d0ma00528b.

3. **Asuo, I. M.**; Ka, I.; Gedamu, D.; Pignolet, A.; Nechache, R.; Cloutier, S. G. Tunable Thiocyanate-Doped Perovskite Microstructure via Water-Ethanol Additives for Stable Solar Cells at Ambient Conditions. *Sol. Energy Mater. Sol. Cells* **2019**, *200*, 110029. https://doi.org/10.1016/j.solmat.2019.110029.

4. **Asuo, I. M.**; Fourmont, P.; Ka, I.; Gedamu, D.; Bouzidi, S.; Pignolet, A.; Nechache, R.; Cloutier, S. G. Highly Efficient and Ultrasensitive Large-Area Flexible Photodetector Based on Perovskite Nanowires. *Small* **2019**, *15* (1), 1804150. https://doi.org/10.1002/smll.201804150.

5. **Asuo, I. M.**; Gedamu, D.; Ka, I.; Gerlein, L. F. L. F.; Fortier, F.-X.; Pignolet, A.; Cloutier, S. G. S. G.; Nechache, R. High-Performance Pseudo-Halide Perovskite Nanowire Networks for Stable and Fast-Response Photodetector. *Nano Energy* **2018**, *51*, 324–332.

Publications not related to the work presented in this thesis

Contribution: In general, for many of these publications, I was involved in the projects right from the initial stages. I helped perform some of the experiments and measurements. I took part in the data analysis and the interpretations of the results. On some occasions, I was involved in writing part of the first version of the manuscripts. In particular, for the publication where I am designated as having 'equally contributed', my involvement was even more significant and extended from the beginning to the end of the process.

6. **Asuo, I. M.**; Banerjee, D.; Pignolet, A.; Nechache, R.; Cloutier, S. G. Perovskite/Silicon-Nanowire-Based Hybrid Heterojunctions for Fast and Broadband Photodetectors. *Phys. Status Solidi - Rapid Res. Lett.* **2021**, *15* (4). https://doi.org/10.1002/pssr.202000537.

7. Gedamu, D.; **Asuo, I. M.**; Benetti, D.; Basti, M.; Ka, I.; Cloutier, S. G.; Rosei, F.; Nechache, R. Solvent-Antisolvent Ambient Processed Large Grain Size Perovskite Thin Films for High-Performance Solar Cells. *Sci. Rep.* **2018**, *8* (1), 12885. https://doi.org/10.1038/s41598-018-31184-0.

8. Ka, I.; **Asuo, I. M.**; Nechache, R.; Rosei, F. Highly Stable Air Processed Perovskite Solar Cells by Interfacial Layer Engineering. *Chem. Eng. J.* **2021**, *423*, 130334. https://doi.org/10.1016/J.CEJ.2021.130334.

9. Ka, I.; Gerlein, L. F.; **Asuo, I. M.**; Bouzidi, S.; Gedamu, D. M.; Pignolet, A.; Rosei, F.; Nechache, R.; Cloutier, S. G. Solution-Processed p-Type Copper Thiocyanate (CuSCN) Enhanced Sensitivity of PbS-Quantum-Dots-Based Photodiode. *ACS Photonics* **2020**, *7* (7), 1628–1635. https://doi.org/10.1021/ACSPHOTONICS.0C00491.

10. Ka, I.; Gerlein, L. F.; **Asuo, I.M.**; Nechache, R.; Cloutier, S. G. An Ultra-Broadband Perovskite-PbS Quantum Dot Sensitized Carbon Nanotube Photodetector. *Nanoscale* **2018**, *10* (19), 9044–9052. https://doi.org/10.1039/C7NR08608C.

11. Ka, I.; **Asuo, I. M.**; Basu, S.; Fourmont, P.; Gedamu, D. M.; Pignolet, A.; Cloutier, S. G.; Nechache, R. Hysteresis-Free 1D Network Mixed Halide-Perovskite Semitransparent Solar Cells. *Small* **2018**, *14* (38), 1802319. https://doi.org/10.1002/smll.201802319.

12. Banerjee D.*; **Asuo I.M.***;Fortier F.; Pignolet A.; Cloutier S.G. High Performance Nanoplasmonic UV/VIS/NIR Photodetector Fabricated in Ambient Condition. **2021**. https://doi.org/10.21203/RS.3.RS-694838/V1.

13. Banerjee, D.*; **Asuo, I. M.***; Pignolet, A.; Nechache, R.; Cloutier, S. G. High Performance Photodetectors Using Porous Silicon-TiO_2 Heterostructure. *Eng. Res. Express* **2020**, *2* (3), 035021. https://doi.org/10.1088/2631-8695/ABB06D.

14. Banerjee, D.*; **Asuo, I. M.***; Pignolet, A.; Cloutier, S. G. Low-Cost Photodetector Architectures Fabricated at Room-Temperature Using Nano-Engineered Silicon Wafer and Sol-Gel TiO_2 – Based Heterostructures. *Sci. Rep.* **2019**, *9* (1), 1–9. https://doi.org/10.1038/s41598-019-54481-8.

15. Trudeau, C.; Bolduc, M.; Beaupre, P.; Ka, I.; **Asuo, I. M.**; Cloutier, S. G. Inkjet-Printing of Methylammonium Lead Trihalide Perovskite-Based Flexible Optoelectronic Devices. In *2018 International Flexible Electronics Technology Conference (IFETC)*; IEEE, 2018; pp 1–6. https://doi.org/10.1109/IFETC.2018.8583950.

16. Guo X.*; **Asuo, I. M.***; Pignolet, A.; Nechache, R.; Cloutier, S. G. Ambient Fabrication of Efficient Triple Cation Perovskite-Based Near-Infrared Light-Emitting Diodes (Accepted, Optical Materials Express, 2021).

* Equal Contribution

Patent

Asuo, I. M.; Gedamu, D. M.; Ka, I.; Cloutier, S.; Nechache, R.; Pignolet, A. Doped Mixed Cation Perovskite Materials and Devices Exploiting Same. WO2020248063A1 (PCT), **2020**. https://patents.google.com/patent/WO2020248063A1/en.

Start-Up Base on this Research Work

Co-Founder of Pi-Sol Technologies. Inc, Canada

Pi-Sol Technologies is now under the umbrella of WattByWatt.Inc

https://whitehaven.ca/en/news/wattbywatt-signs-exclusive-license-agreement/